In situ TEM study of reduction and reoxidation of NiO/ceramic composites

THÈSE N^{O} 6376 (2014)

PRÉSENTÉE LE 31 OCTOBRE 2014

À LA FACULTÉ DES SCIENCES ET TECHNIQUES DE L'INGÉNIEUR

LABORATOIRE D'ÉNERGÉTIQUE INDUSTRIELLE

ET

CENTRE INTERDISCIPLINAIRE DE MICROSCOPIE ÉLECTRONIQUE

PROGRAMME DOCTORAL EN SCIENCE ET GÉNIE DES MATÉRIAUX

ÉCOLE POLYTECHNIQUE FÉDÉRALE DE LAUSANNE

POUR L'OBTENTION DU GRADE DE DOCTEUR ÈS SCIENCES

PAR

Quentin JEANGROS

acceptée sur proposition du jury:

Dr S. Mischler, président du jury
Dr J. Van Herle, Dr A. Hessler-Wyser, directeurs de thèse
Prof. W. Chiu, rapporteur
Prof. T. Epicier, rapporteur
Prof. P. Muralt, rapporteur

ÉCOLE POLYTECHNIQUE
FÉDÉRALE DE LAUSANNE

Suisse
2014

Acknowledgements

While a Ph.D. thesis is associated mainly to the name of its author, in this particular case mine, it is nothing less than a collective effort and can succeed only with the support of numerous people who all contribute in their way, scientifically or not. It's hence my great pleasure to gratefully acknowledge everyone involved in this project, which spanned across different laboratories, entities and countries, and in particular:

Funding Swiss National Science Foundation.

Supervision Dr. MER Aïcha Hessler-Wyser & Dr. MER Jan Van herle for enabling and supervising the project.

Jury Dr. Thierry Epicier, Prof. Wilson Chiu, Prof. Paul Muralt and Dr. MER Stefano Mischler for accepting the task of assessing this Ph.D. thesis.

CIME Prof. Cécile Hébert for supervision and help related to EELS and EFTEM, Dr. Guillaume Lucas for help related to Digital Micrograph scripts, Brian Aebersold for automated crystal orientation mapping experiments and their interpretation, Dr. Antonin Faes for showing me the way, Emad Oveisi for surviving in the same office as me and for general discussions about both electron microscopy and non-scientific topics, Dr. Marco Cantoni & Dr. Duncan Alexander for the time spent training me on the different microscopes at the CIME, Danièle Laub, Colette Vallotton & Fabienne Bobard for the most appreciated help related to sample preparation, Dr. Amélie Bazzoni, Dr. Guillaume Pasche, Dr. Andreas Schuler, Dr. Pierre Burdet, Dr. Jonas Vannod, Prof. Pierre Stadelmann, Annick Evequoz & everyone from the CIME.

CEN Dr. Thomas Hansen & Prof. Jakob Wagner for enabling the project, ETEM access/training and a fruitful collaboration, Prof. Christian Damsgaard for help related to *in situ* XRD experiments, Dr. Takeshi Kasama & Dr. Sadegh Yazdi for general help and holography experiments, Dr. Filippo Cavalca, Dr. Jens Kling, & Wily Huyzer for support when things did not go according to the plan, Andy Burrows & the rest of the CEN collaborators for their kind welcome and help.

Acknowledgements

ERC Prof. Rafal Dunin-Borkowski for enabling the collaboration, fruitful discussions and innumerable inputs.

CLYM Prof. Thierry Epicier, Dr. M. Aouine & co-workers for ETEM experiments.

Fuelmat Dr. Stefan Diethelm for help related to experimental setups, Dr. Henning Lübbe for BET measurements, Alexandra Morrison & everyone from the Fuelmat group and ex-Leni Pile.

ETH Theory Dr. Ulrich Aschauer for DFT calculations.

LC & LTP Jacques Castano & Carlos Morais for access to furnaces & thermogravimetry.

CSEM Dr. Massoud Dadras for ESEM experiments.

HTceramix Dr. Zacharie Wuillemin & Dr. Dario Montinaro for SOFC samples.
SOFCPOWER

Students François Loisy, Mahmoud Hadad, Fazel Parsapour, Leili Batooli, Aslam Mohamed, Fahrang Nabiei, Christina Olk, Konrad Rolle, Evgeniy Ponomarev & Aashika Shah.

CPH Christian Monsson, Christian Bille-Sandø, Davide Deiana, Diego Gardini & Louise Søgaard Jensen for the most appreciated accommodation and company in Copenhagen.

Personal Bernard, Isabelle, Marine, Marguerite, Georges, Simone & at last but not least Céline for past, present and future support!

A warm thank you to all of you and to those I forgot...

Lausanne, 18th August 2014 Q.

Abstract

Nickel/ceramic solid oxide fuel cell anodes exhibit a dimensional instability when experiencing a reduction-oxidation cycle. As fuel is supplied on the anode side, the as-sintered nickel oxide phase (NiO) reduces to metallic Ni and then remains in this state during operation. Yet, several factors may lead to an accidental reoxidation of the Ni, which may rupture parts of the cell, hence degrading its performance.

The mechanisms behind the dimensional instability of Ni/yttria-stabilised zirconia (YSZ) anodes are investigated here through an innovative environmental transmission electron microscopy assessment. NiO particles and NiO/YSZ composites are reduced and reoxidised in the microscope in a few mbar of H_2 and O_2, respectively, up to 500-850 $^{\circ}$C. Images, diffraction patterns, electron energy-loss spectra and energy-filtered micrographs are acquired, usually at constant temperature intervals during the reactions, to capture *in situ* the nanostructure, crystallography and chemistry. The reaction kinetics are retrieved from both the changes in shapes of the Ni $L_{2,3}$ edges in energy-loss spectra and from energy-filtered images (with nm-resolution), analysed to provide quantitative data and correlated to the structure. Complementary data include post-exposure microscopy, *in situ* X-ray diffraction and density functional theory computations.

While the surface nucleation of Ni domains, their growth and impingement control the reduction of NiO particles, the results reveal a modification of the mechanisms in the presence of yttria-stabilised zirconia, with the transfer of oxygen from NiO to the oxygen vacancies of the YSZ ceramic now triggering the reaction. Intragranular voids form in both cases as oxygen is removed. The final Ni structure at high temperature is then observed to coarsen as it minimises its surface energy, with the percolation of the Ni phase influenced by the symmetry of its grain boundaries. The reoxidation of Ni is controlled mainly by the outward diffusion of Ni ions through the grain boundaries of the growing NiO film. While some NiO inward growth occurs through the formation of oxide film cracks, the Ni^{2+} outward diffusion process remains unbalanced and voids form in the NiO phase. These internal voids are responsible for the dimensional instability of the composite along with Ni coarsening at high temperature. Several parameters for improved performance and redox tolerance are then identified based on these results.

Keywords environmental transmission electron microscopy (ETEM); electron energy-loss spectroscopy (EELS); solid oxide fuel cells (SOFC); nickel; reduction; oxidation.

Résumé

Les anodes nickel/céramique des piles à combustible à oxyde solide sont dimensionnellement instables lors d'un cycle d'oxydoréduction. Lors de l'opération d'une pile, un combustible est injecté du côté de l'anode, ce qui réduit l'oxyde de nickel (NiO) initial en métal (Ni), état dans lequel la pile opère. Différents facteurs peuvent cependant induire la réoxydation du Ni, ce qui peut fissurer certaines régions de la pile et ainsi la dégrader.

Les mécanismes qui régissent cette instabilité des composites Ni/zircone yttriée (YSZ) sont étudiés ici par une approche novatrice qui implique de la microscopie électronique en transmission environnementale. Des particules de NiO et des composites de NiO/YSZ sont réduits/réoxydés dans le microscope sous une pression de H_2/O_2 (mbar) jusqu'à 500-850 $^{\circ}$C. Des images, des figures de diffraction, des spectres de perte d'énergie des électrons et des images filtrées en énergie sont obtenus à intervalles de température constants pour saisir *in situ* les changements de structure, cristallographie et chimie. La cinétique de réaction est extraite des pics $L_{2,3}$ des spectres de perte d'énergie et, à l'échelle du nm, des images filtrées. Celle-ci est analysée de manière quantitative et corrélée à la nanostructure. De la microscopie *ex situ* avancée, de la diffraction des rayons X *in situ* et des calculs (théorie de la fonctionnelle de la densité) complètent ces résultats.

Tandis que la nucléation de domaines de Ni sur la surface du NiO, leur croissance et leurs interactions contrôlent la réduction des particules de NiO, la présence de la phase YSZ modifie la réaction, qui est dès lors déclenchée par le transfert d'oxygène du NiO dans les lacunes de la céramique YSZ. Alors que dans les deux cas la structure est poreuse lorsque l'oxygène est enlevé, la structure devient dense à haute température, structure dont la connectivité est déterminée par la symétrie de ses joints de grain. La réoxydation du Ni est contrôlée par la diffusion des ions Ni par les joints de grains du film de NiO. Ce mécanisme de diffusion n'est pas contrebalancé et de la porosité apparaît dans la structure, bien qu'une certaine croissance vers l'intérieur de la structure soit permise par des fissures dans le film d'oxyde. Cette porosité interne ainsi que la réorganisation du Ni sont les processus déterminant l'instabilité lors d'un cycle d'oxydoréduction. Plusieurs paramètres sont identifiés afin d'améliorer la durabilité et la performance de ces anodes.

Mots-clés microscopie électronique en transmission environnementale (ETEM), spectroscopie de perte d'énergie des électrons (EELS), piles à combustible à oxyde solide (SOFC), nickel, réduction, oxydation.

Contents

Introduction

Context and motivations

Dimensional (in)stability of metal/ceramic composite structures during service is important for many applications, where devices are experiencing transient or cycling conditions, external failures or simply long operating times. In this work, the selected system is composed of nickel (Ni) and yttria-stabilised zirconia (YSZ), which is widely employed as the anode structure of solid oxide fuel cells (SOFCs), a promising technology that electrochemically converts the chemical energy of a fuel directly into electricity with a high efficiency.

In SOFCs, the Ni/YSZ anode operates at a temperature within the range 650–1000 °C in a reducing atmosphere and acts as a fuel oxidation catalyst, a hydrocarbon reforming catalyst, a current collector and often as the mechanical supporting layer of the whole fuel cell. For ease of manufacturing, nickel oxide (NiO) particles are usually first co-sintered with YSZ and then reduced to metallic Ni during the first operation of the cell, creating pores in the structure and leaving the YSZ backbone unchanged. The activated Ni/YSZ anode should then remain stable during years of operation in a reducing atmosphere at a high temperature. However, several accidental factors may lead to reoxidation of the Ni phase. Instead of reverting to the initial as-sintered NiO structure, the structure appears irreversibly changed by the reduction-oxidation (redox) cycle. The pores created during reduction cannot accommodate completely the volume expansion associated with the oxidation of the Ni phase. Stress is thus exerted on the YSZ matrix and cracks may appear in the structure, which irreversibly degrades the performance of solid oxide fuel cells. Yet few alternatives compare performance- and cost-wise to the Ni/ceramic composite anode, hence highlighting the importance of a detailed understanding of the mechanisms controlling the reduction reaction, the structural changes of Ni during operation and the reoxidation reaction of Ni, mechanisms that in turn determine the instability of the anode.

While the topic of extensive research, the mechanisms and how a given microstructure is affected by redox cycles are still subject to controversies in the literature. The mechanisms are usually inferred from *in situ* measurements, i.e. measurements performed in gas and temperature conditions that bear some analogy with the real conditions inside an

operating solid oxide fuel cell. Such *in situ* measurements characterise often the evolution of the mass, the conductivity, the crystallography, the structure or the composition of a specimen during reaction/operation. These techniques usually enable the retrieval of only one aspect of the process, for example either the nano/microstructure or the chemistry but not both. As a result, part of the description is missing and post-exposure electron microscopy observations and models that fit the data acquired *in situ* are often required. Yet transient processes are not resolved in post-exposure micrographs and the models often provide only a simplified description. It hence appears difficult to fully grasp all the processes involved as a part of the picture is missing.

The recent advances in environmental transmission electron microscopy (ETEM) appear promising with respect to the points aforementioned. Indeed, these advances now enable a nearly simultaneous assessment of both structure and chemistry on the sub-nanometre scale, whilst the specimen is held at high temperature in a reducing or oxidising atmosphere. While subject to some drawbacks such as the geometry of the sample that can be investigated, the technique appears as a valuable toolbox to assess the mechanisms controlling the reaction of a solid with a gas along with the effects of those mechanisms on the resulting nanostructure. While promising, both the application of this technique to the study of solid oxide fuel cells and an ETEM methodology that captures in real time both the structural and chemical changes associated to a solid-gas reaction and correlates them to infer the mechanisms controlling the reaction had not been reported prior to the start of this Ph.D. thesis.

Objectives

The objectives of this Ph.D. thesis aim at assessing the discrepancies reported in the literature related to the reduction-oxidation of Ni(/YSZ) systems, through the innovative use of environmental TEM. Specifically, this research proposes to:

1. develop new methodologies to obtain, and then correlate through mathematical reaction models, the structural and chemical information observed *in situ* on the nanometre scale, with electron energy-loss spectroscopy and energy-filtered TEM images providing the composition of the specimen;
2. verify the reliability of the results obtained *in situ* in the ETEM through comparisons with complementary *in situ* X-ray diffraction experiments performed under various experimental conditions, some close to those inside the environmental TEM, others comparable to those at which SOFCs are operated;
3. apply such strategies to assess the reduction and oxidation of Ni-based systems on the sub-nanometre scale to yield a detailed understanding of both their reduction and oxidation mechanisms and their redox instability;
4. propose qualitative models that capture each of those mechanisms to suggest microstructures with improved performance and tolerance to accidental reoxidation.

Structure of the thesis

In connection with these objectives, this Ph.D. thesis is divided into 8 chapters that are structured as follows:

- **Chap. 1** introduces the fields of solid oxide fuel cells and environmental transmission electron microscopy and reviews the latest literature reports relevant for this research.
- **Chap. 2** emphasises on the materials and methods used throughout this work, with a particular focus on the analysis of electron energy-loss spectra and energy-filtered TEM images, to yield the reaction kinetics of the processes observed in the microscope.
- **Chap. 3**, the first of 4 main experimental chapters, presents the investigation of the **reduction** mechanisms of **NiO particles** through the use of the environmental TEM methods introduced in Chap. 2 and assesses their reliability and potential artefacts through comparisons with *in situ* X-ray powder diffraction experiments.
- **Chap. 4** monitors, using the same environmental TEM methods, the subsequent **reoxidation** of the **particles**, now in their reduced metallic state.
- **Chap. 5** assesses the effect of the **YSZ** phase on the **reduction** behaviour of **NiO** grains using mainly energy-filtered TEM imaging. This chapter also relies on density functional theory calculations to assist in explaining the observed reduction process of NiO/YSZ composites. An extensive post-exposure analysis that combines different advanced TEM techniques also complements this chapter.
- **Chap. 6** discusses the **reoxidation** of those **Ni/YSZ** composites using environmental TEM techniques.
- **Chap. 7** summarises the implications of Chaps. 3 to 6 with respect to solid oxide fuel cell technology and proposes solutions that address issues related to the performance and redox stability of Ni/YSZ anodes.
- **Chap. 8** closes the loop by summarizing the contributions of this research to the field of environmental TEM, to the understanding of the mechanisms controlling NiO reduction and Ni oxidation, with both reactions of industrial importance extending beyond the field of SOFCs, and then to the comprehension of the redox instability of Ni-based anodes. This chapter also discusses future prospects that result from this research.

1 Literature review

1.1 Solid oxide fuel cells

1.1.1 Introduction

Solid oxide fuel cells (SOFCs) appear as a promising energy conversion technology as the incentive to shift from fossil and other non-renewable energy sources to sustainable and efficient technologies is gaining momentum. In such a device, the chemical energy of a fuel is directly converted into electricity and heat without a direct combustion process allowing for higher efficiencies than alternative technologies [1]. While electric efficiencies close to 60% are obtained now with a SOFC, the overall efficiency increases up to ∼70% when coupled to a gas turbine (Fig. 1.1). Advantages of SOFCs also include flexibility of fuel use (e.g. CO, H_2, CH_4) due to the high operation temperature (650-1000 °C), delocalisation of energy conversion and reduction of pollutants such as NO_x and SO_x [2,3].

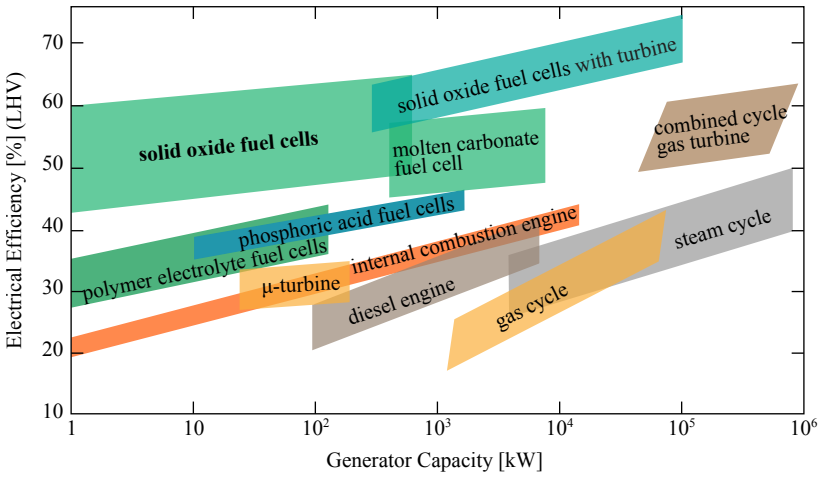

Figure 1.1 – Electrical efficiencies of different conversion technologies, compilation of data from Refs. [4–6] (2009-2013). The efficiencies listed here are expressed with respect to the lower heating value (LHV) based on natural gas for fuel cells, micro turbines, gas turbines and steam turbines.

A SOFC relies on the use of three main components: a porous anode (fuel side) separated by a dense ion conducting electrolyte from a cathode (oxidant gas side). Oxygen gas is injected at the cathode side, where it dissociates and gets ionised by incoming electrons, with O^{2-} ions then migrating through the thin electrolyte towards the anode (Fig. 1.2a). At the anode, O^{2-} reacts with adsorbed H and other fuels to form H_2O (and CO_2 when hydrocarbons are used), which in turn frees electrons that flow through the external load back to the cathode.

Individual cells can take different geometries, either planar (as shown in Fig. 1.2a) or tubular, each with sub-variants [1]. For a planar SOFC, either the anode (as shown in Fig. 1.2a) or the electrolyte usually act as the mechanical support of the cell. While the tubular design does not require gas tight high temperature sealing materials, the areal/volumetric power is significantly lower compared to the planar design and its manufacturing is also more complex. Individual cells are then configured in a stack through the addition of interconnects and sealing materials, which guarantee electrical connectivity between cells, isolate fuel from oxidant gas and prevent gas leakage. Overall, an operation temperature in the range of 650-1000 °C is required to overcome the large energy barriers for O_2 dissociation at the cathode and reduce the ohmic losses associated to the ion conducting electrolyte [7].

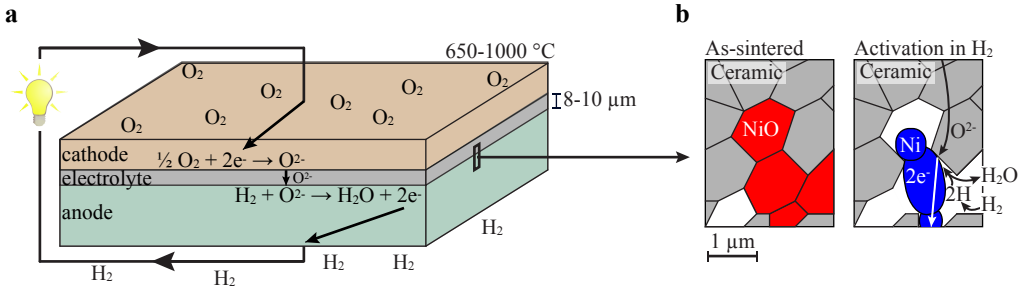

Figure 1.2 – (a) Reactions in an anode-supported planar SOFC with an O^{2-} conducting electrolyte and hydrogen as the fuel. (b) The as-sintered NiO/YSZ anode is activated to the electrochemically active Ni/YSZ state during the first operation of the cell.

1.1.2 Electrolyte, cathode and anode materials

The electrolyte, cathode and anode each have a different functionality that must be maintained during operation at high temperature, hence imposing different constraints on the materials.

The electrolyte must be dense, remain stable both in reducing and oxidising conditions, present a high ionic conductivity and a low electronic conductivity to maintain the high efficiency of the device. With respect to those constraints, the electrolyte is often composed of zirconia (ZrO_2) that is stabilised by yttria (Y_2O_3) in its cubic fluorite

structure (see Appendix A) to enhance the number of oxygen vacancies through charge compensation [3]. While other oxides such as scandia-doped zirconia, gadolinium-doped ceria (CeO_2) and complex perovskite structures have higher ionic conductivities, yttria-stabilised zirconia (YSZ) exhibits a higher stability during operation at high temperature. The higher ohmic losses associated to the lower conductivity of YSZ can be compensated to some extent by reducing the thickness of the electrolyte layer (on the order of 5-10 µm in an anode-supported design).

Conducting perovskites are often used as cathode materials due their high electronic conductivity, stability, compatibility with other components of the SOFC and high catalytic activity for oxygen dissociation and reduction [3]. Strontium-doped lanthanum manganite ($LaMnO_3$), termed LSM, exhibits adequate properties [2]. Alternatively, lanthanum strontium cobalt ferrite (La,Sr)(Co,Fe)O_3 (LSCF) displays faster oxygen reduction kinetics and higher ionic conductivity. However, a thin doped ceria (usually Gd-doped CeO_2) diffusion barrier must be placed on the YSZ electrolyte to prevent diffusion of LSCF and in turn degradation of the electrochemical properties of the cathode.

The anode should present good catalytic properties related to fuel oxidation, a high electronic conductivity, compatibility with the other components of the cell, long-term stability in a reducing atmosphere and allow permeation of the fuel to the reactive sites. In that regard, a porous ceramic/metal composite (cermet) made of YSZ and Ni is the most commonly used anode system [8]. NiO particles are sintered with YSZ and then reduced to metallic Ni during the first operation of the cell as the temperature is increased in a reducing atmosphere on the anode side (Fig. 1.2b). This reaction results in a Ni volume shrinkage of 41.6% [9], creating additional pores in the anode and thereby enhancing gas permeability. The electrochemical reaction takes place at the triple phase boundaries (TPB) YSZ/Ni/porosity (Fig. 1.2b). In addition, the YSZ backbone reduces Ni coarsening [10], a process that results in a degradation of the performance of the cell [11]. Alternatively, YSZ can be replaced by gadolinium-doped ceria (GDC), which has a higher ionic conductivity. In both cases, Ni acts as current collector, hydrogen and methane oxidation catalyst, with carbon depositing at the active sites in the case of methane unless sufficient steam is added to the fuel flow [3]. Anodes composed of Cu and CeO_2 have also been employed to use directly higher-hydrocarbon fuels such as natural gas without the need of a pre-reformer as for Ni/YSZ. Alternative anode materials with improved stability in hydrocarbon fuels also include Gd-doped ceria or lanthanum chromium manganites as well as lanthanum chromites doped with Ni or ruthenium [12]. However, there are only few alternatives performance- and cost-wise to the Ni/YSZ anode, the composite material on which this work will focus.

1.1.3 Degradation mechanisms

Although solid oxide fuel cells have been studied and improved extensively since their discovery in the 1830s by Schoenbein and Grove [13, 14], different processes, ranging from microstructural changes, deactivation of active sites and thermomechanical aspects, degrade their properties during operation as reviewed by Yokokawa *et al.* [15]. The emphasis will be placed here on one of those degradation mechanisms: the reduction-oxidation instability of Ni-based anodes, which is detrimental to anode-supported cells.

1.2 Ni reduction-oxidation instability

While Ni-based anode-supported cells display adequate performance at reasonable costs, the anode exhibits a structural instability in successive reduction-oxidation cycles [16]. Under normal operating conditions, fuel is supplied to the anode side and Ni is kept in its reduced state. However, Ni may reoxidise due to factors such as seal leakage [17], shut-down in the absence of a protecting gas or high fuel utilisation [16]. Ni oxidation is associated with a volume expansion of 71.2% [9], which cannot be accommodated completely by the porosity created during reduction as the microstructure does not appear to revert back to the oxidised as-sintered state [18]. In turn, stress is exerted on the YSZ matrix and cracks may appear in the thin electrolyte [9], thus degrading the performance of the cell [17].

The redox instability of Ni-ceramic anodes appears to stem from a combination of two processes: changes in Ni structure during reduction and operation in a reducing atmosphere at high temperature [18–20] and formation of porous NiO structures during accidental oxidation [9, 17, 21–24]. Both effects modify the Ni structure with respect to its initial as-sintered state and hence prevent accommodation of its volume expansion during oxidation in pores created during reduction. While subject to extensive scientific research as reviewed in Refs. [16, 25, 26], discrepancies remain in relation to reduction/oxidation mechanisms and associated microstructural changes as reviewed in the chapters below.

1.2.1 NiO(/YSZ) reduction mechanism and associated structural changes

NiO reduction

The reduction of NiO to metallic Ni has been extensively covered since the study of Benton and Emmett in 1924 [27] due to its importance in the fields of SOFCs but also catalysis in general [28–31] and ore reduction to produce metallic Ni [32–35]. However, several questions remain about the rate-controlling mechanisms and associated structural changes to obtain a detailed understanding of the reaction

$$NiO + H_2 \rightarrow Ni + H_2O \tag{1.1}$$

Both NiO and Ni exhibit a face-centred cubic structure (with a lattice parameter of 0.418 [36] and 0.352 nm [37], respectively, see Appendix A).

Richardson *et al.* [38], who studied NiO reduction using *in situ* X-ray diffraction, summarised the prevailing features of this chemical reaction as follows:

1. H_2 first dissociates on two Ni atoms surrounding an oxygen vacancy [30], with the presence of such a vacancy leading to an increase in the adsorption energy of H_2 and in turn reducing the energy barrier to break the H–H bond [39],
2. adsorbed H atoms diffuse to NiO reaction centres,
3. Ni-O bonds are ruptured and H_2O desorbs,
4. Ni clusters nucleate and grow after an induction period (related to the slow generation of oxygen surface vacancies - active sites for H_2 adsorption and dissociation),
5. H_2 now dissociates directly on the metallic clusters once their size is large enough,
6. adsorbed H is transferred to the NiO phase at the interfaces with Ni,
7. the reaction rate increases autocatalytically as the metal clusters grow into Ni crystallites.

The incorporation of those mechanisms into an overall description of the NiO reduction kinetics is then subject to controversies. Amongst the different solid-state models that describe the reaction of a solid with a gas to form a solid product, with respect to the mechanism that controls the overall reaction (schematically summarised in Fig. 1.3 and listed in [40,41], with each model exhibiting a characteristic reaction kinetics), the following ones were used to describe NiO reduction as recently reviewed by Zhu and co-workers [42]:

- Avrami, where the surface nucleation, growth and impingement of Ni domains control the reaction (Fig. 1.3a-b and Appendix C.2 for mathematical development) [42–45],
- pseudo-first order, where Ni nucleation is fast and the chemical reaction then controls the reaction rate (Fig. 1.3e) [38],
- shrinking core, where the reaction at the NiO/Ni interface defines the advancement of the reaction front and results in a porous Ni scale surrounding a shrinking dense NiO core (Fig. 1.3f) [46,47],
- Evans–Szekely grain model (porous agglomeration of grains, each undergoing a shrinking core reduction as in Fig. 1.3f), [48–51],
- thermomechanical approach [52].

In addition, the activation energy for reaction 1.1 is observed to scatter in the literature over an order of magnitude, between 10 and 150 kJ mol^{-1} (summarised for work before 2003 in Ref. [38]), with more recent studies yielding values of 53.5 kJ mol^{-1} [53], 96.4 kJ mol^{-1} [54], 91.8–94.5kJ mol^{-1} [55], 15 kJ mol^{-1} [56].

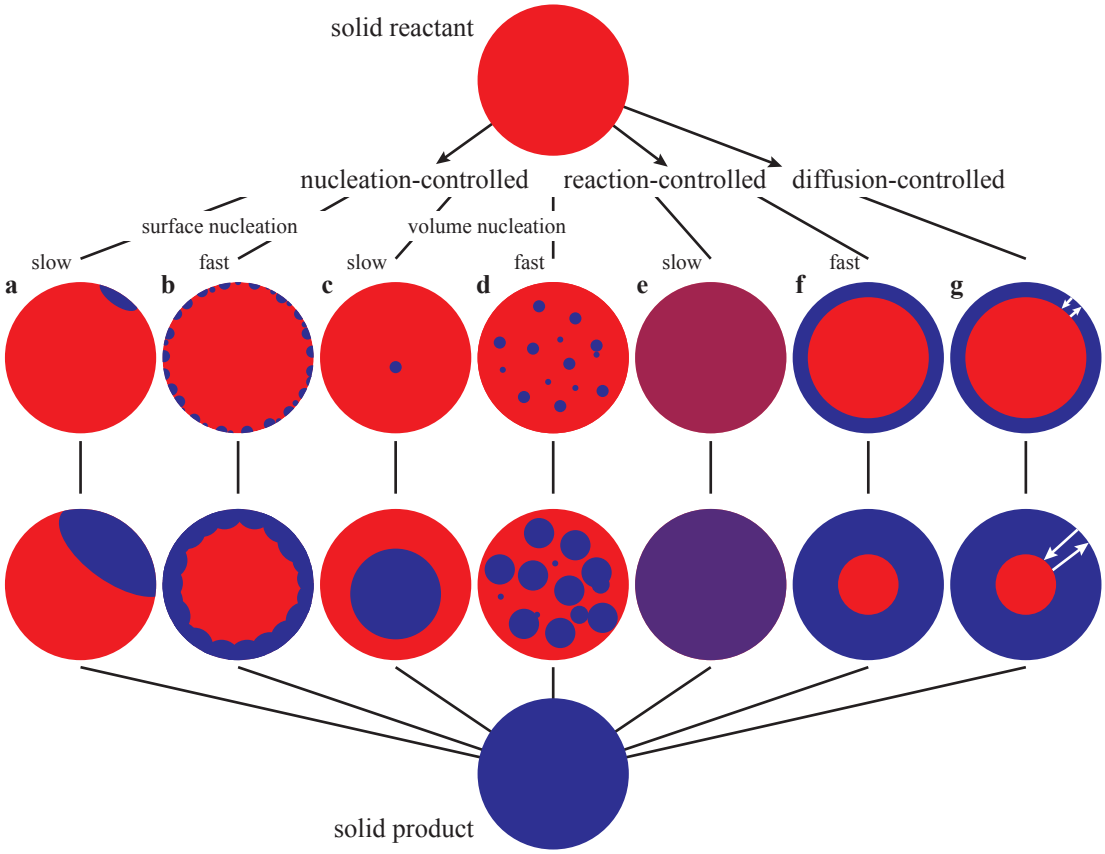

Figure 1.3 – Classification of solid-state reaction models, adapted from Refs. [40, 42]

The lack of consistency between the NiO samples that have been studied in terms of chemistry, size, microstructure, characterisation techniques and other experimental parameters may explain the wide scatter in these results. Indeed, various studies demonstrate that the reduction process is sensitive to the surface properties of NiO [57–60], properties that change depending on the NiO synthesis route and history. Those observations also tend to indicate that nucleation, i.e. the formation of first domains of Ni on the surface, is an important mechanism in the overall description of the reaction. In addition, the reaction may proceed through different processes depending on the specimen size. Dense NiO particles with a diameter larger than 10 µm undergo a transformation that can be described by a shrinking core model [38, 46, 61], with Evans and Szekely implementing this model into a more complex empirical description of the reduction of a porous agglomerate of NiO particles [51] (Fig. 1.3f). However, interface-controlled reactions as in a shrinking core model are not compatible with the concept of induction time, an important feature of the NiO reduction reaction [39]. The nucleation step and the associated induction time hence appear insignificant with respect to the advancement of the reaction front in such large specimens. On the contrary,

those features appear essential in the description of the reduction NiO particles in the nanometre range. On that length scale, pseudo-first order or Avrami kinetics are usually reported [38, 42], with the latter model including an induction period and the possibility for autocatalysis [39]. The presence of H_2O on the surface hinders the reaction by a factor that depends on sample geometry and experimental setup, which may explain the wide scatter in reported values of activation energy [38].

While the consistency of some of these models with the structural transformation of NiO to Ni was verified *ex situ* after the sample was transferred inertly from the reaction chamber into a microscope [47, 51], most of the literature studies did not correlate kinetic data (mainly obtained by thermogravimetry and sometimes by *in situ* X-ray diffraction) with microscopy techniques to assess the microstructure and thus to verify the adequacy of the selected reaction pathway. In that regard, Hidayat and co-workers reported an experimental setup that enables the reaction in a controlled atmosphere of large 10x10x1 mm^3 dense NiO slabs formed by the oxidation of Ni in air during 1 week at 1435 °C [32]. Those NiO sheets were then quenched in liquid nitrogen to freeze the specimen structure at a defined reaction time. Based on scanning electron microscopy images of the quenched Ni/NiO samples, Ni structures were grouped into the following categories depending on reduction temperature and H_2O content in the H_2 gas flow: coarse fibrous with fissures, fine porous with a planar Ni/NiO interface, large porous with an irregular Ni/NiO interface and dense [33–35]. These microstructures were explained in terms of varying contributions from different processes such as Ni sintering, recrystallisation, grain growth, and faceting. The reaction kinetics were inferred from measurements of the reacted layer thickness and those results were compared to prediction in various rate-limiting cases. It was demonstrated that NiO reduction is controlled by the chemical reaction occurring at the Ni/NiO interface at low temperatures (500-600 °C), while the kinetics measured at higher temperatures was found to be controlled by a combination of mass transport processes. The Ni/NiO reaction front was observed to proceed toward the centre of each sample, similarly to a shrinking core process, with cracks and boundaries enhancing locally the advancement of the reaction front. High temperatures (800-1000 °C) and steam-to-hydrogen ratios accelerate the formation of dense Ni layers through coarsening, which in turn hinder the transport of H_2/H_2O to and out of the Ni/NiO reaction front.

NiO/YSZ reduction

The eventual modification of the reduction mechanisms when NiO is co-sintered with YSZ grains to form the SOFC anode is also subject to discrepancies in the literature. While Modena *et al.* did not notice any influence of the YSZ backbone on the reduction of NiO [62], Fouquet and co-workers observed a modification of the reaction kinetics of NiO/YSZ when compared to the same NiO in particles in the form of a powder. This modification was inferred to result from the inhibition of the nucleation step of Ni by

the YSZ phase but yet no evidence of such process was reported [63]. In contrast, other researchers reported an enhancement of the NiO reduction rate in directionally solidified NiO/CaO-doped ZrO_2 composites as a result of the removal of oxygen through the ion conducting zirconia [64]. In addition, the YSZ backbone may prevent Ni sintering during reduction and operation at high temperature and in turn maintain fast permeation paths for H_2 and H_2O. Overall, activation energies in the same range as for the reduction of NiO particles/slabs are reported in the case of NiO/YSZ composites (25-100 kJ mol^{-1} [22, 62, 65, 66]). While a nucleation-controlled Avrami description of the process was found to provide a good description of the data by Pihlatie and co-workers [66], most studies highlight a linear dependence between reduced fraction (or reduced layer thickness) and reaction time during the initial stages of the reaction, hence indicating an interface-controlled process.

When reduced in the range 300-450 °C in dry 9% H_2-N_2, Ni grains in Ni/YSZ composites exhibit porous structures similar to those observed in Ni slabs by Hidayat and co-workers [67]. Other studies highlight the formation of dense Ni grains after reduction of as-sintered NiO/YSZ cermets. Such Ni structures were observed by Klemensø and co-workers, who used environmental scanning electron microscopy (ESEM) to observe *in situ* the structural changes associated to Ni/YSZ reduction and reoxidation [20]. Structural changes resulting from the reaction itself may however be convolved with coarsening of the Ni structure due the high temperature involved in those *in situ* experiments (850 °C).

1.2.2 Ni coarsening

In addition to structural changes directly associated to the reduction reaction, the Ni structure coarsens at high temperature in a reducing atmosphere as grains sinter to minimise the total surface area of the system [68]. The growth of domains is usually inferred to result from one of the two following processes: [69, 70]:

- Ostwald ripening (interparticle transport of atoms by diffusion and/or evaporation and condensation),
- particle migration and coalescence.

Cassidy *et al.* suggested that Ni grains in Ni/YSZ cermets sinter and coalesce into a distribution of larger particles after reduction at 1000 °C [19]. Although the authors did not present any clear evidence of this mechanism, they assumed that during accidental oxidation of the anode the volume expansion of the larger Ni particles that formed as a result of sintering could not be accommodated by the pores created during reduction. In turn, stress was applied on the YSZ phase, which contributed to the reduction-oxidation instability of Ni-based cermets. Simwonis and co-workers provided a clear microstructural evidence of Ni coarsening, with the average Ni grain size shifting to higher values upon exposure to 4% H_2-Ar at 1000 °C up to 4000 h [71]. Surface diffusion of Ni atoms

was inferred to be the main mechanism controlling Ni coarsening in SOFC anodes based on a modelling approach [72]. Sehested and co-workers improved the description through experimental work and density functional theory calculations and demonstrated that OH-bonded nickel dimer (Ni_2-OH) rather than Ni adatom is the dominant surface migration specie in the presence of a H_2/H_2O gas mixture [73]. Their results along with those of other researchers highlight the role of steam in the acceleration of Ni grain growth [74,75]. In wet ageing conditions after reduction, Ni volatilisation through the formation of $Ni(OH)_2$ species and subsequent redeposition was also inferred to increase Ni coarsening [76,77]. While reduced by the YSZ backbone [10], Ni coarsening eventually results in large, dense and isolated Ni grains, which degrades the electrochemical properties of SOFC anodes due to a loss of percolation of the Ni network [11]. Grahl-Madsen *et al.* highlighted through conductivity measurements that Ni coarsening occurred only during reduction in their experimental conditions [78], which appears contrary to reports of Cassidy *et al.* [19] and Klemensø *et al.* [18]. Although the exact reasons appear unclear, steam-related differences in experimental conditions may explain this discrepancy.

1.2.3 Ni(/YSZ) oxidation mechanism and associated structural changes

Ni oxidation

The Ni catalyst of SOFC anodes, which is typically present in the form of sub-micron-sized grains [11,77], may oxidise if the gas environment deviates from the reducing working conditions according to the reaction

$$2Ni + O_2 \rightarrow 2NiO \tag{1.2}$$

As most oxidation processes, once oxide domains have nucleated and impinged on the metal surface (Fig. 1.4a-b), the reaction is then controlled by the transport of ionic and electronic species across the oxide film as schematically illustrated in Fig. 1.3g [79]. However, the exact transport mechanism that controls the final microstructure is complex, with neither of the two primary models for ionic and electronic transport across oxide films seemingly applicable on this sub-micron length scale [79].

The first model is denoted the Mott–Cabrera theory and describes non-linear growth of a thin oxide film [80] (below $\sim$10 nm for NiO [79]). It is assumed that electrons can freely pass from the metal, through the oxide, and to the oxide/gas interface to ionise O_2 molecules that are adsorbed on the oxide surface (Fig. 1.4c). This transfer by tunnelling and/or thermionic emission of negative charges through the film creates an electric field, which drives the non-linear transport of Ni^{2+} ions across the film [81]. In the case of vacancy injection at the metal/oxide interface, the growth rate is controlled by the jumps of metal ions across the metal/oxide interface and follows a logarithmic behaviour. While Liu *et al.* could measure a logarithmic film growth in the early stages

of Ni oxidation [82], Graham and co-workers observed a parabolic rate at 300 °C for films as thin as 3 nm [83]. Such parabolic behaviour is usually associated to the Wagner description, which holds for thicker films (i.e. when the film is in a pseudo-steady state). While the Mott-Cabrera theory provides an useful atomistic description of the thin film growth, it appears unclear up to which thickness > 10 nm this built-in field effect is non-negligible. Moreover, its direct comparison with experiments is difficult, notably due to the mathematical approximations inherent to the model.

On the other hand, the Wagner theory assumes that the oxide film is in local chemical equilibrium and thus that no net electrical current flows through it (coupled-currents approach, Fig. 1.4d). The growth is then controlled by the linear diffusion of ions in a gradient of oxygen chemical potential, which results in parabolic kinetics that is directly related to diffusion coefficients [84]. Such pseudo-steady state conditions are thought to be satisfied in NiO films thicker than 1 µm at 500 °C [79], while the description of the growth of thinner oxide films is subject to controversies. In pseudo-steady state conditions above 1 µm, as the growth rate is directly related to the self-diffusion coefficients of the ions (Ni^{2+} and/or O^{2-}) in the oxide, secondary ion mass spectroscopy (SIMS) has been one method of choice to investigate the oxidation mechanisms under various conditions [85–90]. Good agreement between Wagner theory and experimental results is usually observed during oxidation of Ni at high temperature (> 1000 °C [91]). In these conditions, NiO growth is controlled by diffusion of Ni^{2+} ions through the NiO lattice and has an activation energy of ∼200-250 kJ mol^{-1} [26, 91]. At lower temperatures (< 1000 °C), sub-parabolic kinetics are usually measured. Outward diffusion of Ni^{2+} through the NiO grain boundaries now controls the reaction and since the number of fast-diffusion paths is evolving as a function of time and/or temperature, the growth rate deviates from a purely parabolic behaviour [91]. As shown by Atkinson and co-workers, the description can be modified to take into account the diffusion through the grain boundaries [92]. However, this description does not include the growth of oxide grains, which modifies the number of fast diffusion paths. The reactivity of Ni in this regime is strongly dependent on its purity, pre-treatment and surface properties as these factors affect the number of short-circuit paths for Ni^{2+} diffusion [83, 93–95]. The activation energy for Ni oxidation in this temperature range is on the order of ∼100-200 kJ mol^{-1} [26, 91].

The microstructure that forms during Ni oxidation is closely related to the growth-controlling mechanism. Below 1000 °C, inward diffusion of O_2 was measured to be several orders of magnitude slower than outward diffusion of Ni^{2+}, suggesting that Ni vacancies are injected at Ni/NiO interfaces [79]. If the vacancies cannot be annihilated (e.g. by dislocations or interface recession), then internal porosity that is similar in size to each initial Ni particle can form [96]. Recent studies have made use of this interface phenomenon (also referred to as a nano-Kirkendall effect, even though Ni^{2+} and O^{2-} transports occur at different crystallographic locations) to form core (void)–shell

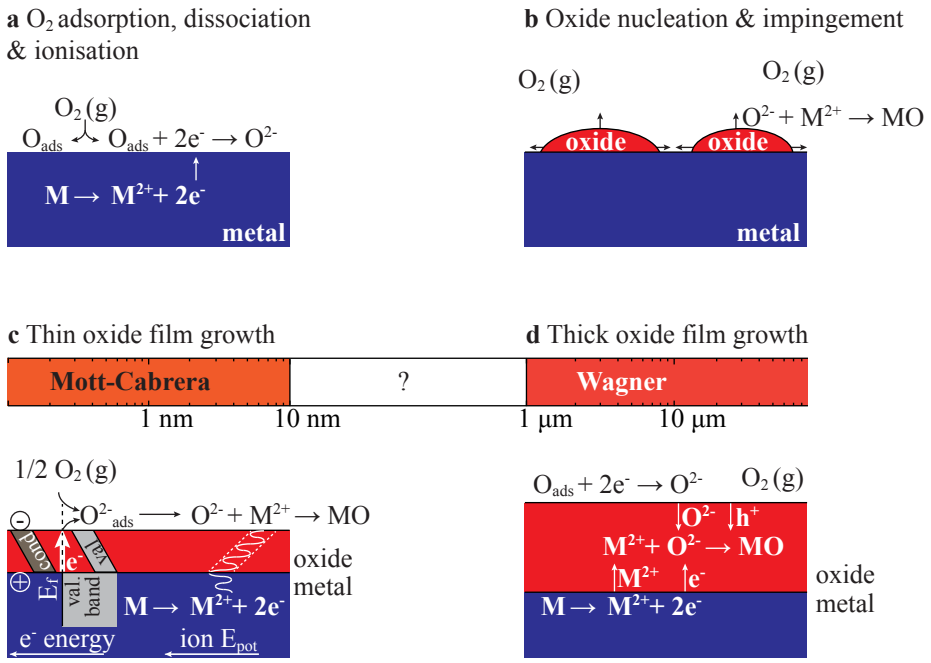

Figure 1.4 – Schematic illustration of the oxidation of a metal. (a) Adsorption, dissociation and ionisation of O_2 on the metal surface. (b) Oxide nucleation and growth until impingement. (c) Mott-Cabrera description for the growth of a thin oxide film (thickness < 10 nm for NiO [79]), across which electrons tunnel from the metal to ionise adsorbed oxygen, resulting in a large electric field that drives ion transport and oxide growth (illustrated here for metal ions). (d) Wagner description once the oxide film is in local chemical equilibrium at larger thicknesses (above 1 µm for NiO at 500 °C [79]), which assumes that oxide growth is controlled by ion diffusion in a gradient of oxygen chemical potential and results in a parabolic growth rate.

(NiO) structures by the oxidation of Ni nanoparticles (Fig. 1.5a) [97–100]. Although the oxide film should not be in pseudo-steady state on this nm length scale, such structures are usually explained to arise from the difference between the Ni^{2+} and O^{2-} diffusion coefficients. Those coefficients are measured at much larger length scale (µm) and it remains to be verified if those can be used on this nanometre scale. The structure becomes more complex when the initial Ni particle size increases to 100 nm, with multiple voids observed within a NiO shell after oxidation (Fig. 1.5b) [99]. At larger length scale, Sarantaridis *et al.* examined focused ion beam cross sections of micron-sized NiO particles after oxidation at 800 °C and observed both small internal voids and NiO grains at the initial position of Ni as illustrated in Fig. 1.5c [23]. It was suggested that, while outward diffusion of Ni^{2+} may dominate during the beginning of oxidation, inward transport of oxygen occurs but still leaves some small voids inside the NiO particles. However, the process through which inward growth occurs was not detailed. In a planar geometry, NiO films with a thickness of 1 µm formed by oxidation at temperatures < 1000 °C exhibit a simplex porous NiO structure, i.e. one

kind of NiO grain structure, which forms mainly outward with respect to the initial Ni slab (Fig. 1.5d). Thicker films display a duplex NiO structure, i.e with two different grain structures, with additional NiO growth occurring inwards (at the metal/oxide interface) as shown in Fig. 1.5e [79, 101–103]. Microchannels in NiO scales are thought to act as paths for the inward permeation of O_2 toward unreacted Ni [88, 91, 104–107]. Such processes are usually predicted to occur on the basis of post-exposure microscopy observations and acoustic emission studies but are not yet well characterised. NiO films grown on planar Ni display different surface morphologies ranging from disc-shaped platelets to ridge structures depending on oxidation parameters [101, 108, 109].

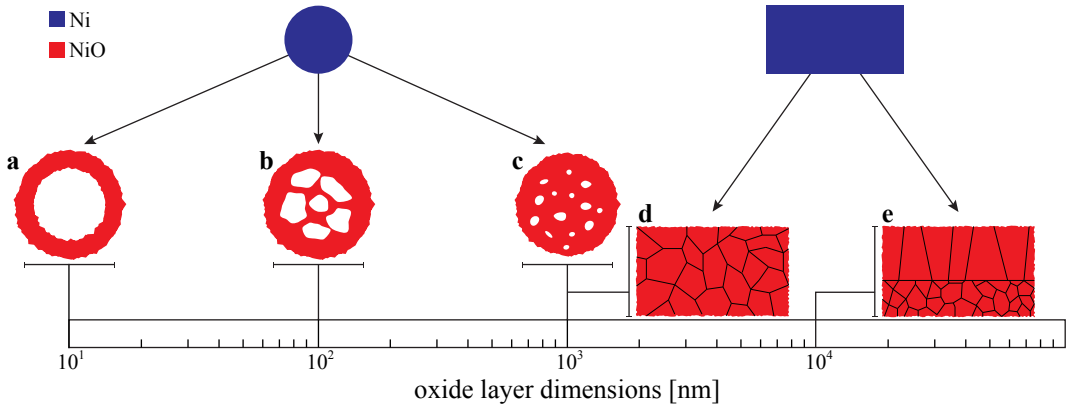

Figure 1.5 – Schematic description of the different oxide structures obtained after oxidation of Ni at temperatures $< 1000\ ^{\circ}C$ depending on size and geometry. In a spherical geometry: (a) NiO shell surrounding a single void in the 10 nm range [97–100], (b) NiO with multiple internal voids in the 100 nm range [99], (c) NiO structure with small internal voids in the µm range [23]. In the planar case: (d) simplex porous structure in the 1 µm range [79, 101–103], (e) duplex structure in the 10 µm range [79, 101–103].

As it is difficult to relate microstructural changes to reaction-controlling mechanisms solely on the basis of post-exposure examinations, attempts were made to study Ni oxidation *in situ* across different length scales using techniques that include transmission electron microscopy (TEM) [110–114], scanning tunnelling microscopy [115], environmental scanning electron microscopy [116, 117] and full-field transmission X-ray microscopy [118]. Although different stages of oxidation were described, such as NiO nucleation on Ni and the formation of characteristic NiO morphological features, they have not been followed in detail or related to rate-controlling mechanisms from the formation of the first nm of oxide to completion of the reaction.

Ni/YSZ oxidation

When NiO is co-sintered with YSZ and reduced to Ni/YSZ, Fouquet *et al.* measured using thermogravimetry a modification of the Ni oxidation kinetics when compared to particles. In addition, Faes *et al.* underlined the transition from a solid-state diffusion-controlled oxidation regime at low temperature ($< 600/700$ °C) to a gas permeation-controlled process at higher temperature [26]. When O_2 gas diffusion through the structure is limiting the reaction, the reaction becomes inhomogeneous and proceeds through the advancement of a reoxidised layer in the SOFC anode, which in turn increases the internal stress in the structure and leads to bending of the anode. Mass transfer limitations of O_2 may hence alter the oxidation rate of Ni grains in SOFC anodes.

Irregular NiO grain structures containing small randomly oriented crystallites were observed using scanning electron microscopy after oxidation [17, 63, 119], with similar irregular morphologies also monitored *in situ* using environmental SEM [20, 120]. Overall, reoxidation of the Ni catalyst of SOFC anodes results in a porous structure. The size and distribution of those closed voids both change with oxidation temperature as shown by Faes *et al.*, who used scanning electron microscopy images of NiO/YSZ cross sections prepared by focused ion beam milling [9]. While NiO grains contain small and distributed pores after reoxidation at 550-800 °C, a single large pore is observed at the centre of Ni grains oxidised at 1000 °C. Those observations indicate that, although outward diffusion of Ni^{2+}, most likely at the NiO grain boundaries in this temperature range, controls the overall reaction, other processes that allow inward growth of NiO and reorganisation of internal voids also contribute to the final structure as for particles.

The expansion of the NiO phase with respect to the as-sintered state due to the presence of internal porosity and reorganisation of the Ni phase during operation creates stresses in the different parts of the SOFC. In the case of an anode supported planar design, an expansion criterion due to redox cycling of $< 0.2\%$ is usually defined to prevent the rupture of the thin electrolyte [16, 26]. Overall, literature reports values of expansion due to redox cycling ranging from 0.1-5% depending on different parameters such as temperature, initial microstructure, as-sintered porosity, magnitude of Ni coarsening and presence of steam [18, 121, 122].

1.2.4 Ni/YSZ microstructure and redox tolerance

The integration of the mechanisms reviewed above and their associated structural changes at the SOFC level and the resulting tolerance of a given anode microstructure towards reduction-oxidation cycles appear unclear. Indeed, certain parameters such as initial porosity are controversially interpreted. As Ni expansion upon oxidation does not appear to be accommodated completely by the voids that were created during reduction, anode structures that contain additional porosity after sintering should exhibit a different redox behaviour.

Waldbillig *et al.* [22] performed a thermomechanical and thermogravimetric analysis of Ni/YSZ anodes during redox cycling and demonstrated that a coarse microstructure was more redox resistant due to the accommodation of the Ni volume changes by the large initial pores of the microstructure. On the other hand, cracks were observed when using a fine-grained microstructure. Based on those observations, microstructural modifications were suggested in order to enhance the redox tolerance [123]. Fouquet *et al.* suggested that the compliance of the YSZ network is a key factor determining the redox tolerance [63]. A low sintering temperature of 1200 °C of the NiO/YSZ anode creates a fine-grained microstructure with an improved elasticity of the YSZ skeleton, which in turn is able to accommodate better the volume changes of the Ni phase due to redox cycling according to the authors. However, their suggestion that a fine microstructure is more tolerant to redox cycles appears inconsistent with the observations made by Waldbillig *et al.* [123].

According to Klemensø and co-workers, porous ceramics are supposedly weaker and the redox stability of Ni/YSZ anodes is reduced accordingly [124], which contrasts to the work of Ettler *et al.*, who showed no difference by changing the porosity [125]. On the other hand, Robert *et al.* reduced cracks in anode supports by increasing their thickness and improving gas permeability by introducing a porosity gradient [126]. In addition to that latter study, separate studies by Faes and Pihlatie *et al.* both demonstrated an improvement of the redox stability of Ni/YSZ anodes with increasing porosity [127–129]. In a detailed assessment, Faes *et al.* showed that redox safety could be achieved by introducing an initial porosity on the order of 50% through the use of pore formers in the sintering process, which had the negative effect of reducing the electrochemical properties of the cell [128, 129].

Overall, those discrepancies related to the redox tolerance of SOFCs are likely to stem from differences in initial microstructure, especially porosity, which is often not characterised in detail.

1.2.5 Ni/YSZ redox instability models

Although the topic is subject to discrepancies as mentioned in previous chapters, qualitative microstructural models were developed to summarise the main structural changes associated to reduction, coarsening and reoxidation along with their effects on the anode microstructure. Klemensø and co-workers based their models notably on environmental SEM images of the surface of Ni/YSZ acquired during multiple reduction-oxidation cycles [18,130]. Nonetheless, their description of the redox instability of Ni-based anodes appears incomplete as only Ni coarsening is included, while the expansion of the NiO phase due to the injection of voids inside the NiO grains during reoxidation is missing. The latter effect was added later by Faes *et al.* in a more detailed microstructural model, which is shown in Fig. 1.6 [131].

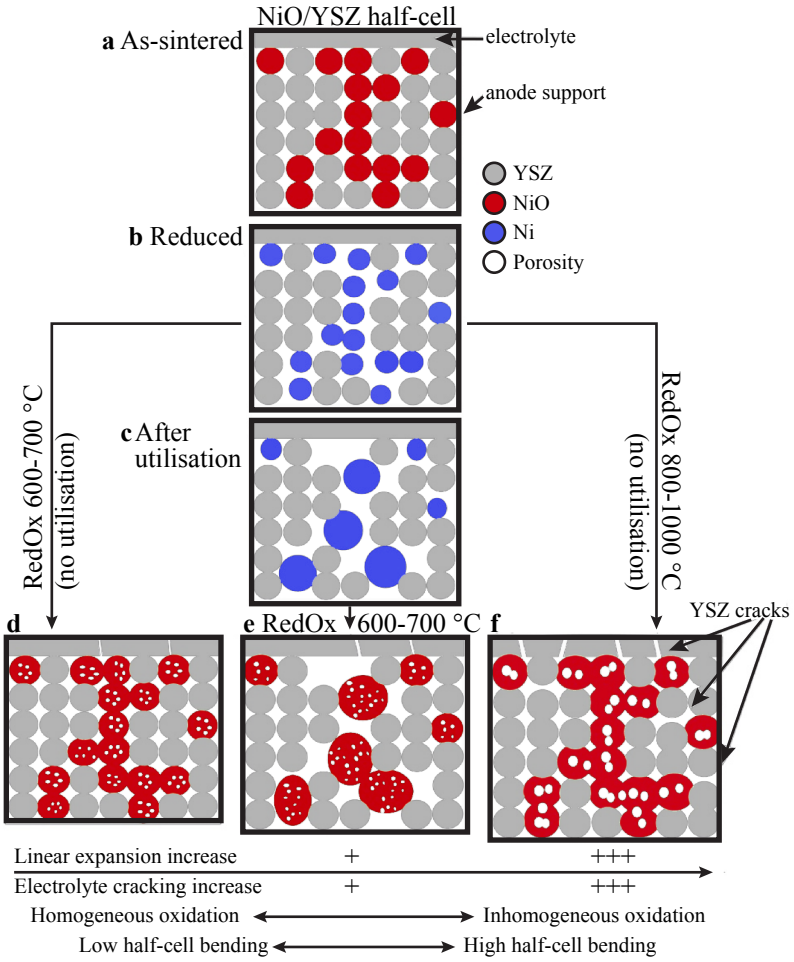

Figure 1.6 – Schematic model of the redox instability of Ni/YSZ anodes of Faes *et al.* [131].

Overall, those models shed light onto the redox instability of Ni-based anodes and associated structural changes but yet appear simplistic and do not fully grasp all the structural changes occurring in SOFC anodes in reducing and oxidising atmospheres. Most studies assessing the redox instability of Ni-based anodes rely on a combination of post-exposure 2D microscopy examinations and models based on *in situ* measurements such as thermogravimetry, conductivity or impedance spectroscopy, which average over the entire structure or large volumes. As a result, local transient details are usually lost in the description. In addition, *in situ* techniques such as environmental SEM, which provide information about the morphology of the surface on the 10 nm scale, cannot resolve changes occurring within the structure if not combined to other techniques such as post-exposure focused ion beam milling. The development of predictive models that describe the reduction and reoxidation of Ni-based anodes will depend on the ability of *in situ* techniques to retrieve in real time both nanostructural and chemical changes during reaction/coarsening in conditions as close as possible to those inside a SOFC during operation.

1.3 *In situ* characterisation techniques

1.3.1 Overview of techniques applied to SOFCs

Various aspects of solid oxide fuel cells have been investigated over the years using characterisation techniques that allow the retrieval of information *in situ* (characterisation in conditions with some similarities to SOFCs), with some of those techniques extended to *in operando* (specimen characterised, while operating in conditions as similar as possible to SOFCs). A non-exhaustive list of the techniques includes:

- electrochemical voltammetry to measure current and power density of cell, electrodes and/or electrolyte [132, 133];
- impedance spectroscopy to measure the resistance of cells, electrodes and/or electrolyte to infer ohmic losses and activation barriers [133–138];
- *in situ* X-ray related techniques, including X-ray photoelectron spectroscopy to infer surface composition and structure [139, 140], X-ray diffraction to assess crystallographic changes [141,142] and internal stresses [143,144], X-ray absorption near edge structure to analyse notably changes in oxidation states [145,146], X-ray nano computed tomography to assess microstructural changes in three-dimensions [147], full-field transmission X-ray microscopy to relate morphology changes to chemical composition [118], X-ray reflectivity, total-reflection X-ray fluorescence, ultra-small angle X-ray scattering to yield site segregations, lattice expansion, oxidation states and coarsening [148];
- optical studies such as Raman spectroscopy (composition, structure, temperature of surface and adsorbed species), infrared spectroscopy (surface species) and imaging (emission and temperature) [149–155];
- microscopy techniques such as environmental SEM to obtain surface morphology on the 10 nm scale [20, 120], environmental transmission electron microscopy to reveal structural changes on the sub-nm scale, chemical changes, mobility of ions [156–160] and scanning probe microscopy to measure topography and conductance during reaction [67].

With respect to the reduction-oxidation instability of Ni-based anodes, recent advances in full-field transmission X-ray microscopy combined with X-ray absorption near edge structure open new perspectives as the technique can provide two-dimensional and three-dimensional structural and chemical information of bulk samples yet with a spatial resolution now in the range of a few tens of nm [161–163]. However, fine details of the reduction-oxidation processes that occur on the nm level and below such as nucleation of the first domains of product may not be resolved with such techniques. While limited to the study of thin electron transparent specimens ($\leq 100/200$ nm depending on the acceleration voltage applied to the electrons, usually in the range of 80-300 kV), environmental transmission electron microscopy (ETEM) appears as a promising approach

due to its ability to obtain both a structural and a chemical diagnostic on the (sub-)nm scale in a matter of seconds/minutes during reaction at high temperature. While ETEM records a two dimensional projection of the structure and chemistry of a thin specimen, which may in turn complicate the analysis of the data, it may yet provide information about the internal structure of the specimen unlike techniques such as environmental SEM and others mentioned above.

1.3.2 Environmental transmission electron microscopy

Background

High temperature controlled atmosphere electron microscopy appeared as early as the 1970s and resulted from a combination of developments related to ambient temperature gas stages [164] and heating stages [165,166]. The technique gained momentum when lattice fringes could be resolved in an environmental TEM around 15-20 years ago [167,168]. Furthermore, the development of spherical aberration correction (bringing the spatial resolution of images to the sub-Ångstrom level) and monochromation (bringing the energy resolution of the incident electron beam down to a few hundred meV), has been adapted to environmental microscopy in the last few years, providing new insights into the mechanisms of gas-solid reactions in a variety of nanostructured materials [169]. Those developments are also complemented by recent advances in specific techniques that are now available in the environmental transmission electron microscope such as electron energy-loss spectroscopy, energy-filtered imaging and energy-dispersive X-ray spectroscopy [170–172].

Unlike conventional transmission electron microscopes that operate with the entire column in high vacuum conditions ($\leq 10^{-7}$-10^{-6} mbar), environmental TEM relies on the confinement of a pressure of gas around the specimen, while the other parts of the microscope are kept in high vacuum conditions [173]. Two different techniques were developed to achieve this objective: differential pumping microscopes, where small apertures and extra pumps maintain a pressure difference of nine orders of magnitude between the specimen and the electron gun [167, 174], and closed cell holders with electron transparent windows [175–177]. The latter allows the confinement of a pressure of 1 bar and above around the specimen, while differentially pumped microscopes only allow the introduction of < 20 mbar. However, the differential pumping approach is more widespread as the images are not distorted by the two thin membranes of the closed cell holder and it allows larger field of views, more freedom in terms of sample geometry and facilitate energy-dispersive X-ray spectroscopy analysis [178].

The temperature at the specimen position can be raised using a heating holder. The older generation of heating holders relies on the use of a heating coil inside an inconel (or tantalum) cup in which the specimen and its support are mounted (diameter of 3 mm) and control of the temperature is done through a thermocouple attached to the cup. On the other hand, the newest heating holders are based on a microelectromechanical

system (MEMS), which reduces the amount of material that is heated and hence thermal drift but yet appears incompatible with some sample geometries [179]. In many cases, the temperature of MEMS-based holders is inferred from the current input and a high vacuum calibration file, which may not apply in the presence of a gas in environmental conditions.

Applications

ETEM was applied to various topics mostly related to catalytic nanoparticles as reviewed in Refs. [173, 174, 180–182], including to the study of changes in size and shape [168, 183–185], nucleation of nanotubes [186], visualisation of gas adsorption [187], reduction-oxidation cycles of nanoparticles in various atmospheres [114,188–194] and measurement of the catalyst activity using electron energy-loss spectroscopy [195, 196]. In addition, Sharma *et al.* demonstrated that the time- and temperature-resolved data obtained *in situ* either from images or electron energy-loss spectra could be used to obtain reaction rates and values of activation energy [197].

Only a few of the ETEM studies that are reported are in direct connection with SOFCs. Two PhD theses were recently carried out on the topic but those appear distant to the objectives of this research. Sharma investigated the synthesis of ceria-based SOFC anodes along with their *in situ* characterisation [156]. Based on previous work done at Arizona State University [189], electron energy-loss spectroscopy (EELS) was used to monitor the oxidation state of Pr- or Gd-doped ceria particles through the determination of the Ce $M_{4,5}$ white lines ratio as a function of temperature in H_2. The results highlighted a higher reducibility for a particle size < 30 nm. Amorphisation of ceria was also observed during reduction. When loading Ni on Pr-doped ceria particles in a H_2 atmosphere, ceria regions located at the interfaces with Ni were observed to reduce as a result of interactions between H_2, Ni and ceria at the three-phase boundary [190]. This spillover process was discussed with respect to surface diffusion properties of H and O. Preliminary results assessing the reduction of a co-sintered NiO/Gd-doped ceria SOFC anode were also reported in this thesis. Images showing the structure before and after reduction were presented and those showed the shrinkage of some Ni grains as a result of reduction, while other NiO grains remained intact after reaction in 4 mbar of 50% H_2-N_2 at 700 °C. Only few images were presented and a detailed investigation of the changes occurring during reaction of the NiO/Gd-doped ceria anode appears missing.

In the other thesis on the topic [158], Tavabi investigated a model platinum/YSZ system through *in situ* holography experiments and observed a phase modification of the electron wave in the YSZ at the interfaces with Pt when the temperature was increased to 400 °C in a small pressure of O_2 [157, 160]. This modification was interpreted as an accumulation of negative charges at the interface. Additionally, a preliminary study on the operation of a model single chamber SOFC in 1% CO-20% O_2-79% N_2 at 400 °C was reported without any conclusive analysis due to the evaporation of the Ni electrode [159].

Some studies related to catalytic nanoparticles report the *in situ* characterisation of materials that are used in SOFC anodes. Chenna and co-workers investigated the oxidation and reduction pathways of Ni nanoparticles (5-30 nm) supported on larger SiO_2 spheres in various gas atmospheres up to 800 °C [114]. During oxidation, irregular NiO shell structures were observed to surround a central void that formed at the position of the initial Ni particles. Such structure was concluded to result from the unbalanced outward diffusion of Ni^{2+} along the NiO grain boundaries similarly to the literature findings reported in Chap. 1.2.3 (Fig. 1.7a). During a subsequent reduction process, a dense Ni domain appears to nucleate in projection at the position of the internal void within the NiO shell. Such structure was interpreted as a Ni (core)-NiO(shell) and was deduced to result from the diffusion of Ni^{2+} along the grain boundaries similarly to the oxidation process (Fig. 1.7b). While their description of the oxidation process is in agreement with theoretical [79,92] and microstructural [97–100] assessments from the literature, the reduction pathway illustrated in Fig. 1.7b appears in contradiction with the solid-state kinetic models usually employed to describe NiO reduction (Fig. 1.3a,b,e,f, see Chap. 1.2.1). The schematic description shown in Fig. 1.7 is based on images and is not supported by a kinetic analysis of the reduction and oxidation reactions, which would allow an assessment of the reliability of the proposed reaction pathways.

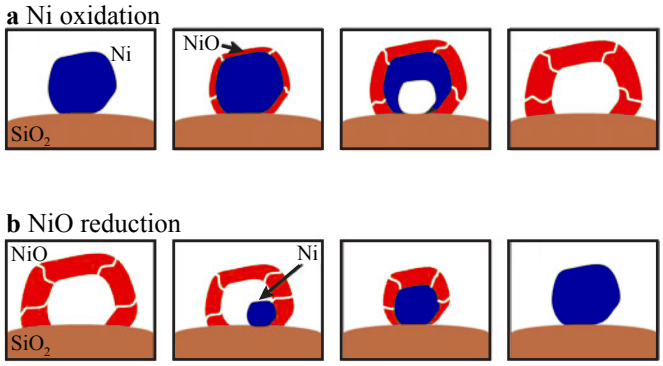

Figure 1.7 – Schematic representation of Chenna *et al.* illustrating the oxidation and subsequent reduction of Ni nanoparticles (5-30 nm) supported on SiO_2 spheres [114].

Rez and co-workers reported two different electron energy-loss spectroscopy techniques to quantify the oxidised fraction of Ni nanoparticles supported on SiO_2 as a function of temperature in high vacuum conditions [113]:

- profile matching of the Ni $L_{2,3}$ white lines using reference spectra for Ni and NiO,
- quantification of the Ni $L_{2,3}$ edge with respect to a pre-peak in the O K ionisation edge attributed to NiO (in contrast to the SiO_2 phase).

The authors presented four values of NiO percentage in the probed area when heating up to 600 °C but did not relate those values to structural changes. Along with other similar methods that rely on the use of the changes in shape of the $L_{2,3}$ ionisation edge

to infer the oxidation state [189,198], such an approach appears promising as it allows the retrieval of reaction kinetics, which could in turn be correlated to structural changes and solid-state models.

1.4 Concluding remarks

Overall, it appears that a methodology that relates structural changes, reaction kinetics, both obtained *in situ* in the environmental TEM, and solid-state kinetic modelling is yet to be developed. The reaction kinetics may be obtained from electron energy-loss spectroscopy by analysing fine details of the Ni $L_{2,3}$ ionisation edge similarly to the reports of Sharma and Rez *et al.* [113,189]. In addition, the application of energy-filtered TEM images to obtain quantitative structural and chemical information [170], while the specimen is reacting with a gas at high temperature, has not been reported for any solid-gas reaction but appears as a promising approach to obtain spatially-localised kinetic data. In addition, a detailed analysis of diffraction patterns to assess the changes in crystallography with respect to the structure and chemistry also appears unexploited.

In more detail, such a methodology that allows a direct and quantitative structural and chemical diagnostic on the nm scale should improve the description of the redox instability of Ni(/YSZ) systems. Specifically, the following aspects that were found to be subject to discrepancies in Chap. 1.2 mostly due to a lack of knowledge about the nano/microstructure must be clarified:

- correlation between Ni structure and reduction/oxidation kinetics,
- effect(s) of YSZ on NiO reduction and Ni oxidation mechanisms,
- transport mechanisms of ions on the nm length scale during Ni oxidation,
- formation of internal voids during Ni oxidation,
- process allowing inward growth of NiO during oxidation,
- volume swelling of NiO due to a reduction/oxidation cycle.

2 Materials and methods

The as-received nickel oxide (NiO) powder and as-sintered NiO/yttria-stabilised zirconia (YSZ) composites are described along with the main methods employed throughout this work. In that regard, the advanced transmission electron microscopy techniques that were applied both *in situ*, i.e. whilst the specimen was reacting with H_2 or O_2, and *ex situ* are discussed with respect to the materials science information that could be obtained. In particular, the focus is placed on the electron energy-loss spectroscopy methodology that was developed to retrieve the reaction kinetics from the changes in shapes of both the Ni $L_{2,3}$ and O K ionisation edges during reduction and oxidation. In addition, the analysis of X-ray powder diffraction patterns that were acquired *in situ* during reaction is described. Finally, the methods that were used to yield quantitative kinetic information from the data obtained *in situ* in the environmental microscope and in the X-ray diffractometer are discussed.

2.1 NiO particles and NiO/YSZ composites

The investigation of the reduction and oxidation reactions of Ni-based SOFC anodes relied on the characterisation of two different sets of materials: raw NiO powders and as-sintered NiO/YSZ composites. As the NiO reduction and oxidation reactions are both sensitive to various parameters such as size of the NiO domains and impurities (Chap. 1), the same NiO powder was investigated as such and when co-sintered with YSZ. In turn, the objective was to infer the influence of the YSZ ceramic on both reduction and oxidation reactions.

The first investigated system was a commercial NiO powder from JT Baker™ (with NiO $>$ 99.0 %wt), which is commonly used in Ni-based SOFC anodes. An inductively coupled plasma mass spectrometry analysis resulted in the following concentrations of trace elements:

	Ca	Na	K	Fe	Si	Al	Cu	Co	Zn	S
[ppm]	76	61	36	51	114	17	21	216	97	84

Table 2.1 – Inductively coupled plasma mass spectrometry quantification of trace elements in the JT Baker™ NiO powder, expressed in parts per million (ppm), equivalent to mg kg^{-1}.

The smallest particles were measured to be ∼50 nm using optical diffraction, with an average agglomerate size of ∼1 µm. Scanning electron microscopy (SEM) images highlight a heterogeneous microstructure as shown in Fig. 2.1.

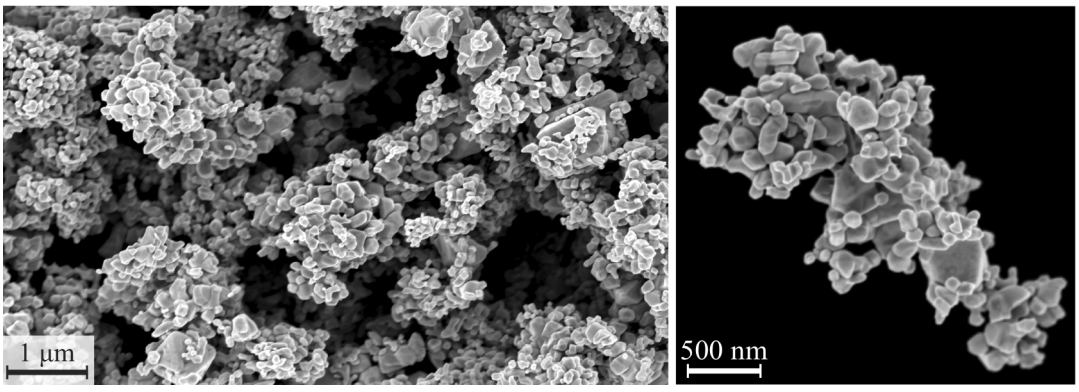

Figure 2.1 – Secondary electron SEM micrographs of the raw NiO powder from JT Baker™.

SOFC anodes investigated here were composed of NiO particles from JT Baker™ (55 %wt) co-sintered with YSZ particles from Tosoh™ (45 %wt YSZ that itself consists of 50 %wt of ZrO_2 stabilised with 3 %mol of Y_2O_3 and 50 %wt of ZrO_2 stabilised with 8 %mol of Y_2O_3).

2.2 Transmission electron microscopy

Transmission electron microscopy (TEM) relies on the interaction of a thin electron-transparent specimen with a high energy electron beam (typically in the range 80-300 keV). Only the specific methods that were used in this work are discussed with respect to the information that could be obtained, along with their limitations/advantages to study solid-gas reactions at high temperature. Transmission electron microscopy and related techniques are described in numerous textbooks to which the reader is referred for further information [170, 172, 199–202]. Specific details regarding each experiment will be given along with the results in Chapters 3-6.

2.2.1 Sample preparation techniques

Electron transparency is usually reached when the specimen thickness is on the order of ∼100/200 nm or less with a beam energy of 300 keV. In turn, an extensive procedure is sometimes required to prepare bulk samples for electron microscopy observations.

NiO particles

A small quantity of NiO particles (mg) was put into suspension in isopropanol and treated in an ultrasonic bath for 30 min to break up the agglomerates and to disperse the powder. As the particles need to be smaller than ∼100/200 nm to be electron transparent, the suspension was left to decant for a few minutes and a few drops were then taken from the supernatant to select only the smallest particles. These drops of suspension were dispersed onto either copper grids covered with a continuous silicon oxide film (Cu-SiO_x, for reduction experiments) or gold (Au) grids with holey SiO_x films (for both reduction and oxidation experiments). The grids were then exposed to heat for 30 min (UV light) to evaporate the solvent. To prevent contamination by carbonaceous materials, the grids were plasma cleaned during 7 min prior to TEM examination.

NiO/YSZ composites

In a dual beam focused ion beam FIB/SEM (Zeiss NVision 40 CrossBeam), a 20 x 4 µm protective C mask was deposited on the surface of the NiO/YSZ composite using first electron beam-induced deposition and then ion beam-induced deposition. Then, a thin specimen was prepared at the position of the C layer using 2 different techniques:

- conventional lift-out technique, where a thin slice of NiO/YSZ was extracted, welded onto stainless steel grids using a C welding and finally thinned down to a thickness of 100 nm (Fig. 2.2a-d),
- H-bar technique, where the NiO/YSZ composite was cut into the shape of a half electron microscopy grid and mechanically polished into a wedge shape until a thickness of ∼50 µm prior to the deposition of the C protective mask in the FIB, with 2 to 3 thin windows then prepared on the H-bar using FIB milling (Fig. 2.2e-f).

In both cases, final thinning was performed at a low Ga^+ energy of 2 or 5 kV to minimise surface amorphisation and Ga^+ implantation [203]. The H-bar geometry allowed higher reaction temperatures, especially in oxygen, as it did not involve any C welding.

While the FIB preparation technique is known to result in surface amorphisation and Ga^+ implantation, which may induce artefacts, it allows the preservation of the structure and results in specimens with a constant thickness, which simplifies the analysis of energy-filtered transmission electron microscopy images [204]. Alternative techniques include tripod polishing combined with a precision ion polishing system (PIPS) but those did not preserve the structure as well as FIB techniques and were found to result in redeposition of materials in the initial porosity of the as-sintered sample. This redeposited material may then also introduce artefacts during *in situ* experiments.

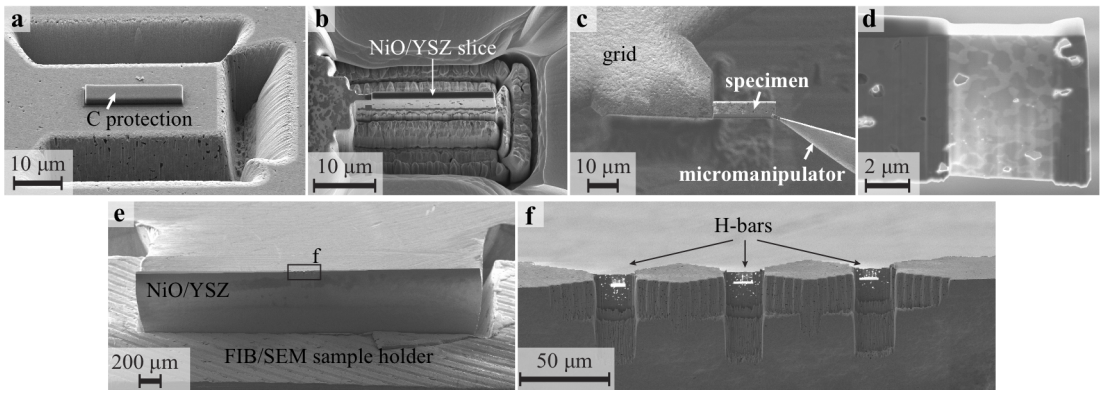

Figure 2.2 – Secondary electron SEM micrographs showing different steps of the two different NiO/YSZ sample preparation techniques employed in this work. (a-d) Conventional FIB lift-out technique, where, after deposition of a protective C layer, a thin lamella is extracted and attached onto a metallic grid using a micromanipulator and finally thinned to electron transparency (∼100 nm). (e-f) H-bar geometry, where the NiO/YSZ composite is cut and polished into the shape of a half TEM grid and thinned down to electron transparency at various positions.

2.2.2 Heating specimen holders

In situ heating experiments in the microscope were conducted using mainly two different types of Gatan 652 double-tilt heating holders:

- inconel holder for reducing and oxidising atmospheres in the environmental TEM,
- tantalum holder for reducing conditions only.

In both cases, a heating coil in an inconel/tantalum cup is positioned around the specimen and its support (3 mm of diameter) and allows temperatures up to 850 °C (inconel holder) and 1000 °C (tantalum holder). While subject to significant thermal drift due to the amount of material that is heated, such holders are compatible with the two geometries of specimen used in this work. In addition, the temperature is directly monitored through a thermocouple attached to the furnace.

A Philips single-tilt holder that uses the same heating technology was also employed in separate experiments. In addition, a single tilt heating holder based on a microelectromechanical system (MEMS) from Protochips™ was also used to study the reduction/oxidation of NiO particles [179]. Due to the low amount of material that is heated, thermal drift is reduced considerably when compared to the Gatan 652 double-tilt holders. However, electrostatic charging did not allow the attachment of FIB-prepared NiO/YSZ lamellae onto the heating chips. Such holders also did not provide a direct temperature reading as this value was inferred from the current input through a high vacuum calibration file that did not necessarily apply in the presence of a gas flow in the microscope. In addition, the precise orientation of the specimen to obtain zone axis diffraction patterns was not possible due to the single tilt axis. For those reasons, the older generation of Gatan 652 holders was favoured.

2.2.3 Environmental transmission electron microscopy

The NiO particles and NiO/YSZ samples were then characterised during reduction and oxidation in an FEI Titan E-Cell 80-300 ST environmental transmission electron microscope (ETEM), in which a differential pumping system allows the introduction of a selected mixture of gases up to a pressure of 20 mbar around the specimen. The microscope, which is schematically illustrated in Fig. 2.3, is described in detail in [174]. In addition to conventional bright-field and dark-field imaging modes and diffraction capabilities [199], the microscope includes an image corrector (CETCOR unit from CEOS [169]), which compensates for the spherical aberration (Cs) of the objective lens and brings the spatial resolution to the sub-Å level, and a post-column Gatan 865 GIF Tridiem energy filter, which enables electron energy-loss spectroscopy (EELS) and energy-filtered TEM analysis (EFTEM) [170, 172]. The microscope was operated at 300 kV throughout this work.

In separate experiments, H_2 and O_2 were introduced in the microscope at a flow rate of 2 $ml_N\ min^{-1}$, which resulted in 1.3 mbar of H_2 and 3.2 mbar of O_2 around the specimen, respectively, to study the reduction and reoxidation of the NiO(/YSZ) samples. Isothermal experiments at sufficiently high temperatures (350–850 °C) are difficult to make inside this first generation of FEI Titan ETEM. Indeed, as the gas cannot be preheated and the gas flow rate can be increased only with limited control, the introduction of gas, whilst the specimen was held at high temperature, resulted in a temperature decrease of tens of °C and hence induced a significant thermal drift. One possibility was to heat the sample quickly at the desired temperature after the introduction of the gas in the environmental chamber. However, the large thermal drift of the tantalum and inconel holders associated to the rapid rise of temperature was found to prevent the acquisition of usable images during the first minutes of the reaction at the desired temperature. It was hence decided in this work to probe the reduction/oxidation of NiO(/YSZ) samples as a function of temperature rather than as function of time. In other words, reduction

and oxidation experiments that approximate temperature-programmed reactions at constant heating rates were investigated in the ETEM. In that regard, small heating steps (10-40 °C) followed by isothermal measurement sequences of a few minutes were designed to minimise thermal drift and approximate experiments at constant heating rates (from 2 to 7 °C min^{-1} up to 500-850 °C). As a consequence, temperature-resolved structural and chemical information could be retrieved both during reduction in H_2 and oxidation in O_2 using the techniques listed in the following sections.

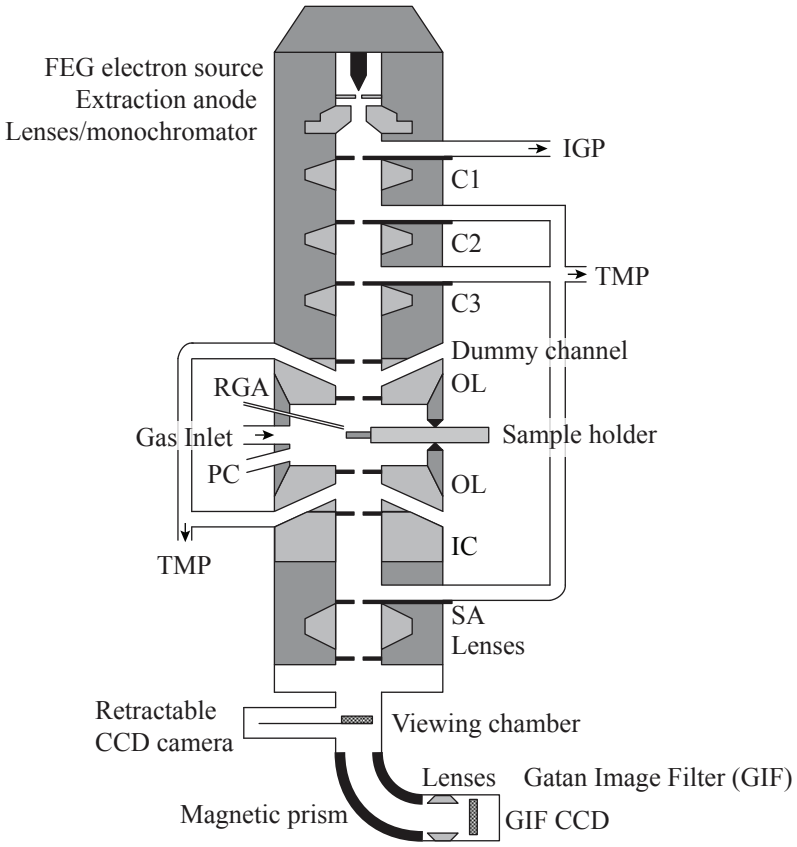

Figure 2.3 – Cross-section of the components of the FEI Titan ETEM, where the objective lens is labelled OL, the Cs image corrector IC and the selected area aperture SA. Apertures, turbomolecular pumps (TMPs) and an ion getter pump (IGP) allow a gas pressure of up to 20 mbar around the sample, while retaining an ultra-high vacuum (<10^{-8} mbar) at the field emission gun (FEG) electron source. Other additional components of the ETEM include a plasma cleaner (PC) and a residual gas analyser (RGA).

In general, experiments approximating constant heating rates were performed at a fixed electron dose rate so that the different samples/experiments could be compared. Complementary experiments also investigated radiation damages through the comparison of irradiated and non-irradiated regions at different temperatures and various electron dose rates.

2.2.4 Imaging and diffraction techniques

TEM imaging

Characterisation of the specimens involved the acquisition of TEM images using the following modes (Fig. 2.4), which are reviewed in detail in [205]:

- conventional at low magnification (no contrast aperture),
- bright-field (BF) that gives rise to a diffraction contrast (objective aperture in the back focal plane to select the direct beam),
- dark-field (DF) that also introduces a crystallographic orientation contrast (objective aperture in the back focal plane to select (a) diffracted beam(s)),
- high-resolution (HRTEM), in which a phase contrast gives rise to lattice fringes of spacing related to the distance between lattice planes.

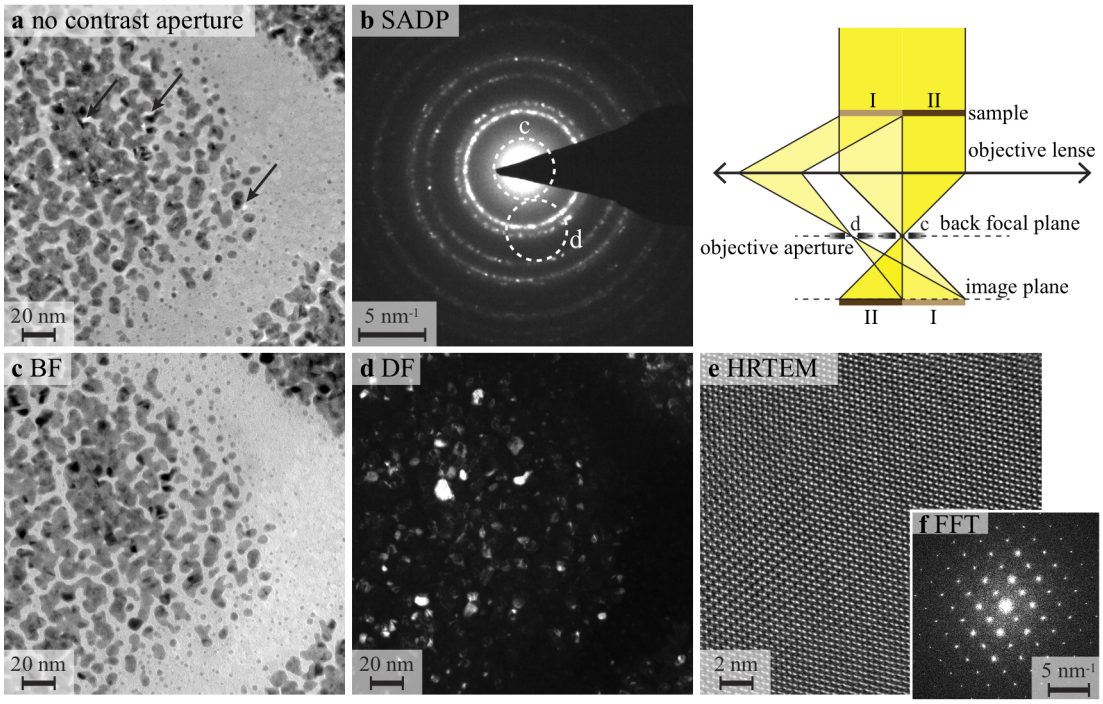

Figure 2.4 – (a) TEM image of Au nanoparticles supported on a carbon film without any aperture in the back focal plane, with arrows pointing to dark-field images (bright features). (b) Selected area diffraction pattern (SADP) of the region shown in (a), where the position of the objective aperture used to induce a contrast in (c) and (d) is shown. (c) Corresponding bright-field (BF) TEM image exhibiting a diffraction contrast (objective aperture selecting the direct beam in the back focal plane as shown in the sketch in the top-right corner). (d) Corresponding dark-field (DF) image of the same region, where the grains in the diffraction conditions selected by the objective aperture appear bright (see sketch). (e) High-resolution (HR)TEM image (of ZrO_2), in which lattice fringes are resolved (phase contrast, objective aperture selecting several diffracted reflections). (f) Fourier transform of (e).

The images were acquired as a function of reaction temperature/time in addition to before and after exposure to the reactive gas in the ETEM. The introduction of the objective aperture close to the heating holder to form bright-field and dark-field images, while the specimen was held at high temperature, resulted in a variation of temperature ($> 20\ ^{\circ}$C) and required the adjustment of the current in the heating coil of the holder.

Bright-field and dark-field images were acquired to monitor the grain structure of the specimens as grains of different crystallographic orientation exhibit a different contrast. HRTEM images were acquired to assess characteristic structural changes such as nucleation, with the objective to obtain details about the crystallographic orientation relationships between the Ni/NiO domains, along with their evolution on the nm scale.

Scanning TEM imaging

Scanning TEM (STEM) bright-field, dark-field (Fig. 2.5a-b, both exhibiting a crystallographic orientation contrast) and high-angle annular dark-field (HAADF, Fig. 2.5c, mass-thickness contrast) images were also acquired to assess the structure both *in situ* and *ex situ* [202]. STEM HAADF images provided interpretable insights into the internal structure of the specimen in contrast to the other aforementioned imaging techniques. In general, scanning TEM images appeared less suited to the study of dynamic processes such as those observed here as the image is formed by scanning the electron beam in a raster. As a result, the technique was used *in situ* at high temperature during reaction only once the thermal drift had stabilised and no significant structural change was observed to occur over a time scale of $\sim$1 min.

TEM diffraction

Selected area diffraction patterns (SADPs) were acquired to assess the crystallography of the specimen [206]. NiO and Ni both present cubic Fm-3m face centred structures, with lattice parameters of 0.418 nm for NiO [36] and 0.352 nm for Ni [37] (see Appendix A).

In the case of NiO particles, polycrystalline agglomerates were investigated using SADPs, which hence exhibited ring patterns. Alternatively, SADPs of individual NiO grains orientated along a zone axis (ZA) were acquired when studying FIB-prepared NiO/YSZ composites. In both cases, the change in crystallography during reduction/oxidation was monitored through the acquisition of SADPs at various temperatures. A rotational average of each temperature-resolved SAPD was computed using the Digital Micrograph plugin PASAD [207]. Then, a background $I_{\text{background}}(d)$ was subtracted from each rotationally averaged profile in Mathematica [208] as illustrated in Fig. 2.6 using:

$$I_{\text{background}}(d) = Ed^{-F} + Gd + H \tag{2.1}$$

where E, F, G and H are fitting parameters and d the reciprocal space distance measured in the SADP (in nm^{-1}). The change in integrated intensity of each background-subtracted

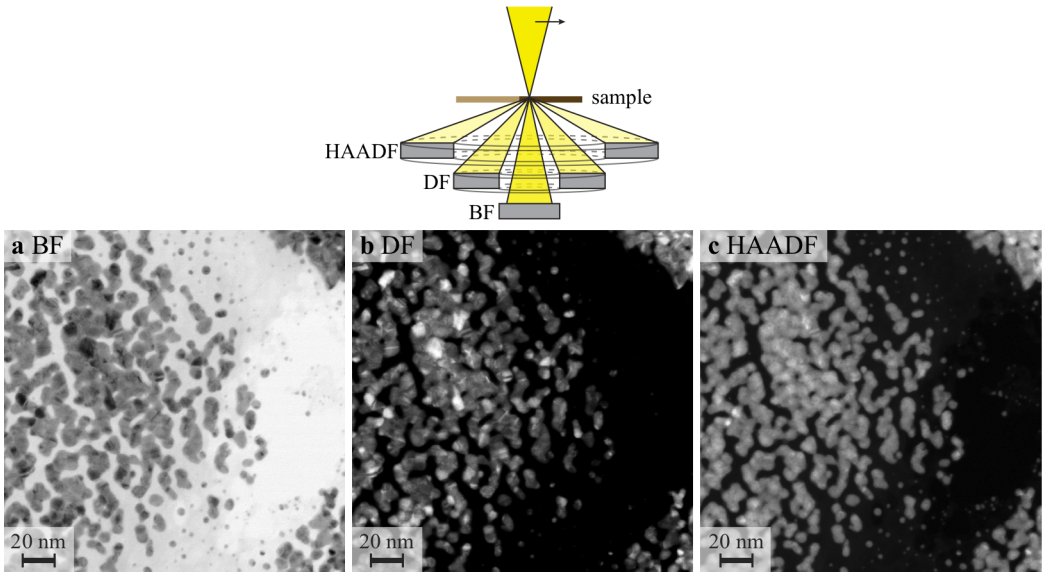

Figure 2.5 – (a) STEM bright-field (BF) image (diffraction contrast) of Au nanoparticles supported on C (same sample as in Fig. 2.4). (b) STEM dark-field (DF) image (diffraction contrast, with many reflections captured by the annular detector). (c) STEM high-angle annular dark-field (HAADF) image (mass-thickness contrast).

NiO/Ni reflection was monitored as a function of temperature. Consequently, the progress of the reaction, i.e. the reaction kinetics, could be estimated. However, small variations in specimen orientation and in aperture position with respect to the specimen, both induced by thermal drift, may affect those results. In that regard, EELS appears more suited to assess the chemistry of the samples as demonstrated in the next section.

2.2.5 Electron energy-loss spectrometry

EELS records the change in kinetic energy of an incident electron after it has passed through and interacted with the specimen [170, 172]. This analytical technique can be used to provide chemical and thickness information about the sample. In this work, different features of the EEL spectrum were used to infer the degree of reduction/oxidation of Ni in the investigated area as a function of temperature, whilst the specimen was reacting with a gas atmosphere in the ETEM. In turn, this temperature-resolved data could be correlated to changes observed in the (S)TEM images and SADPs and to solid-state kinetic models (see Chap. 2.5).

Fig. 2.7 shows a typical EEL spectrum of one NiO grain of a FIB-prepared NiO/YSZ specimen, where both the low-loss and the core-loss regions are shown. In the low-loss, the first peak is the zero-loss (ZL), which regroups electrons that have lost no energy or less energy than the resolution of the system (defined by the full width at half maximum, FWHM, of the ZL), while the second set of peaks contains the plasmon excitations and interband transitions (interactions with outer-shell electrons of the specimen). At higher

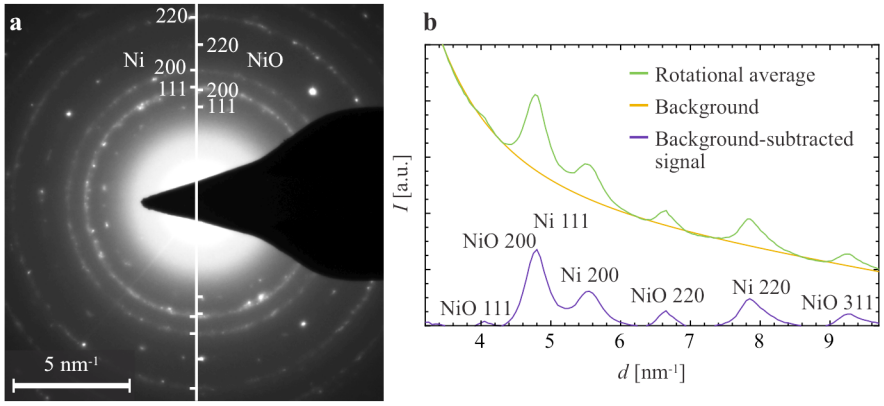

Figure 2.6 – Partially reduced NiO agglomerate of particles with (a) SADP of the entire agglomerate and (b) rotational average intensity of (a) along with the background-subtracted profile.

energy-losses, O K and Ni $L_{2,3}$ core-losses are observed to be superimposed onto a decaying background that arises from the high energy tail of excitations of electrons of lower binding energy. While the microscope is equipped with a monochromator that brings the energy resolution of the incident electron beam down to a few hundred meV, it was not used here as the features of interest in the EEL spectrum could be monitored with a sufficient resolution without monochromation. In general, a dispersion of 0.5 eV/channel was used to capture both the O K and Ni $L_{2,3}$ edges and the energy resolution was ∼1.5 eV.

Incident electrons may undergo plural scattering, i.e. one or more low-loss excitations in addition to a core-loss ionisation. This plural excitation process changes the shape of the recorded ionisation edges. Plural scattering of incident electrons can be removed through a deconvolution of the low-loss from the core-loss spectrum [209, 210]. Such deconvolution techniques involve the acquisition of both spectra (in the same conditions), which lengthens and complicates the experiments performed in the ETEM, whilst the specimen is reacting with a gas at high temperature. Moreover, the thickness of the NiO/Ni particles investigated here was not homogeneous over the recorded area, which falsifies to some extent the deconvolution procedure (Chap. 4, p. 238 of [172]). In view of this, low-loss spectra were not acquired and core-losses were not deconvolved to accelerate the acquisition of experimental data and facilitate the study of the NiO reduction/oxidation reactions.

The background below core-losses can be removed using a power law in the form:

$$I_{\text{background}}(E) = AE^{-r} \tag{2.2}$$

where A and r are fitting parameters and E is the energy-loss (in eV). After subtraction

of the background from the spectrum, the integrated intensity in the ionisation edge of an element (as those coloured in purple in Fig. 2.7) is related to the areal density of this element and hence enables an elemental analysis.

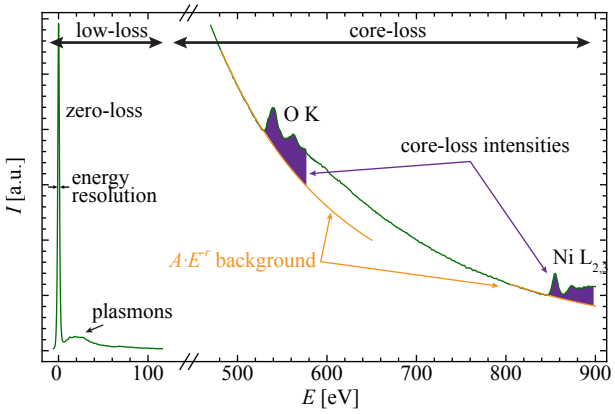

Figure 2.7 – Independently acquired EEL spectra of both low-loss and core-loss regions of one NiO grain in a FIB-prepared as-sintered NiO/YSZ composite.

Indeed, when the specimen is not supported by a film containing oxygen and is studied in high vacuum or H_2 atmospheres, the integrated intensity in the O K edge after background subtraction as shown in Fig. 2.7 is directly related to the areal density of O in the investigated area. This relation will be used in Chap. 2.2.6 to obtain spatially-resolved oxygen elemental maps of the FIB-prepared NiO/YSZ composites during reduction using energy-filtered TEM.

In the case of SiO_x supported NiO particles, the oxygen-rich amorphous film prevents the use of the O K edge in the EEL spectrum as such as the latter contains both contributions from the specimen and its support. Fine details of the O K edge may however provide a quantitative assessment of the O amount in the investigated area as shown by Rez *et al.* [113]. Indeed, as illustrated in Fig. 2.8a-b, the O K edge from the NiO phase has an onset at 532.0 eV, whilst contributions from the SiO_x are shifted to higher energy-losses by $\sim$5 eV. Rez and co-workers demonstrated that this pre-peak could be used to infer the fraction of Ni oxidised to NiO as a function of temperature in an ETEM operated in high vacuum conditions. However, such a technique is incompatible with EELS studies performed in the presence of O_2 as the gas gives rise to a large peak at 532.0 eV that superposes to the small NiO pre-peak as shown in Fig. 2.8c.

As a result, it was decided to focus on the shape of the Ni $L_{2,3}$ ionisation edges, which also provides information about the atoms surrounding the excited Ni atoms. Indeed, it allowed an assessment of the chemical environment of Ni independent of the eventual presence of O_2 gas in the environmental cell. The Ni $L_{2,3}$ white lines (L_3 at 855 eV and L_2 at 872 eV) correspond to energy-losses induced by the transitions of Ni electrons from $2p_{3/2}$ and $2p_{1/2}$ core states to empty 3d states (Fig. 2.10), with the latter hybridising with oxygen 2p orbitals in an oxide [198, 211].

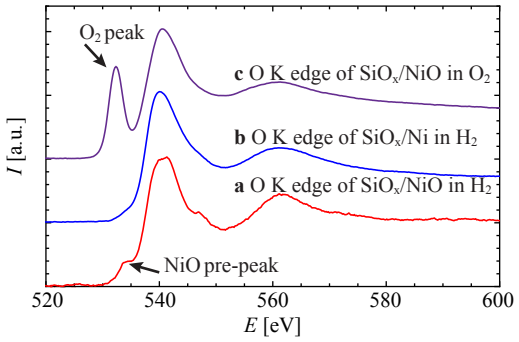

Figure 2.8 – O K ionisation edge from the same NiO agglomerate of particles as a function of gas atmosphere and oxidation state; SiO_x support and (a) NiO in 1.3 mbar of H_2, (b) Ni in 1.3 mbar of H_2 and (c) NiO in 3.2 mbar of O_2.

While the shift of the L_3 edge provides some insights into the oxidation state, this chemical shift was not assessed here due to its small magnitude (shift of 0.2 eV when NiO is reduced to Ni). The focus was placed here on the analysis of the shapes of the $L_{2,3}$ ionisation edges, and in particular on the ratio between the L_2 and L_3 lines (branching ratio), which depends on the oxidation state as shown in Fig. 2.10. Different methods enabled the quantitative analysis of those changes in shapes to infer the average oxidation state of Ni in the investigated area. In that regard, the first step involved the removal of the background (using Eq. 2.2) from the sequence of $L_{2,3}$ edges that captured the reduction and oxidation reactions as a function of temperature. The Ni $L_{2,3}$ edges were then aligned by cross-correlation, and principal component analysis was performed to minimise noise [212–214].

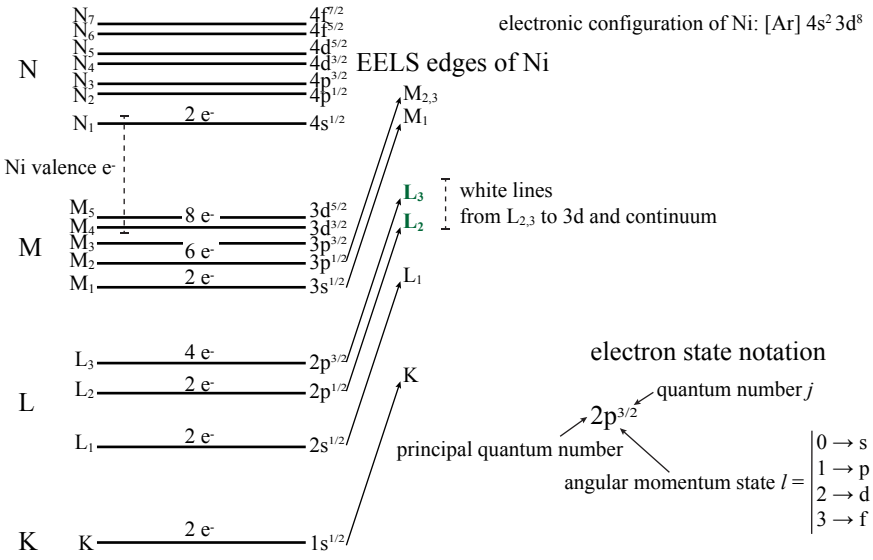

Figure 2.9 – Electronic structure of Ni and EELS transitions.

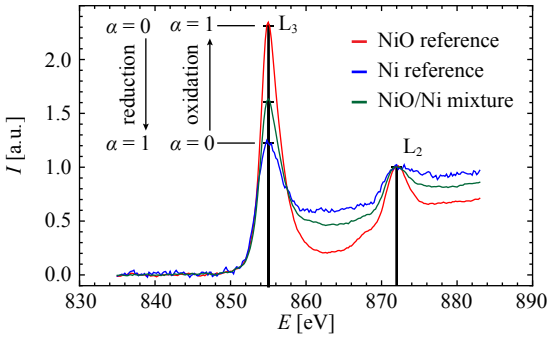

Figure 2.10 – Changes in shapes of the Ni $L_{2,3}$ ionisation edges depending on the NiO fraction in an investigated area. L_2 was normalised to unity for comparison of the ratios. The conversion fraction α of the reaction varies from $\alpha = 0$ in the initial state to $\alpha = 1$ in the final state.

The analysis of the oxidation state of an element from $L_{2,3}$ white lines then usually involves the removal of the transitions to the continuum. Indeed, the Ni $L_{2,3}$ white lines contain contributions from both intense transitions to 3d bound states and less intense transitions to the continuum [215]. The latter contributions can be subtracted before the white lines are analysed to provide information about the valency of the transition metal [216, 217]. In that regard, different techniques were developed over the years to remove these contributions as reviewed by Riedl and co-workers [198]. However, those methods involve the fitting of empirical functions of different level of complexity to the experimental data and these were found to introduce additional errors due to differences in the fitting quality between the spectra acquired *in situ*. As the objective here was not to accurately measure the valence of Ni but to assess how the Ni $L_{2,3}$ edges were changing with respect to experimental NiO and Ni $L_{2,3}$ references depending on temperature during reaction, it was decided to use two simplified techniques. These two methods did not involve the removal of the contributions to the continuum and directly assessed the changes in shapes of the Ni $L_{2,3}$ ionisation edges either:

- through the measurement of the L_3 to L_2 ratio (white lines ratio method [189, 198])
- or through the fit of an experimental spectrum to the NiO and Ni reference spectra using a multiple linear least squares algorithm (MLLS [113]).

In both cases, the methods relied on the fact that our system at a given reaction temperature was a mixture of Ni and NiO as no other oxide was expected during those reactions [38, 91]. In turn those techniques were able to extract a value of the fraction of reactant $0 < \alpha < 1$ that was converted to the product by the chemical reaction at each temperature step (as illustrated in Fig. 2.10). Finally, the sequence of α measurements provided the kinetics of the reaction.

To calculate the white lines ratio, the L_3 and L_2 edges were fitted using either an interpolated polynomial function or the sum of Lorentzian and the square of a Gaussian, the latter given by the expression:

$$F_{L_{2,3}}(E) = I_L \frac{w_L^2}{w_L^2 + (E - E_{edge})^2} + \left(I_G e^{-2\pi (E - E_{edge})^2 w_G^{-2}} \right)^2 \tag{2.3}$$

where E is the energy-loss in eV, E_{edge} the energy-loss at the position of the edge (855 eV for L_3, 872 eV for L_2), I_L and I_G are parameters determining the height of the fit, while w_L and w_G determine the width of the curve. Using both fits, the intensity in each L_3 and L_2 white line was then measured using different integration windows centred on the L_3 and L_2 maxima. The $I(L_3)/I(L_2)$ ratios were then normalised using the experimental Ni and NiO reference ratios ($I(L_3)/I(L_2)_{Ni}$ and $I(L_3)/I(L_2)_{NiO}$, respectively, which were obtained using the same microscope settings and verified using SADPs). Finally, the degree of conversion α at a temperature T during reduction was obtained in the form:

$$\alpha_{reduction} = \frac{I(L_3)\Big/I(L_2)_{NiO} - I(L_3)\Big/I(L_2)_T}{I(L_3)\Big/I(L_2)_{NiO} - I(L_3)\Big/I(L_2)_{Ni}} \tag{2.4}$$

Similarly, α during oxidation resulted in:

$$\alpha_{oxidation} = \frac{I(L_3)\Big/I(L_2)_T - I(L_3)\Big/I(L_2)_{Ni}}{I(L_3)\Big/I(L_2)_{NiO} - I(L_3)\Big/I(L_2)_{Ni}} \tag{2.5}$$

Alternatively, each experimental spectrum $F(E)$ acquired at a temperature T was fitted to NiO and Ni experimental reference spectra ($R_{NiO}(E)$ and $R_{Ni}(E)$, respectively) using a multiple linear least squares algorithm (MLLS) as in Ref. [113]. The factors m and n, which minimised the least squares error between the experimental spectrum $F(E)$ and that calculated using the reference spectra $R(E)$, were obtained for the entire spectral series acquired as a function of temperature T:

$$F_T(E) = m_T R_{NiO}(E) + n_T R_{Ni}(E) \tag{2.6}$$

The result for α in the case of reduction/oxidation was then:

$$\alpha_{reduction} = \frac{n_T}{m_T + n_T} \tag{2.7}$$

$$\alpha_{oxidation} = \frac{m_T}{m_T + n_T} \tag{2.8}$$

In general, the EEL spectra were acquired in diffraction mode. The study of the SiO_x supported NiO particles by EELS involved the use of a large SA aperture (corresponding

to 10 µm^2 in the image) so that the region of interest could drift but still remained in the SA aperture during the acquisition of each EEL spectrum (1-2 minutes). As a consequence, an average information of the entire NiO agglomerate of particles was obtained with this technique, i.e. the reaction kinetics α obtained represented the entire NiO/Ni phase located in the 10 µm^2 area. In the case of FIB-prepared NiO/YSZ specimens, energy-filtered TEM images rather than EEL spectra were acquired to yield a spatially-resolved information.

2.2.6 Energy-filtered transmission electron microscopy

The use of an energy-selecting slit placed in the EEL spectrum in an imaging filter enables the selection of spectral features and in turn the acquisition of TEM images that are filtered in energy. These energy-filtered TEM (EFTEM) images provide spatially-resolved quantitative information about the structure and the chemistry of the specimen on the position of each pixel [170]. In this work, the reaction of FIB-prepared NiO/YSZ composites in H_2 and O_2 atmospheres was investigated as a function of temperature using series of EFTEM images acquired *in situ* at different energy-losses to make use of different characteristic features of the EEL spectrum.

The thickness t of a specimen (in nm) can be mapped through the acquisition of an unfiltered image I_t (or the total area in a low-loss spectrum) and an image I_0 of the zero-loss (or the area under the zero-loss peak) as illustrated in Fig. 2.11. As a result, a total inelastic mean free path image t/λ is obtained using the relation (Chap. 5 in [172]):

$$t/\lambda = \ln(I_t/I_0) \tag{2.9}$$

where λ is the total mean free path for all inelastic scattering (in nm). λ can be estimated in Ni and NiO as shown in Appendix D.1 using the collection semi-angle $\beta_{\text{collection}}$ (in mrad, defined here by the objective aperture), the initial energy of the electrons and the effective atomic number of the specimen. By this approach, quantitative insights into the variation of the thickness of the NiO/Ni domains in the specimen could be obtained when acquiring series of total inelastic mean free path images during experiments that approximated constant heating rates. Such results provided details about the evolution of the volume of the NiO phase, which could be correlated to theoretical predictions (-41.6 %vol for NiO reduction and +71.2 %vol for Ni oxidation [9]).

The elemental distribution of O at a given temperature and its evolution, while the temperature is increased by small steps, could be obtained by analysing the intensity in background-subtracted O K ionisation edge images. To this purpose, the conventional 3-window method was used to remove the background and it involved the acquisition of three images: two images were acquired with the slit positioned before the O K edge onset $I_{\text{pre-edge 1}}$ and $I_{\text{pre-edge 2}}$, while a third image $I_{\text{post-edge}}$ was then acquired at the

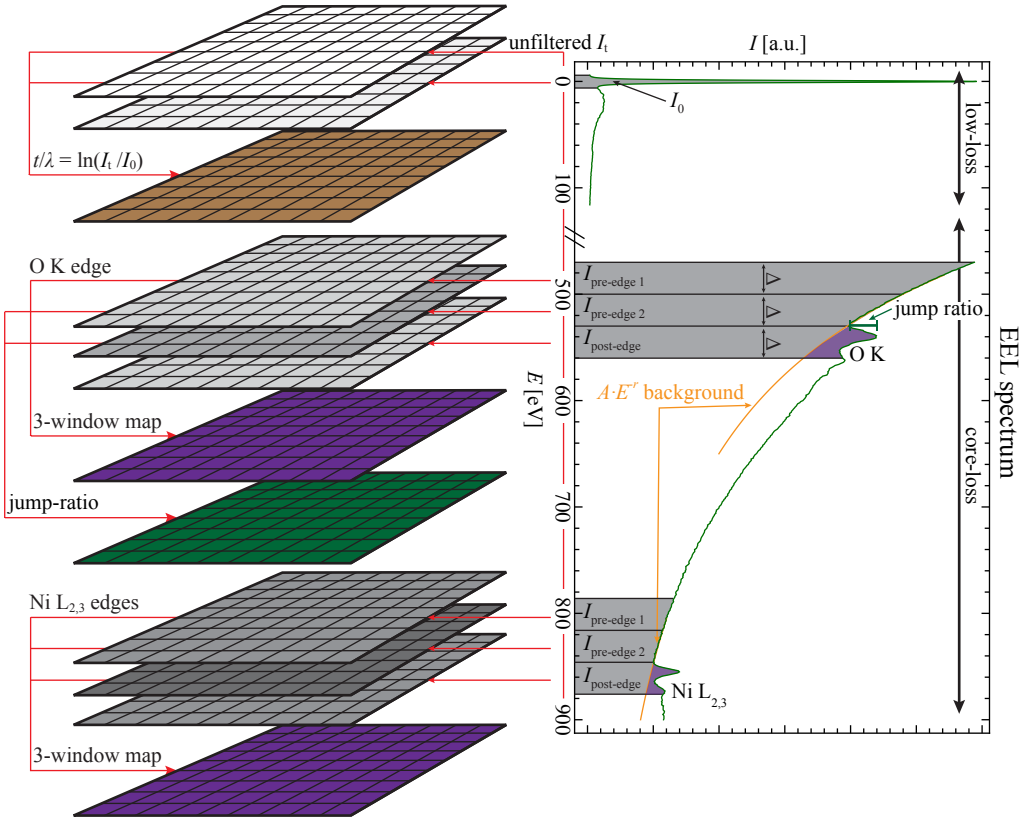

Figure 2.11 – Positions of the energy-selecting slit (coloured in grey) to select parts of the energy-loss spectrum to yield t/λ total inelastic mean free path images, 3-window elemental maps and jump-ratios, where the filtered information is on the position of each pixel.

position of the edge (as illustrated in Fig. 2.11). Prior to the removal of the power law background from the $I_{\text{post-edge}}$ image, the images were aligned by cross-correlation to ensure that each region of the structure remained at the same pixel coordinates in the sequence of $I_{\text{pre-edge 1}}$, $I_{\text{pre-edge 2}}$ and $I_{\text{post-edge}}$ images acquired at a temperature T, but also throughout the entire sequence of filtered images acquired at different temperatures. However, EFTEM images and especially images acquired *in situ* with short acquisition times, so as to maximise the temporal resolution, are usually noisy and in turn the cross-correlation procedure may be affected accordingly. To ensure an adequate alignment procedure, a Sobel filter (isotropic 3x3 gradient operator) was applied to each $I_{\text{pre-edge 1}}$, $I_{\text{pre-edge 2}}$, $I_{\text{post-edge}}$ image acquired at different temperatures to mark the edges of each image [218]. The filtered images were then aligned by cross-correlation to yield the shift vectors, which were in turn applied to the original $I_{\text{pre-edge 1}}$, $I_{\text{pre-edge 2}}$, $I_{\text{post-edge}}$ images. Both the filtering procedure and the alignment through cross-correlation were performed using the Digital Micrograph plugin SDSD [219].

By an in-house Mathematica code [208], the background was extrapolated and subtracted from each temperature-resolved $I_{\text{post-edge}}$ image to yield 3-window O K edge elemental maps (Appendix D.2). In the same code, the 3-window maps were then analysed to provide details about the evolution of the number of O atoms in the NiO phase on the pixel scale depending on temperature. Indeed, the O intensity measured within a group of pixels of coordinates (x,y) is related to the number of oxygen atoms per unit area $N_{\text{O}}(x,y)$ according to (Chap. 4.5, p. 271 of [172]):

$$N_{\text{O}}(x,y) = \frac{I_{\text{O}}(\beta_{\text{collection}},\Delta)(x,y)}{I_{\text{low-loss}}(\beta_{\text{collection}},\Delta)(x,y)\cdot\sigma_{\text{O}}(\beta_{\text{collection}},\Delta)} \tag{2.10}$$

where:

- $I_{\text{O}}(\beta_{\text{collection}},\Delta)(x,y)$ is the intensity in the 3-window O K edge elemental map on the pixel position (x,y) that was collected with a slit width Δ (in eV) and a collection semi-angle $\beta_{\text{collection}}$ (in mrad),
- $I_{\text{low-loss}}(\beta_{\text{collection}},\Delta)(x,y)$ is the signal in the low-loss image (zero-loss and plasmons) integrated over Δ and collected using $\beta_{\text{collection}}$,
- $\sigma_{\text{O}}(\beta_{\text{collection}},\Delta)$ is the partial ionisation cross-section of oxygen, which also depends on Δ and $\beta_{\text{collection}}$.

Then, assuming that $I_{\text{low-loss}}(\beta_{\text{collection}},\Delta)$ remains constant throughout each experiment (performed using constant microscope settings), a value of α (fraction of reactant converted to product) could be obtained on the position of each pixel or group of pixels (x,y) at each temperature step T, by normalising the data using the experimental NiO ($I_{\text{O}_{\text{NiO}}}$) and Ni ($I_{\text{O}_{\text{Ni}}}$, which should be 0) reference intensities measured at the same (x,y) position. In the case of reduction, the conversion fraction $0<\alpha<1$ at a position (x,y) at T then results in:

$$\alpha_{\text{reduction}}(x,y) = \frac{I_{\text{O}_{\text{NiO}}}(\beta_{\text{collection}},\Delta)(x,y) - I_{\text{O}_T}(\beta_{\text{collection}},\Delta)(x,y)}{I_{\text{O}_{\text{NiO}}}(\beta_{\text{collection}}\Delta)(x,y) - I_{\text{O}_{\text{Ni}}}(\beta_{\text{collection}}\Delta)(x,y)} \tag{2.11}$$

As an objective aperture must be used when acquiring EFTEM images to guarantee a sufficient spatial resolution [204], diffraction effects are always present to some extent and those modify the intensity in the EFTEM images. As a result, the 3-window elemental maps were altered and artefacts were introduced in the subsequent chemical analysis. To reduce those diffraction effects, an alternative approach was considered, which involved the division of each $I_{\text{post-edge}}$ by its corresponding $I_{\text{pre-edge 2}}$ image after the alignment procedure to yield an O K edge jump-ratio at each temperature. The division both minimised diffraction effects and also eliminated the background. While jump-ratios required only two images and hence could be obtained faster than 3-window elemental maps, the division procedure may introduce additional artefacts and comparison with 3-window elemental maps is recommended [204]. Jump-ratios usually provide only a

qualitative picture of the elemental distribution. However, such images could yield here a quantitative assessment of reaction kinetics through the comparison of the intensity in the jump-ratios of the partially-reacted structure to the reference NiO and Ni jump-ratios. I_O measured in O K edge jump-ratios rather than in the 3-window elemental maps was used as an input in Eq. 2.11 to yield a complementary set of values of α.

The acquisition of sequences of 3-window and jump-ratios of the O K edge was performed only during NiO reduction, whilst t/λ images were obtained both in reducing and oxidising conditions. In addition, 3-window Ni $L_{2,3}$ elemental maps as shown in Fig. 2.11 were acquired to differentiate the YSZ grains from NiO prior to reduction. As the YSZ was not expected to react in the conditions used in the ETEM, the intensity in the YSZ phase measured in the O K edge 3-window maps and jump-ratios was used as an invariant reference to assess the intensity changes in the NiO phase.

While EFTEM is also able to monitor the changes in shapes of the Ni $L_{2,3}$ edges through the acquisition of two separate post-edge images centred on the L_3 edge and on the L_2 edge, respectively [220], such a technique appeared less suited to the study of dynamic processes due to the longer acquisition time required at higher E and smaller Δ.

2.2.7 Energy-dispersive X-ray spectroscopy

Scanning TEM energy-dispersive X-ray spectroscopy (STEM EDX) chemical maps were acquired before and after reaction in the ETEM to assess the chemical changes induced by the reduction and oxidation reactions [171]. STEM EDX was performed in a dedicated microscope (FEI Tecnai Osiris), which is equipped with a high brightness field effect electron gun and four windowless silicon drift detectors (ChemiSTEM) [221]. The microscope is optimised for STEM EDX analysis and allowed a spatially-resolved assessment of the impurities present in the NiO/YSZ anodes prior to and after reaction in the ETEM. Quantification of EDX spectra was performed using the Bruker Esprit software and the procedure involved background removal, deconvolution of the X-ray peaks and relation of the intensity in the peaks to the concentrations using Cliff-Lorimer factors [222]. In the case of a compound of elements A and B, the intensities I_A and I_B of the X-ray peaks of elements A and B are related to the concentrations C_A and C_B using the Cliff-Lorimer factor k_{AB} according to:

$$\frac{C_A}{C_B} = k_{AB}\frac{I_A}{I_B} \tag{2.12}$$

Quantification of EDX maps was sometimes required to remove varying background contributions and to highlight the segregation of trace elements in irregular structures.

2.2.8 STEM HAADF tomography

Three dimensional reconstructions of the specimens after reaction in the ETEM were obtained using scanning TEM high-angle annular dark-field tomograms [223]. STEM HAADF images that each capture a 2D projection of the thin specimen were acquired in a JEOL 2220FS at various specimen tilt angles, usually from -65 to + 65° with an increment of 1°. Using the software TomoJ [224], tilt series were first aligned by cross-correlation. The analysis of the trajectory of local minima of the specimen structure was used to refine the alignment and to yield the tilt axis. 3D reconstructions were then obtained using the Simultaneous Iterative Reconstruction Technique (SIRT) with 30-40 iterations [225]. Visualisation of the structures in 3D involved the use of the software Chimera [226]. Information could thus be obtained about the surface morphology and the pore structure of the specimen after reaction in the ETEM.

2.2.9 Automated crystal orientation mapping

To complement SADP data acquired *in situ* during reaction, automated crystal orientation maps were acquired after reaction in the ETEM using the ASTAR system installed on a JEOL 2200FS microscope [227]. Diffraction patterns were acquired in nano beam conditions on the position of each pixel using a parallel beam of $\sim$2 nm that was scanned in a raster over the region of interest. The experimental diffraction patterns were indexed using the crystal structures shown in Appendix A through a template matching procedure [228]. The correlation index $Q(i,\phi_i)$ between the diffraction template $T_i(x,y,\phi_i)$ of rotation ϕ_i and the experimental pattern $P(x,y)$ was calculated on the position of each pixel of coordinates (x_j,y_j) according to:

$$Q(i,\phi_i) = \frac{\sum_{j=1}^{m} P(x_j,y_j)T_i(x_j,y_j,\phi_i)}{\sqrt{\sum_{j=1}^{m} P^2(x_j,y_j)}\sqrt{\sum_{j=1}^{m} T_i^2(x_j,y_j,\phi_j)}} \tag{2.13}$$

In doing so, the template $T_i(x,y,\phi_i)$ that maximised $Q(i,\phi_i)$ was identified on the position of each pixel. However, this template matching procedure always provides a solution, coherent or not. As a result, a measurement of the quality of the procedure, i.e. the reliability index R, must be defined:

$$R = 100\left(1 - \frac{Q_2}{Q_1}\right) \tag{2.14}$$

where Q_1 and Q_2 are the two highest correlation indices calculated for each pixel. If the two solutions have nearly the same Q, then R tends to 0 and the proposed solution should be rejected. Pixels where the value of R exceeds 15 are usually considered properly indexed [228]. In this work, crystallographic orientation or phase maps were

superimposed to reliability images to assess visually the quality of the template matching procedure.

The template matching results provided information about the disorientation between two crystallographic domains, i.e. the minimum rotation angle between those two crystal lattices. In addition, pole figures were also provided to assess the texture of the specimen. These pole figures capture the orientation of a defined set of (hkl) crystal planes in the form of a stereographic projection as illustrated for the (111) planes of a cubic crystal in Fig. 2.12. Pole figures also enabled to investigate whether a set of planes was common to two neighbouring grains and if it coincided with the boundary plane. Combined with an assessment of the disorientation across given grain boundaries, pole figures enabled the analysis of the symmetry of grain boundaries (coherent or incoherent) and crystallographic features such as twinning. Therefore, modifications in reaction behaviour due to differences in grain boundary symmetry could be investigated.

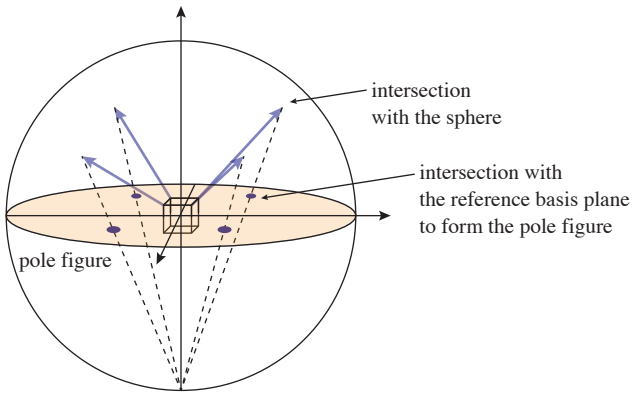

Figure 2.12 – Construction of the pole figure (coloured plane) of the (111) planes of a cubic structure oriented along a given direction.

2.3 *In situ* X-ray powder diffraction

ETEM data assessing the reduction of the NiO particles was complemented by *in situ* X-ray powder diffraction (XRD) [229]. This technique allowed the retrieval of kinetic and crystallite size information from a larger sample volume, which could be correlated to that obtained at much smaller length scale in the ETEM. In addition, the effects of H_2 gas pressure (12-600 mbar) and flow rate (2-40 ml_N min^{-1}) on the reduction kinetics were investigated as those experimental parameters are known to influence the reaction mechanisms [230]. In turn, the reliability of the data collected in the ETEM at low gas pressure and flow could be assessed.

A PANalytical X'Pert PRO diffractometer equipped with *in situ* capabilities was used in this work (Fig. 2.13a). As in the ETEM, temperature-programmed reactions at

slow constant heating rates were performed (1-4°C min^{-1} up to 700 °C). The 2θ scan range was from 35 to 54° so that the reflections (111) and (200) of both the NiO and Ni phases were included (Fig. 2.13b). A single scan time was 277 s and each Ni and NiO reflection was thus assigned a specific temperature inferred from the acquisition time of the scan and the heating rate. Like for EEL spectra, XRD scans acquired at different temperatures were aligned using a cross-correlation procedure and noise was reduced using principal component analysis [212–214]. Background was subtracted using a 10th order polynomial in the form (Fig. 2.13b):

$$I_{\text{background}}(2\theta) = \sum_{i=0}^{10} a_i (2\theta)^i \tag{2.15}$$

where a_i are fitting parameters and θ is the diffraction angle in degrees. To remove the K_{α_2} shoulder, the first half of each background-subtracted peak (up to the peak maximum) was fitted using a Pseudo-Voigt function $V(2\theta)$ as shown in Fig. 2.13c in the form:

$$V(2\theta) = I_{\text{peak}}\left(\eta \frac{w_L^2}{w_L^2 + (2\theta - 2\theta_0)^2} + (1-\eta) e^{-2\pi(2\theta - 2\theta_0)^2 w_G^{-2}}\right) \tag{2.16}$$

where θ_0 is the Bragg angle of the reflection to fit (in °), I_{peak} is the height of the reflection, η the linear combination parameter ($0 \leq \eta \leq 1$), while w_{L} and w_{G} determine the width of the curve. Peaks with an intensity lower than 2 times above the noise level were discarded due to fitting issues.

The full width at half maximum (FWHM) of each peak was inferred from both the $V(2\theta)$ fit and the width of the first half of the interpolated polynomial fit as illustrated in Fig. 2.13c. In turn, each measured $\text{FWHM}_{\text{meas}}$ was related to crystallite size L_{cryst} (in nm) using the Scherrer equation [231]:

$$L_{\text{cryst}} = \frac{K\lambda}{(\text{FWHM}_{\text{meas}} - \text{FWHM}_{\text{instr}})\cos(\theta)} \tag{2.17}$$

where λ is the wavelength of the Cu K_{α_1} source (0.154 nm), K is a factor that depends on the crystallite shape and the reflection (hkl) (in case of cubic crystallites: 0.8551 for (111) reflections, 0.8859 for (200) from Ref. [232]), θ is the Bragg angle (in radian), $\text{FWHM}_{\text{meas}}$ is obtained either from $V(2\theta)$ or the interpolated polynomial function and converted to radians and $\text{FWHM}_{\text{instr}}$ is the broadening induced by the PANalytical X'Pert PRO diffractometer (in rad), which was obtained from a Si standard composed of grains beyond the resolution limit of the apparatus. An interpolation function defined the $\text{FWHM}_{\text{instr}}$ as a function of 2θ based on the measurement of the FWHM of 9 Si reflections (Fig. 2.13d). The evolution of L_{cryst} was then investigated as a function of temperature and provided insights into the decrease/growth kinetics of NiO/Ni crystallites.

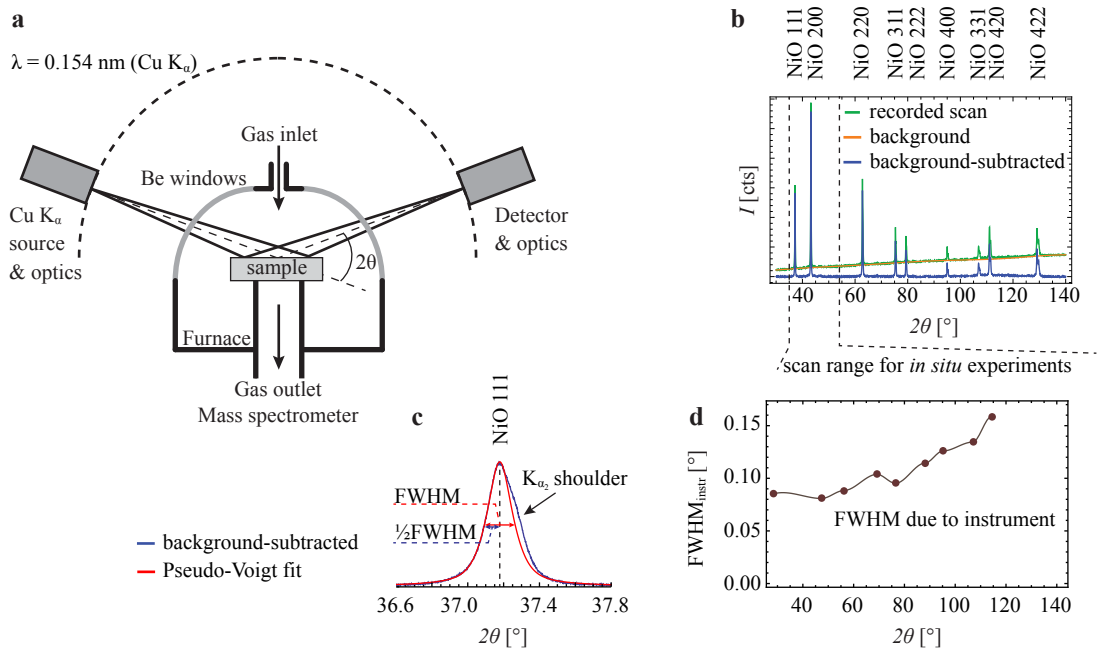

Figure 2.13 – (a) Schematic view of the *in situ* X-ray diffraction apparatus. (b) XRD pattern of the JT Baker™ NiO powder, where the scan range used during the *in situ* experiments is indicated. (c) Magnified view of the NiO (111) reflection along with a Pseudo-Voigt fit. (d) Instrument broadening function based on the measurement of the FWHM of the reflections of a Si standard.

In addition to the measurement of the maximum of each peak, the integral intensity of all of the Ni/NiO (111)/(200) reflections was measured using both Pseudo-Voigt and polynomial functions (in the latter case: 2 times the integral intensity of the first half of the reflection to remove K_{α_2}). Finally, the evolution of the intensity in the NiO reflections $I_{\mathrm{NiO\,(hkl)}_T}$ as a function of temperature provided information about the reduction kinetics with respect to the initial $I_{\mathrm{NiO\,(hkl)}_i}$ and final $I_{\mathrm{NiO\,(hkl)}_f} = 0$ intensities in the form:

$$\alpha_{\mathrm{reduction}} = \frac{I_{\mathrm{NiO\,(hkl)}_i} - I_{\mathrm{NiO\,(hkl)}_T}}{I_{\mathrm{NiO\,(hkl)}_i} - I_{\mathrm{NiO\,(hkl)}_f}} \tag{2.18}$$

The entire procedure described in this section was implemented in Mathematica [208].

2.4 Thermodynamics

NiO reduces according to reaction 1.1, while Ni oxidises following the path shown in 1.2. Both reactions proceed if the change in free enthalpy ΔG associated to the reaction is negative for given partial and total pressure P and temperature T conditions, which translates in the case of the reduction reaction 1.1 to:

$$\Delta_{1.1}G = \Delta_{1.1}G^0 + RT\ln\left(\frac{P_{\mathrm{H_2O}}/P^{\mathrm{o}}_{\mathrm{H_2O}}}{P_{\mathrm{H_2}}/P^{\mathrm{o}}_{\mathrm{H_2}}}\right) < 0 \tag{2.19}$$

and in the case of the oxidation reaction 1.2 to:

$$\Delta_{1.2}G = \Delta_{1.2}G^0 + RT\ln\left(\frac{1}{P_{O_2}/P^o_{O_2}}\right) < 0 \tag{2.20}$$

where R is the universal gas constant (8.314 J mol^{-1} K^{-1}) and P^o the standard states of H_2O, H_2 and O_2. Ellingham diagrams plot the standard free enthalpy ΔG^0 of a reaction as a function of temperature [233] with nomographic scales giving the equilibrium partial pressures P_{H_2}/P_{H_2O} and P_{O_2} [234]. In turn, the equilibrium conditions so that $\Delta G = 0$ can be determined quickly (Fig. 2.14).

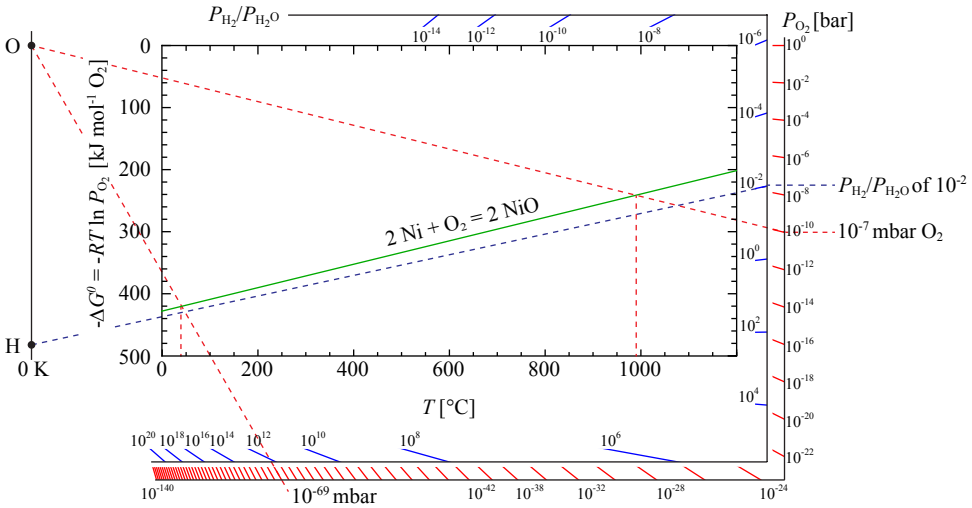

Figure 2.14 – Ellingham diagram for NiO constructed using the thermodynamic data in Appendix B.1 from Refs. [235,236], with the standard states $P^o_{H_2O} = P^o_{H_2} = P^o_{O_2} = 1$ bar.

The thermodynamic driving force for NiO reduction to Ni depends on the ratio P_{H_2}/P_{H_2O} and is hence sensitive to the presence of water in the reaction chamber. A ratio $P_{H_2}/P_{H_2O} \geq 10^{-2}$ is required to reduce NiO to Ni (Fig. 2.14). As result, a sufficient H_2 gas flow is required to remove H_2O from the reaction sites so that the reduction reaction remains thermodynamically favourable in all regions of the specimen.

In the case of Ni oxidation, the equilibrium P_{O_2} at 30 °C is on the order of 10^{-69} mbar (Fig. 2.14), which means that Ni should oxidise in the high vacuum of the microscope (P_{O_2} on the order of 10^{-7} mbar at the position of the specimen holder). A temperature on the order of 1000 °C is required to reduce NiO to Ni in the ETEM in a P_{O_2} of 10^{-7} mbar.

2.5 Kinetics

While thermodynamics determines whether a reaction may proceed in given experimental conditions, reaction kinetics analyses the real reaction rates and hence provides details about the rate-controlling mechanisms. Different *in situ* methods that involve electron energy-loss spectroscopy, energy-filtered TEM and *in situ* X-ray powder diffrac-

tion were implemented to obtain measurements of the fraction α of reactant converted to product as a function of temperature, as shown in the previous sections. In turn, those results could be analysed to provide details about the mechanisms controlling the reaction, mechanisms that could be correlated to the structural changes observed in the ETEM images. In addition, those mechanisms also provided information not necessarily visible in the images. Finally, the kinetic data could be assessed with respect to the data obtained in the literature using more conventional kinetic analysis techniques (e.g. thermogravimetry) to assess the reliability of the data obtained in the ETEM in the presence of the electron beam.

As mentioned in Chap. 2.2.2, isothermal experiments at temperatures relevant for this study (500-850 °C) were prevented by both the large thermal drift of the TEM heating holders and the fact that the gases were introduced at room temperature inside the ETEM. Subsequently, constant heating rate experiments, which involved small heating steps of < 40 °C, were approximated in the ETEM to reduce thermal drift and hence acquire interpretable data. Therefore, the analysis of the kinetic data became more complex when compared to isothermal data as shown in the next paragraphs.

The rate of a single step solid-state reaction $\mathrm{d}\alpha/\mathrm{d}T$ is usually described as the product of a function $f(\alpha)$, which gives the reaction model depending on the fraction α of reactant converted to product, and the rate constant $k(T)$ that depends on temperature T (in K) through an Arrhenius function [41]:

$$\frac{\mathrm{d}\alpha}{\mathrm{d}t} = k(T)f(\alpha) = Ae^{-E_a/RT}f(\alpha) \tag{2.21}$$

where E_a is the activation energy (in J mol^{-1}), A a pre-exponential factor related to the collision frequency (s^{-1}), and R the universal gas constant (8.314 J mol^{-1} K^{-1}). In an isothermal experiment, separation of the variables and integration simply results in:

$$g(\alpha) = \int_0^\alpha \frac{\mathrm{d}\alpha}{f(\alpha)} = Ae^{-E_a/RT}t \tag{2.22}$$

where $g(\alpha)$ is the integral reaction model. In the case of an experiment performed at a constant heating rate $\beta = \mathrm{d}T/\mathrm{d}t$ (in K s^{-1}), 2.21 yields:

$$\frac{\mathrm{d}\alpha}{\mathrm{d}T} = \frac{A}{\beta}e^{-E_a/RT}f(\alpha) \tag{2.23}$$

and in turn:

$$g(\alpha) = \int_0^\alpha \frac{\mathrm{d}\alpha}{f(\alpha)} = \frac{A}{\beta}\int_0^T e^{-E_a/RT}\mathrm{d}T \tag{2.24}$$

The integral solid-state reaction model $g(\alpha)$ describes mathematically how a solid reactant is transformed into a solid product. The different possible models can be categorised

as follows (see also Fig. 1.3): nucleation and domain growth (power law, Avrami, Prout and Tompkins autocatalytic model), geometrical contraction (shrinking cylinder, sphere), diffusion (1D, 2D, 3D Ginstling-Brounshtein, 3D Jander) and reaction order (zero-, first-, second-, third- order). The main reaction models are listed in Ref. [41].

Different methods then allowed the retrieval of $g(\alpha)$, E_a, A from the non-isothermal experiments that approximated a constant β in the ETEM and in the XRD.

Kissinger method

Kissinger published a model-independent method to extract the activation energy E_a from Eq. 2.23 [237]. The second temperature derivative of α is assigned to 0 at the temperature at which the reaction rate is maximum. The development, which is shown in Appendix C.1, results in:

$$\ln\Big(\frac{\beta}{T_{\max}^2}\Big) = \Big(-\frac{E_a}{R}\Big)\frac{1}{T_{\max}} - \ln\Big(\frac{E_a}{RA}\Big) + \ln\Big(-\frac{\mathrm{d}f(\alpha)}{\mathrm{d}\alpha}\Big)_{T=T_{\max}} \tag{2.25}$$

where $-\ln(E_a/RA) + \ln(-\mathrm{d}f(\alpha)/\mathrm{d}\alpha)_{T=T_{\max}}$ is constant for models where $f(\alpha)$ is linear in α and holds approximately for many models at the maximum rate [238]. It is therefore possible to extract from Eq. 2.25 the activation energy by obtaining the temperature at which the rate is maximum for different heating rates β experiments through the slope of $\ln(\beta/T_{\max}^2)$ versus $1/T_{\max}$. However, the Kissinger method does not provide any information about the reaction pathway $g(\alpha)$.

Model-dependent method

Information about the kinetic triplet $g(\alpha)$, E_a and A can be obtained using different methods which involve either numerical integration, approximations of the temperature integral or master plots [238,239]. As the objective here was to determine the solid-state reaction model category (illustrated in Fig. 1.3) and not the fine details of complex reaction models, the third rational approximation of the temperature integral introduced by Senum *et al.* was used [240]. Defining x as E_a/RT, Eq. 2.24 then results in the expression:

$$g(\alpha) = \int_0^\alpha \frac{\mathrm{d}\alpha}{f(\alpha)} = \frac{A}{\beta}\int_0^T e^{-E_a/RT}\mathrm{d}T \approx \frac{A}{\beta}\frac{E_a}{R}\left[\frac{e^{-x}}{x}\frac{x^2+10x+18}{x^3+12x^2+36x+24}\right]_{x_0}^{x} \tag{2.26}$$

In a Mathematica code [208], a Nelder-Mead procedure was used to yield the values of E_a and A that minimised the least squares difference between $g(\alpha)$ and the approximation of the temperature integral for a specific reaction model [241]. As E_a and A are invariant with β, $\alpha(T)$ curves obtained experimentally at different heating rates were fitted simultaneously to yield a single set of E_a and A for each reaction [40]. Boundary values inferred from a prior Kissinger analysis and literature data were applied to E_a in

the least squares algorithm to ensure that it remained in a realistic domain. The different fits were then compared with each other and with the ETEM images to yield the most realistic triplets $g(\alpha)$, A and E_a. All of the models listed in Ref. [41] were tested and compared in addition to those specific to oxidation developed in [81, 242, 243].

Parabolic rate constant in diffusion-controlled reactions

In the case of a diffusion-controlled reaction such as Ni oxidation (see Chap. 1.2.3), the growth of the oxide thickness L_{oxide} in a planar geometry at a constant temperature T in O_2 is parabolic with respect to the reaction time t [244]:

$$L_{\text{oxide}}^2 = k_p(T)t \tag{2.27}$$

where k_p is the parabolic rate constant, which is usually defined in units of $cm^2\ s^{-1}$. $k_p(T)$ is directly related to the diffusion coefficients of the rate-controlling species as shown by Wagner [84]. In the case of Ni oxidation above 1100 °C, Mrowec defined $k_p(T)$ based on experimental diffusion coefficients $D^*_{\text{lattice}}(T)$ of Ni^{2+} in the NiO lattice [245]:

$$k_p(T) = 3D^*_{\text{lattice}}(T) = 3 \cdot 9.3 \cdot 10^{-3} P_{O_2}^{1/6} e^{-E_a/RT} \tag{2.28}$$

where $D^*_{\text{lattice}}(T)$ is the tracer diffusion coefficient expressed in $cm^2\ s^{-1}$, P_{O_2} is the O_2 partial pressure (in Pa) and the activation energy E_a of this diffusion process was defined as 232 kJ mol^{-1}. In the case of Ni oxidation at temperatures below 1000 °C, diffusion through the NiO grain boundaries must be included in the description as demonstrated by Atkinson and co-workers in Ref. [92] and $k_p(T)$ is defined as follows:

$$k_p(T) = 6.4\left(D^*_{\text{lattice}}(T) + \frac{2(D'\delta)^*(T)}{g_{\text{size}}(T)}\right) \tag{2.29}$$

where $(D'\delta)^*(T)$ is the tracer grain boundary diffusion coefficient (in $cm^3\ s^{-1}$), δ is the grain boundary width and $g_{\text{size}}(T)$ is the oxide grain size (in cm). In addition, $k_p(T)$ is independent of P_{O_2} at those oxidation temperatures [91]. Here, values of the parabolic rate constant $k_p(T)$ were determined as a function of temperature based on the knowledge of E_a, A and the specific integral diffusion model $g(\alpha)$ (which defined the details of the function $k_p(T, E_a, A)$), which were inferred from the fitting of the EELS data acquired in the ETEM. In turn, those estimates of $k_p(T)$ could be compared to both predictions based on diffusion coefficients (Eqs. 2.28-2.29) and experimental values of $k_p(T)$ measured in the literature using more conventional techniques such as thermogravimetry to determine the diffusion pathway.

3 Reduction of NiO particles

In this first experimental chapter, reduction of NiO particles in H_2 is studied *in situ* using environmental TEM and X-ray diffraction. In the ETEM, images, diffraction patterns and electron energy-loss spectra are acquired to monitor the structural and chemical evolution of the particles during reduction in 1.3 mbar of H_2, whilst increasing the temperature up to 600 °C. Ni nucleation on NiO is either observed to be epitaxial or to involve the formation of randomly oriented grains. The growth of Ni crystallites and the movement of interfaces result in the formation of pores within the NiO grains to accommodate the volume shrinkage associated with the reduction. Densification of the Ni(O) structure is then observed when the sample is nearly fully reduced. The reaction kinetics is obtained using electron energy-loss spectroscopy by monitoring changes in the shapes of the Ni $L_{2,3}$ white lines. These results are correlated with *in situ* X-ray diffraction measurements performed at various pressure, flow and temperature conditions to confirm their reliability and assess their limitations. The activation energy for NiO reduction, calculated from the electron energy-loss spectroscopy and *in situ* X-ray diffraction data using both a physical model-fitting technique and a model-independent method, is coherent with data found in the literature. The results of the model-fitting procedure suggest that the reaction is described by an Avrami mechanism (whereby the nucleation, growth and impingement of Ni domains control the reaction), in agreement with the environmental TEM observations.

3.1 Experimental details

3.1.1 Materials

The as-received commercial NiO powder from JT Baker™ (NiO $>$ 99.0 %wt with Co, Si, Zn, S as the main impurities, see Tab. 2.1) was studied in this chapter.

3.1.2 Electron microscopy

Heating sequences to probe the reduction kinetics and resulting structural changes

NiO particles were dispersed onto Cu-SiO_x grids, which were then mounted in a Gatan 652 double-tilt heating holder and plasma cleaned for 7 min. *In situ* reduction was performed using the FEI TITAN ETEM microscope schematically illustrated in Fig. 2.3. H_2 was introduced into the environmental cell at a flow rate of 2 ml_N min^{-1} (volume flow at 273 K and 101.3 kPa), resulting in a pressure of 1.3 mbar around the sample. The introduction of H_2 in the environmental cell along with the removal of other gases such as O_2 was monitored using mass spectrometry. The specimen was then heated to 250 °C, as no reaction was found to occur below this temperature in the ETEM. The temperature was kept constant for 30 min to reduce thermal drift. At this point, three different ramping procedures were started to approximate linear heating rates of 2, 4 and 7 °C min^{-1} to probe the evolution of the system as a function of temperature. Fig. 3.1 shows the three different temperature profiles. At each step, the temperature was kept constant for 4–5 min (depending on the heating rate) to perform the measurements. With a selected area aperture inserted, a 10 μm^2 region of interest was characterised by acquiring a low magnification image, a diffraction pattern and a core-loss EEL spectrum (recorded in diffraction mode for 1–2 min using an energy range of 500–900 eV). The temperature was then increased quickly by 15, 25 or 35 °C over 1 or 2 min to maintain an equivalent heating rate of 2, 4 or 7 °C min^{-1} respectively, up to 600 °C. The region of interest for each experiment was chosen so that it contained a similar NiO structure and a similar number of particles compared to other specimens. Each region was selected to be in the center of the TEM grid and in the center of a grid square to ensure a constant temperature difference ΔT between the observed area and the thermocouple, which is welded onto the outside of the furnace. The uncertainties in the temperature measurements were estimated to be ± 10 °C for the three experiments. An electron dose rate of $\sim$400 e^- nm^{-2} s^{-1} was chosen as a compromise between beam damage and sufficient EELS signal over each measurement sequence. This value was kept the same for each kinetic experiment, with the region of interest imaged constantly over the length of each experiment. To obtain a fully reduced specimen as a reference, the sample reduced at 2 °C min^{-1} up to 600 °C was then kept at a constant furnace current for 100 min, with the resulting temperature increasing to 615 °C over this time.

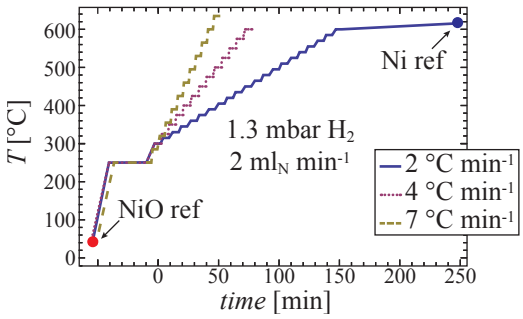

Figure 3.1 – Time and temperature parameters used to approximate constant heating rates. A set of measurements (involving the acquisition of an image, a diffraction pattern and an EEL spectrum) was performed at each step. The red and blue dots indicate when the NiO and Ni electron energy-loss reference spectra were acquired.

NiO reduction kinetics using EELS

The reaction kinetics can be inferred from the changes in shapes of the Ni $L_{2,3}$ ionisation edge as a function of temperature (Chap. 2.2.5). The spectra that were acquired, whilst heating at 2, 4 and 7 °C min^{-1}, contain the oxygen K edge (532 eV), which is dominated by contributions from the SiO_x support, and the Ni(O) white lines (L_3 at 855 eV and L_2 at 872 eV) [246]. Spectra acquired during the three experiments were aligned by cross-correlation, meaning that the change in the position of the L_3 edge by -0.2 eV between Ni and NiO was not followed here [211]. Principal component analysis was then used to reduce noise [214]. The first 15 principal components were considered, with the remaining components assumed to contain only noise. Gatan Digital Micrograph software was used to subtract a power law background (Eq. 2.2) fitted over 50 eV before the L_3 edge. The spectra were not deconvolved to remove plural scattering, as the thickness was not homogeneous over the recorded area.

Each L_3 and L_2 edges were fitted with a polynomial or the sum of a Gaussian and a Lorentzian and then integrated using 2 eV windows centred on their respective maxima. The $I(L_3)/I(L_2)$ ratios measured at each temperature T were then normalised using the experimental Ni and NiO reference ratios ($I(L_3)/I(L_2)_{Ni}$ and $I(L_3)/I(L_2)_{NiO}$, respectively) to obtain the degree of conversion α of the reaction, i.e. the reaction kinetics (Eq. 2.4). The Ni experimental reference was obtained by keeping the sample reduced at 2 °C min^{-1} for 100 min at 600–615 °C (Fig. 3.1). Alternatively, the reaction kinetics was determined using Eqs. 2.6 and 2.7, where each experimental spectrum $F(E)$ acquired at a temperature T was fitted to NiO and Ni experimental reference spectra ($R_{NiO}(E)$ and $R_{Ni}(E)$, respectively) using a multiple linear least squares algorithm (MLLS). The model-independent Kissinger technique was used to yield the activation energy E_a (Eq. 2.25). In addition, E_a, A (pre-exponential factor) and the reaction model that describe the reaction were obtained using a least-squares minimisation algorithm (Eq. 2.26).

Additional *in situ* reduction experiments

In order to identify the detailed characteristic structural changes occurring during the low magnification experiments, complementary studies were performed. These involved the acquisition of scanning TEM (STEM) and high-resolution TEM (HRTEM) images of particles during reduction in a H_2 atmosphere. The commercial NiO powder was dispersed onto gold grids supporting a porous SiO_x film (holey Au-SiO_x), mounted in a Philips single-tilt heating holder and plasma cleaned for 7 min before performing *in situ* reduction in the ETEM (1.3 mbar of H_2 at 2 ml_N min^{-1}). Instead of Cu grids with continuous SiO_x films, holey Au-SiO_x grids were used to perform HRTEM in thin NiO areas located over the holes of the film. After thermal drift stabilisation, the temperature was kept constant until the structural evolution of NiO was judged to be negligible. The temperature was then increased by one current step (corresponding to 5–10 °C) up to a final value of 600 °C (no defined heating ramp). The electron dose rate was varied during these complementary experiments, but kept to a minimum value, which still allowed the acquisition of images with a sufficient electron count over 0.5–1 s (depending on the thermal drift).

3.1.3 *In situ* X-ray powder diffraction

A PANalytical X'Pert PRO diffractometer (XRD) equipped with *in situ* capabilities was used to complement the data obtained in the ETEM and investigate the influence of experimental parameters on the reaction kinetics (Fig. 2.13). H_2 was injected at various gas flows (2, 20 and 40 ml_N min^{-1}) and the reaction chamber pressure set at different values (12, 100 and 600 mbar). The temperature was increased continuously at 1, 2 and 4 °C min^{-1} from 150 up to 700 °C. The scan range was set to 35-54° (scan time of 277 s) to include the reflections (111) and (200) of both NiO and Ni. A mass spectrometer was used to analyse the gases involved in the reaction. The temperature of each individual Ni/NiO reflection was inferred from the acquisition time knowing the heating rate.

The XRD scans were aligned by cross-correlation and noise was reduced using principal component analysis [214]. The number of first components used to reconstruct the data were adapted according to the number of scans (11 principal components at 1 °C min^{-1}, 8 at 2 and 4 °C min^{-1}). The remaining components were assumed to contain only noise. Background was then subtracted using a 10^{th} order polynomial (Eq. 2.15). Each Ni and NiO reflection was fitted using both a polynomial and then a Pseudo-Voigt function (Eq. 2.16). Peaks with an intensity less than 2 times above the noise level were discarded due to curve fitting issues. The full width at half maximum (FWHM) of each Ni and NiO reflection was measured to yield the crystallite size (Eq. 2.17). The evolution of both integrated and maximum peak intensity as a function of temperature were used to infer the reaction kinetics. The Kissinger method (Eq. 2.25) and the model fitting procedure (Eq. 2.26) were used to obtain quantitative kinetic data, which could be compared to EELS measurements.

3.2 Experimental results

3.2.1 NiO structural evolution during reduction using ETEM

Fig. 3.2 shows a selection of TEM images and corresponding electron diffraction patterns, which illustrate the characteristic changes that occur in the NiO microstructure during a 2 °C min^{-1} ramp from 300 to 600 °C. Fig. 3.2a shows results obtained from initial NiO particles recorded at 300 °C in 1.3 mbar of H_2. At 405 °C (Fig. 3.2b), voids or surface irregularities appear within larger particles in the form of irregular contrast features (arrowed), while Ni reflections are observed in the diffraction pattern. Fig. 3.2c demonstrates that at 525 °C the grains restructure, with the pores/surface irregularities starting to disappear. Smaller particles shrink when compared to the initial structure (see the regions marked with a circle). In Fig. 3.2d at 600 °C, the smaller Ni grains disappear in favour of the larger ones (see the region marked with a circle), whilst fewer Ni reflections appear in the diffraction pattern. Fig. 3.2e focuses on one region of interest and highlights these effects in detail: voids (or at least surface irregularities) form, which induce an irregular contrast in the particles at the onset of the reaction (405 °C), and, as the temperature increases, these irregular features (arrowed) along with some small grains (circled) disappear. Images acquired at 4 and 7 °C min^{-1} exhibit similar behaviours, with delays of $\sim$50 and $\sim$90 °C, respectively (not shown here).

Fig. 3.3 shows the radial profiles of the electron diffraction patterns acquired, whilst heating at a rate of 2 °C min^{-1}. The evolution of the NiO (220) and Ni (200) reflections, which do not overlap with other reflections, demonstrates the simultaneous disappearance of NiO and appearance of Ni, as shown in Fig. 3.3b and c. A small amount of NiO is still present at the end of the ramp at 600 °C. Using JEMS software [36], all of the observed reflections are indexed as either Ni or NiO.

High-resolution TEM images show that the nucleation of Ni on NiO already takes place at < 400 °C (Fig. 3.4). Ni domains grow on the surfaces of NiO grains and can be identified by their lattice fringes using fast Fourier transforms (FFT) of the high-resolution TEM images. In some areas, Ni nucleation is nearly epitaxial on the initial NiO grain, while elsewhere the orientation relationship is more complex (Fig. 3.4). The nucleation step could not be observed for every NiO particle due to thermal drift associated with each increment of temperature. The grains then evolved into inhomogeneous structures (Fig. 3.5) through the displacement of interfaces, inducing particle shrinkage and pore creation within larger particles to accommodate the volume loss due to the removal of oxygen during reduction (-41% [9]).

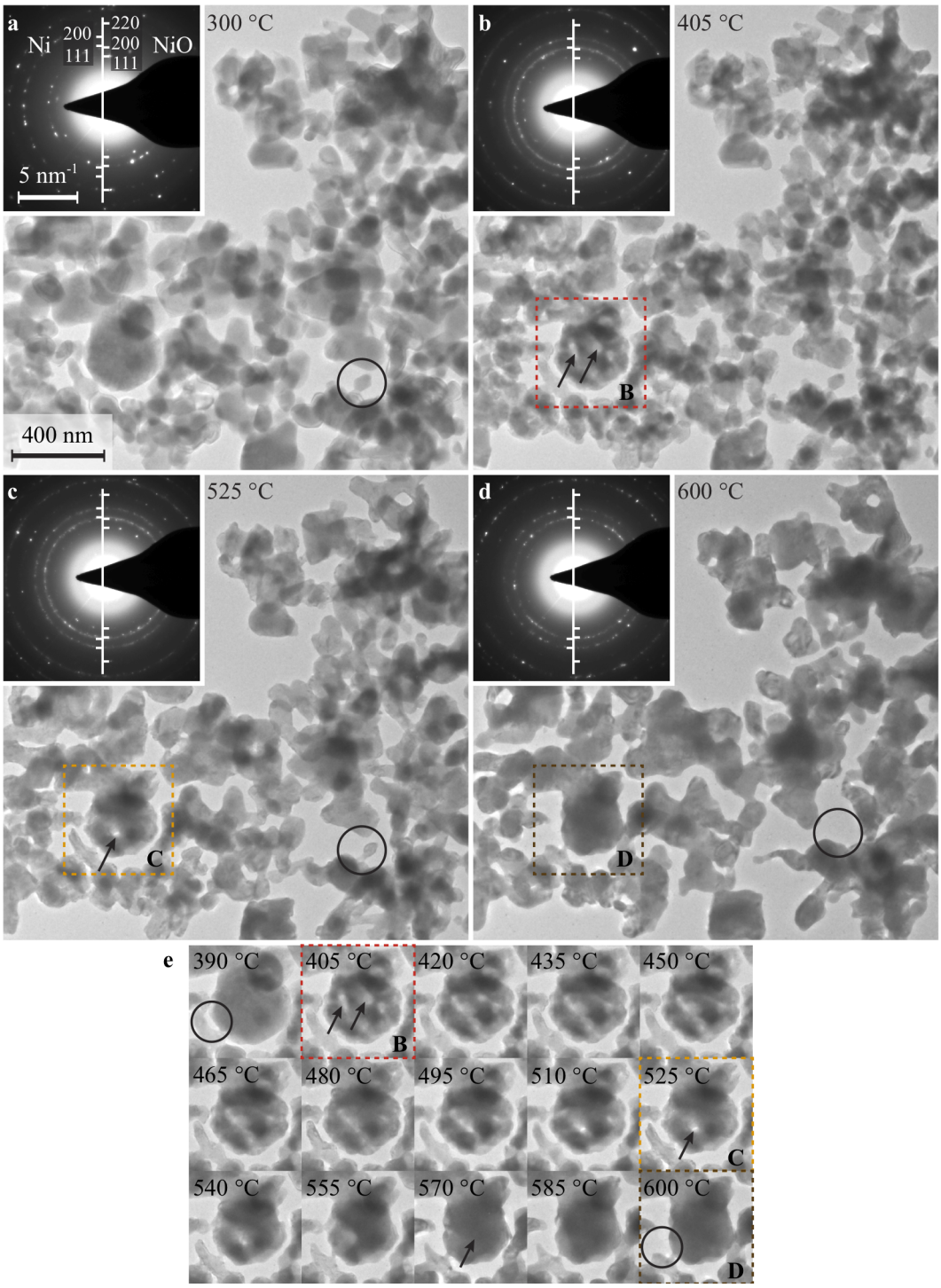

Figure 3.2 – (a-d) Sequence of TEM images and electron diffraction patterns acquired in 1.3 mbar of H_2 during NiO reduction, whilst increasing the temperature at 2 °C min^{-1}. The insets (e) show the evolution of one region of interest from 390 to 600 °C. Arrows mark the appearance and evolution of irregular contrast features, while circled areas highlight the disappearance of small particles during ramping.

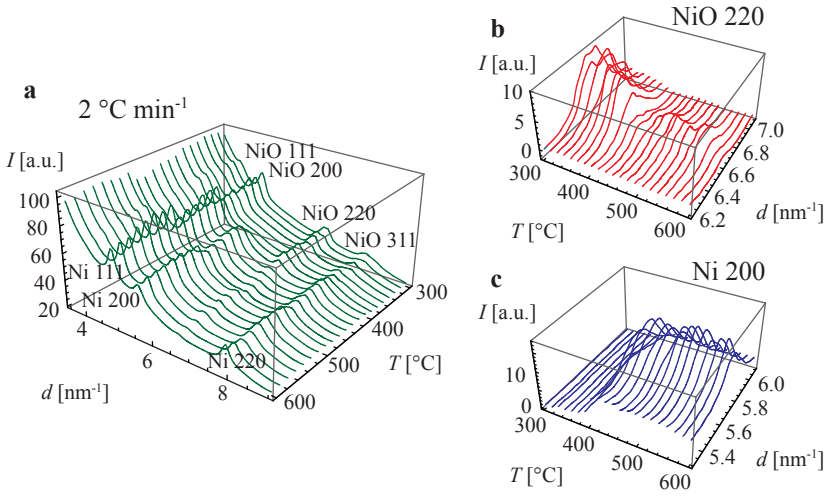

Figure 3.3 – (a) Radially averaged profiles of electron diffraction patterns acquired during *in situ* reduction at 2 °C min^{-1}. (b) The NiO (220) reflections disappear, as shown after removing a power law background (Eq. 2.1), whilst (c) the Ni (200) reflections appear simultaneously as the temperature increases.

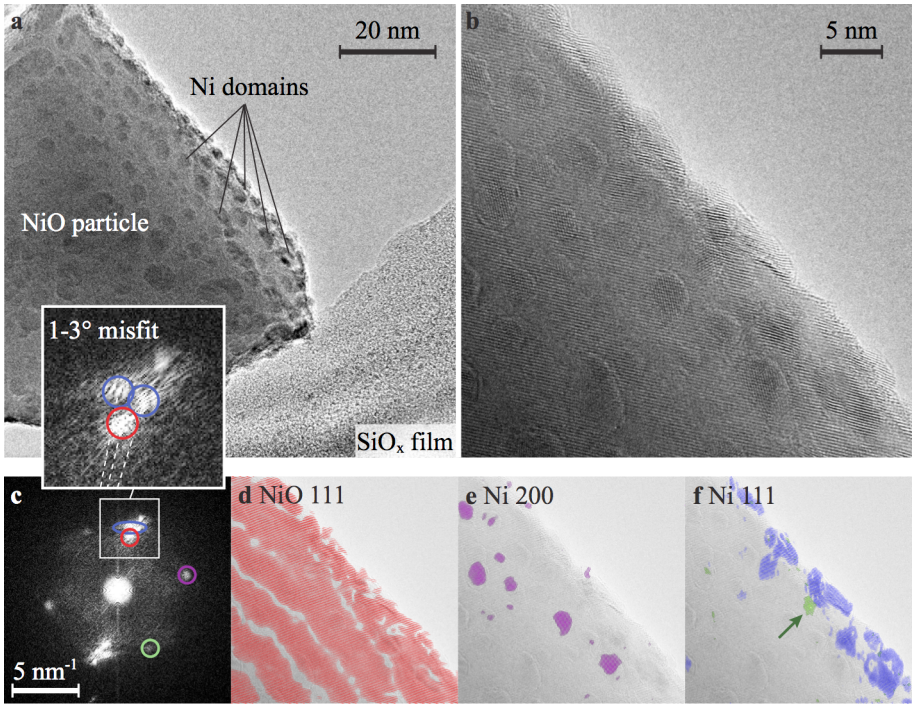

Figure 3.4 – Ni nucleation on NiO observed using ETEM at 370 °C in 1.3 mbar of H_2, showing (a) nucleation on the whole surface and (b) an HRTEM image of the nucleation stage, alongside FFT (c) and inverse FFT, i.e. pseudo-dark-field images, which are coloured, with the HRTEM image added as a background (d-f). The inset illustrates in (c) the angular misfit observed between the NiO (111) and Ni (111) reflections in the FFT.

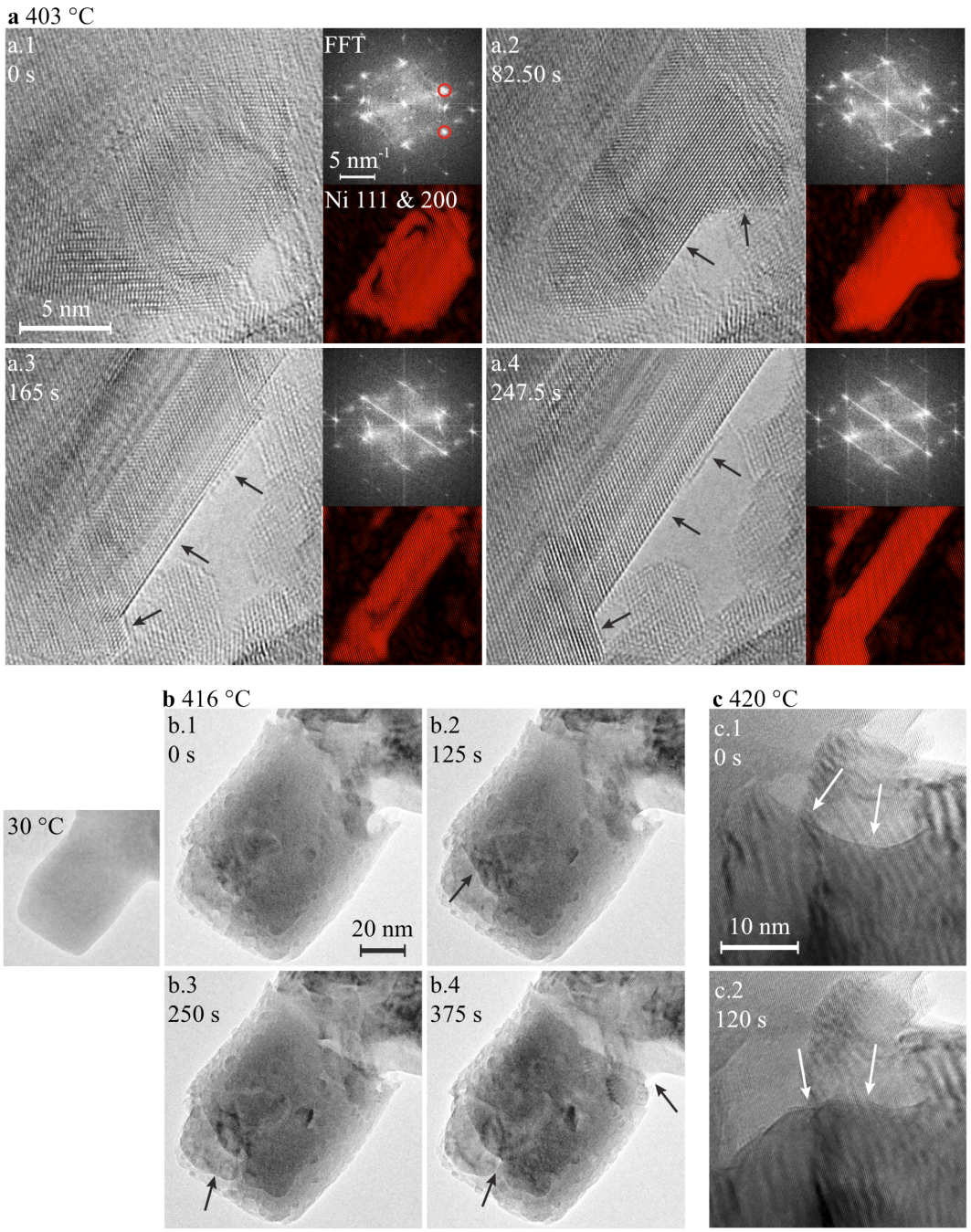

Figure 3.5 – (a-c) Selection of frames showing the evolution of different Ni(O) regions during reaction in 1.3 mbar of H_2 above 400 °C. (a.1-4) High-resolution TEM micrographs and corresponding FFTs and inverse FFTs of Ni (111) and (200) reflections showing the evolution of one Ni region as a function of time at 403 °C. (b.1-4) Lower magnification view of the evolution of one region of interest into an inhomogeneous structure during reduction at 416 °C. (c.1-2) Movement of an interface during reaction at 420 °C. Arrows highlight characteristic structural changes.

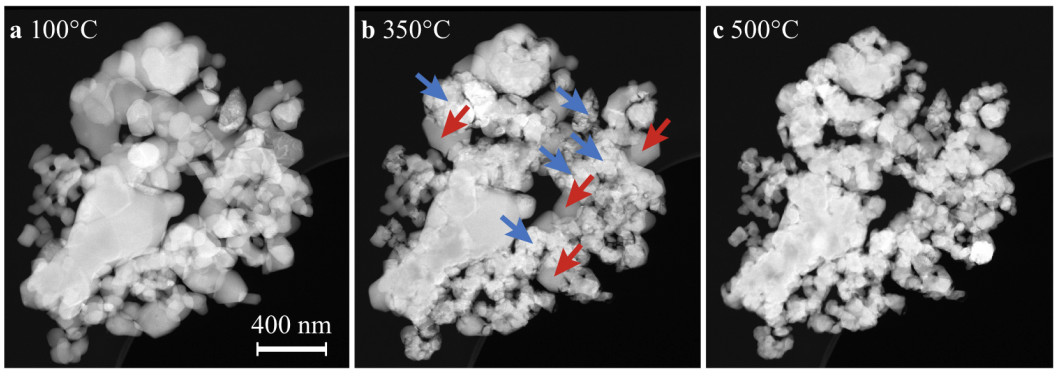

Figure 3.6 – (a-c) STEM HAADF images sequence of a Ni(O) agglomerate of grains recorded in 1.3 mbar of H_2 at 100, 350 and 500 °C, respectively. In (b), some changes in contrast (related to thickness and mass) due to reduction are arrowed in blue, while regions that have not reacted are arrowed in red.

Some NiO grains react at a lower temperature when compared to other particles. A sequence of STEM HAADF images (Fig. 3.6) shows that some grains become irregular due to the removal of oxygen, whilst other grains are left unchanged and have not reacted yet (Fig. 3.6b).

In addition, Ni nanoparticles are observed on the surfaces of larger Ni(O) particles at elevated temperature (500 °C, Fig. 3.7a). A careful investigation of diffraction patterns acquired at 600 °C (e.g. the pattern in Fig. 3.2d and the corresponding radial profile in Fig. 3.3b) shows that some NiO is still present at temperatures close to 600 °C. Figure 3.7b shows that NiO is still present within particles that contain mainly Ni, with some Moiré patterns forming where the two overlap (also where Ni grains superimpose).

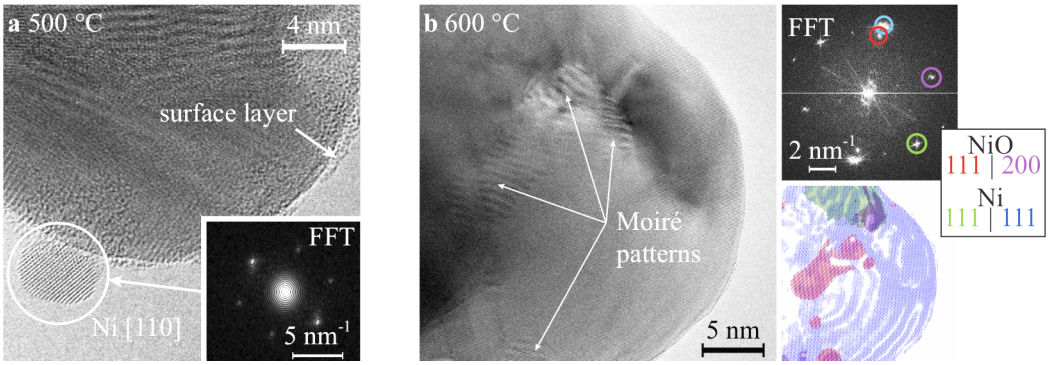

Figure 3.7 – HRTEM micrographs at high temperature in 1.3 mbar of H_2 (a) Ni nanoparticle oriented along [110] (indexed by its FFT) on the surface of a Ni(O) grain at 500 °C. Some blurring is present due to thermal drift. A surface layer (probably amorphous carbon) is present on the surface of the larger Ni(O) grain. (b) Image acquired at 600 °C, its FFT and corresponding inverse FFTs (pseudo-dark-field images), showing NiO within Ni grains. Moiré patterns are visible in the regions where Ni and NiO are superimposed.

When the temperature is increased directly from room temperature up to 600 °C at a fast rate, some small NiO regions are still observed using dark-field imaging as long as 180 min after reaching 600 °C (Fig. 3.8). In addition, coarsening of Ni is not observed in those conditions. On the other hand, when the temperature is ramped up to 600 °C at a slow rate of 2 °C min^{-1} and then maintained during 100 min at this temperature in 1.3 mbar of H_2, NiO is observed to tend towards full reduction, with the structure evolving to minimise its surface energy, as shown in Fig. 3.9. Pores created at a lower temperature to accommodate the volume shrinkage associated with reduction are observed to disappear. Larger grains are found to grow and get denser, whilst smaller grains also disappear.

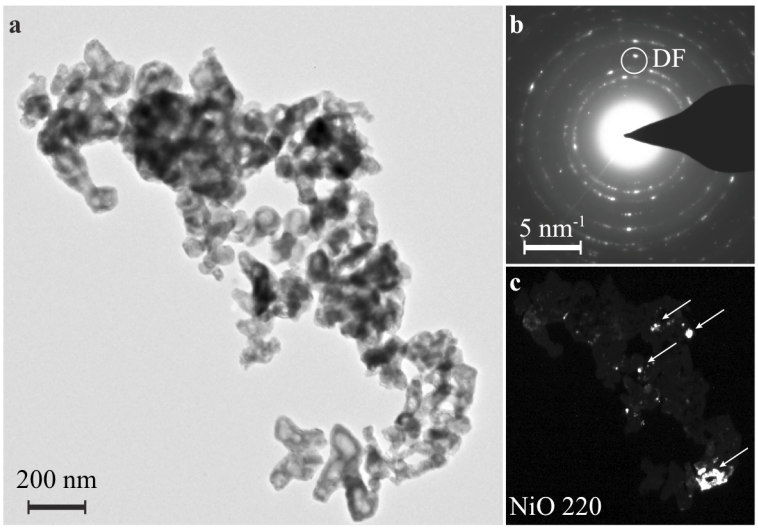

Figure 3.8 – (a) Bright-Field (BF) TEM image recorded 180 min after reaching 600 °C at a fast heating rate in 1.3 mbar of H_2. (b) Corresponding diffraction pattern. (c) Dark-field (DF) TEM image formed using mostly a NiO (220) reflection (and some faint Ni (111) reflections), highlighting unreduced regions.

3.2.2 Reaction kinetics inferred from EELS

EEL spectra recorded at a heating rate of 2 °C min^{-1} and the resulting reaction kinetics are illustrated in Fig. 3.10. The fits of the experimental spectra obtained using the MLLS technique have correlation coefficients above 0.98. Reduction is observed to proceed quickly until the remaining NiO fraction reaches a level of about 30-40% (Fig. 3.10). The reaction then slows down, with full reduction achieved only at temperatures above 600 °C (also confirmed using electron diffraction; see Fig. 3.9d).

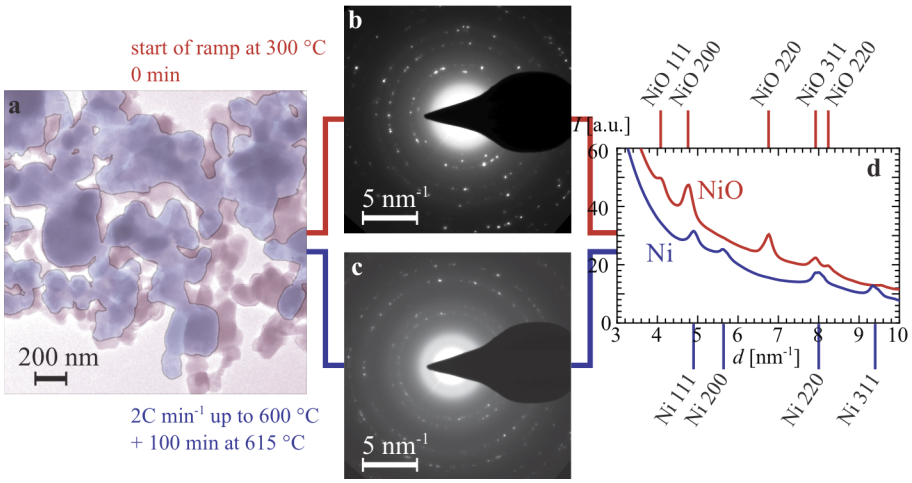

Figure 3.9 – Superposition of 2 TEM images showing a comparison between the initial NiO grain structure at 300 °C (coloured in red) and the final Ni microstructure at 615 °C after 100 min above 600 °C (coloured in blue). (b) Diffraction pattern from NiO at 300 °C at the start of the experiment (corresponding to image (a) coloured in red). (c) Diffraction pattern from Ni after reduction at temperatures up to 615 °C (corresponding to image (a) coloured in blue). (d) Radial profiles of the NiO and Ni diffraction patterns shown in (b) and (c), respectively, alongside the position of peaks simulated using JEMS [36].

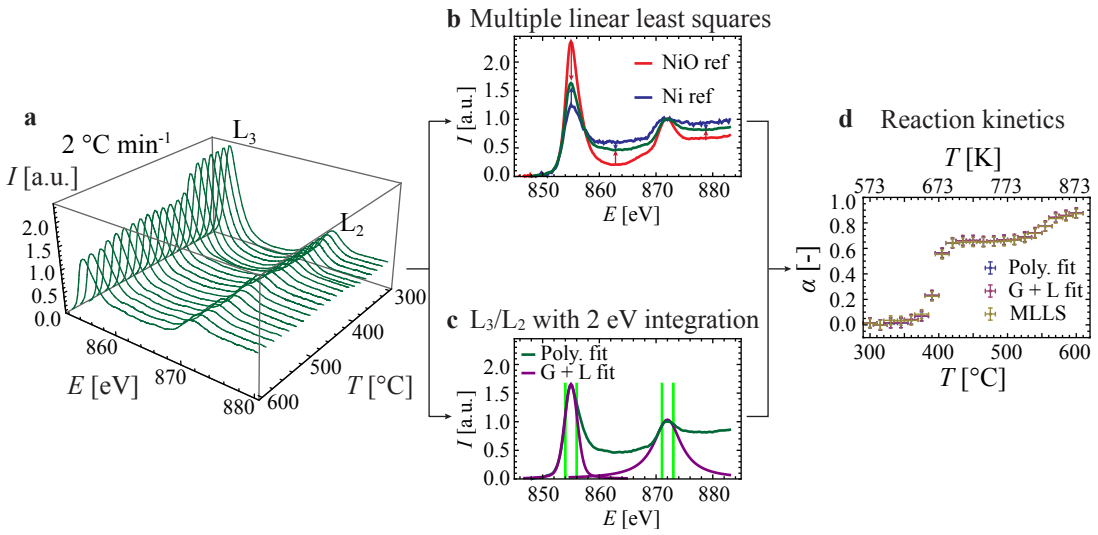

Figure 3.10 – (a) Background-subtracted EEL spectra acquired as a function of temperature for a 2 °C min^{-1} ramp (all spectra normalised to unity at L_2). NiO and Ni experimental reference spectra are used to determine the reduction kinetics (d) using either (b) a multiple linear least squares (MLLS) technique or (c) the ratio of the Ni L_3/L_2 intensities fitted using polynomial or Gaussian–Lorentzian fits and integrated using 2 eV windows. The vertical uncertainties in (d) are obtained from the statistical deviation of the measured values of α when NiO is fully reduced (3σ). The horizontal uncertainties are estimated to be ±10 °C.

3.2.3 Reaction kinetics and crystallite size evolution using *in situ* XRD

Fig. 3.11 shows the patterns obtained by *in situ* XRD during reduction at 2 °C min^{-1} from 150 to 700 °C in a H_2 pressure of 600 mbar and a flow of 40 ml_N min^{-1}. The mass spectrometer data recorded during the experiment is shown along with the processing steps of the XRD patterns to yield the crystallite size evolution and the reaction kinetics.

The sequence of XRD patterns shown in Fig. 3.11a demonstrates the simultaneous emergence and disappearance of Ni and NiO reflections, respectively. The reaction starts just above 200 °C, which is consistent with mass spectroscopy. The H_2 signal starts to drop at 220 °C as the H_2 gas is consumed by the reaction, while the H_2O signal increases as the reaction proceeds. Both H_2 and H_2O signals return to their base value at temperatures above 350 °C.

The FWHM values of the NiO (111) and (200) reflections are identical and remain constant before dropping quickly to 0 (Fig. 3.11d). The initial NiO crystallite size is estimated to be in the order of 100-150 nm, which corresponds to TEM observations (Fig. 3.2). This value remains identical even when the reaction has already started (see data points above 220 °C). The values of the FWHM of the Ni (111) and (200) differ but exhibit the same trend. The smallest crystallite measured are in the order 20-30 nm as (broad) peaks close to the noise level could not be fitted properly, with this value increasing until the resolution limit of the instrument (>150 nm) is reached at a temperature of at ∼450 °C.

The maximum and integral intensities of the NiO reflections remain constant until the reaction starts at ∼220 °C and then quickly tend to 0 (Fig 3.11e). NiO reflections are not detected above ∼280 °C and the region investigated by XRD is assumed to have fully reacted. Alternatively, the maximum intensity of the Ni reflections increases quickly when the reaction starts and then continues to increase even when the sample is fully reduced (up to 480 °C) due to coarsening of the Ni crystallites. At higher temperature, the maximum intensity decreases as a result of sintering. Voids created as a result of the volume shrinkage induced by NiO reduction (-41% [9]) disappear and the structure gets denser, i.e. the apparent volume decreases, which eventually misaligns the sample with respect to the X-rays. In turn, the integral intensity of the Ni reflections (Fig. 3.11e - top-right inset), which is a more reliable measurement of the amount of a phase, is observed to gradually decrease as the temperature increases, indicating that the amount of Ni in the investigated area is decreasing.

The intensity in the Ni reflections hence cannot be directly used as an indicator of the reaction kinetics. Consequently, the reaction kinetics is inferred from the NiO (200) reflection, with all four techniques (maximum intensity, integral intensity, with or without fitting using a Pseudo-Voigt function) yielding identical results. In accordance with the mass spectrometer and crystallite size data, the reaction is observed to start at ∼220 °C and is completed at ∼280 °C.

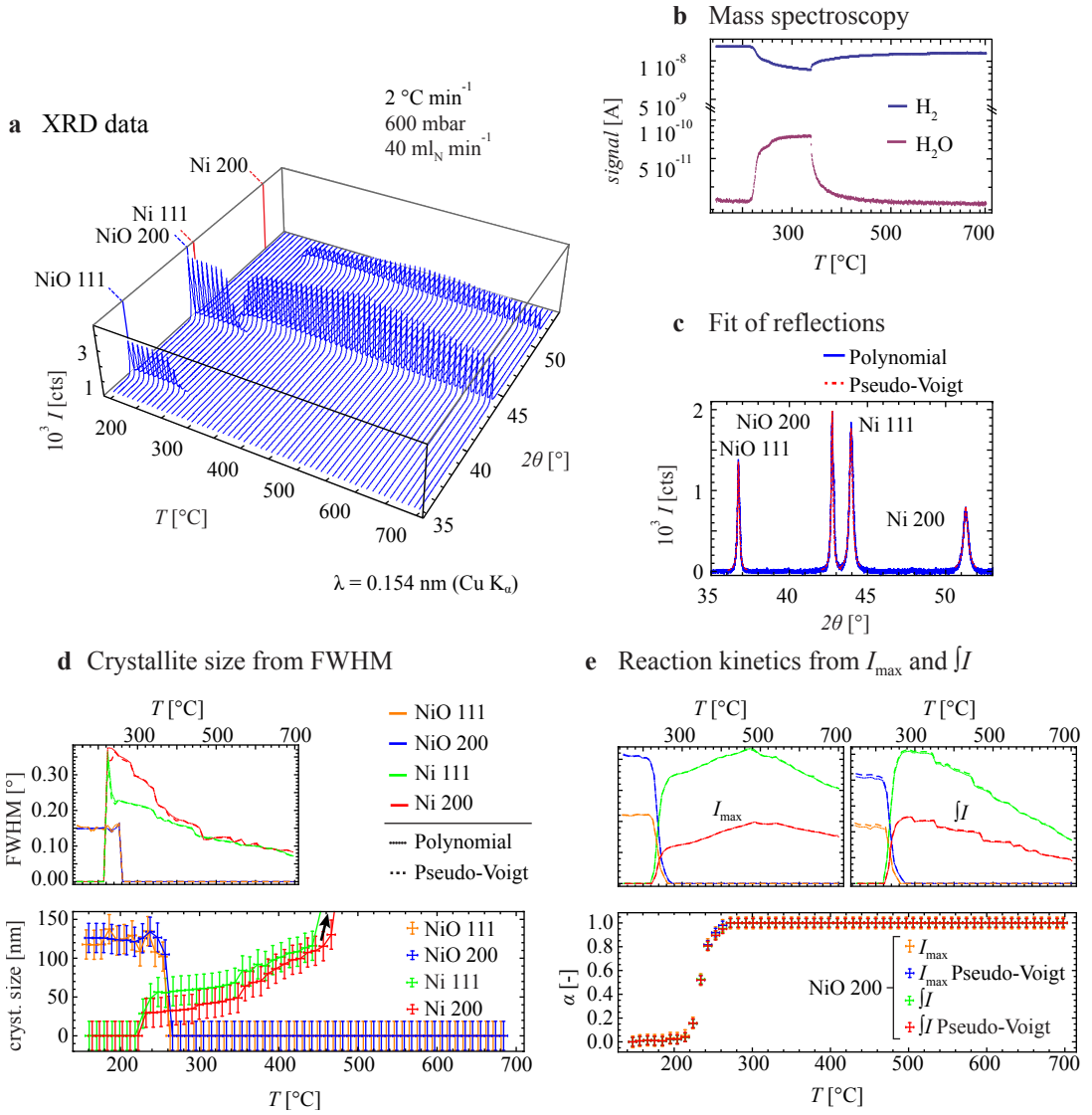

Figure 3.11 – (a) *In situ* X-ray diffraction patterns obtained, whilst ramping the temperature at 2 °C min^{-1} from 150 to 700 °C in a H_2 pressure of 600 mbar and a flow of 40 ml_N min^{-1}, with (b) the corresponding mass spectrometer signals of H_2 and H_2O. (c) Fitting of each Ni and NiO reflections using a polynomial function or a Pseudo-Voigt. (d) Full width at half maximum (FWHM) as a function of temperature of each reflection using polynomial and Pseudo-Voigt fits to yield the crystallite size evolution. (e) Maximum intensity I_{max} and integral intensity $\int I$ measurements to yield the reaction kinetics (using the NiO (200) reflection). The vertical uncertainties in (d) and (e) are obtained from the statistical deviation of the crystallite size and α when NiO is unreduced (3σ). The horizontal uncertainties are estimated to be ±5 °C

The procedure illustrated in Fig. 3.11 was repeated for different heating rates (1, 2 and 4 °C min^{-1}), gas flow (2, 20, 40 ml_N min^{-1}) and pressure conditions (12, 100 and 600 mbar). Fig. 3.12 shows the effect of pressure and flow on the reaction kinetics (integral intensity of the NiO (200) reflection using polynomial fits), as well as a direct comparison with data obtained using EELS. Low pressure and flow conditions delay and modify the shape of the $\alpha - T$ curves. While one mechanism intrinsic to NiO reduction appears to control the reaction over the entire range ($0 < \alpha < 1$) in high pressure and flow conditions (600 mbar, 40 ml_N min^{-1}), other rate-controlling mechanisms appear and modify the reaction rate when the pressure and gas flow are decreased (Fig. 3.12). This set of other mechanisms is related to experimental parameters and is hence not intrinsic to the chemical reaction itself. These are likely to be related to diffusional effects [55]. In low flow and pressure conditions, H_2 diffusion/permeation to the reactive sites may become a limiting factor (H_2 starvation) and H_2O formed during reduction may not be evacuated sufficiently fast and screens the reaction sites [38,247]. Locally, the reaction may become thermodynamically unfavourable for a specific temperature if the P_{H_2} to P_{H_2O} ratio decreases sufficiently (Chap. 2.4). Here, H_2 diffusion/permeation to the reactive sites appears to be rate-limiting at low values of α when the pressure and flow are low, which reduces the reaction rate when compared to measurements performed in high pressure and flow conditions (arrows labelled 1 in Fig. 3.12a and b). At higher values of α, H_2O created during reduction decreases the reaction rate and delays the termination of the reaction (arrows labeled 2 in Fig. 3.12a and b).

3.2.4 Comparison between *in situ* XRD and EELS measurements

Results obtained in various conditions using *in situ* XRD can be related to those obtained in the ETEM to verify if the EELS data measures the intrinsic reaction kinetics (Fig. 3.12). Although a direct comparison between XRD and ETEM data is not straightforward due to the different geometries of the reaction chambers and the quantity of materials investigated (a few g using *in situ* XRD versus µg in the ETEM), the $\alpha - T$ curves obtained using EELS in the ETEM and *in situ* XRD have some similarities. Overall, the reaction in the ETEM is delayed to higher temperature due to the lower H_2 pressure involved, i.e. the induction time is longer. The first part of the $\alpha - T$ curves obtained in the ETEM ($0 < \alpha < 0.6$) exhibits the same shape as that measured by *in situ* XRD in non-limiting conditions (600 mbar and a flow of 40 ml_N min^{-1}). H_2 starvation/diffusion effects do not appear to limit the initial stages of the reduction of the NiO particles observed in the ETEM, which appears coherent with the fact that only a few µg of reducible material is investigated in the microscope and is directly accessible to H_2. The reaction rate measured by EELS is then observed to decrease at $\alpha > 0.6$ similarly to *in situ* XRD measurements performed in low pressure and flow conditions. As mentioned in Chap. 3.2.3, this decrease in reaction rate is linked to the presence of H_2O, which forms during reduction and eventually hinders the reaction at high values of

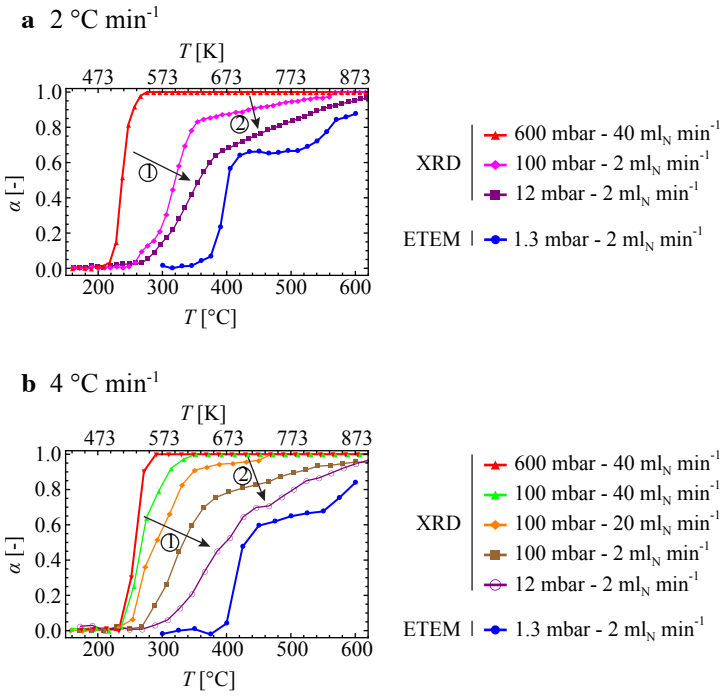

Figure 3.12 – Reaction kinetics obtained using *in situ* XRD (integral intensity of NiO (200) reflection) and EELS in the ETEM (white lines ratios), (a) comparison of data obtained using *in situ* XRD at 2 °C min^{-1} in high H_2 pressure and flow conditions (600 mbar at 40 ml_N min^{-1}), at low flow and varying pressure (12 and 100 mbar at 2 ml_N min^{-1}) and EELS measurements (1.3 mbar with a flow of 2 ml_N min^{-1}). (b) Data obtained using *in situ* XRD at 4 °C min^{-1} in high H_2 pressure and flow conditions (600 mbar at 40 ml_N min^{-1}), at constant pressure and varying flow (100 mbar at 2, 20 and 40 ml_N min^{-1}), at low pressure and flow (12 mbar and 2 ml_N min^{-1}) along with EELS measurements (1.3 mbar at 2 ml_N min^{-1}).

α [38, 55, 247]. The transition between the first kinetic regime, which is representative of the chemical resistance of NiO to reduction, and the second one, which reflects experimental limitations, is sharp and thus indicates that these appear to occur in succession. The reaction kinetics measured in the ETEM is likely to be representative of the intrinsic kinetics up to ~0.6 and is then modulated by experimental parameters.

3.2.5 Extraction of quantitative kinetic data from EELS and *in situ* XRD

Kinetic data intrinsic to NiO reduction can be extracted from measurements performed in non-limiting experimental conditions. Two sets of data were selected: full range of measurements ($0 < \alpha < 1$) obtained by *in situ* XRD obtained in a H_2 pressure of 600 mbar (40 ml_N min^{-1}, heating rates of 1, 2 and 4 °C min^{-1}), and first part of the EELS measurements ($0 < \alpha < 0.6$) obtained in 1.3 mbar of H_2 (2 ml_N min^{-1}, heating rates of 2, 4 and 7 °C min^{-1}).

To use the Kissinger method (Chap. 2.5), the $\alpha - T$ curves that are obtained at different heating rates β must be differentiated to extract the temperature at which the reaction rate is maximum. As only a small number of experimental data points were obtained using EELS and to a lesser extent by *in situ* XRD, an empirical function similar to that developed in Ref. [248] was used to fit the measurements within the range ($0 < \alpha < \epsilon$):

$$\alpha(T) = \epsilon\left(1 - e^{-(\frac{T-T_0}{\beta\kappa})^{\gamma}}\right) \tag{3.1}$$

where κ and γ are fitting parameters, T_0 is the onset temperature of the reaction and ϵ corresponds either to 1 for the measurements performed by *in situ* XRD or to 0.6 for ETEM data. The best-fitting curves to the data are shown in Figs. 3.13a and 3.14a ($R^2 > 0.99$). Each curve is then differentiated to determine the temperature at which the reaction rate is greatest, $T_{\max}$ (Figs. 3.13b and 3.14b). Table 3.1 lists the values of $T_{\max}$ obtained using the different methods, the value of α at this temperature $\alpha_{\max}$ and the activation energy for NiO reduction obtained using the Kissinger method. Measurements of the quality of the linear fits used to determine E_a are expressed in terms of the coefficient R^2.

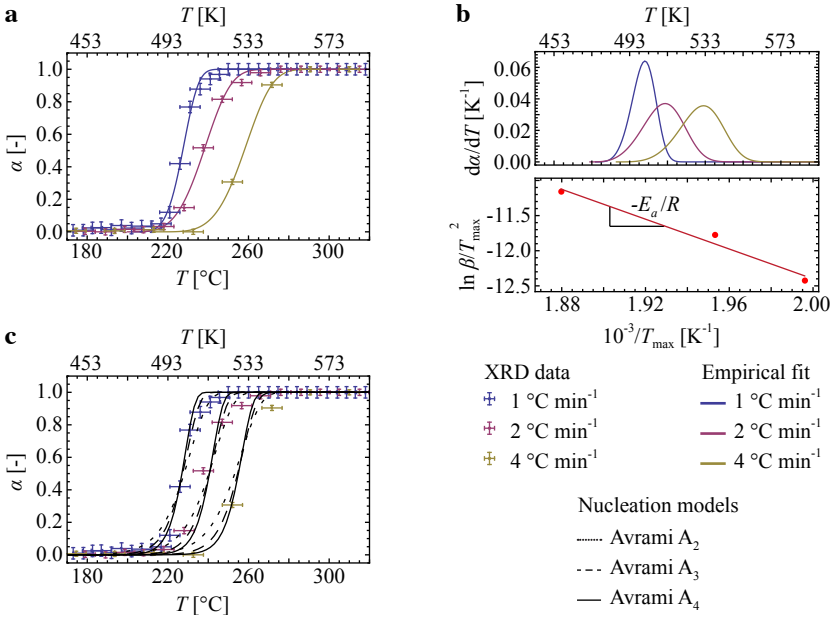

Figure 3.13 – Analysis of reaction kinetics obtained by *in situ* XRD (integral intensity of NiO (200) reflection using a polynomial fit) in high flow and pressure conditions (600 mbar, 40 ml_N min^{-1}), whilst ramping the temperature at 1, 2 and 4 °C min^{-1}. (a) Experimental points along with the fits obtained with Eq. 3.1. (b) Temperature-derivatives to determine $T_{\max}$ and plots of $\ln(\beta/T_{\max}^2)$ against $1/T_{\max}$ to determine E_a from the slope. (c) Fits of $\alpha - T$ curves with Avrami A_2, A_3 and A_4 models.

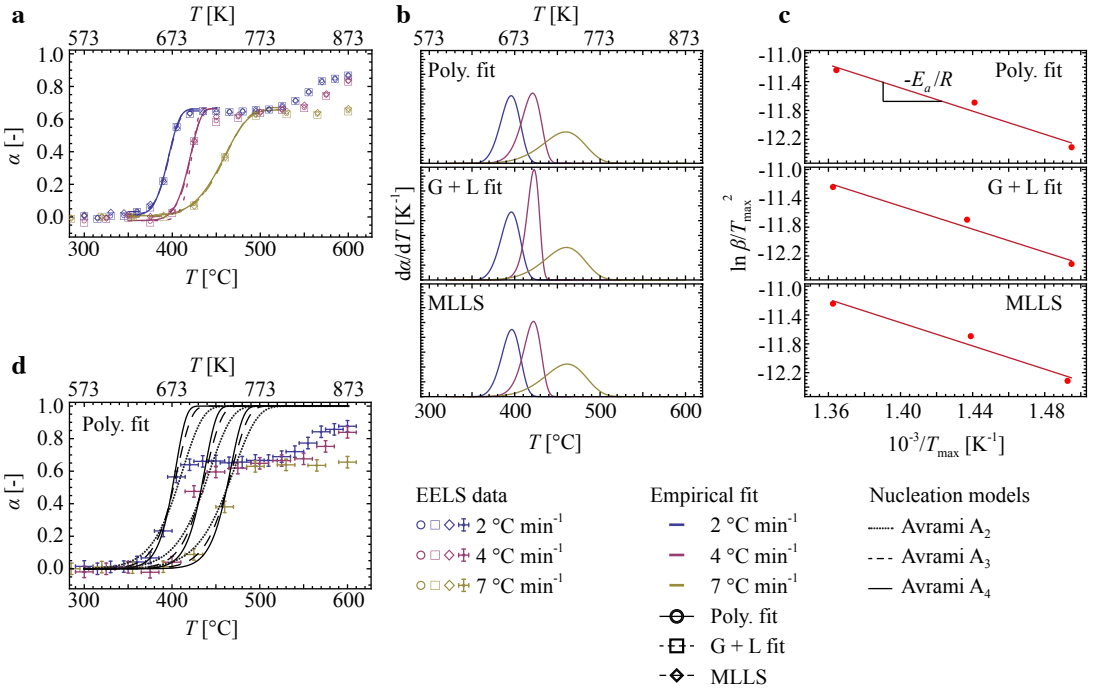

Figure 3.14 – (a) Reaction kinetics obtained from $I(L_3)/I(L_2)$ ratios and MLLS fitting from EELS, plotted as a function of temperature for the three different heating rate experiments along with fits to the data obtained using Eq. 3.1 (error bars are not shown for clarity). (b) Temperature-derivatives to determine T_{max} and (c) plot of $\ln(\beta/T_{max}^2)$ against $1/T_{max}$ to determine E_a from the slope. (d) Fits of $\alpha - T$ curves measured obtained using $I(L_3)/I(L_2)$ ratios (with polynomial fits) with Avrami A_2, A_3 and A_4 models.

An alternative approach involves the use of the integral reaction model $g(\alpha)$, activation energy E_a and pre-exponential factor A to model the data acquired (Eq. 2.26). As few experimental data points are available when compared to conventional methods used to obtain reaction kinetics (e.g. thermogravimetry), this method cannot be used to distinguish between similar reaction models and the results must be interpreted with caution. Nevertheless, the fitting procedure appears to indicate qualitatively how NiO is transformed into Ni. Only the nucleation models (involving descriptions of the growth of Ni domains by power law, Avrami or Prout-Tompkins derivations) yield realistic fits with reasonable activation energy and pre-exponential factor values to the measurements obtained by both *in situ* XRD and EELS. The power law descriptions of the nucleation process yield good results of the initial stages of the reaction. However, these models do not describe the termination of the reaction process, as there is no restriction on the growth of the product domains [41]. The Prout-Tompkins model describes an autocatalytic reaction, in which the formation of the product results in the evolution of cracks and/or dislocations at the reaction interface (in the form of a branching process) [41]. For NiO reduction, the autocatalytic behaviour results from the

	Method	T_{max} [°C]	α_{max} [-]	E_a [kJ mol^{-1}]	R^2
		1, 2, 4 °C min^{-1}	1, 2, 4 °C min^{-1}		
in situ XRD	Poly.	228, 239, 259	0.54, 0.54, 0.54	88	0.97
	P-V	228, 239, 259	0.52, 0.53, 0.53	88	0.97
		2, 4, 7 °C min^{-1}	2, 4, 7 °C min^{-1}		
EELS	Poly.	396, 421, 460	0.37, 0.38, 0.38	67	0.96
	G + L	396, 423, 461	0.37, 0.41, 0.38	66	0.98
	MLLS	397, 422, 461	0.38, 0.40, 0.38	67	0.96

Table 3.1 – Activation energies obtained with the Kissinger approach for both *in situ* XRD (α from the integral intensity of the NiO (200) reflection) and EELS data. The coefficient of determination of the linear fitting procedure to yield E_a is also indicated. Acronyms are the following: Poly. - polynomial fits, P-V - Pseudo-Voigt, G + L - Gaussian-Lorentzian, MLLS - multiple linear least squares algorithm.

fact that H_2 adsorption and dissociation occur preferentially on Ni, with subsequent transfer to NiO [38]. Our ETEM observations, in combination with an assessment of the physical meaning of the models, suggest that the Avrami mathematical derivations, which are referred to as A_2 in Ref. [41] (1-D or 2-D growth of nuclei), A_3 (2-D or 3-D growth of nuclei) and A_4 (3-D growth of nuclei), appear to describe the transformation of these NiO particles well when compared to the other kinetic models tested (Figs. 3.13 and 3.14). A summary of the derivation of these models is given in Appendix C.2. The values of activation energy obtained using the Avrami models A_2, A_3 and A_4 are shown in Tab. 3.2 and are similar to those obtained using the Kissinger method above (Tab. 3.1).

	Model	$g(\alpha)$	A [s^{-1}]	E_a [kJ mol^{-1}]	R^2
in situ XRD	A_2	$[-\ln(1-\alpha)]^{1/2}$	$3.6{\cdot}10^8$	112	0.99
	A_3	$[-\ln(1-\alpha)]^{1/3}$	$3.5{\cdot}10^7$	102	0.99
	A_4	$[-\ln(1-\alpha)]^{1/4}$	$1.8{\cdot}10^7$	100	0.99
EELS	A_2	$[-\ln(1-\alpha)]^{1/2}$	$9.2{\cdot}10^2$	80	0.91
	A_3	$[-\ln(1-\alpha)]^{1/3}$	$3.2{\cdot}10^2$	73	0.94
	A_4	$[-\ln(1-\alpha)]^{1/4}$	$2.6{\cdot}10^2$	72	0.92

Table 3.2 – Kinetic triplets (Avrami model, activation energy, pre-exponential factor) used to fit the $\alpha - T$ curves obtained using *in situ* XRD (1, 2, and 4 °C min^{-1}, α obtained using the integral intensity of the NiO (200) reflection inferred from polynomial fits) and EELS in the ETEM (2, 4 and 7 °C min^{-1}, α obtained using $I(L_3)/I(L_2)$ ratios inferred from polynomial fits).

3.3 Discussion

3.3.1 Structural evolution of NiO particles during reduction using ETEM

The first Ni domains nucleate after an induction time and appear below 400 °C. These Ni domains can be either epitaxial or non-epitaxial with respect to the initial NiO grain, as seen in Fig. 3.4. Moreover, small angular differences are observed between NiO (111) and Ni (111) reflections, corresponding to the formation of two sets of crystallites with clockwise and counter-clockwise rotations of 1–3° compared to the initial NiO orientation. This process may reduce the NiO/Ni interfacial energy, as the NiO unit cell parameter differs by 16% to that of Ni. Random nucleation events are also observed: whilst only a few NiO grains are initially in diffracting conditions (Fig. 3.2a), a large number of Ni grains are observed to diffract with random orientations a few minutes after the start of the reaction, forming a continuous ring in the diffraction pattern shown in Fig. 3.2b. Buckett and Marks [249] reported Ni/NiO epitaxy during electron beam-induced reduction. Little *et al.* [250] also observed the formation of both epitaxial and non-epitaxial Ni domains on NiO using TEM, with the number of randomly oriented Ni domains increasing as the reaction proceeded and the number of epitaxial Ni nuclei decreasing. They stated that the loss of epitaxy results either from the rotation of the Ni domains as they grow or from the fact that non-epitaxial Ni regions take a longer time to nucleate, but grow faster once they have formed. Similar rotation angles between Ni and NiO are observed in the present study and in the work of Ostyn and Carter who reported angles ranging from 0 to 3.3° after the ion irradiation-induced reduction of NiO [251]. The authors explained this loss of coherence by the presence of dislocations around the Ni domains, a process that could not be verified here. They also stated that the appearance of cracks around some parts of the Ni may induce a rotation of those domains, with a repetition of this process inducing a polycrystalline and randomly oriented Ni structure. In the present study, epitaxy is still observed at 600 °C when reduction is in an advanced state (Fig. 3.7b). The NiO/Ni orientation relationships are therefore likely to be highly sensitive to the experimental parameters and surface properties. Epitaxial relationships are observed here primarily when the heating rate is low, i.e. during experiments performed with long isothermal steps to stabilise thermal drift. The low driving force for nucleation in these nearly isothermal experiments may favour energetically some specific orientation relationships, e.g. epitaxy.

The Ni domains are three dimensional (Fig. 3.4) and evolve by the movement of interfaces (Fig. 3.5). The irregular movement of the Ni/NiO reaction front and/or the merging of Ni/Ni domains creates heterogeneous and porous Ni structures (Figs. 3.2 and 3.6). The reaction is spatially non-uniform, with Ni seeds forming at different temperatures on different particles (Fig. 3.6). On some NiO grains, reduction is observed to proceed through a neighbouring NiO particle, which had started to react at a lower temperature. The initiation of the reaction depends on the presence of oxygen surface defects, which may not be distributed homogeneously [30]. As the reaction is

autocatalytic [30], it proceeds rapidly once sufficiently large domains have formed.

The presence of Ni nanoparticles at high temperature during the reduction process (Fig. 3.7) may be associated with the redeposition of Ni (through the evaporation and recondensation of volatile nickel hydroxide [76, 252, 253]) or due to the separation of Ni nuclei from the bulk [250]. The deposition of a carbon layer in the electron beam may influence these observations, as it may keep those particles separated from the bulk material. Nevertheless, such particles have also been observed in areas that were barely irradiated by the electron beam and using scanning electron microscopy after *ex situ* reduction [131].

Grain growth and densification of individual particles is observed when the sample is kept at a higher temperature ($\sim$550 °C). The system then minimises its surface energy, with small particles disappearing in favour of larger ones. This reorganisation depends on the amount of NiO present within the Ni, with a decrease in grain growth occurring when the amount of NiO within the particles is high. Significant coarsening was observed at 600 °C for a heating rate of 2 °C min^{-1} (with the sample nearly fully reduced; Fig. 3.9), whilst the effect was less significant for the 7 °C min^{-1} sample, in which $\sim$40% of the initial NiO was still present. This densification of Ni may also decrease the reaction rate by creating a compact Ni layer around unreacted NiO domains. This reorganisation of Ni, which occurs at temperatures lower than those at which SOFCs are operated ($\sim$800 °C), is detrimental to the connectivity of the Ni catalyst and to the reduction-reoxidation stability of SOFCs [16, 26].

3.3.2 Relationship between structural and chemical changes in the ETEM

After an induction time to generate the first Ni domains, the Ni content increases rapidly at temperatures below 400 °C, up to a value of α of $\sim$0.6 for a heating rate of 2 °C min^{-1} (Fig. 3.10). The reaction then slows down in the temperature range 420–520 °C. At higher temperatures ($>$ 520 °C), the amount of NiO within the illuminated area slowly tends to 0. The reaction rate also decreases for heating rates of 4 and 7 °C min^{-1} when α reaches values of $\sim$0.6 (Fig. 3.14). As mentioned in Chap. 3.2.4 through a comparison between EELS and *in situ* XRD kinetics data, this decrease in reaction rate at high values of α appears to be associated with the presence of H_2O on the surface of the particles, which hinders the reaction. Other observations mentioned below tend towards the same conclusion.

Indeed, if H_2 shortage was limiting the reaction, experiments performed at a lower heating rate should be less affected as more time is allowed to refill the reaction chamber with H_2, an effect that is not observed (Fig. 3.14). Moreover, the H_2 signal from the mass spectrometer was constant and did not decrease during the reduction experiment. In addition, the width of temperature range in which the reaction rate is minimum does not appear to be related to temperature, indicating that this change in kinetics is not associated with solid-state diffusion. It is therefore likely that the presence and

stagnation of H_2O, which is created upon reduction, blocks H_2 access to the reactive sites, decreasing the reaction rate at a high conversion fraction (once a sufficient amount of H_2O has been created, i.e. when α reaches values of $\sim$0.6). The gas flow rate is only 2 ml_N min^{-1} and, in combination with the pumping system, may then not evacuate the product gas efficiently from the Ni(O) particles. Similar effects resulting from the presence of water have been observed using *in situ* XRD by Richardson *et al.* [38,247], who demonstrated that the reaction is delayed when H_2O is injected along with H_2 in the reaction chamber.

The kinetics can be related to the images shown in Fig. 3.2. The fast reaction that is observed up to a reduced fraction of 0.6, which occurs in the range 350 °C$< T <$ 420 °C, creates the porous Ni(O) structure shown in Fig. 3.2b. The structure then evolves slowly as the subsequent reaction is blocked. The changes that occur between Fig. 3.2b and Fig. 3.2c are mostly due to the effect of temperature and are only slightly influenced by the chemical reaction. The particles tend slowly towards full reduction at 600 °C, but most of the structural changes are due to the elevated temperature, which induces a reorganisation of the Ni phase to reduce its surface energy.

Reduction starts earlier, but at a higher temperature, i.e longer induction times, when the heating rate is increased (Fig. 3.14, 380 °C at 2 °C min^{-1} compared to 420 °C at 7 °C min^{-1}), corresponding to literature reports [54,55,248]. The formation of Ni domains depends on the number of oxygen surface vacancies, which depend in turn on the temperature and on the time for which the sample has been kept at this temperature. Due to the low pressure in the environmental cell, the reaction starts at higher temperatures compared to those found in the literature [38,248] and those measured by *in situ* XRD (Fig. 3.12).

3.3.3 Crystallite size and reaction kinetics using *in situ* XRD

As mentioned in Chap 3.2.3, the NiO crystallite sizes measured by XRD from NiO (111) and (200) reflections remain constant throughout the entire reaction (Fig. 3.11) before dropping to 0 as the reaction terminates. This observation indicates that individual NiO particles reduce nearly instantaneously once the first Ni domains have formed. At a time t during reaction, particles are either fully oxidised or fully reduced, with only few particles being in an intermediate state. In qualitative terms, it appears that formation of the first Ni domains on one NiO particle is an important rate-limiting step.

The discrepancy between crystallite size measurements obtained from the Ni (111) and (200) reflections (Fig. 3.11d) may arise from anisotropy in the microstructure [254]. The crystallite dimensions could indeed be different along the [111] or [200] directions at the start of reaction ($>$ 220 °C), before converging to the same value as the temperature increases ($>$ 400 °C). Overall, the crystallite size perpendicular to the (111) planes is always measured to be larger than this perpendicular to the (200) planes at the start of the reaction, independent of pressure, flow and heating rate conditions. A more detailed analysis of such anisotropy in the growth of the Ni crystallites would require

measurements over a larger 2θ range to analyse more diffraction peaks. It turn, this larger scan range would reduce the number of data points for each peak and be detrimental to the kinetic analysis. While some anisotropy is observed in Ni domains in Fig. 3.5a, quantitative ETEM measurements acquired during the reduction of NiO films of known orientations would be able to complement these observations. The Ni crystallite size increases with temperature due to sintering: it reaches the initial NiO crystallite size at $\sim$450 °C and the resolution limit of the apparatus at $\sim$500 °C. The now metallic Ni sample gets denser as small particles and voids disappear at high temperature, which results in a misalignment of the sample with respect to the X-ray optics and in turn reduces the integral intensity measured in the Ni diffraction peaks as observed in Fig. 3.11e.

As mentioned in Chap. 3.2.3, the reaction kinetics measured from the disappearance of the NiO (200) reflection is influenced by the experimental conditions. The shape of the $\alpha - T$ curves changes whether the reaction is controlled by mechanisms intrinsic to reduction or by effects related to experimental conditions (namely H_2 starvation and presence of H_2O around the active sites, Fig. 3.12). The broad range of pressure and flow conditions that can be achieved in the *in situ* XRD is crucial to assess the reliability of the data acquired in the ETEM in specific low pressure and flow conditions.

3.3.4 Quantitative kinetic analysis

When analysing *in situ* XRD data acquired in high pressure and flow conditions (600 mbar and 40 ml_N min^{-1}), i.e. measurements that are assumed to be representative of the intrinsic chemical resistance of NiO to reduction, the activation energy obtained from the Kissinger method is comparable to the values found in the literature: 88 kJ mol^{-1} here (Tab. 3.1) compared to 65-98 kJ mol^{-1} in the case of results representative of a chemical control [38]. Although the results of the model fitting procedure must be analysed with caution due to the relatively small number of experimental points and the mathematical approximation inherent to Eq. 2.26, the models derived by Avrami [43–45] appear to give a satisfying description of the measurements, with values of E_a (100 to 112 kJ mol^{-1} depending on the Avrami model) close, yet slightly larger, when compared to the value obtained using the Kissinger method and those found in the literature. The values of A found here (10^7-10^8 s^{-1}) are within the same orders of magnitude as those measured in similar conditions using *in situ* XRD by Richardson and co-workers [38].

As mentioned earlier, it is assumed that the reaction in the ETEM is not affected by external processes up to a conversion fraction of 0.6. Although the use of ETEM and EELS results in a small number of experimental data points, the activation energy that was calculated using the model-free Kissinger method ($\sim$70 kJ mol^{-1} within the range $0 < \alpha < 0.6$) corresponds approximately to values found in the literature and to XRD results. Even though the model-fitting technique was also applied to a small number of experimental data points, the advantage of this approach is that it can be correlated

directly with ETEM images to determine the most likely reaction model. For example, the images show that the reaction interface is not sharp in an initial NiO grain and that some particles change their shape and shrink upon reduction. A shrinking spherical core model (describing the formation of a porous Ni scale separated by a sharp reaction front from a shrinking NiO domain) [46,47] or the Evans–Szekely grain model (agglomeration of grains, each undergoing a shrinking core reduction) [51] cannot therefore describe the reduction of these NiO particles. Based on the EELS data and corresponding images, the nucleation models introduced by Avrami appear to provide a satisfying description of how NiO is transformed into Ni, suggesting that the reaction is controlled by the growth and impingement of Ni domains, which previously nucleated on the surface of the NiO. The initial slow reaction rate is linked to the generation of Ni seeds on the surface, whilst the rate increases at higher temperature as Ni domains grow and consume NiO. The kinetics deviates from theoretical predictions at values of $\alpha > 0.6$ as the reaction is affected by external processes (Fig. 3.14). The activation energy extracted from the fitted $\alpha - T$ curves is consistent with that obtained by the Kissinger method ($\sim$70 kJ mol^{-1}). It should be noted that only simple physical models are assessed here to identify general trends in the reduction mechanisms, in correlation with images of the resulting structural changes.

3.3.5 Comparison with literature

In situ oxidation and reduction of Ni nanoparticles (5-30 nm) supported on larger SiO_2 spheres were also studied using ETEM by Chenna *et al.* [114]. NiO shell structures containing holes in their cores were created upon oxidation of Ni nanoparticles in a gas mixture of CH_4 and O_2. These NiO nanoparticles were then reduced *in situ* between 400 and 700 $^{\circ}$C in H_2, CH_4, CO and/or H_2O. The observed reduction mechanisms were different from those reported here, with Ni forming inside the porous cores of the NiO shell structures. The authors state that oxygen must be present continuously on the surface to react with the reducing gas and that Ni diffusion along NiO grain boundaries must be the dominant diffusion mechanism to form Ni cores within NiO shells. The differences in experimental parameters (gas atmosphere, temperature), NiO structures (nanoparticles obtained after oxidation of Ni, compared to the present large and dense NiO particles) and stoichiometry may explain the differences between their observations and the present results. Surface Ni may also have grown in single domains due to the high temperature and small size of the NiO particles ($\sim$10 nm) and appeared on top of the NiO cores. Although such effects were not observed in the present study, the use of SiO_2 spheres may also play a role in the nucleation process, perhaps as a result of electron beam-induced charging.

As summarised by Zhu and co-workers [42], a wide range of solid-state models have been applied in the literature to describe the reduction kinetics of NiO to Ni. Similarly to the findings of this chapter, those authors demonstrated that the Avrami nucleation

models were found to provide the most successful description of the reduction kinetics of supported and unsupported NiO. As illustrated here through *in situ* XRD measurements performed in various experimental conditions, the measured reaction kinetics is easily modulated by experimental parameters and may hence not fully represent the intrinsic reaction kinetics, i.e. the chemical resistance of NiO towards reduction (Chap. 3.2.4). Other processes may hence become rate-limiting, which may explain the discrepancies in literature. In addition, the small samples investigated using ETEM, where NiO particles are in direct contact with the H_2 environment, may react differently than NiO regions located within bulkier samples, where diffusional effects may be severe [55].

3.3.6 Factors affecting ETEM observations

ETEM observations may be affected by a number of different factors, such as specimen preparation, specimen geometry and the presence of the high-energy electron beam. The effects of electron beam-induced damage on TEM specimens have been described in detail by Egerton *et al.* [255]. Buckett and Marks [249] studied the special case of the effects of electron irradiation on NiO; most of the effects described by the authors were also observed here and are listed below, alongside the measures that were taken to reduce their influence on the measurements.

A superstructure (spinel Ni_3O_4 according to [249], with a lattice parameter twice that of NiO) forms in the presence of the electron beam when the H_2 gas is introduced in the environmental cell at room temperature in ETEM mode, creating extra reflections in the FFT (see arrows Fig.3.15a). This oxidation effect is reversible and may be prevented by only acquiring high-resolution images in H_2 at a temperature above 200 °C, at which such a structure is not observed to form in the electron beam. Anisotropic erosion and knock-on damage were also observed when acquiring HRTEM images at a high electron dose (observed within minutes at dose rates higher than $\sim 10^5$ e^- nm^{-2} s^{-1} at a temperature of 365 °C; see Fig. 3.15b). Spreading the beam and the use of a small (70 µm) condenser aperture reduced these effects.

The presence of hydrocarbons can be problematic for TEM experiments, as they are cracked and C deposits on the specimen in the presence of the electron beam. Such a carbon layer may promote reduction, hinder it in the extreme case when a continuous layer forms around Ni(O) particles and block H_2 access to the reaction sites, or trap Ni crystallites on the specimen surface and separate them from the bulk (Fig. 3.15c). Carbon deposition may be especially severe in STEM mode. Reduction of NiO was observed to occur at lower temperatures in STEM mode than in TEM mode. The presence of carbon contamination was monitored using EELS and removed by plasma cleaning the sample for 7 min prior to observations. This decontamination procedure did not appear to modify the reduction stability of the NiO.

At temperatures above ~500 °C, nanoparticles from the grid materials (Au or Cu) may form on the SiO_x film (Fig 3.15d) [256]. Nanoparticles that are ~2 nm (most likely

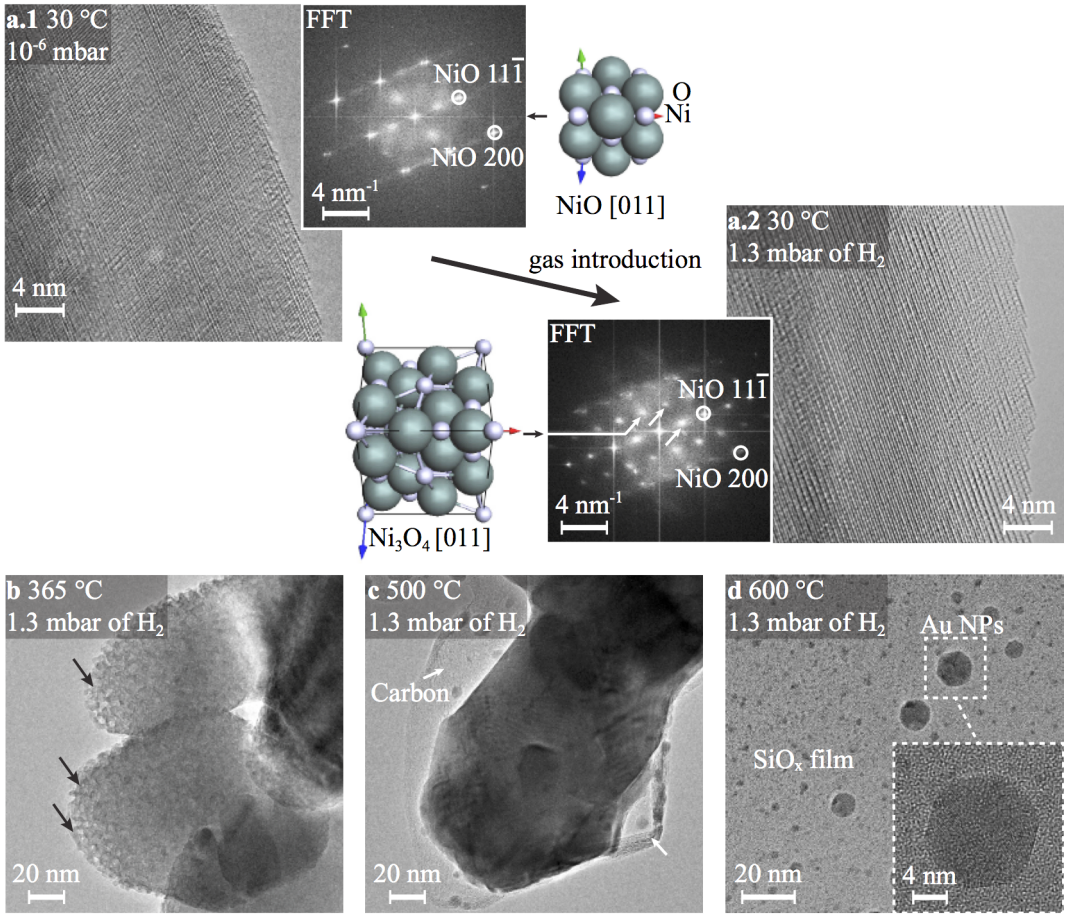

Figure 3.15 – ETEM artefacts: (a) formation of a Ni_3O_4 spinel phase in the electron beam when H_2 is introduced in the environmental cell at room temperature, with arrows showing in the FFT extra reflections due to the spinel phase, (b) anisotropic erosion and knock-on damage during irradiation at a high electron dose at 365 °C, (c) carbon encapsulation of particles during reaction at 500 °C, (d) Au nanoparticles on the SiO_x film at 600 °C.

Au, indexed by their lattice fringes) were sometimes observed at the step edges of some NiO particles at lower temperatures (∼300 °C). These contaminated particles were rare and were then discarded from the analysis. Si nanoparticles may also appear on SiO_x at a higher temperature (∼600 °C) [256]. Electron beam-induced charging effects were only observed in high vacuum conditions, resulting in rapid movement of the film and ejection of the supported NiO particles. This effect was not observed during *in situ* experiments in the presence of the H_2 gas in the ETEM. The use of different sample holders and grid materials (Cu or Au) did not affect the observations significantly. As the two furnaces use the same heating technology, the temperature difference between the region of interest and that measured by the thermocouple is therefore similar. Moreover, the characteristic structural changes, such as Ni nucleation, occurred in the same temperature range for different setups.

Areas of the specimen that were exposed to a condensed electron beam were observed to be reduced faster, presumably due to a combination of heating, desorption of oxygen due to electron impact on the specimen surface and ionisation of the molecular hydrogen gas by the electron beam, which changes the adsorption energy of hydrogen. As the electron dose rate was kept constant when assessing the reaction kinetics at different heating rates, the heating effect was not considered to be problematic as it should result in a similar local temperature increase for all experiments.

In separate experiments, NiO was observed to reduce in the microscope at high temperature in the absence of H_2 through a combination of low O_2 partial pressure and electron beam induced effects. In 10^{-7} mbar of O_2, Ni domains started to nucleate coherently on NiO grains at $\sim$500 °C, whilst heating at a rate of 2 °C min^{-1} from 300 °C. Only the surface of the NiO particles was observed to reduce in these experiments, even when reaching temperatures as high as 700 °C at the end of the 2 °C min^{-1} ramp. With the same heating rate, the reduction kinetics was hence much slower in those separate experiments performed in high vacuum conditions compared to ETEM measurements in 1.3 mbar of H_2. Overall, those differences in Ni/NiO crystallographic orientations (epitaxial in the absence of H_2 and random with 1.3 mbar of H_2) and in reaction kinetics demonstrate that the ETEM observations of this chapter result from the reaction of the NiO particles with the H_2 gas and not solely with the electron beam.

As the thermocouple is welded onto the outside of the furnace, the region of interest is at a lower temperature compared to the measured value. This systematic error on the temperature measurements ΔT affects the values of the activation energy. The activation energy decreases by $\sim$10 kJ mol^{-1} if the data is manually offset by a value of 30 °C (using both the model-independent technique and the model-fitting procedure). If the temperature error is set to -100 °C, the activation energy decreases by $\sim$20 kJ mol^{-1} using both methods. A comparison of the reaction kinetics obtained by EELS in the ETEM and *in situ* XRD, in which the temperature measurement is more reliable due to the position of the thermocouple within the furnace close to the sample, provides some insight into the temperature at the region of interest in the ETEM (Fig. 3.13). The ETEM reaction kinetics, which was measured at a pressure that is one order of magnitude lower than the lower pressure reachable in the X-ray diffractometer, occurs within the expected temperature range when the *in situ* XRD data is extrapolated. Based on this comparison, the temperature difference ΔT between the temperature at the region of interest and the one measured by the thermocouple is estimated to be < 50 °C in the ETEM.

In order to rule out the influence of the electron beam on the measurements, areas of interest were compared every 100 °C to new regions that had not been illuminated before (as irradiation damage appeared after minutes of illumination rather than seconds). Similar structures were observed with or without long exposures to the electron beam (at reasonable dose rates), denoting a similar reaction mechanism initially and then at higher temperature a similar sintering/coarsening process. In addition, the Avrami

reaction mechanism that is inferred from the EELS data, whereby the nucleation and then growth and impingement of Ni domains control the reaction, corresponds to results obtained using both *in situ XRD* (Chap. 3.2.3) and thermogravimetry [42], which in turn provides confidence that the reduction mechanism of NiO to Ni observed in the ETEM is not significantly altered by the electron beam or other ETEM-related artefacts.

3.3.7 Qualitative description of the reduction mechanism of NiO particles

Based on the present ETEM observations and on previous studies in the literature, it is possible to propose a structural model that describes NiO reduction and subsequent structural evolution in the presence of H_2 in the ETEM. This model is illustrated in Fig. 3.16. The characteristic steps are as follows. In Fig. 3.16a, H_2 adsorbs and dissociates on two Ni atoms, which are adjacent to an oxygen vacancy [39]. An induction time is necessary to generate a sufficient number of such active sites for H_2 dissociation, with the low H_2 pressure in the ETEM extending this induction time with respect to atmospheric pressure data. In Fig. 3.16b, Ni clusters are shown to nucleate into larger domains at temperatures between 350 and 400 °C, with H_2 now adsorbing directly onto Ni, with H_2O desorbing. In Fig. 3.16c, Ni domains are shown to grow by the movement of interfaces, with pores forming within larger particles, whilst smaller particles shrink to accommodate the volume loss that results from the reduction process to create an irregular structure. Water formed by the reduction process starts to stagnate on/around the particles, which decreases the reaction rate. In Fig. 3.16d, some NiO becomes trapped within the Ni structure and H_2O hinders further reaction. Finally, when the temperature exceeds 600 °C, the system tends towards full reaction. In turn, larger Ni grains grow, whilst smaller grains disappear as the system minimises its surface energy (Fig. 3.16e). The Ni structure hence reflects the NiO reduction mechanism at lower temperatures and then the coarsening/sintering process, which may induce the formation of dense Ni.

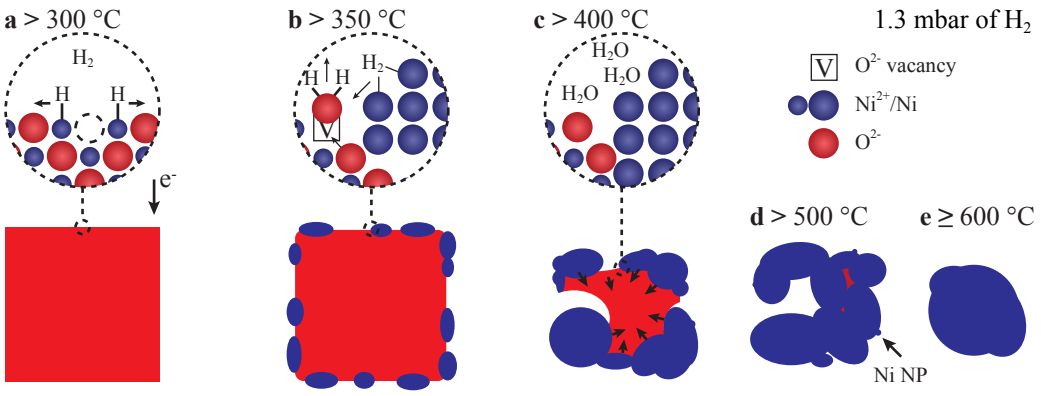

Figure 3.16 – Model for NiO reduction and subsequent Ni densification based on the present results and literature.

3.4 Concluding remarks

Reduction of NiO particles was performed in a differentially pumped environmental TEM and in an *in situ* X-ray diffractometer. *In situ* XRD measurements highlighted the importance of non-limiting experimental parameters to probe the intrinsic reaction kinetics, i.e. reaction kinetics representative of the chemical resistance of NiO towards reduction. In the ETEM, images, diffraction patterns and electron energy-loss spectra were acquired to study the structural and chemical evolution of NiO in the presence of H_2. Changes in the shapes of the Ni $L_{2,3}$ white lines measured using EELS were used to follow the progress of the reaction and to determine the reaction kinetics for different heating rates, which could be related directly to the observed structural changes.

Although the approach introduced here to relate structure and chemistry nearly simultaneously is only semi-quantitative as a result of several limitations (including electron beam effects and the precision of the EELS and temperature measurements), the observed chemical changes could be correlated directly to changes in microstructure. Such comparisons are not possible using more conventional kinetic analysis techniques (such as thermogravimetry, X-ray diffraction and differential scanning calorimetry). Models describing the reaction kinetics were compared to the observed microstructure to verify their applicability.

Through a comparison with the reaction kinetics obtained by *in situ* XRD in non-limiting conditions, the reaction kinetics obtained by EELS were found to be intrinsic to the NiO reduction initially and then to be modulated by experimental parameters (H_2O inhibition of the reaction). Both model-based and model-independent methods were used to estimate a value for the activation energy for NiO reduction of $\sim$70 kJ mol^{-1}. The results of the model-based fitting procedure and the ETEM observations are consistent with Avrami nucleation models for the reduction process. These kinetic results are comparable to previous reports in the literature and to *in situ* XRD measurements, providing confidence in the estimation of kinetic information using environmental TEM. Possible artefacts resulting from electron irradiation and systematic errors in specimen temperature (the latter through a comparison with *in situ* XRD data) have been assessed and discussed. The use of environmental TEM to link microstructural changes at the nanoscale with the measured reaction kinetics allows a model for NiO reduction to be proposed, involving the growth of epitaxial and non-epitaxial Ni nuclei onto NiO domains by the movement of Ni/Ni and NiO/Ni interfaces.

The present methodology provides new details into the reduction mechanism of NiO particles. However, predictive modelling of the reduction process requires additional data, especially related to the nucleation mechanism and the Ni/NiO crystallographic orientation relationship that results from this process depending on the experimental parameters. In addition, H_2 and H_2O mass-transfer limitations are difficult to assess as those are closely related to the geometry of the sample, support, environmental cell, etc.

4 Oxidation of Ni particles

In this chapter, the subsequent reoxidation of the nickel particles that were investigated during reduction in Chap. 3 is studied *in situ* in the environmental transmission electron microscope in 3.2 mbar of O_2 between ambient temperature and 600 °C. Several different transmission electron microscopy imaging techniques, electron diffraction and electron energy-loss spectroscopy are combined to study the evolution of the microstructure and the local chemical composition of the particles during oxidation. The results suggest that built-in field effects control the initial stages of oxidation, with randomly oriented NiO crystallites and internal voids then forming as a result of outward diffusion of Ni^{2+} along NiO grain boundaries, self-diffusion of Ni and vacancies, growth of NiO grains and nucleation of voids at Ni/NiO interfaces. The formation of transverse cracks in a growing NiO film is also observed *in situ* in the electron microscope.

4.1 Experimental details

4.1.1 Materials

Similarly to Chap. 3, the NiO powder was obtained from JT Baker™ (NiO $>$ 99.0 wt%). NiO was chosen as the starting material, rather than Ni, in order to take the specimen through one complete reduction-oxidation cycle using environmental TEM (ETEM).

4.1.2 Electron microscopy

NiO particles were dispersed onto Au grids covered with holey silicon oxide films (Au-SiO_x), plasma cleaned during 7 min and then examined at 300 kV using a Gatan Inconel 652 double-tilt heating holder in the ETEM (Fig. 2.3). Prior to oxidation, each NiO specimen was reduced to Ni inside the microscope in 1.3 mbar of H_2 at 600 °C for 210 min. The specimen was then cooled down to room temperature, before the H_2 gas was pumped out of the environmental cell (see Fig. 4.1). A flow rate of 2 ml_N min^{-1} of O_2 was then introduced, corresponding to a pressure of 3.2 mbar. Oxidation of the Ni particles was investigated *in situ* in the electron microscope using conventional bright-field (BF) and dark-field (DF) imaging, high-resolution TEM (HRTEM), selected area electron diffraction (SAED), high-angle annular DF (HAADF) scanning TEM (STEM) and electron energy-loss spectroscopy (EELS).

Heating sequences to probe the oxidation kinetics and resulting structural changes

During oxidation, each region of interest was characterised after chosen time intervals by recording conventional TEM images, SAED patterns and core-loss EEL spectra (in diffraction mode using an acquisition time of 60-120 s and an energy range of 500-900 eV). Three different temperature ramps were followed, each for a different sample, to achieve three different heating rates (Fig. 4.1). The starting temperature for each ramp was 250 °C, as the oxidation kinetics was found to be negligible at lower temperatures. The temperature was kept constant for 5 min at each step while TEM images, SAED patterns and EEL spectra were acquired, before increasing the temperature by 12, 24 or 36 °C over 1-2 min to achieve overall heating rates of 2, 4 or 6 °C min^{-1}, respectively, up to a maximum temperature of 600 °C. This approach minimised the influence of thermal drift of the holder and the grid on the measurements. The uncertainty in the sample temperature was estimated to be ±10 °C. An electron dose rate of $\sim 10^3$ e^- nm^{-2} s^{-1} was chosen as a compromise between beam damage and EELS signal. Each specimen was irradiated continuously during each experiment.

Ni oxidation kinetics using EELS

EEL spectra acquired during the heating experiments were used to infer the reaction kinetics using a procedure that is described in detail in Chap. 2.2.5 and makes use of the dependence of the shape of the Ni $L_{2,3}$ ionisation edge and in particular the ratio

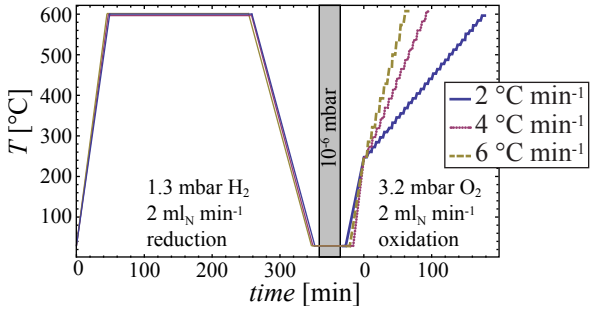

Figure 4.1 – Time and temperature parameters used to approximate constant heating rates during reduction of different samples. A set of measurements was performed at each step.

between the intensities of the L_2 and L_3 white lines on the degree of oxidation [198,211]. Each spectrum contained the O K edge (532 eV), which is dominated by contributions from the SiO_x support and O_2 gas, and the Ni white lines (L_3 at 855 eV and L_2 at 872 eV). All of the spectra were aligned by cross-correlation. Noise was reduced using principal component analysis (the first eight components were selected) [214] and background subtraction was performed using a power law (Eq. 2.2) fitted over an energy range of 50 eV before the L_3 edge.

The three sets of EEL spectra acquired at heating rates of 2, 4 and 6 °C min^{-1} exhibited slight differences in energy resolution due to variations in post-column filter tuning. In order to ensure comparable results, each set of spectra was convoluted with an artificial point spread function, which was chosen so that the initial NiO spectra of each set/sample (acquired before reduction) had the same energy resolution (full width at half maximum, FWHM) at the position of the L_3 edge. NiO and Ni reference spectra were acquired from a similar specimen (with the same NiO particles dispersed on a Au-SiO_x film), either at room temperature for NiO or at 700 °C for Ni after full reduction in 1.3 mbar of H_2 (the full reaction was confirmed by diffraction). The shape of the L_3 and L_2 edge in each spectrum was fitted using either polynomial functions or a sum of Lorentzian and Gaussian functions. The fitted functions were then integrated using 4 eV windows centred on their maxima. $I(L_3)/I(L_2)$ ratios were measured from the spectra that had been acquired during oxidation and normalised using the reference spectra to obtain the fraction of NiO in the observed area (Eq. 2.5). The NiO and Ni reference spectra were also fitted directly to each experimental spectrum using a multiple linear least squares (MLLS) method (Eq. 2.8 [113]). By using these approaches, the total amount of NiO and thus the conversion degree of the oxidation reaction α could be measured as a function of temperature. In turn, the activation energy E_a, the pre-exponential factor A and the reaction model could be obtained from a least-squares minimisation algorithm (Chap. 2.5). Similarly to Chap. 3, the aim of this procedure was to infer the mechanism that controls the oxidation of the Ni particles. The mechanism could then be interpreted with reference to the observed structural changes.

Additional *in situ* oxidation experiments

HRTEM images (showing lattice fringes) were initially acquired before the introduction of O_2 gas into the microscope column to study the nucleation of NiO on Ni, as Ni is predicted to oxidise at room temperature when H_2 is removed from the microscope column and the pressure reaches $\sim 10^{-6}$ mbar (the partial pressure of O_2 is then $\sim 10^{-7}$ mbar, Chap. 2.4). After the introduction of 3.2 mbar of O_2, BF TEM micrographs were recorded every 100 °C between room temperature and 600 °C and STEM HAADF images were recorded at 300 °C. Regions that had not been irradiated using the electron beam were also characterised and compared to areas that had been studied previously to assess electron-beam-induced artefacts.

4.2 Experimental results

4.2.1 Ni structural evolution during *in situ* oxidation

After the NiO particles had undergone reduction at 600 °C for 210 min in 1.3 mbar of H_2, the surface of the metallic Ni particles is allowed to oxidise in the microscope at room temperature in a total pressure of $\sim 10^{-6}$ mbar, as shown in Fig. 4.2. Using computed pseudo-DF images of the HRTEM image, a stable 3-4 nm film of NiO is observed to form on their surfaces.

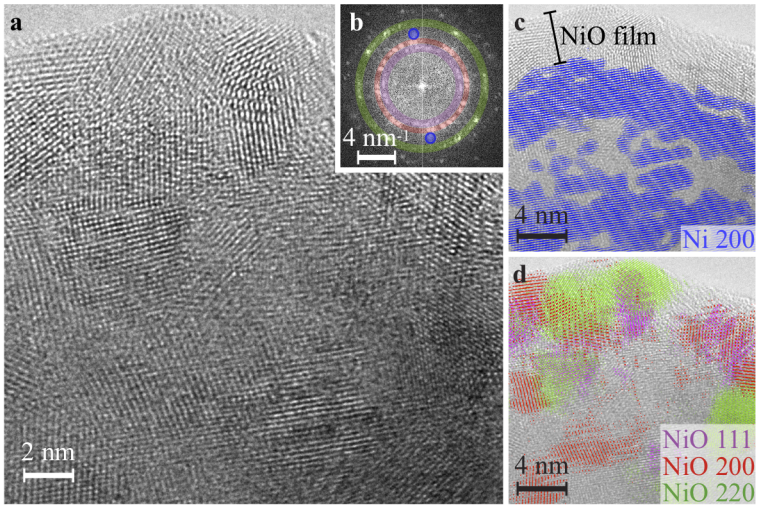

Figure 4.2 – NiO nucleation on Ni observed at room temperature in the ETEM at an O_2 partial pressure of $\sim 10^{-7}$ mbar. (a) HRTEM image showing the nucleation stage of NiO and (b) its FFT. (c) Inverse FFT (pseudo-DF) image generated from Ni (200) reflections (blue), with the HRTEM image added as a background. (d) Inverse FFT images of the NiO (111), (200) and (220) reflections (magenta, red and green, respectively), with the HRTEM image as a background.

3.2 mbar of O_2 is then introduced into the microscope. Fig. 4.3 shows a selection of TEM images and diffraction patterns illustrating the changes that occur during the 4 °C min^{-1} ramp. Fig. 4.3a shows the initial microstructure. Faint NiO reflections with specific orientations can be observed in the diffraction pattern. The microstructure is not affected noticeably as the temperature is raised to 250 °C (to the start of the temperature ramp; Fig. 4.3b). At 321 °C (Fig. 4.3c), weak NiO reflections with random orientations become visible in the diffraction pattern (arrowed in Fig. 4.3c), even though no clear changes can be identified in the images. At 417 °C (Fig. 4.3d), the particle surfaces become irregular (see inset) and rings in the diffraction patterns from NiO domains become clearly visible. The insets labeled d' show recession of the internal surface (the Ni core) and expansion of the NiO shell between 345 and 467 °C. Fig. 4.3e (514 °C) corresponds to a nearly fully oxidised state, when the particles have expanded significantly and their contrast is irregular due to the presence of crystallites (and voids). The end of the heating ramp is reached at 608 °C (Fig. 4.3f).

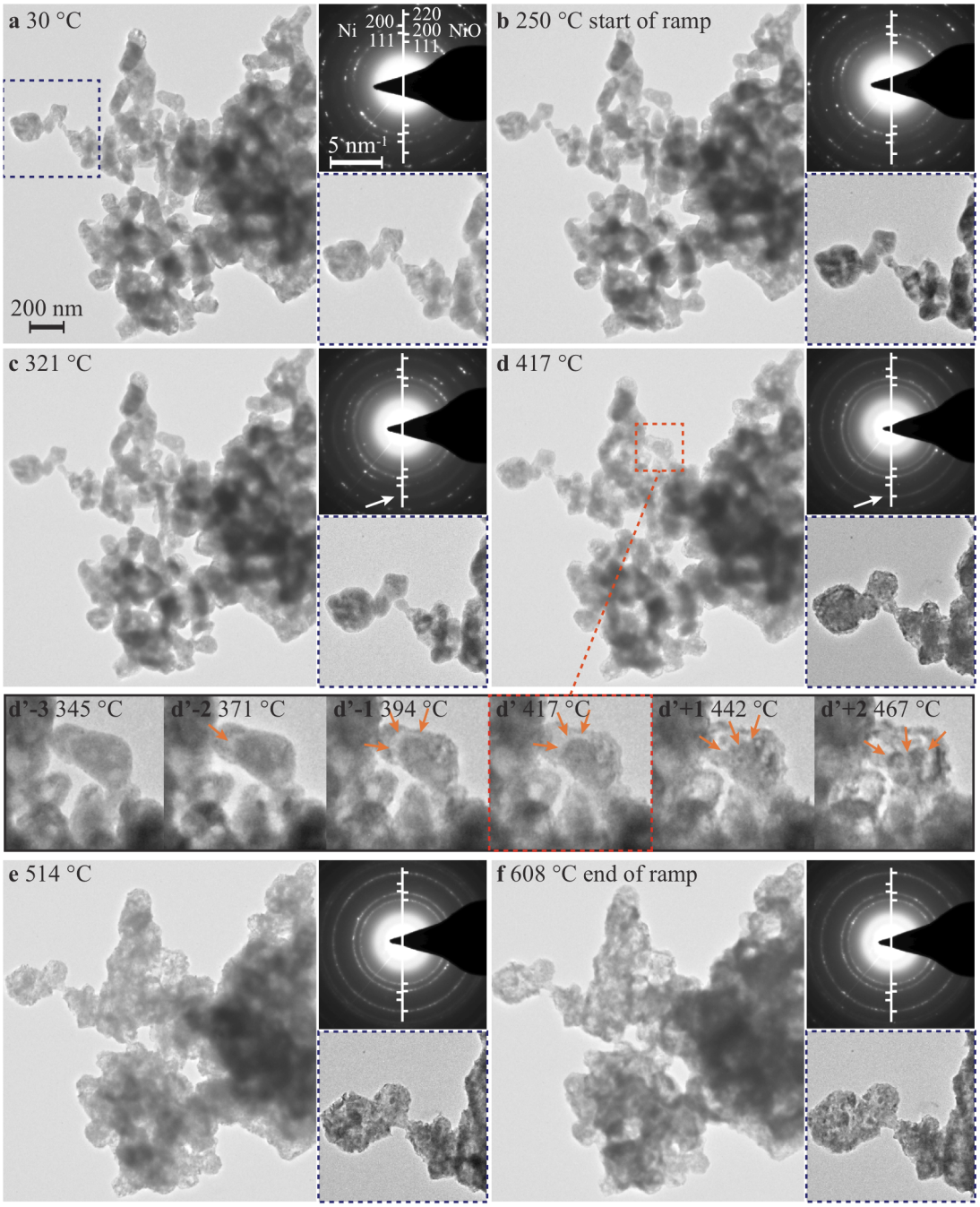

Figure 4.3 – BF TEM images and diffraction patterns acquired in the ETEM in 3.2 mbar of O_2 during Ni oxidation. (a) The structure at room temperature soon after introducing O_2. (b-f) The structural changes that occur when the specimen is heated at 4 °C min^{-1}. Insets labeled d' illustrate changes that occur between 345 and 467 °C. Arrows highlight contraction of the Ni and the appearance of the NiO (220) reflections in (c-d).

Fig. 4.4 shows the radial profiles of the electron diffraction patterns acquired during oxidation, whilst heating at a rate of 4 °C min^{-1}. The evolution of the Ni (200) and NiO (220) reflections, which do not overlap with other reflections, demonstrates the simultaneous disappearance of Ni and appearance of NiO, as shown in Fig. 4.4b and c. Some faint NiO reflections are observed initially, presumably as a result of an incomplete reduction reaction (Fig. 4.4c). All of the reflections in the diffraction patterns acquired during the ramps can be indexed as either Ni or NiO (with reference to simulations performed using JEMS software [36]).

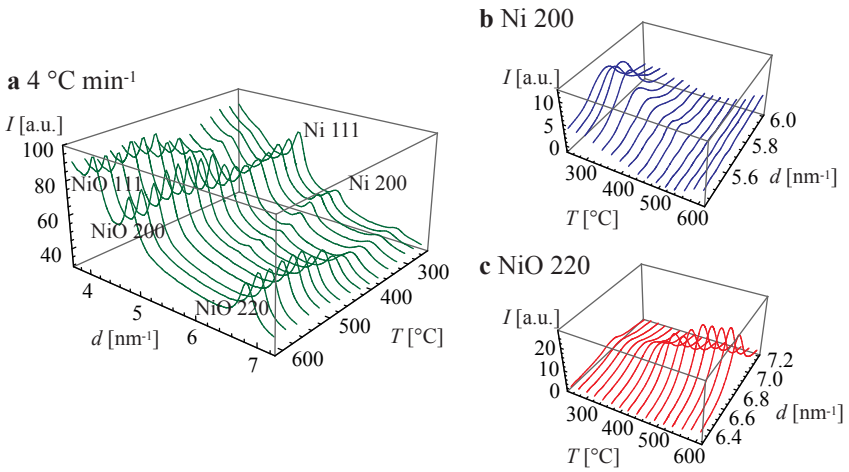

Figure 4.4 – (a) Radially averaged profiles of electron diffraction patterns acquired during *in situ* oxidation at 4 °C min^{-1}. (b) The Ni (200) reflections disappear, as shown after removing a power law background (Eq. 2.1), whilst (c) the NiO (220) reflections appear simultaneously as the temperature increases.

STEM HAADF images, which are sensitive to mass-thickness contrast, were acquired at 300 °C in 3.2 mbar of O_2 (Fig. 4.5). A line profile shown in Fig. 4.5a exhibits a drop in intensity at the interface between NiO and Ni, suggesting the presence of voids and a loss of contact between the two materials. Adjustment of the contrast in the image can be used to highlight the voids, as shown in Fig. 4.5c. The NiO film also appears to be ruptured in some regions (see circles in Fig. 4.5a and c).

Changes in diffraction contrast in BF TEM images can be used to provide information about the evolution of the Ni grain size during oxidation (Fig. 4.6). While the particles initially consist of large Ni crystallographic domains (∼100 nm in size in Fig. 4.6a), NiO domains below 50 nm in size are observed at 600 °C after oxidation (Fig. 4.6b). A double-layer structure observed after oxidation (ellipse in Fig. 4.6b) may have resulted from fracturing of the outer NiO, allowing inward permeation of O_2 and the formation of NiO directly at the Ni/NiO interface.

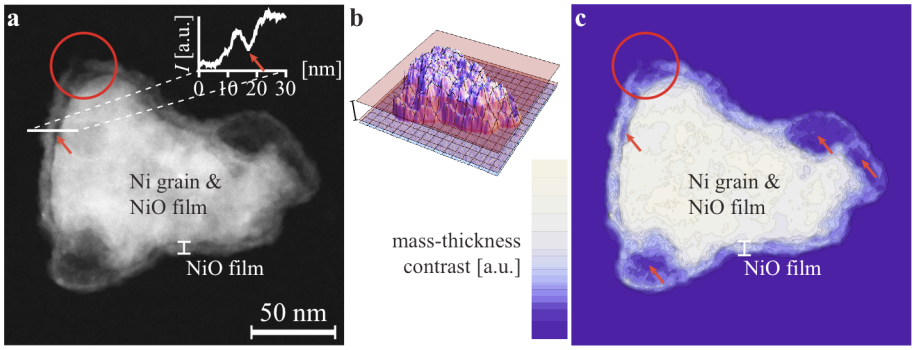

Figure 4.5 – (a) STEM HAADF image of a Ni(O) particle acquired at 300 °C in 3.2 mbar of O_2. An intensity profile across the NiO/Ni interface is also shown. The arrow marks a decrease in intensity at the position of the interface. (b) Three-dimensional visualisation of the image. (c) Contour plot, with the contrast adjusted to show the difference in intensity between planes marked in red in (b). Arrows mark features that are likely to be voids at the Ni/NiO interface. Areas that are circled in (a) and (c) show a fracture in the NiO film.

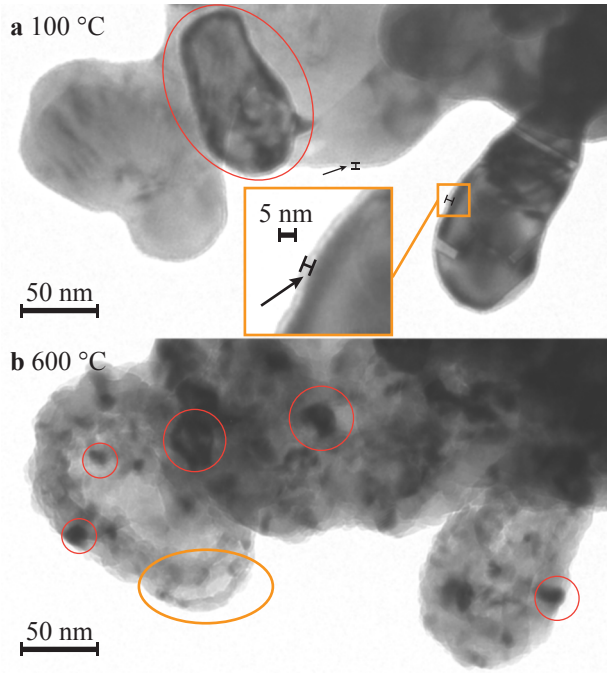

Figure 4.6 – BF TEM images acquired at (a) 100 and (b) 600 °C in 3.2 mbar of O_2. The arrows indicate a thin (< 5 nm) NiO layer around the particles in (a). A ~100 nm crystallographic domain is circled in (a). Selected crystallites, which diffract strongly and correspond to NiO domains that are below 50 nm in size at the end of the oxidation process, are circled in (b). The ellipse in (c) marks a double-scale structure.

4.2.2 EELS kinetic analysis

Fig. 4.7 shows, for the specific case of the 4 °C min^{-1} ramp, how the reaction kinetics are inferred from the EEL spectra, which are recorded every 6 min, corresponding to one spectrum every 24 °C (Fig. 4.7a). As mentioned above, the reaction kinetics in Fig. 4.7d are obtained either by fitting each spectrum using a linear combination of NiO and Ni reference spectra (Fig. 4.7b) or by using the Ni L_3/L_2 ratio (determined using polynomial or Lorentzian-Gaussian fits and 4 eV integration windows), which was normalised using ratios of intensities measured from the NiO and Ni reference spectra (Fig. 4.7c). The two techniques yield indistinguishable results. The fraction of NiO at room temperature in the presence of O_2 is found to be ∼0.1 for this sample. This amount cannot be attributed solely to the < 5 nm oxide layer that forms after removal of H_2 from the ETEM. Some NiO domains are therefore inferred to be present at the beginning of the reaction and to contribute to the total fraction of NiO (see also Fig. 3.8). As these domains do not form during the oxidation process, the fraction α of Ni converted to NiO is chosen to be 0 at the beginning of the reaction (right axis in Fig. 4.7d). In this way, the 3-4 nm NiO film that forms in high vacuum is neglected. This assumption is justified by the fact that a negligible fraction of the Ni is converted to NiO compared to the particle size (> 100 nm).

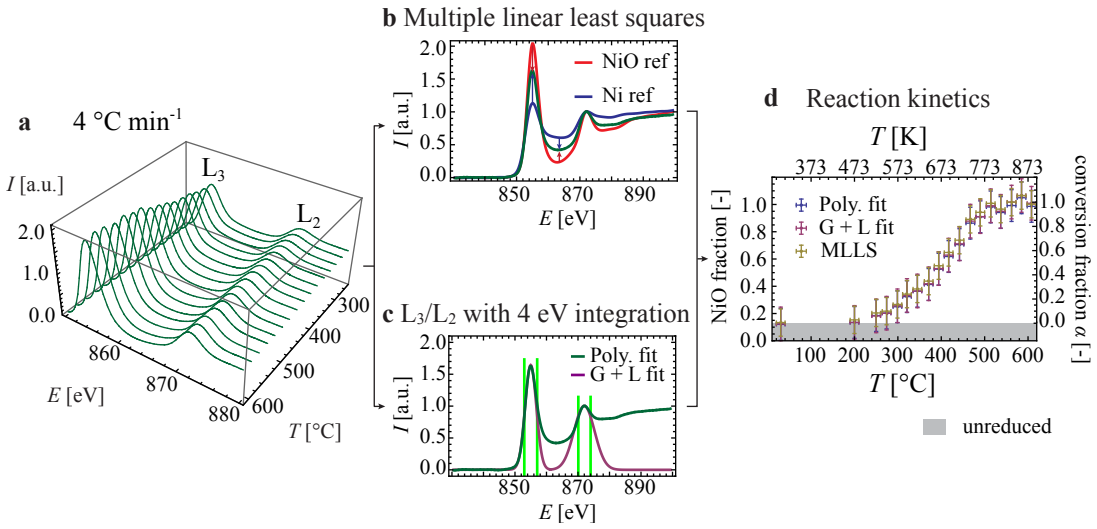

Figure 4.7 – (a) Background-subtracted EEL spectra acquired as a function of temperature for a 4 °C min^{-1} ramp (normalised to unity at L_2). NiO and Ni experimental reference spectra are used to determine the oxidation kinetics (d) using either (b) a multiple linear least squares (MLLS) technique or (c) the ratio of the Ni L_3/L_2 intensities fitted using polynomial or Gaussian-Lorentzian fits and integrated using 4 eV windows. The vertical uncertainties in (d) are obtained from the statistical deviation of the measured values of α when NiO is fully oxidised (3σ). The horizontal uncertainties are estimated to be ±10 °C.

Fig. 4.8a shows the reaction kinetics obtained for heating rates of 2, 4 and 6 °C min^{-1} by the white lines ratio method (using polynomial fits for integration; the other techniques yield the same results). Those results show that none of the samples is fully reduced after 210 min at 600 °C in 1.3 mbar of H_2, with the unreduced fraction varying from 0.1 to 0.2.

Out of the solid-state kinetic models that are investigated (nucleation, reaction order, geometrical contraction, etc. [41]), only the models that describe the reaction as a diffusion-controlled process yield results that are consistent with the experimental data. Although these diffusion models (listed in Refs. [41,242,243]) yield comparable results with similar values of E_a and A, the phenomenological description of oxidation of spherical particles derived by Niklasson and Karmhag appears to be better suited here [81]. Indeed, it describes the oxidation of nanometre-sized particles and thus includes built-in field effects for the initial stages of the reaction (up to a critical thickness L_{cr}, which is chosen here to be 10 nm, as in Ref. [24]), while the rest of the reaction is described as a linear diffusion process. The model is rewritten in Eq. 4.1 as a function of the initial Ni particle diameter d_0 and using the Pilling-Bedworth ratio q (the volume of product formed per volume of reactant; here 1.65 for NiO/Ni [257]). The full mathematical development shown in Appendix C.3 results in the following expression of the integral reaction model $g(\alpha)$:

$$g(\alpha) = \int_0^{\alpha} \frac{1}{(1-\alpha)^{1/3}[q+(1-q)(1-\alpha)]^{1/3} \sinh[\frac{2L_{cr}}{d_0} \frac{1}{[q+(1-q)(1-\alpha)]^{1/3}-(1-\alpha)^{1/3}}]} \, \mathrm{d}\alpha \quad (4.1)$$

The value of d_0 can be estimated from the TEM images and knowing the correspondence between α and T for a heating rate β (Fig. 4.8a), $g(\alpha)$ can be integrated for an experimental value of α, while the corresponding values of T and β are inserted on the right side of Eq. 2.26. E_a and A can then be estimated using an algorithm that minimises the least squares differences between the values of $g(\alpha)$ and their corresponding approximation of the temperature integral (Nelder-Mead method [241]). As the particle size is not homogeneous here and is observed to range from ∼100 to 400 nm (Fig. 4.3), these two boundary values are used as separate d_0 to infer two different sets of values of E_a and A, as lower and upper limits of the kinetic description (Tab. 4.1). A rational description for the data is obtained at heating rates of 2 and 4 °C min^{-1}, while the measurements obtained at 6 °C min^{-1} are shifted to lower temperatures when compared to the model (Fig. 4.8). This shift prevents the use of the Kissinger method (Chap. 2.5).

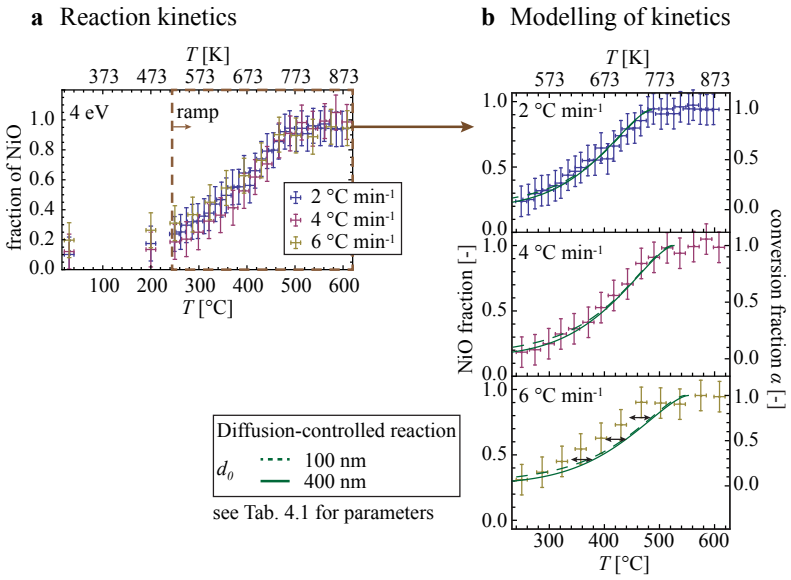

Figure 4.8 – (a) $\alpha - T$ curves measured for heating rates of 2, 4 and 6 °C min^{-1} obtained using $I(L_3)/I(L_2)$ ratios (with polynomial fits). (b) Fits of the $\alpha - T$ curves derived using the parameters in Tab. 4.1.

d_0	100 nm	400 nm	
E_a	80 kJ mol^{-1}	73 kJ mol^{-1}	
A	617 s^{-1}	700 s^{-1}	with L_{cr} = 10 nm
R^2	0.92	0.90	q = 1.65

Table 4.1 – Results of the kinetic model fitting procedure for particle sizes of 100 and 400 nm using $g(\alpha)$ expressed in Eq. 4.1. The model assumes that diffusion is non-linear up to 10 nm and then linear until full oxidation.

The results of the model fitting procedure (E_a and A) can be used to determine the parabolic rate constant k_p (in units of cm^2 s^{-1}), which gives the speed of the reaction according to the expression (see Appendix C.3 for more details):

$$k_p(T) = \frac{qL_{cr}d_0}{6} A e^{\frac{-E_a}{RT}} \tag{4.2}$$

Fig. 4.9 plots $k_p(T)$ as a function of temperature for particle sizes chosen as 100 and 400 nm. Values obtained for the rate constant inferred from EELS measurements can then be compared to those obtained experimentally in the literature. As the reaction appears to be diffusion-controlled, the values can also be compared to predictions based on diffusion coefficients. For a reaction that is controlled by linear diffusion in an oxide

film, which is in local chemical equilibrium, the value of k_p at a certain temperature is related directly to the diffusion coefficients of the ionic species that control the reaction (Ni^{2+} in the NiO lattice and grain boundaries) [92] in the form of Eq. 4.3 that was introduced in Chap. 2:

$$k_p(T) = 6.4\left(D^*_{\text{lattice}}(T) + \frac{2(D'\delta)^*(T)}{g_{\text{size}}(T)}\right) \tag{4.3}$$

where $D^*_{\text{lattice}}(T)$ is the tracer diffusion coefficient of Ni^{2+} in the NiO lattice (from Ref. [92]: $4.5{\cdot}10^{-19}$ cm^2 s^{-1} at 500 °C and $3.7{\cdot}10^{-17}$ cm^2 s^{-1} at 600 °C in 1.01 bar of O_2), $(D'\delta)^*(T)$ is the tracer grain boundary diffusion coefficient ($7.4{\cdot}10^{-20}$ cm^3 s^{-1} at 500 °C, $1.6{\cdot}10^{-18}$ cm^3 s^{-1} at 600 °C) and $g_{\text{size}}(T)$ is the oxide grain size (estimated from the images to be ~50 nm at the end of the oxidation process; see Fig. 4.4). $k_p(T)$ is proportional to $P_{O_2}^{1/4}$-$P_{O_2}^{1/6}$ above 1000 °C and appears independent of P_{O_2} at temperatures on the order of 700 °C [91].

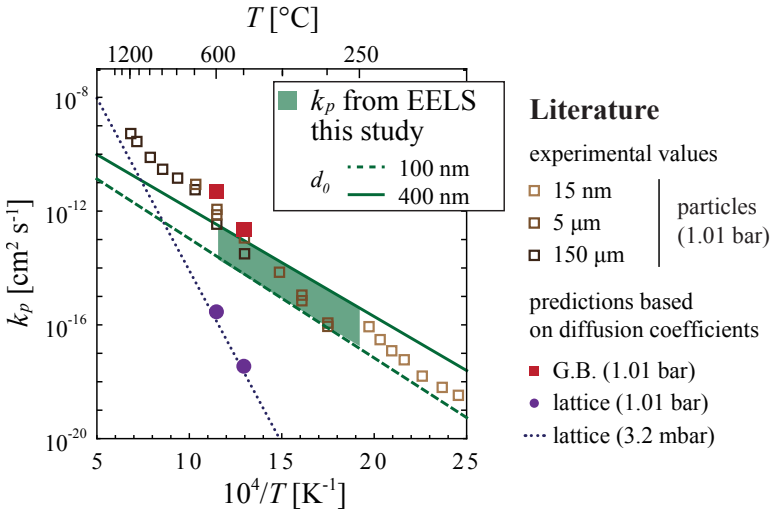

Figure 4.9 – Rate constants determined from the modelling procedure plotted alongside predicted and experimental values from the literature. Predictions for a planar geometry involve diffusion of Ni^{2+} through the NiO lattice, either without (Ref. [245] at 3.2 mbar, Ref. [92] at 1.01 bar) or with additional diffusion along grain boundaries (G.B., Ref. [92] at 1.01 bar). Experimental values for Ni particles of different size were obtained using thermogravimetry [258].

4.3 Discussion

4.3.1 Initial stages of oxidation process

After reduction in H_2, the samples are exposed to a partial pressure of $\sim 10^{-7}$ mbar of O_2. NiO domains then nucleate with random orientations, impinge and grow to form continuous shells around the particles, which stabilise at a thickness of 3-4 nm (Fig. 4.2). Similar oxide structures have been observed *ex situ* by Railsback *et al.* [99] and Graham and Cohen [83]. In the present study, even though the dynamics of the thin NiO layer growth could not be captured, the behaviour can be related qualitatively to the description of Cabrera and Mott [80]. According to this model, once the NiO domains have impinged to form a continuous layer, oxide growth continues by field-driven transport of Ni^{2+} through the NiO. Over this length scale, electrons can tunnel from the metal across the oxide film to ionise adsorbed oxygen. A large electric field then builds up in the film, driving the transport of Ni^{2+} through the NiO without the need for thermal activation. Once the oxide layer has reached a thickness of 3-4 nm, electron transfer becomes negligible and the oxide growth rate approaches zero. In those experiments, the polycrystalline oxide does not grow further, either at room temperature when O_2 is introduced at a pressure of 3.2 mbar or when the temperature is increased to 100 °C (Fig. 4.6a). Moreover, the reaction rate measured using EELS remains slow up to 250 °C (Fig. 4.7d).

4.3.2 Structural evolution of Ni particles until full oxidation

Voids nucleation at Ni/NiO interfaces

The contrast in the STEM HAADF image shown in Fig. 4.5 suggests that at 300 °C voids have already formed at the Ni/NiO interface, i.e. that transport of Ni^{2+} across the NiO film is faster than that of O^{2-}, as expected based on the diffusion coefficients of Ni^{2+} and O^{2-} [79]. New NiO domains therefore form outwards at the NiO/O_2 interface, while Ni vacancies are injected at the Ni/NiO interface to balance the outward mass flux. The mobility of these vacancies, which accumulate and coalesce at the interface, results in the nucleation of multiple voids along the Ni/NiO interface [99]. Voids that have sizes of ~10 nm are observed in the vicinity of convex Ni regions, while in other regions the pores take the form of thin flat layers that have a thickness below 5 nm. It appears that Ni/NiO contact may be more difficult to maintain in curved than in flat regions, where the interface may recess more easily [259].

Formation of transverse cracks in the NiO film

The NiO film is also observed to break in some regions, creating a new temporary permeation channel for gaseous O_2 to a fresh Ni surface [79] (circled regions in Figs. 4.5a-c and ellipse in 4.6b). New NiO domains can then form directly on the Ni core surface, in turn closing the O_2 permeation channel. The oxide growth rate is sufficiently slow

at 300 °C (taking at least a few seconds) so that this process can be captured in STEM mode. In contrast to other techniques, such as post-O_2 exposure structural examination or acoustic emission, ETEM has the ability to resolve this process *in situ* and spatially, allowing the underlying mechanisms to be discussed with regard to geometrical/structural considerations. The same phenomenon was reported to occur in planar NiO films that have a thickness of above a few µm and to result in the formation of a characteristic duplex microstructure [101]. The oxide fracture observed in the present experiment is located at the edge of an irregular Ni structure and runs through an oxide film of thickness ∼10 nm. While different models have been proposed to describe the formation of cracks in oxide films [79, 259, 260], the irregular geometry of the Ni particles investigated here probably results in additional stress in the oxide [260]. While oxide growth stress is usually compressive and would be expected to close any potential crack, inhomogeneities arising from local differences in oxide growth rate, which could be caused by local loss of contact between NiO and Ni (as observed in Fig. 4.5), may be sufficient to rupture the film locally [261]. Growth of the NiO film near the curved edges is probably hindered, as the supply of Ni^{2+} through the film is disrupted by the loss of contact between Ni and NiO, resulting in a higher rate of NiO growth in the flatter regions where the Ni/NiO contact area is higher.

Polycrystalline NiO structures with internal voids

Above 400 °C (Fig. 4.3d-f), the contrast in the images becomes irregular as the NiO film grows, with NiO reflections in diffraction patterns indicating random grain orientations. As shown in Fig. 4.3d, the internal Ni surface retracts in one direction, maintaining contact with the NiO that covers it in some areas while leaving voids elsewhere. This observation is similar to that of Railsback *et al.* [99] and requires self-diffusion of Ni along with that of vacancies to maintain contact between Ni and NiO as oxidation continues. The final microstructure contains internal voids and small randomly oriented NiO crystallites of < 50 nm in size when the temperature reaches 600 °C (Fig. 4.3e-f). Ni reflections are not detected above 500 °C (Figs. 4.3 and 4.4), with EELS results confirming full oxidation at this temperature (Fig. 4.7d).

4.3.3 Chemical evolution of Ni particles until full oxidation

Diffusion model describing the oxidation kinetics

Close examination of the structural changes that occur during oxidation provides some information about the mechanisms involved. Further insights can be inferred by assessing the oxidation kinetics. Progress of the reaction with temperature exhibits a similar shape for overall rates of 2, 4 and 6 °C min^{-1} (Fig. 4.8), indicating that the same mechanism probably controls the reaction in each case. In contrast to theoretical predictions (see Eq. 2.23), the curve measured at 6 °C min^{-1} is shifted to lower temperature when compared with the curves obtained at 2 and 4 °C min^{-1}. Although the reason behind

this observation is unclear, slight differences in the Au grids and SiO_x films used could introduce a systematic error. Specimen-dependent charging effects were observed in the ETEM (in the form of the movement of the SiO_x film in the absence of gas), suggesting differences in the conductivity and therefore the temperature of the region of interest. Such effects can alter the results of kinetic modelling, which should therefore be regarded as semi-quantitative. The model derived in Ref. [81] and in Appendix C.3, which describes a process that is first controlled by non-linear transport up to a thickness of 10 nm and then predominantly by linear diffusion up to full oxidation, provides consistent values for the NiO fraction from EELS for heating rates of 2 and 4 °C min^{-1} (Fig. 4.8b), while measurements obtained for a rate of 6 °C min^{-1} are systematically shifted by -40 °C. The activation energy E_a of 80/73 kJ mol^{-1} inferred for the reaction for 100/400 nm particles with R^2 of 0.92/0.90 (Tab. 4.1) is similar, although slightly lower, to values usually reported in the literature (∼100-200 kJ mol^{-1} [26]). It therefore appears that the reaction is limited by the diffusion of active species across the film rather than by the Ni/NiO and NiO/O_2 interfacial reactions, in agreement with other similar oxidation processes [79].

Transition between non-linear and linear regimes

Non-linear effects accelerate the reaction during its initial stages. Their magnitude depends on the particle size compared to the critical oxide thickness L_{cr} for the transition between non-linear and linear behaviour (10 nm here as in Ref. [24]). The use of values for L_{cr} above 10 nm, i.e., increasing the magnitude of non-linear effects, overestimates the fraction that is converted during the initial stages of the reaction. The value of 10 nm that was chosen appears to be an upper limit. For a particle size of 400 nm, built-in field effects are negligible when compared with uncertainties in the measurement and the entire reaction can be regarded as an apparently linear process (similar to that derived by Fromhold [243]). For a particle size of 100 nm, the reaction rate is enhanced at lower conversion fractions ($\alpha \leq 0.2$), resulting in a slightly higher coefficient of determination (0.92 compared to 0.90; see Tab. 4.1). This result does not indicate that the latter description is better, as the difference arises from the fact that the modelled curve is closer to the first few points obtained at 6 °C min^{-1} , which are affected by a systematic error in the measurement (Fig. 4.8b). While non-linear diffusion of Ni^{2+} controls the growth of the first 3-4 nm of oxide formed in high vacuum conditions (not modelled in the kinetic fitting procedure) and perhaps also influences the formation of oxide up to a thickness of < 15 nm (the value of L_{cr} added to the initial 3-4 nm), it appears that most of the process can be seen as apparently linear and thermally activated.

Diffusion mechanism

The rate constants that are obtained from EELS are consistent with values measured when oxidising 5 µm Ni particles in 1.01 bar of O_2 in a thermogravimetry apparatus [258],

providing confidence in the reliability of the results acquired *in situ* in the ETEM (Fig. 4.9). The rate constants obtained here are also close to those predicted when linear diffusion of Ni^{2+} along the NiO grain boundaries controls the reaction [92]. Alternatively, the values predicted solely on the basis of Ni^{2+} lattice diffusion are several orders of magnitude lower [92,245]. Figs. 4.3 and 4.5 suggest that mass transport of Ni^{2+} is faster than that of O^{2-}. Based on this kinetic analysis, it can be deduced further that diffusion of Ni^{2+} along NiO grain boundaries is likely to play a significant role in the oxidation process.

This picture is, however, still oversimplified. The activation energy for oxidation measured here ($\sim$70-80 kJ mol^{-1}; Tab. 4.1) is lower than that expected for a process that is controlled solely by linear diffusion of Ni^{2+} along NiO grain boundaries (171 kJ mol^{-1} [79]). Different mechanisms that each contribute to the decrease in E_a must be included in the description. First, the density of grain boundaries evolves during the part of the reaction that is modelled as the NiO crystallite size changes from 3-4 nm to $\sim$30-50 nm (Fig. 4.6b). The reaction rate is enhanced at the beginning of the reaction when compared to that at its end and in turn E_a is lowered [79]. In addition, a space charge separation region should occur close to the interfaces. This region is estimated to have a thickness of $\sim$10-100 nm, which is significant when compared to the particle size of 100-400 nm [79]. Local electrical neutrality in the oxide film is therefore unlikely to be a fully valid assumption, especially in the presence of the electron beam. As a consequence, the transport of ions, such as the diffusion of Ni^{2+} along NiO grain boundaries, is likely to be field-assisted to an extent. This effect is probably more significant during the initial stages of oxidation (when the oxide is thin and further away from local electrical neutrality), which could decrease the value of E_a for the process. Other effects that are observed but not taken into account in the kinetic model include permeation of O_2 through NiO cracks and thus direct formation of NiO and nucleation of voids at the Ni/NiO interfaces, which disrupts the supply of Ni^{2+} to the oxide film in some regions (both effects are seen in Fig. 4.5). The latter effect results in Ni self-diffusion, along with that of Ni vacancies, to maintain contact between the Ni particle and the NiO film to continue the supply of Ni^{2+} that can diffuse through the oxide. The overall Ni/ NiO contact area should decrease with increasing α and in turn lower E_a.

4.3.4 Factors affecting ETEM observations

The high-energy electron beam may affect ETEM observations, as described in detail by Egerton *et al.* [255]. Buckett and Marks investigated the effect of electron irradiation on NiO [249]. An assessment of electron beam effects during NiO reduction in an ETEM can also be found in Chap. 3.

In order to understand the influence of the electron beam on the measurements, areas of interest were compared every 100 °C with regions that had not been illuminated previously. No significant structural differences were observed between irradiated and non-irradiated areas between room temperature and 600 °C.

However, electron beam effects may introduce more subtle artefacts. The movement of charged species that drive the oxidation process can be influenced by the electron beam. These effects are difficult to investigate. However, the parabolic rate constant for the reaction measured here is consistent with values obtained using thermogravimetry, providing confidence that such effects do not alter the growth-controlling mechanism significantly. In addition, the electron beam may ionise the molecular oxygen gas, which may in turn change the adsorption energy of oxygen on NiO. However, this mechanism is usually not rate-limiting when compared to diffusion of Ni^{2+} and O^{2-} [79].

The electron beam may also increase the local specimen temperature and accelerate the reaction. This effect was not considered to be problematic here. The electron dose was kept constant in all three kinetic experiments, which should result in similar local increases in temperature. As the thermocouple is welded onto the outside of the furnace, the region of interest is likely to be at a slightly lower temperature when compared to the measured value. This difference is difficult to estimate as it depends on parameters such as gas flow and temperature, sample geometry, etc. It was estimated to be ≤ 50 °C in Chap. 3. However, a systematic error does not influence the value of the measured activation energy significantly. E_a only decreases by $\sim$10 kJ mol^{-1} if the temperature of each measurement point is decreased by 30 °C. As only a semi-quantitative description of the process is sought, those two effects are not considered significant.

4.3.5 Qualitative description of the oxidation mechanism of Ni particles

The oxidation mechanism of the metallic Ni particles observed here is summarised schematically in Fig. 4.10. Growth of the first 3-4 nm of oxide (Fig. 4.10b), which occurs at room temperature in 10^{-7} mbar of O_2, is not thermally activated and appears to be controlled by built-in field effects, as described by Cabrera and Mott [80]. This NiO film does not grow significantly upon increasing the temperature to 250 °C in 3.2 mbar of O_2, when an apparent linear diffusion process starts (Fig. 4.10c). Ni^{2+} is then observed to diffuse faster than O^{2-}, resulting in the formation of voids at the Ni/NiO interfaces. The modelling procedure suggests that linear diffusion of Ni^{2+} along NiO grain boundaries is an important rate-controlling mechanism. However, this description is incomplete. First, the oxide film is not in a steady state on these length scales, which affects the diffusion of Ni^{2+} across the NiO. This effect is likely to be increased by the presence of the electron beam. Second, interface recession and the movement of dislocations do not balance the nucleation of voids at the Ni/NiO interface. Contact between the Ni and NiO may therefore be lost in some regions, hindering the reaction locally. Ni must then self-diffuse, along with vacancies, to continue the oxidation process in some regions. Curved edges of the particles may rupture locally due to geometrically induced stresses, allowing direct reaction between O_2 and freshly exposed Ni. As a result of all these effects, both polycrystalline NiO grains with irregular geometries and voids are observed (Fig. 4.10d).

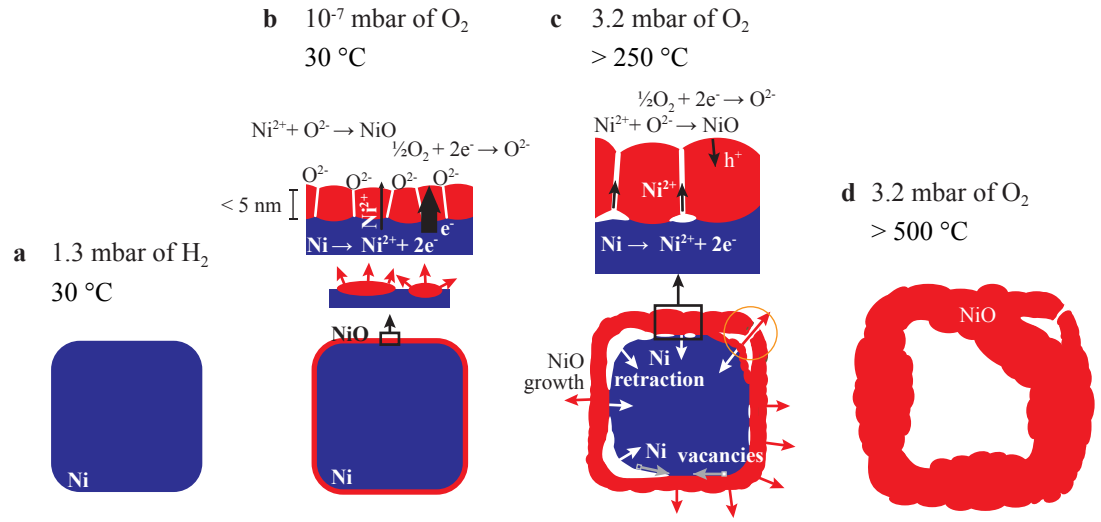

Figure 4.10 – Schematic description of the oxidation of Ni particles. (a) Starting cross-section of a Ni particle in a H_2 atmosphere. (b) In an O_2 pressure of 10^{-7} mbar, a thin NiO layer forms as a result of a process described by Cabrera and Mott [80]. (c) Above 250 °C, in 3.2 mbar of O_2, the growth of NiO appears to be controlled primarily by the diffusion of Ni^{2+} along NiO grain boundaries (see inset in c). This process is likely to be field-assisted. Ni must self-diffuse along with vacancies to maintain Ni/NiO contact (grey arrows in c). Transverse oxide cracks may also appear as a result of geometrically induced stresses (circled in c). (d) A porous, asymmetric, polycrystalline NiO structure finally forms.

4.4 Concluding remarks

Several different TEM and STEM imaging techniques, SAED and core-loss EELS were applied in combination in an environmental transmission electron microscope, to investigate the structural and chemical changes that occur at the nanoscale during the oxidation of Ni particles in 3.2 mbar of O_2 at temperatures of up to 600 °C. By making use of changes in the shapes of the Ni $L_{2,3}$ ionisation edges, the reaction kinetics could be inferred and compared with models to assess the mechanism that controls the reaction and its relationship to the observed structural changes, similarly to Chap. 3. While the procedure is only semi-quantitative, valuable insights could be obtained about the different mechanisms involved during oxidation, including local transient processes.

Nucleation and growth of the first few nm of NiO on Ni was observed to occur rapidly at room temperature in high vacuum conditions as a result of built-in field effects. When O_2 was introduced at a pressure of 3.2 mbar and the temperature was increased in increments up to 600 °C, inhomogeneous randomly oriented NiO crystallites and voids formed as a result of several different mechanisms: Ni^{2+} diffusion along NiO grain boundaries (probably field-assisted), self-diffusion of Ni^{2+} and Ni vacancies and the formation of transverse cracks in the NiO film, creating channels for O_2 permeation towards unreacted Ni. The formation of transverse channels in NiO was predicted to

occur on the basis of post-exposure observations and acoustic emission studies but to our knowledge had not previously visualised *in situ* at such spatial resolution.

The oxidation mechanisms are likely to be affected to an extent by the presence of the electron beam. However, the NiO structures that were obtained *in situ* in the present study are comparable to those reported on the basis of *ex situ* studies in the literature. The overall reaction rate also corresponds to that measured using other methods, providing confidence that the mechanisms observed *in situ* in the environmental transmission electron microscope are representative.

While the present methodology provides new insights into the oxidation mechanism of Ni particles, additional work is required to obtain a fully quantitative description of the process. One of the most important unknown parameters is the strength of the electric field in the NiO film during oxidation.

5 Reduction of NiO/YSZ composites

Reduction of NiO/YSZ composites is studied here using environmental TEM and density functional theory calculations. Images, diffraction patterns and energy-filtered images are acquired to monitor the structural and chemical evolution of the composite samples during reduction in 1.3 mbar of H_2 up to temperatures ranging from 500 to 850 °C. The acquisition of energy-filtered images at different temperatures during reduction allows temperature-resolved quantitative information to be obtained about both reaction kinetics (using O K edge images) and specimen thickness (using total inelastic mean free path images) on the pixel scale. The results, which are detailed in a qualitative model, reveal that the transfer of oxygen from NiO to YSZ triggers the reduction reaction at these interfaces and forms a porous Ni structure that is epitaxial with the initial NiO. The NiO free surface reacts at a higher temperature and results in a similar porous and coherent structure. At higher heating rate and in mass-transfer limited conditions, reaction occurs directly through the free surface without activation at the interfaces with YSZ. Densification of the Ni grains is then observed above 600 °C.

5.1 Experimental details

5.1.1 Materials

Standard SOFC anodes characterised here contained co-sintered particles of NiO Baker™ (55 %wt) and yttria-stabilised zirconia (YSZ, 45 %wt). Specimens were prepared for environmental (ETEM) observations using a conventional focused ion beam (FIB) lift-out technique in a dual beam FIB/SEM (Zeiss NVision 40 CrossBeam) and were welded onto stainless steel grids using C. Alternatively, weld-less H-bar samples were prepared by cutting and polishing NiO/YSZ as-sintered anodes into the shape of half TEM grids and thinning electron transparent windows using FIB. In all cases, final thinning was performed at a low Ga^+ energy of 2 or 5 kV.

5.1.2 Electron microscopy

Structural and crystallographic changes during NiO/YSZ reduction

TEM lamellae welded onto stainless steel grids were mounted in a Gatan Inconel 652 double-tilt heating holder and their reduction behaviour was studied using the environmental transmission electron microscope schematised in Fig. 2.3. The microscope was operated at 300 kV and at an electron dose rate of $\sim 10^3$ e^- nm^{-2} s^{-1}, which was maintained constant throughout the entire experiment. This first set of experiments involved the use of bright-field (BF) TEM images and selected area diffraction patterns (SADP) to qualitatively assess the structural and crystallographic changes occurring in two regions of interest during NiO/YSZ reduction. Prior to heating the sample, H_2 was introduced into the cell at a flow of 2 ml_N min^{-1}, corresponding to a measured pressure of 1.3 mbar at the sample. After 30 min of stabilisation at 200 °C to minimise the thermal drift associated with the rapid rise of temperature, the temperature was increased to 250 °C and then to 300 °C. From this point, the sample was heated by 10 °C every 5 min up to 500 °C to maintain an overall 2 °C min^{-1} heating rate (Fig. 5.1). At each step, BF images of the NiO/YSZ microstructure and SADPs from one NiO grain were acquired after the sample was thermally stable (1 min after the increase in temperature). The zone axis was identified through comparisons with diffraction patterns simulated with the software JEMS [36]. Scanning TEM high-angle annular dark-field (STEM HAADF) images and STEM electron energy-loss spectra (EELS) were acquired at 500 °C after the temperature ramp was completed.

Measurements of NiO/YSZ reduction kinetics and volume shrinkage using EFTEM

Using similar NiO/YSZ lamellae welded onto stainless steel mounted in the same Gatan Inconel 652 double-tilt heating holder, another set of experiments was designed to obtain temperature-resolved quantitative information about both chemistry and structure using energy-filtered transmission electron microscopy (EFTEM) images. As above, the ETEM was operated at 300 kV at a constant electron dose rate of $\sim 10^3$ e^- nm^{-2} s^{-1} and H_2 was

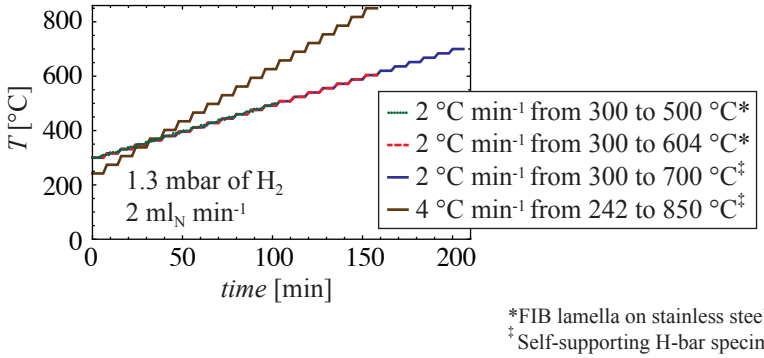

Figure 5.1 – Time and temperature parameters used to approximate constant heating rates during reduction of different samples. A set of measurements was performed at each step.

introduced at 2 ml_N min^{-1}, resulting in a H_2 pressure of 1.3 mbar. A similar heating rate of 2 °C min^{-1} was used between 300 and 604 °C to minimise thermal drift and hence maximise the quality of EFTEM images. The temperature was manually increased in steps of 16 °C over a duration of 2 minutes and then maintained constant for 6 minutes to perform structural and chemical measurements (Fig. 5.1). Each acquisition sequence included the following BF TEM images (collection semi-angle of 6.8 mrad): one unfiltered image I_t, one filtered zero-loss image I_0 (slit width Δ of 10 eV) and three images $I_{\text{pre-edge 1}}$, $I_{\text{pre-edge 2}}$ and $I_{\text{post-edge}}$ at energy loss onsets of 472 eV, 502 eV and 532 eV, respectively (Δ of 30 eV). The acquisition time was set to 40 s for most of the frames and sometimes reduced to 20 s to maintain the overall heating rate. All of the recorded images were aligned by cross-correlation after filtering using a Sobel operator [219].

As illustrated in Fig. 5.2a, images I_t and I_0 were used to construct a t/λ thickness map (using Eq. 2.9, where t is the sample effective thickness in nm and λ is the total inelastic mean free path, estimated here to be $\lambda_{\text{Ni}} = 127$ nm in Ni and $\lambda_{\text{NiO}} = 155$ nm in NiO, see Appendix D.1). These images were then used to infer values of thickness (and thus volume) shrinkage of the sample due to the removal of oxygen as a result of reduction. Plasmonic contributions of H_2 and H_2O were neglected, which appeared reasonable as the intensity measured within holes of the t/λ images did not increase upon insertion of 1.3 mbar of H_2 and during reduction.

Images $I_{\text{pre-edge 1}}$, $I_{\text{pre-edge 2}}$ and $I_{\text{post-edge}}$ were processed to obtain elemental maps of the oxygen K edge (532 eV) using the conventional 3-window method, whereby the two $I_{\text{pre-edge}}$ images were used to extrapolate a power law background that was subtracted from the $I_{\text{post-edge}}$ image that contains the oxygen K edge signal (Fig. 5.2b, see procedure in Appendix D.2).

Alternatively, the $I_{\text{post-edge}}$ images were divided by their corresponding $I_{\text{pre-edge 2}}$ images to yield jump-ratios of the O K edge (Fig. 5.2c). Differences in structure due to the undergoing reaction, coarsening, drift and/or misalignment between those 2 images

(acquired 40 s apart) may generate pixels with an artificially high intensity due to division. As a result, a threshold was applied to the jump-ratios to select these pixels and set their value to 0. Moreover, the intensity measured within the holes of the structure yielded values of ∼1 as these did not change with temperature/time. To set the value of these pixels to 0, an outline of the holes was obtained by applying a gradient filter to each jump-ratio before applying a function to fill all extended minima that are surrounded by the outline of the holes. After inversion, masks with a value of 0 within the holes and 1 elsewhere were obtained and these were multiplied by their corresponding jump-ratio to yield images with non-zero intensities that relate to the oxygen content. Thickness maps could not be used to yield masks of the holes due to the structural changes occurring during the 1 min interval that separated the acquisition of the t/λ images and the O K edge images.

Experimental NiO and Ni references were required to scale the data and hence assess reaction kinetics and relative thickness changes. References for 3-window O K elemental maps, O K jump-ratios and t/λ images were obtained at 30 °C (NiO reference) and then at 604 °C, 130 min after the end of the ramp (Ni reference; full reduction of Ni regions confirmed by EELS on individual grains).

To analyse the changes in thickness and chemistry induced by reduction of NiO to Ni, the Ni phase was segmented from the YSZ using an elemental map of the Ni $L_{2,3}$ edges acquired at room temperature before the reduction experiment (acquisition time of 40 s, Δ of 40 eV, pre-edge images at energy-loss onsets of 770 and 810 eV, post-edge image at an onset of 855 eV). A threshold was applied to the image, which was binarised to obtain separate masks of the Ni and YSZ phases that could be applied to each t/λ map, 3-window elemental map and jump-ratio.

As the ceramic phase was found to be structurally and chemically stable at these temperatures, the masked YSZ backbone in each thickness map, 3-window O K elemental map and O K jump-ratio was used as an invariant reference to monitor intensity changes in the adjacent evolving NiO phase. Each thickness map, 3-window O elemental map or O jump-ratio was divided by the average number of counts in its YSZ phase and then multiplied by the average intensity the YSZ phase measured within each thickness maps, 3-window O elemental maps or O jump-ratios sequence. In turn, possible intensity offsets were minimised and images with comparable intensities were obtained. In other words, the intensity in the NiO phase was analysed in relation to that in the YSZ backbone.

The thickness maps, 3-window elemental maps and jump-ratios could then be analysed quantitatively on the pixel scale, which corresponded to an area of $\sim$6 x 6 nm^2, by comparing their intensity to that of their respective experimental NiO and Ni references. The reaction kinetics $\alpha(T)$ was inferred from 3-window elemental maps and jump-ratios by measuring the average intensity $\bar{I}_O(T)$ within the same region of interest throughout the reaction (i.e in the sequence of temperature-resolved 3-window elemental maps and

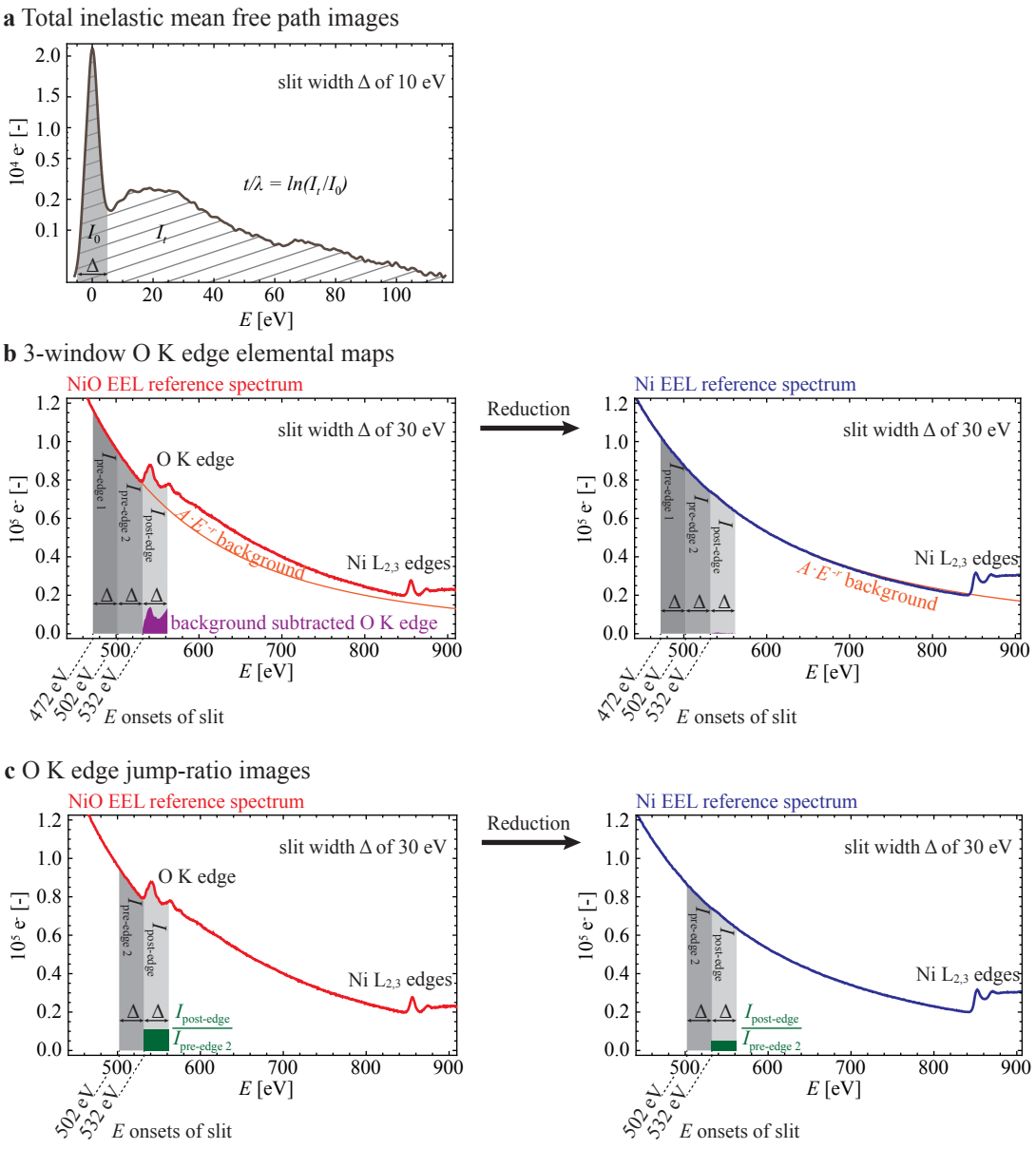

Figure 5.2 – Positions of the energy-selecting slit (coloured in grey) to select parts of the energy-loss spectrum at fixed temperature intervals during reduction to yield (a) t/λ total inelastic mean free path images, (b) 3-window elemental maps, (c) O K jump-ratios.

jump-ratios). Those values of $\bar{I}_O(T)$ were normalised using the average values $\bar{I}_{O_{NiO}}$ and $\bar{I}_{O_{Ni}}$ measured within the exact same region in the NiO and Ni reference images, respectively, to yield $\alpha(T)$ (Eq. 2.11).

Moreover, ignoring excitations at the interfaces of the structure (between voids, NiO and/or Ni) [262] and assuming a defined NiO/Ni reaction front, the simultaneous

knowledge at the same position of degree of reduction $\alpha(T)$ and t/λ allowed the estimation of the equivalent NiO thickness $t_{\mathrm{NiO}}(T)$, Ni thickness $t_{\mathrm{Ni}}(T)$ and total thickness $t(T)$ using Eqs. 5.1-5.3:

$$t_{\mathrm{NiO}}(T) \approx t/\lambda(T)[1-\alpha(T)]\lambda_{\mathrm{NiO}} \tag{5.1}$$

$$t_{\mathrm{Ni}}(T) \approx t/\lambda(T)\alpha(T)\lambda_{\mathrm{Ni}} \tag{5.2}$$

$$t(T) \approx t_{\mathrm{NiO}}(T) + t_{\mathrm{Ni}}(T) \tag{5.3}$$

Pre- and post-H_2 exposure characterisation involved the acquisition of STEM energy dispersive X-ray spectroscopy (EDX) maps to assess segregation and redeposition of elements. EDX maps were obtained using a microscope equipped with four windowless silicon-drift detectors (FEI Tecnai Osiris microscope). Automated crystal orientation maps were acquired after the sample had reacted in the ETEM using the ASTAR system installed on a JEOL 2200FS microscope [227]. At room temperature in high vacuum conditions, a parallel beam of $\sim$2 nm was set up in nano beam diffraction mode (C2 aperture of 10 µm) and maps of 400 x 400 pixels to 600 x 600 pixels were acquired with a step size of 2 to 10 nm at 100 frames per second. The diffraction patterns at the position of each pixel were indexed using cubic crystal structures of both Ni and ZrO_2 (Appendix A) through a template matching procedure (using Eq. 2.13 [228]). Moreover, STEM high-angle annular dark-field (HAADF) tomograms of different regions of the specimen that was reduced *in situ* were acquired from -65 to +65° with an increment of 1° (JEOL 2220FS). Using the software TomoJ [224], tilt series were aligned using cross-correlation. The analysis of the trajectory of local minima throughout the tilt series was then used to improve the alignment and to yield the tilt axis. Reconstructions were then obtained using the Simultaneous Iterative Reconstruction Technique (SIRT) algorithm with 40 iterations [225]. The structures were visualised in 3D using the software Chimera [226].

Additional NiO/YSZ *in situ* reduction experiments

While previous sections focused on the retrieval of structural, crystallographic and chemical information during reduction up to 500 and 600 °C, the objective of this set of experiments was to investigate the behaviour of NiO/YSZ during reduction up to higher temperatures, i.e. 700-850 °C. The H-bar design was selected for these experiments as it maintained the initial NiO/YSZ structure but did not involve any C welding thus allowing higher temperatures, especially during subsequent reoxidation in Chap. 6. As above, the ETEM was operated at 300 kV at a constant dose rate of $\sim 10^3$ e^- nm^{-2} s^{-1} and samples were mounted in the Gatan Inconel 652 double-tilt heating holder. H_2 was introduced in the environmental cell at 2 ml_N min^{-1} hence resulting in 1.3 mbar of H_2.

A H-bar sample was reduced up to 700 °C with an overall heating rate of 2 °C min^{-1} (steps of 16 °C during 2 min, measurement time of 6 min, Fig. 5.1). The specimen was characterised using BF TEM images, both unfiltered and filtered at the position of the zero-loss (I_t, I_0, Δ of 10 eV, collection semi-angle of 6.8 mrad) to yield t/λ images at different reduction temperatures. Another H-bar specimen, which contained 2 thin windows, was reduced up to 850 °C with an overall rate of 4 °C min^{-1} (steps of 32 °C during 2 min, measurement time of 6 min, Fig. 5.1). One thin window was characterised *in situ* using BF EFTEM images (I_t, I_0, Δ of 10 eV, collection semi-angle of 6.8 mrad) to obtain t/λ images, while the other one served as a reference to assess irradiation damages and was observed in H_2 at room temperature before and after reduction. After both experiments, the frames were aligned by cross-correlation after filtering using a Sobel operator [219].

Pre- and post-exposure characterisation involved the acquisition of STEM EDX maps (FEI Tecnai Osiris), EEL spectra (FEI Titan ETEM), EFTEM images (FEI Titan ETEM) and selected area diffraction patterns (FEI Titan ETEM).

5.1.3 Density functional theory calculations

The results of this chapter were complemented by density functional theory calculations performed by Dr. U. Aschauer (now at ETH Zürich). Experimental details are given in Appendix E.

In summary, a model atomistic structure of the NiO/YSZ interface was constructed. In turn, a nudged elastic band (NEB) calculation was performed to assess the transfer of O from the NiO to the oxygen vacancies inherent to the ion conducting YSZ phase. The NEB method was used to determine the reaction pathway from the known initial state (here O in NiO) to the known final state (O in YSZ) through the minimisation of the energy of the set of intermediate images (using here DFT to calculate the atomic forces in each image) [263, 264]. In other words, a string of images of the intermediate states was created and connected by springs and this chain was deformed to find the pathway that minimised the energy barrier of the process.

5.2 Experimental results

5.2.1 Initial NiO/YSZ structure

Fig. 5.3 shows a STEM BF micrograph of the initial as-sintered structure along with corresponding EDX maps of the main elements. A detailed quantification of the elements that are detected in Fig. 5.3 is shown in Tab. 5.1. Ga and C traces result from the FIB sample preparation. Other samples exhibited similar structure and chemistry with similar traces of Hf, Al, As, which cannot be resolved in EDX maps due to their low concentration (at the detection limit), and Si, which concentrates on the top surface and in the YSZ phase. The stainless steel grid prevents the analysis of Fe and Cr that may be present in the sample.

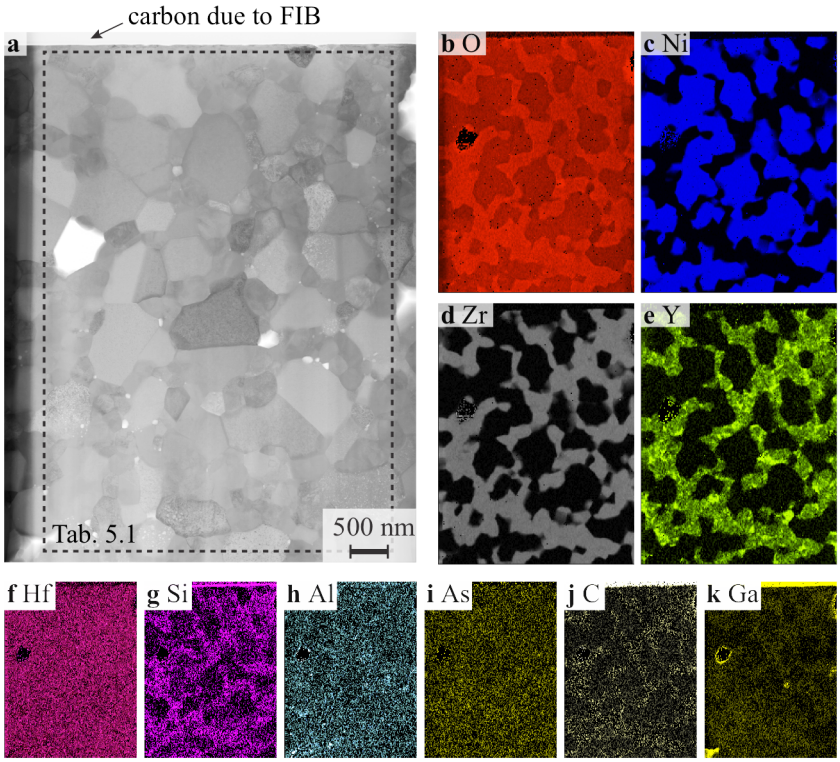

Figure 5.3 – Initial as-sintered NiO/YSZ structure. (a) STEM BF image along with corresponding quantitative STEM EDX elemental distribution mapping (deconvolved and background-subtracted, with contrast/brightness adapted for visibility), of the following peaks: (b) O Kα, (c) Ni Kα, (d) Zr Kα, (e) Y Kα, (f) Hf Lα, (g) Si Kα, (h) Al Kα, (i) As Kα (j) C Kα and (k) Ga Kα.

5.2.2 Structure and crystallography during NiO/YSZ reduction

A sequence of bright-field TEM images, which reveals the evolution of the microstructure in the specimen during *in situ* reduction, is shown in Fig. 5.4. Fig. 5.4a shows the as-sintered microstructure at 300 °C at the beginning of the 2 °C min^{-1} temperature

	O Kα	Ni Kα	Zr Kα	Y Kα	Hf Lα	Si Kα	Al Kα	As Kα	C Kα	Ga Kα
%wt	21.0	43.4	31.0	2.1	1.6	0.2	0.1	0.1	0.3	0.2
Error(3σ)	2.0	4.0	2.9	0.3	0.6	0.1	0.1	0.1	0.1	0.1

Table 5.1 – EDX quantification using Cliff-Lorimer factors of the sample shown in the region of interest dotted in Fig. 5.3.

ramp, with a processed Ni elemental map shown in the top right corner and a [012] diffraction pattern from one NiO grain (circled). The first changes in the images appear at 340/350 °C in the form of blurred white spots in the images (indicated by arrows in the inset shown in Fig. 5.4b). These are small voids, which form in the NiO grains at the interfaces with YSZ to accommodate the volume shrinkage that results from the reduction of NiO to Ni. In Fig. 5.4c, the voids grow and new ones form closer to the centres of NiO grains as the temperature increases (indicated by arrows). When the temperature reaches 430 °C, the NiO free surface is observed to reduce directly, and porosity forms uniformly across the NiO grains (Fig. 5.4d). Pores are observed at NiO/NiO grain boundaries only when the free surface reduction has started. At the end of the temperature ramp, coalescence of the porosity is observed (Fig. 5.4e).

Both the additional reflections and the satellite spots that are observed in the diffraction patterns in Fig. 5.4c, d and e indicate that the Ni grows coherently on its oxide and maintains the same crystallographic orientation after reduction. Ni reflections are observed within the selected area at ∼390 °C. The diffraction pattern acquired at 500 °C shows that NiO is still present in the grains, although the intensity of the NiO spots has decreased (Fig. 5.4e).

In addition, particles of only a few nanometres in diameter are observed in large numbers across and around Ni grains after reduction in STEM HAADF images (Fig. 5.5). STEM EELS of particles located away from the bulk Ni grains reveal that they contain Ni.

5.2.3 Energy-filtered imaging during NiO/YSZ reduction

Reaction kinetics

Fig. 5.6 shows a sequence of unfiltered BF TEM images acquired at different temperatures in 1.3 mbar of H_2 during reduction up to 604 °C, alongside corresponding t/λ and 3-window O K elemental maps (after normalisation using the intensity in the YSZ backbone). An EEL reference spectrum of one NiO grain acquired at 30 °C is shown in the top-right corner. As in Fig. 5.4, the first changes in NiO appear in the form of small voids at grain boundaries with the YSZ phase just below 350 °C (Fig. 5.6b). These voids are observed directly in the t/λ image (Fig. 5.6b.2) and correspond to regions depleted in O, i.e. dark regions in the O elemental map (Fig. 5.6b.3). New porous regions appear

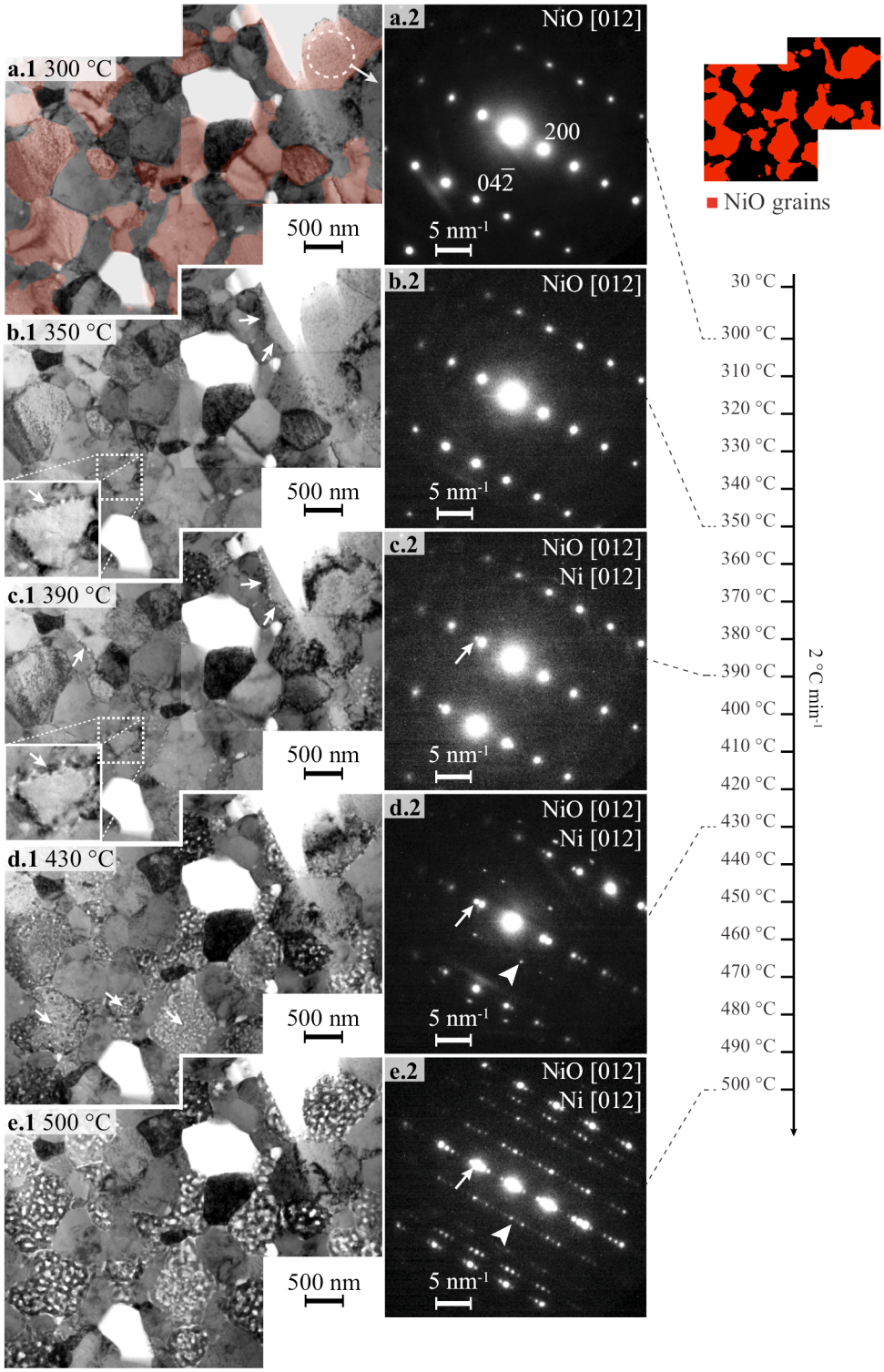

Figure 5.4 – (a-e) Stitching of 2 BF TEM images acquired during *in situ* reduction of a NiO/YSZ anode in 1.3 mbar of H_2 up to 500 °C. Corresponding diffraction patterns from the region circled in (a) are shown as insets, along with a processed Ni map obtained using EFTEM, which is coloured in red and superposed to (a.1). Arrows highlight voids in the images and Ni reflections in the diffraction patterns. Arrowheads show reflections resulting from double diffraction.

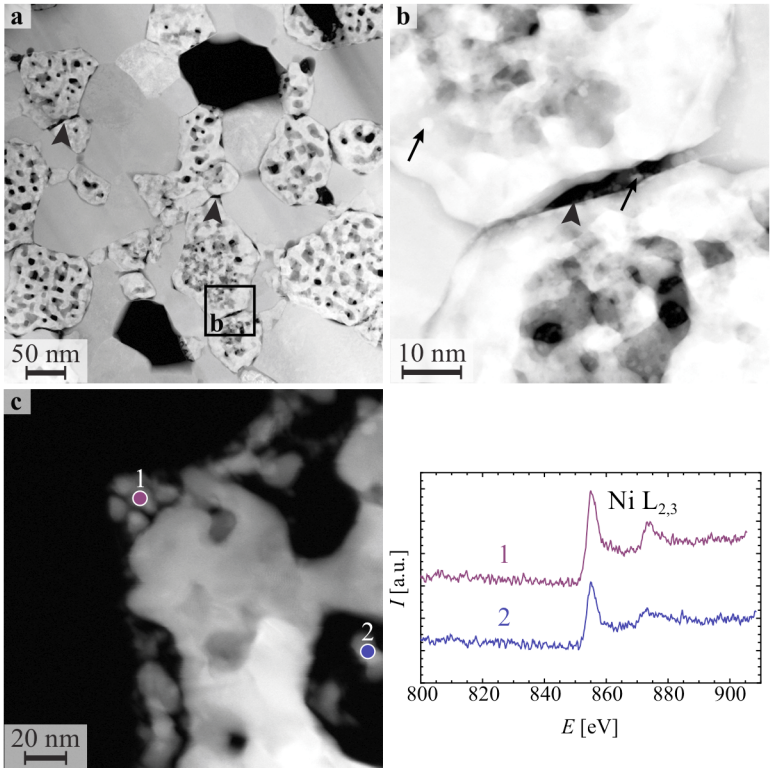

Figure 5.5 – (a-c) STEM HAADF images at various magnification acquired at 500 °C in 1.3 mbar of H_2 after the 2 °C min^{-1} heating ramp. Nanoparticles are arrowed in (b), while arrowheads indicate in (a) and (b) the presence of voids at Ni/Ni interfaces. (d) STEM EEL spectra of the nanoparticles labelled 1 and 2 in (c).

closer to the centres of the NiO grains as the temperature increases to 428 °C (Fig. 5.6c). Voids are observed over the entire Ni grains at 460 °C, with larger voids appearing at the initial positions of some NiO/NiO grain boundaries (arrowheads in Fig. 5.6d). Intragranular voids become larger as the temperature increases to 604 °C (Fig. 5.6e). Images acquired 130 minutes after reaching 604 °C reveal a coarser reduced Ni structure (Fig. 5.6f). An EEL spectrum of one Ni grain acquired just before the set of data shown in Fig. 5.6f demonstrates full reduction (bottom-right inset in Fig. 5.6).

Fig. 5.7a shows the full sequence of O K elemental maps acquired during reduction up to 604 °C. The chemical information at the position of each pixel evolves as a function of temperature and time. In order to obtain statistically relevant information, groups of NiO pixels that exhibit the same structural features (interfaces with YSZ or bulk material) are selected by masking the map accordingly. Due to noise, averaging intensities over a large number of pixels is indeed essential to yield reliable data. Using the Ni $L_{2,3}$ elemental map, 9 different Ni regions are identified. In each of these 9 Ni regions, the average intensity $\bar{I}_O(T)$ is measured in 4 different areas taken by the masks M_1 to M_4, which were chosen to progressively select the entire Ni regions starting at the

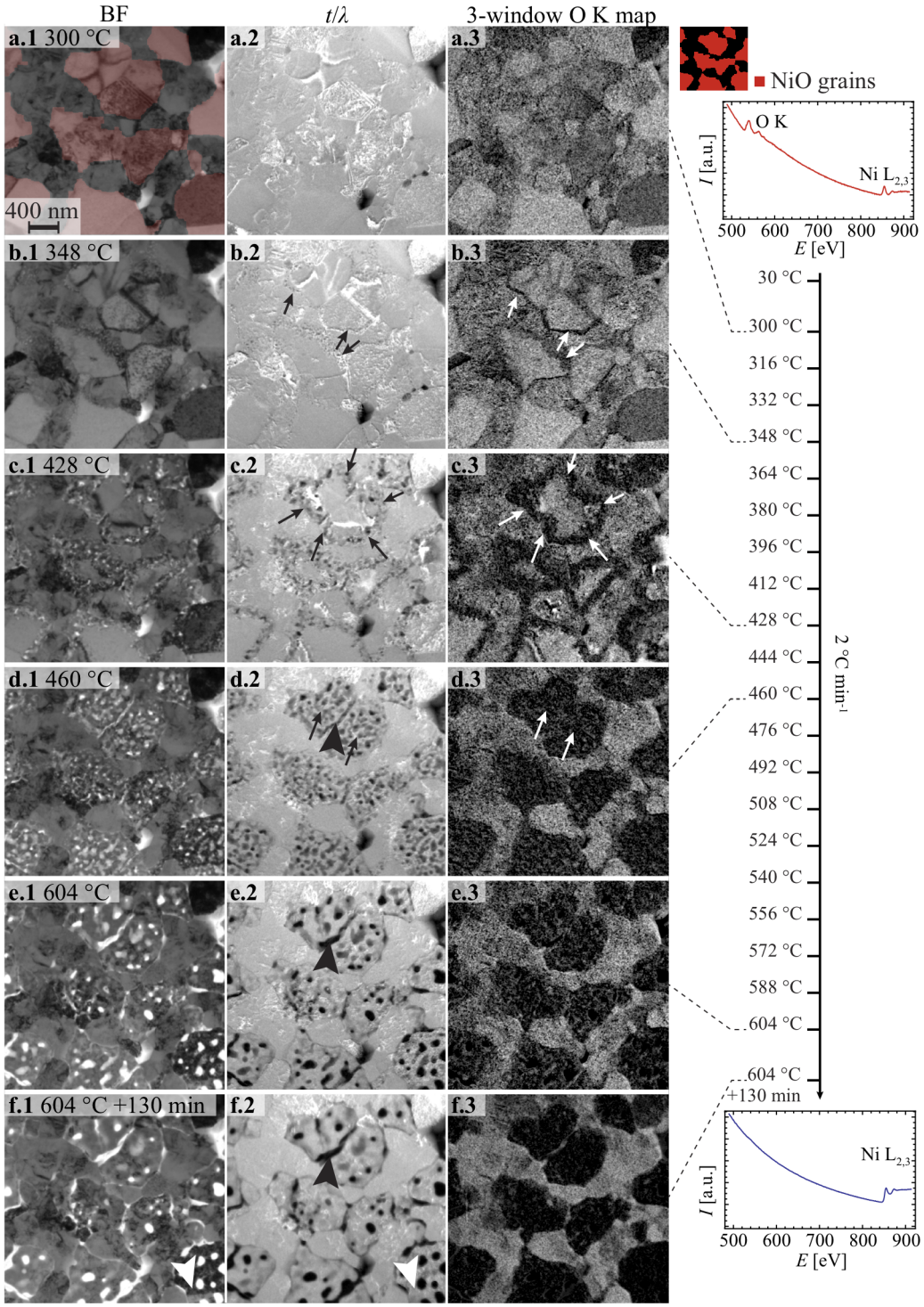

Figure 5.6 – (a-e) Selection of (1) BF TEM images, (2) t/λ and (3) oxygen maps acquired during ramping at 2 °C min^{-1} in 1.3 mbar of H_2. A red Ni EFTEM map is superimposed to (a.1). The images in (f) were acquired 130 minutes after reaching 604 °C (full reduction confirmed by EELS, bottom-right spectrum). Arrows indicate voids in NiO at interfaces with YSZ in (b-c) and in the center of grains in (d). Black arrowheads show pores at the position of some initial NiO/NiO boundaries. White arrowheads show remaining Ni/Ni boundaries in (f).

interfaces with YSZ. These average values $\bar{I}_{O}(T)$ measured for each temperature T are then normalised using the corresponding average value $\bar{I}_{O_{NiO}}$ and $\bar{I}_{O_{Ni}}$ measured in the NiO and Ni reference images, respectively, to yield the conversion fraction α of the reduction reaction as a function of temperature (Fig. 5.7b).

Out of the 9 Ni regions identified in the micrographs, only regions labelled 1 and 2 are entirely within the field of view. In the mask including Ni close to the interfaces with YSZ in the regions 1 and 2 (top mask M_1 in Fig. 5.7b), α is observed to gradually increase over a temperature range of 100 °C (348 °C to 444 °C). On the other hand, two rate-controlling mechanisms are observed to occur in succession when full Ni regions are analysed (bottom mask M_4 in Fig. 5.7b). Indeed, α in the region M_4 increases by a few percent from 348 °C to 412 °C due to the reaction at the interfaces with YSZ and then quickly up to 90% from 412 °C to 444 °C, as a result of free surface reduction (arrowheads in Fig. 5.7a). Above 444 °C, α appears identical for the 4 different masks, demonstrating a homogeneous reaction of the Ni regions. A fraction of ∼10% of NiO is left unreduced at the end of the heating ramp, which is consistent with previous *in situ* XRD and EELS experiments assessing the reduction of NiO particles in Chap. 3. While measurements of the reaction kinetics in regions 3 to 9 must be interpreted carefully since these do not contain entire NiO regions, similar trends are observed. The decrease in α measured at 556 °C is due to drift during acquisition (arrowheads in Fig. 5.7b). Bend contours (diffraction) also induce an artificial decrease of α (arrows in Fig. 5.7b).

The artefacts induced by diffraction are limited when using O K jump-ratios instead of 3-window elemental maps (Fig. 5.8a). However, obtaining a jump-ratio involves a division that in turn induces pixels with intensities not related to changes in chemistry and these must be removed to infer reliable reaction kinetics results (Fig. 5.8b). The same procedure as the one employed to yield spatially-localised reaction kinetics from 3-window O K elemental maps is then employed. The same masks M_1 to M_4 are used to select different regions of the jump-ratios and the average intensity in these regions is measured as a function of temperature (excluding pixels with a value of 0 from the measurements). Using Eq. 2.11 with intensities $\bar{I}_{O}(T)$, $\bar{I}_{O_{NiO}}$ and $\bar{I}_{O_{Ni}}$ obtained from jump-ratios instead of 3-window elemental maps, the reaction kinetics are obtained within the regions M_1 to M_4 (Fig. 5.8c)

Similarly to the measurements inferred from the O K elemental images, the jump-ratio results show that the reaction starts at the interfaces with YSZ at ∼348 °C. In the masks encompassing the Ni regions close to the interfaces with YSZ (top mask M_1 in Fig. 5.8c), α increases regularly up to a value of 0.9 at 444 °C. In the masks incorporating the entire Ni regions (bottom mask M_4 in Fig. 5.8c), the reaction rate increases at 412 °C as a result of NiO free surface reduction. Similarly to Fig. 5.7b and Chap. 3, α is observed in Fig. 5.8c to stabilise at a value of ∼0.8-0.9 above 444 °C.

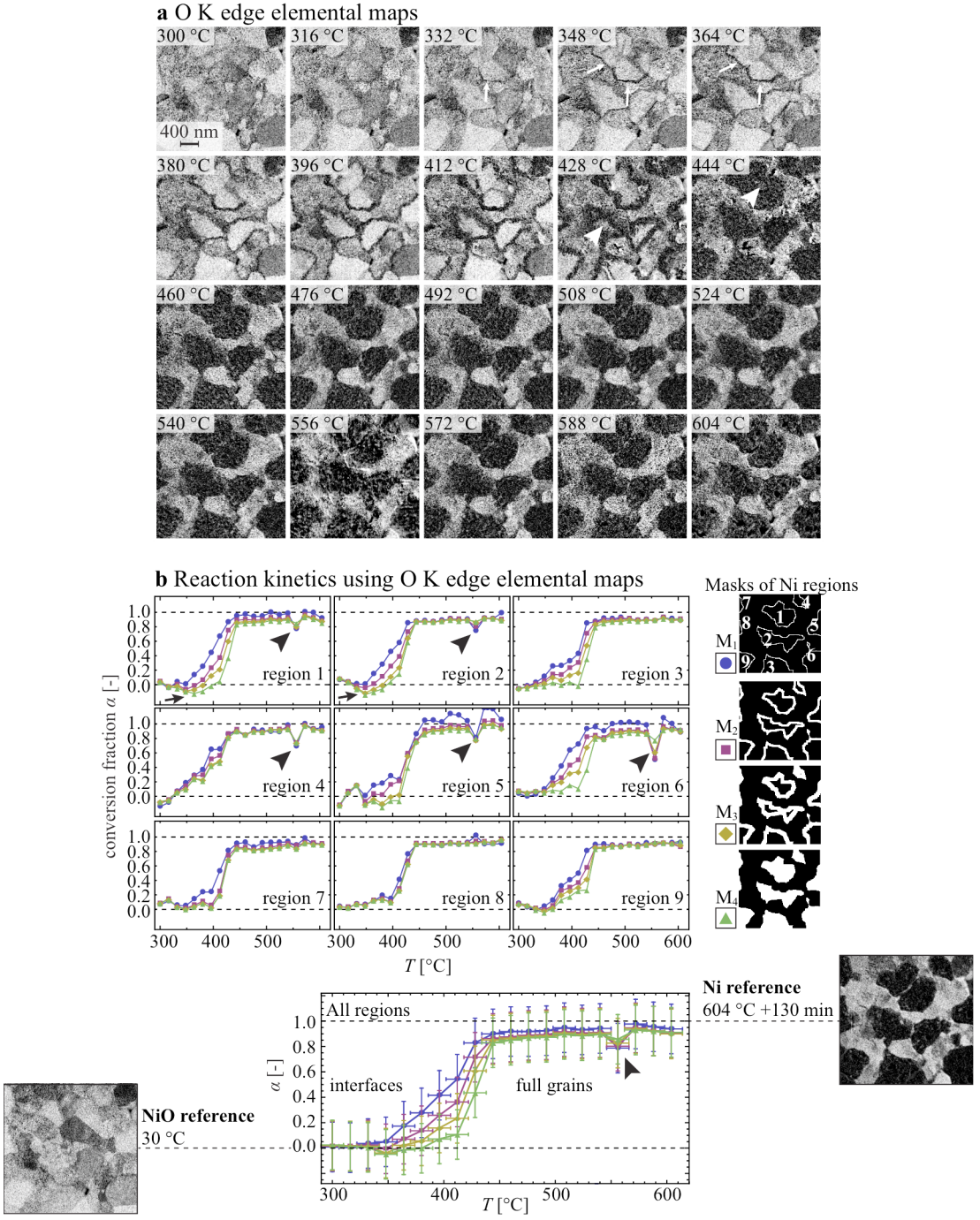

Figure 5.7 – (a) O K elemental maps during reduction (after normalisation using the intensity in the YSZ phase). For each Ni region identified in the Ni $L_{2,3}$ map, the average intensity in 4 different masks starting at the YSZ interfaces (M_1), progressively selecting the entire Ni regions (to M_4), was normalised using the NiO and Ni experimental references to yield in (b) the conversion fraction $\alpha(T)$ of the reduction reaction in each Ni region M_1 to M_4. The uncertainties in the determination of α are obtained using the statistical deviation when the sample is unreduced (3σ), while the horizontal uncertainties are estimated to be ±10 °C.

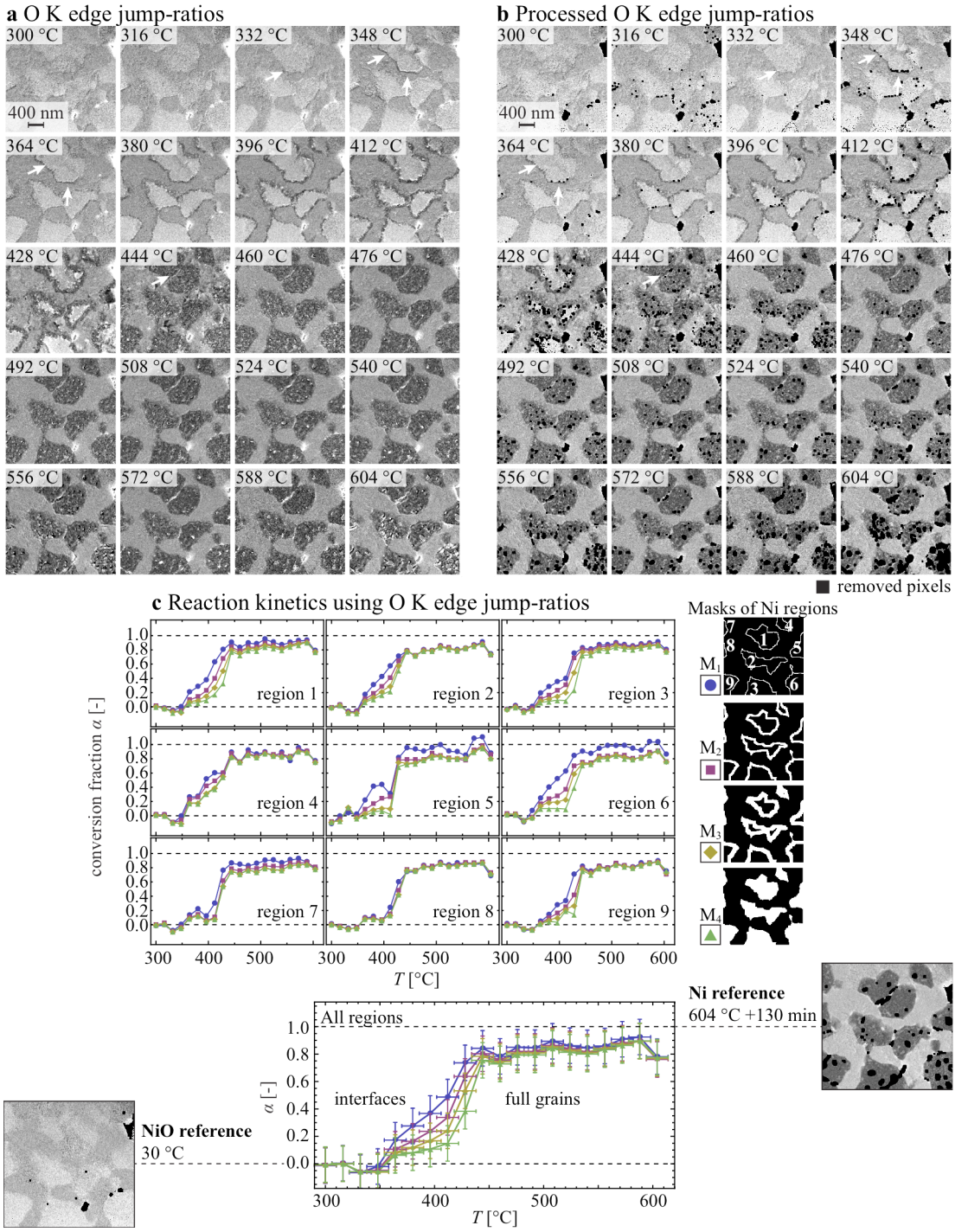

Figure 5.8 – (a) O K jump-ratios during reduction (after normalisation using the intensity in the YSZ phase). (b) Processed O K jump-ratios after removal of pixels corresponding to holes and with high intensities. The average intensity in the Ni regions is measured using 4 different masks (M_1 to M_4), which progressively select the Ni phase starting at the interfaces with YSZ. These values are normalised using the average values measured in the corresponding regions of the NiO and Ni experimental references to yield in (c) the reaction kinetics $\alpha(T)$ in each Ni region. The uncertainties are obtained as in Fig. 5.7.

Volume shrinkage

Fig. 5.9 shows the volume shrinkage induced by NiO reduction to Ni. The intensity in the NiO phase of the initial t/λ image is compared to the intensity in the Ni regions of the final t/λ image after multiplication by λ_{NiO} and λ_{Ni}, respectively (collection semi-angle of 6.8 mrad). An overall volume shrinkage of -41% is measured here, which is consistent with theoretical predictions of -41.6% [9]. The volume shrinkage measured in each Ni region varies from -36% to -46% due to diffraction contrast.

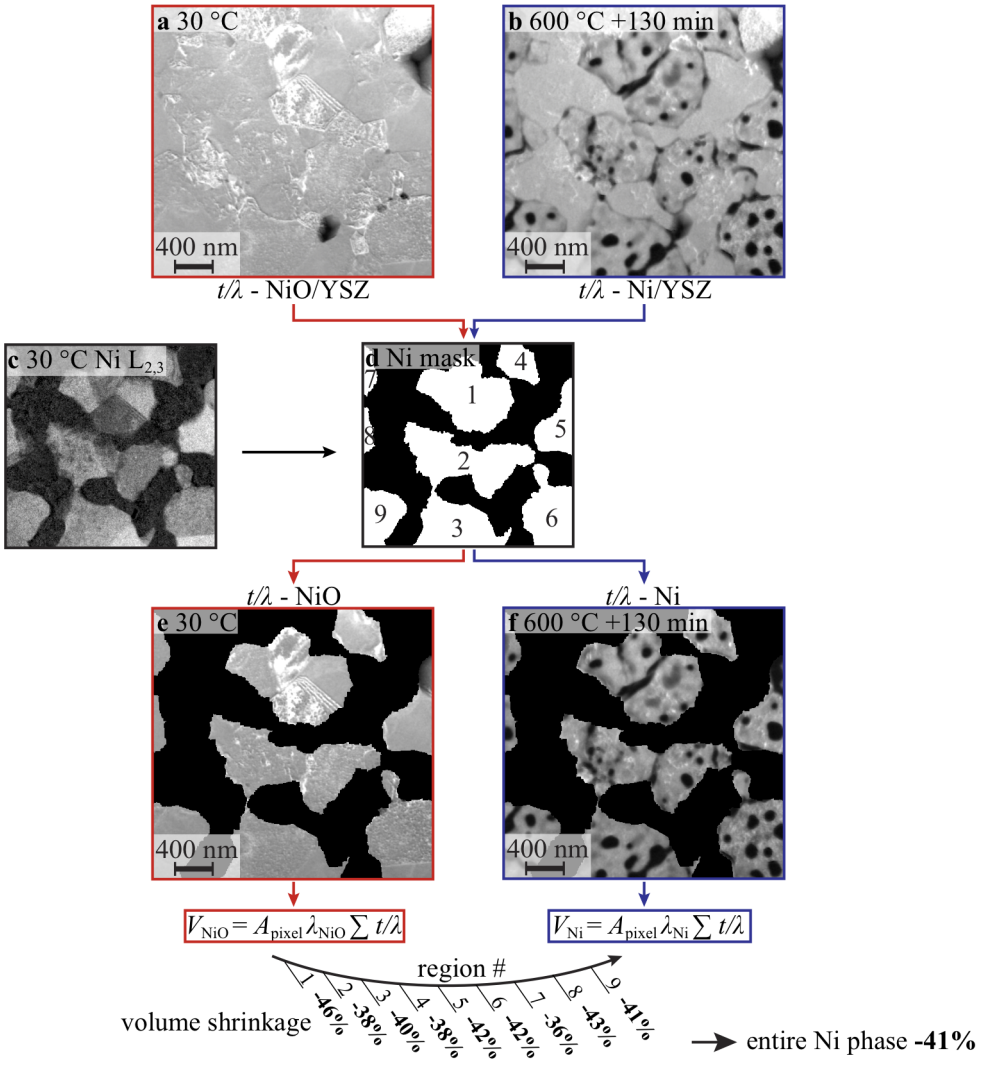

Figure 5.9 – Measurement of volume shrinkage. (a) Initial t/λ image of NiO/YSZ. (b) Final t/λ image of Ni/YSZ (reduction confirmed by EELS in Fig. 5.6), (c) Ni $L_{2,3}$ elemental map to infer (d), a mask of the Ni phase with 9 Ni regions labelled. (d) is used to segment (a) and (b) to yield (e) and (f), the NiO and Ni phase before and after reduction, respectively. From (e) and (f) and using λ_{NiO} and λ_{Ni} (155 and 127 nm, respectively), the volume shrinkage is obtained.

Reaction front dynamics along x,y and z directions

The dynamics in 3D of the reduction reaction can be assessed by combining reaction kinetics and volume shrinkage measurements. Indeed, the reaction is observed to start from specific Ni regions of the specimen, i.e. Ni regions located at the interfaces with YSZ, and proceeds towards the centres of the Ni regions with a reaction front that appears well defined in projection. The speed of this reaction front in the x,y plane can be compared to the speed at which the thickness of the sample is reducing (along the z direction). These measurements allow the assessment of whether the reaction proceeds with different mechanisms along the x,y and z directions. The analysis is detailed here using 3-window O K elemental maps for regions labelled 1 and 2.

The procedure to measure the position of the reaction front projected on the x,y plane (specimen plane) is explained in Fig. 5.10. It involves the measurement of the average intensity $\bar{I}_{\mathrm{O}}(T)$ in 3-window elemental maps in pixels that are equidistant from the interfaces with YSZ (Fig. 5.10b). In other words, $\bar{I}_{\mathrm{O}}(T)$ is measured in successive 1-pixel wide regions M_i^* that, starting at the interfaces with YSZ, progressively decrease in size until reaching the center of the NiO region. The kinetics $\alpha(T)$ in each M_i^* is obtained using Eq. 2.11 by scaling the values of $\bar{I}_{\mathrm{O}}(T)$ using the reference average intensities $\bar{I}_{\mathrm{O_{NiO}}}$ and $\bar{I}_{\mathrm{O_{Ni}}}$ obtained when fully oxidised and fully reduced (Fig. 5.10c).

As these regions M_i^* are composed of a small number of pixels (140-1000), diffraction effects and noise are significant. Noise is reduced by applying a Gaussian filter to each $\alpha(T)$ sequence. Diffraction contrast is mostly observed in the NiO phase, i.e. when α should be 0 but is actually negative (Fig. 5.10c). To correct this issue and yield comparable results, $\alpha(T)$ measurements are rescaled from 0 to 1 in each region M_i^* using the minimum value of α that is measured in the sequence to yield $\alpha^\bullet(T)$ (Fig. 5.10d). In turn, the positive values $\alpha^\bullet$ that are measured until $\alpha^\bullet = 0$ are set to 0 to yield $\alpha^*(T)$, an interpretable estimate of the kinetics (Fig. 5.10e).

Using $\alpha^*(T)$ measurements, the projected position of the reaction front $w(T)$ is then estimated by determining for each temperature the smallest distance l with respect to the YSZ interfaces that encompasses all the regions that contain at least 10% of Ni (Fig. 5.10f). The values of $w(T)$ estimated automatically from this procedure are coherent with periodic measurements done directly on 3-window maps.

To assess the speed of the reaction front propagating along the z axis, i.e. along the thickness of the sample, the average intensity $\overline{t/\lambda}(T)$ is obtained from t/λ images in the same M_i^* regions that were used to infer $\alpha^*(T)$ (Fig. 5.11). $\alpha^*(T)$ is inserted in Eqs. 5.1-5.3 to yield estimates of total, Ni and NiO thicknesses ($t(T)$, $t_{\mathrm{Ni}}(T)$ and $t_{\mathrm{NiO}}(T)$, respectively). Assuming the YSZ/Ni/NiO geometry shown in Fig. 5.11e, an estimate of the depth $d(T)$ of the NiO/Ni reaction front is obtained by subtracting half of the remaining NiO thickness at a temperature T to the initial total half thickness (Fig. 5.11f).

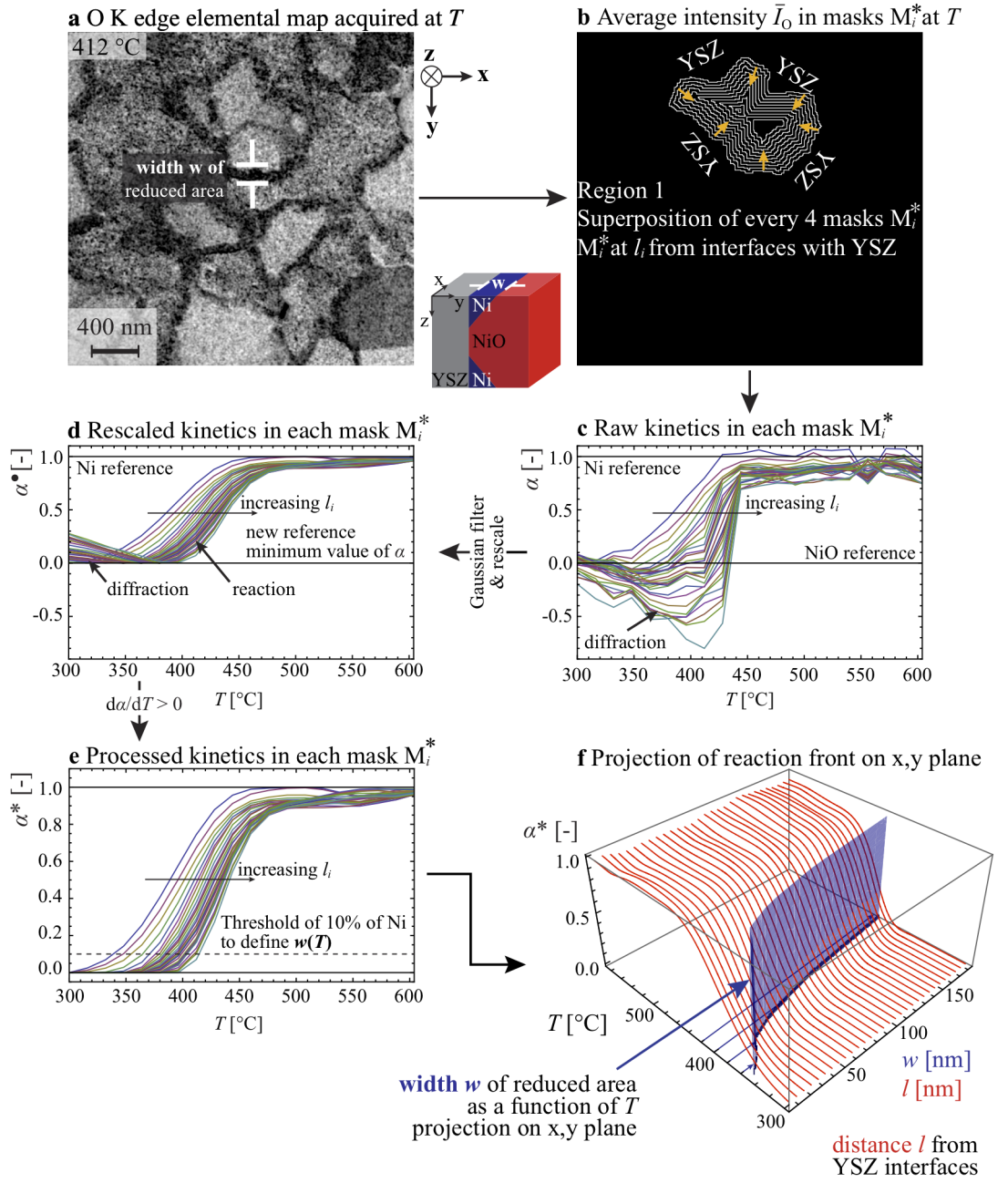

Figure 5.10 – Procedure to yield the reaction width $w(T)$ (shown for region 1). (a) Using 3-window elemental maps acquired at T, (b) the average intensity $\bar{I}_O(T)$ is measured in a series of masks M_i^*, which successively select pixels that are equidistant from the interfaces with YSZ. Using the average intensities $\bar{I}_{NiO}$ and $\bar{I}_{Ni}$ measured when the sample is fully oxidised and fully reduced, respectively, the reaction kinetics $\alpha(T)$ in each region M_i^* is obtained. Due to diffraction effects, $\alpha(T)$ raw data (c) is rescaled in (d) using the minimum value of α measured within M_i^* and a Gaussian filter is applied to reduce noise and yield $\alpha^\bullet$. (e) Values of $\alpha^\bullet$ that are not representative of the reaction kinetics before the reaction onset are set 0 to obtain $\alpha^*(T)$. Based on (e), the width $w(T)$ (x,y plane) of the reaction front is obtained by determining the smallest distance l measured from the interfaces with YSZ, which encompasses all M_i^* where $\alpha^* \geq 0.1$.

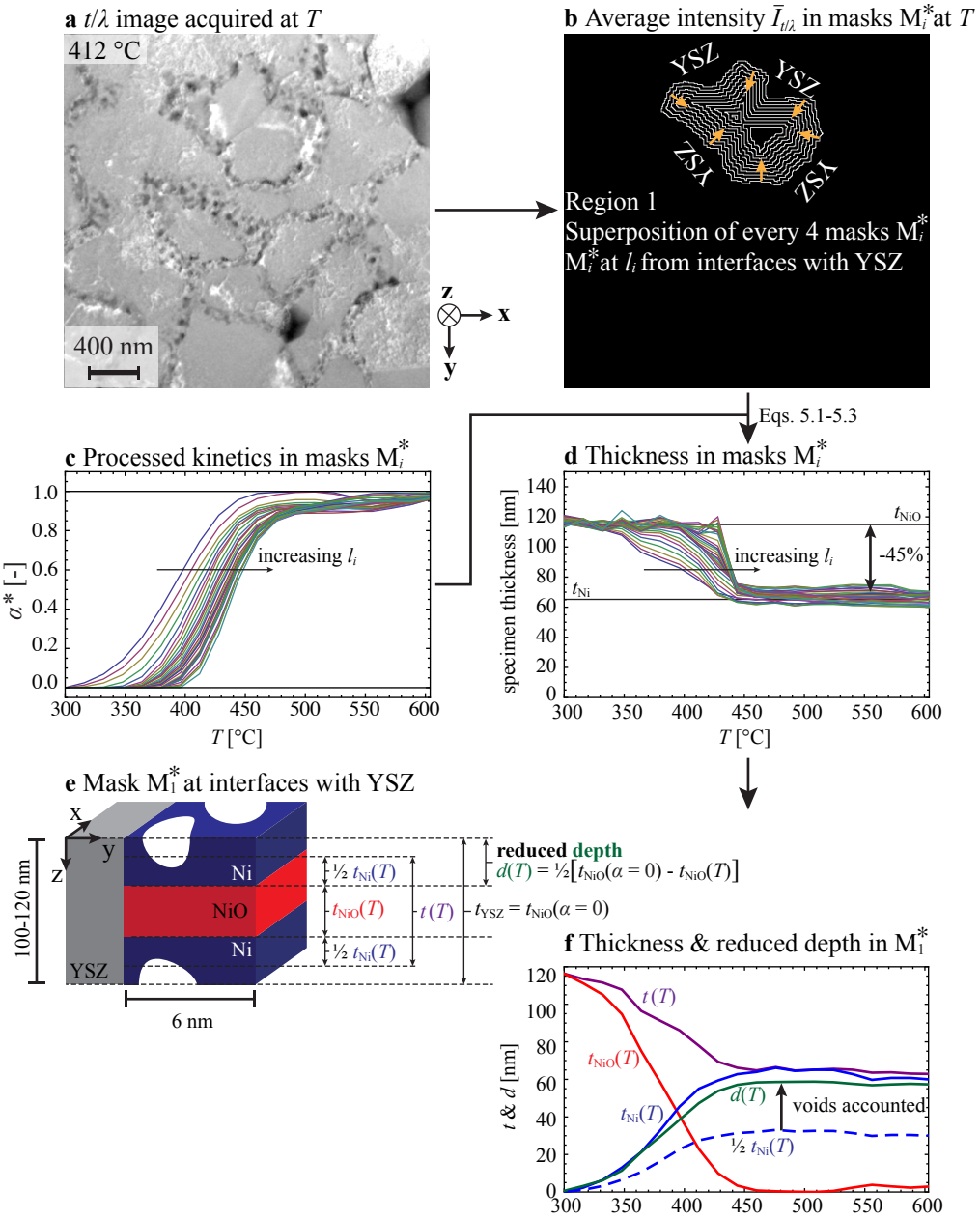

Figure 5.11 – Procedure to yield the reaction front along the z direction (shown for region 1). (a) Using t/λ maps acquired at T, (b) the average intensity $t/\lambda(T)$ is measured in a series of 1-pixel wide masks M_i^*, which successively select pixels that are equidistant from the interfaces with YSZ. Using (c) the reaction kinetics $\alpha^*(T)$ measured within each region M_i^* obtained in Fig. 5.10e and the average intensities $t/\lambda(T)$ obtained in (b), the evolution of total thickness in each region M_i^* is estimated in (d) using Eqs. 5.1-5.3. Assuming a planar NiO/Ni reaction front in the first mask M_1^* located at the interfaces with YSZ as shown in (e), the evolution of total, NiO and Ni thicknesses ($t(T)$, $t_{NiO}(T)$, $t_{Ni}(T)$), as well as of the reaction depth $d(T)$ can be estimated in (f).

The estimate of the NiO/Ni reaction front position projected on the x,y plane $w(T)$ (Fig. 5.10) and along the z axis $d(T)$ (Fig. 5.11) are then plotted in Fig. 5.12. The results are shown here for the regions labelled 1 and 2. $d(T)$ instead of $\frac{1}{2}t_{\mathrm{Ni}}$ is compared to $w(t)$ as both reduced regions defined by $d(T)$ and $w(T)$ include reduction-induced voids. Fig. 5.12 demonstrates that the reaction rate is anisotropic, i.e. the reaction proceeds faster along the x,y plane than along the z direction.

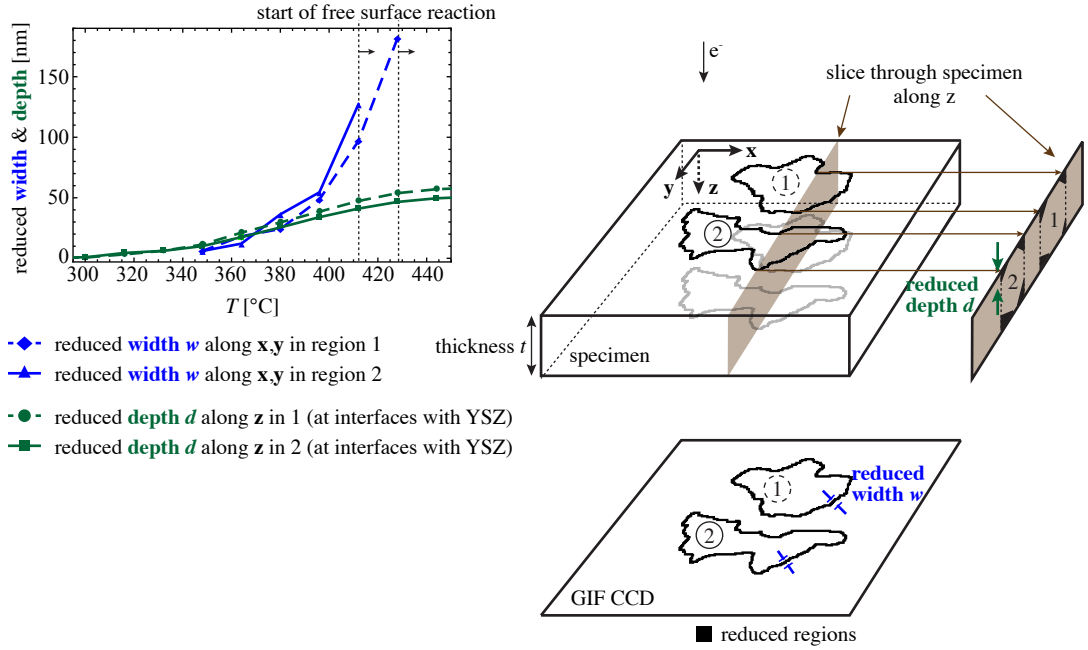

Figure 5.12 – Comparison of the position of the NiO/Ni reaction front projected on the x,y plane $w(T)$ and along the z axis $d(T)$ in regions labelled 1 and 2. $w(T)$ and $d(T)$ are inferred from Figs. 5.10 and 5.11, respectively.

Post-exposure chemical characterisation

Fig. 5.13 shows a post-exposure EDX chemical mapping of the TEM lamella reduced in the ETEM. The results demonstrate that Al, As and Si, which were initially detected in the specimen prior to reduction (Fig. 5.3, Tab. 5.1), segregate at Ni interfaces as arrowed. Traces of K, an element not detected before reduction, also appear to concentrate at some interfaces after reduction.

In Fig. 5.14a and b, a larger magnification quantitative STEM EDX analysis details a film rich in O, Al and Si but also containing K, As and maybe S, which formed at the position of an initial NiO/NiO grain boundary. In addition, this film supports Ni nanoparticles that are similar to those observed in STEM HAADF images in Fig. 5.5. Through qualitative STEM EDX maps, Ga traces that result from the FIB preparation process are observed to form oxidised islands (most likely on the Ni surface).

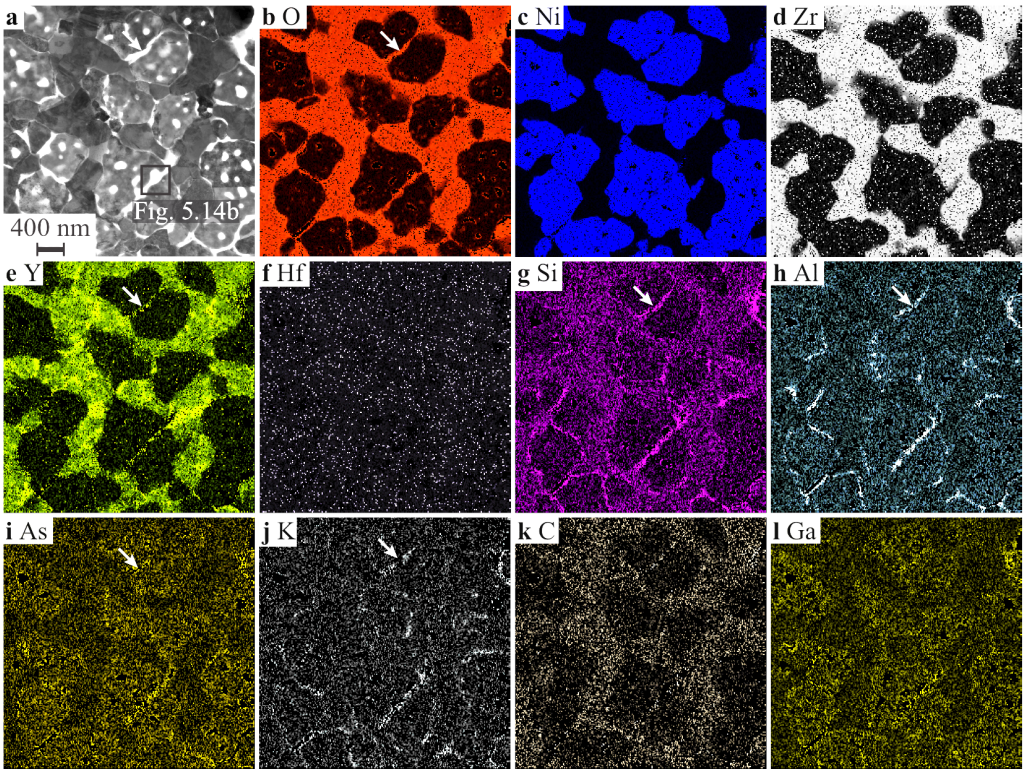

Figure 5.13 – (a) STEM BF image of the Ni/YSZ structure structure after reduction up 600 °C along with corresponding quantitative STEM EDX elemental distribution mapping (deconvolved and background-subtracted, with contrast/brightness adapted for visibility): (b) O Kα, (c) Ni Kα, (d) Zr Kα, (e) Y Kα, (f) Hf Lα, (g) Si Kα, (h) Al Kα, (i) As Kα, (j) K Kα, (k) C Kα and (l) Ga Kα.

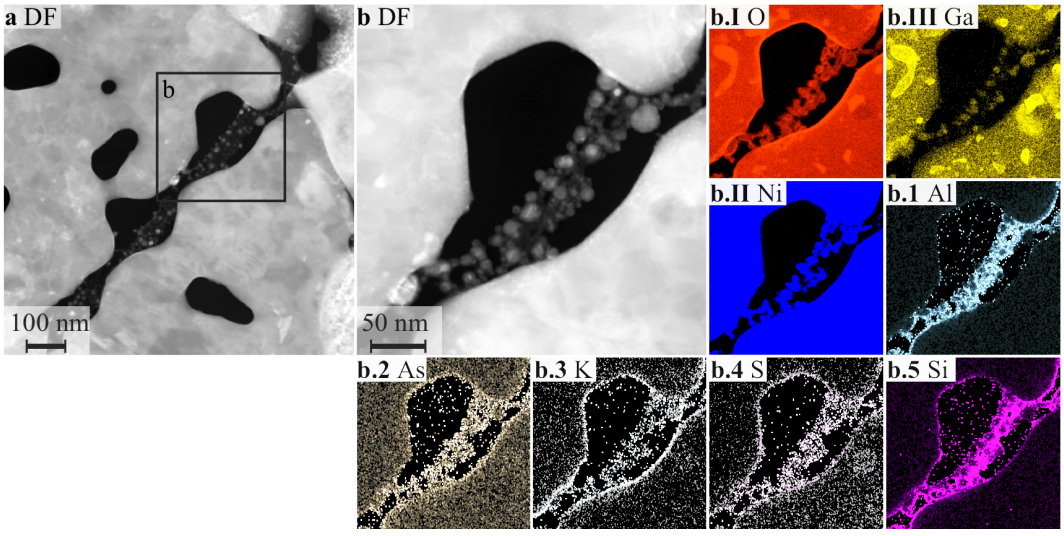

Figure 5.14 – (a-b) DF images of the Ni/YSZ structure structure after reduction up 600 °C, with (b.I-III) STEM EDX (intensity related to raw X-ray counts) maps of O Kα, Ni Kα and Ga Kα (X-ray counts) and (b.1-5) quantitative STEM EDX elemental distribution mapping (deconvolved and background-subtracted, contrast/brightness adapted) of Al Kα, As Kα, K Kα, S Kα, Si Kα.

Post-exposure automated crystal orientation mapping

During the heating ramp, voids appear at the position of some initial NiO/NiO grain boundaries (arrowheads in Fig. 5.15a-b), while contact is maintained between other neighbouring Ni grains throughout the reaction (arrows in Fig. 5.15a-b), denoting different grain boundary characteristics. In addition, some contrast features are present in BF images within seemingly monocrystalline Ni grains at high temperature (inset in Fig. 5.15b). These two crystallographic-related features are assessed here using automatic crystal orientation mapping in the TEM.

The phase and the orientation maps of the area that was investigated in the ETEM during reduction are shown in Fig. 5.15c-d, respectively, with both maps superimposed with a reliability image. The grain boundaries 1 and 2 (Fig. 5.15d), which label two grain boundaries where Ni/Ni contact is maintained throughout reduction, exhibit a specific disorientation of 60° (Fig. 5.15e). Alternatively, labels 3 to 5 mark voids that appeared during reduction at the interfaces between two Ni/Ni grains, with these measured to be disoriented by 25-50° and hence not related by any specific orientation relationship.

In both grain boundaries 1 and 2, the pole figure of the (111) planes demonstrate that one set of those planes is common to the two Ni grains (circled in Fig. 5.15f). Moreover, the projection of the normal to the common (111) planes (arrow in Fig. 5.15f) coincides with the line perpendicular to the projected interface (line in Fig. 5.15f). While a crystal orientation map acquired at a different tilt angle would verify in 3D the coincidence between the common (111) planes and the interface plane, the grain boundaries 1 and 2 are likely to be coherent twin boundaries. Indeed, these have the required characteristics: the disorientation between the two neighbouring Ni grains corresponds to a rotation of 60° about the normal to the common (111) planes and the interface plane coincides with the common (111) planes [265–267]. Throughout reaction, contact between Ni grains is hence maintained across coherent twin boundaries but lost across incoherent interfaces.

A careful investigation of the reduced structure observed at room temperature in high vacuum conditions (Fig. 5.16a) reveals similar features to these observed at 604 °C in 1.3 mbar of H_2 (inset of Fig. 5.15b). These nm-sized features exhibit characteristic shapes in STEM BF and DF images (Fig. 5.16b-c), which can be identified in the orientation map shown in Fig 5.16e. The disorientation along a line that runs perpendicular to the interface between those local features and the Ni grain is measured to correspond to $\sim$60° (Fig. 5.16f). The pole figure shown in Fig. 5.16g demonstrates that (111) appears to be the common set of planes across the boundary and, if the small angle mismatch is ignored, the projection of this common set of planes appears to coincide with the projection of the grain boundary plane. It thus appears likely that the contrast features observed in Figs. 5.15b and 5.16b-c are coherent twinned domains, which formed during the reduction process within larger Ni grains.

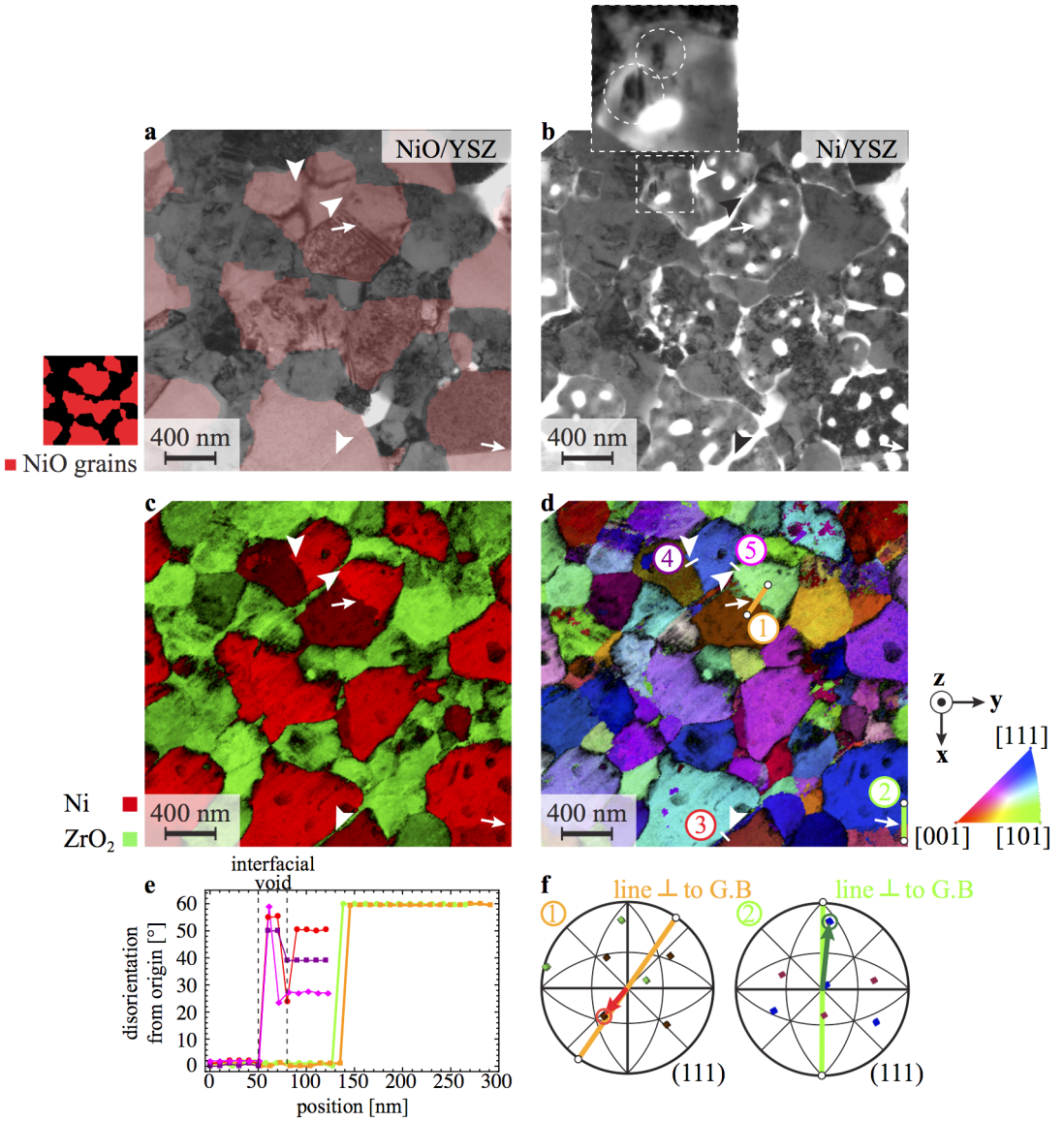

Figure 5.15 – (a) Initial TEM BF image of the as-sintered NiO/YSZ microstructure acquired at 30 °C before reduction, with arrows and arrowheads marking different grain boundaries. A Ni elemental map is shown. (b) TEM BF image of the reduced Ni/YSZ microstructure acquired at 604 °C, 130 min after the end of the 2 °C min^{-1} heating ramp, with arrows marking grain boundaries with 2 Ni grains still in contact and arrowheads marking voids at the position of some initial NiO/NiO grain boundaries. A region that exhibits dark contrast features within one reduced Ni grain is shown as in inset in (b). Using the ASTAR system, the following maps are obtained: (c) phase map of Ni and ZrO_2 superimposed with a reliability image of the Ni/YSZ and (d) orientation map of Ni and ZrO_2 superimposed with the reliability image, where 5 grain boundaries are labelled. (e) Plot showing the disorientation with respect to the initial orientation across the 5 grain boundaries. (f) Pole figures showing the (111) planes of the Ni grains across boundaries 1 and 2 with the common planes circled. The line along which (e) is plotted is shown in (f) and it coincides with the projection of the normal to the common (111) planes (arrow), showing that 1 and 2 are coherent twin boundaries (symmetry maintained during reduction).

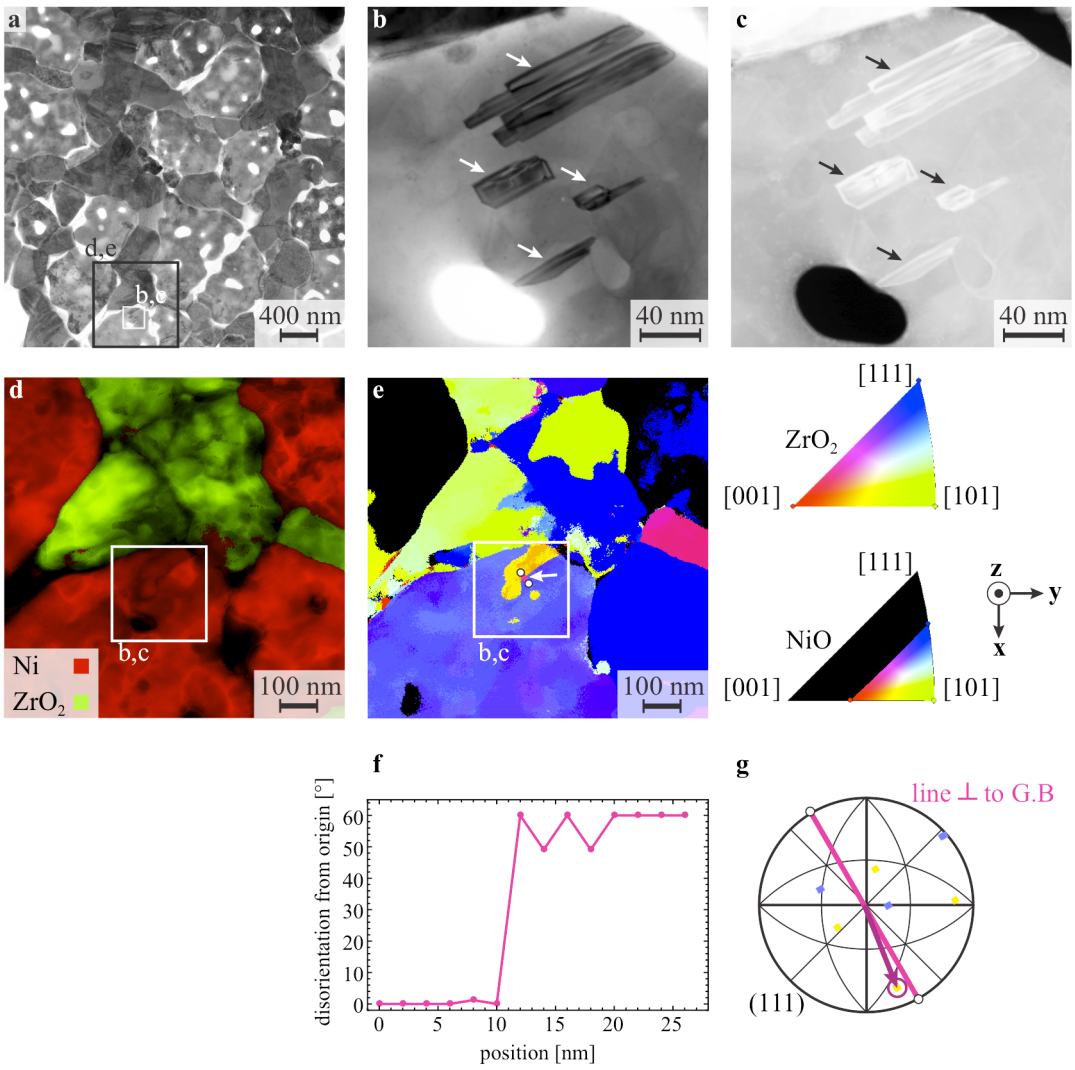

Figure 5.16 – (a) STEM BF image of the reduced Ni/YSZ structure acquired at room temperature in high vacuum conditions. (b) STEM BF image showing contrast features in Ni (arrowed), with (c) the corresponding STEM DF image. (d) Phase map superimposed with the reliability image of a region that encompasses (b) and (c), with (e) the corresponding orientation map. The largest features observed in (b) and (c) appear in orange in (e). The grain boundary that separates these features from the bulk is arrowed. The disorientation along a line perpendicular to this boundary is plotted in (f), while the corresponding pole figure is shown in (g). From (f) and (g), these features arrowed in (b,c) are most likely coherent twinned domains with respect to the Ni grain.

Post-exposure STEM HAADF tomography

The 3D structure of the Ni/YSZ sample is investigated using STEM HAADF tomography (Fig 5.17). While difficult to notice in 2D projected (S)TEM images, voids can be observed at the Ni/YSZ interfaces after reduction up to 600 °C (black arrowheads in Fig. 5.17b-c). These voids appear when the temperature reaches 600 °C. The surface of the NiO grains now appears irregular as a result of both the reduction process and Ni sintering/coarsening at high temperature.

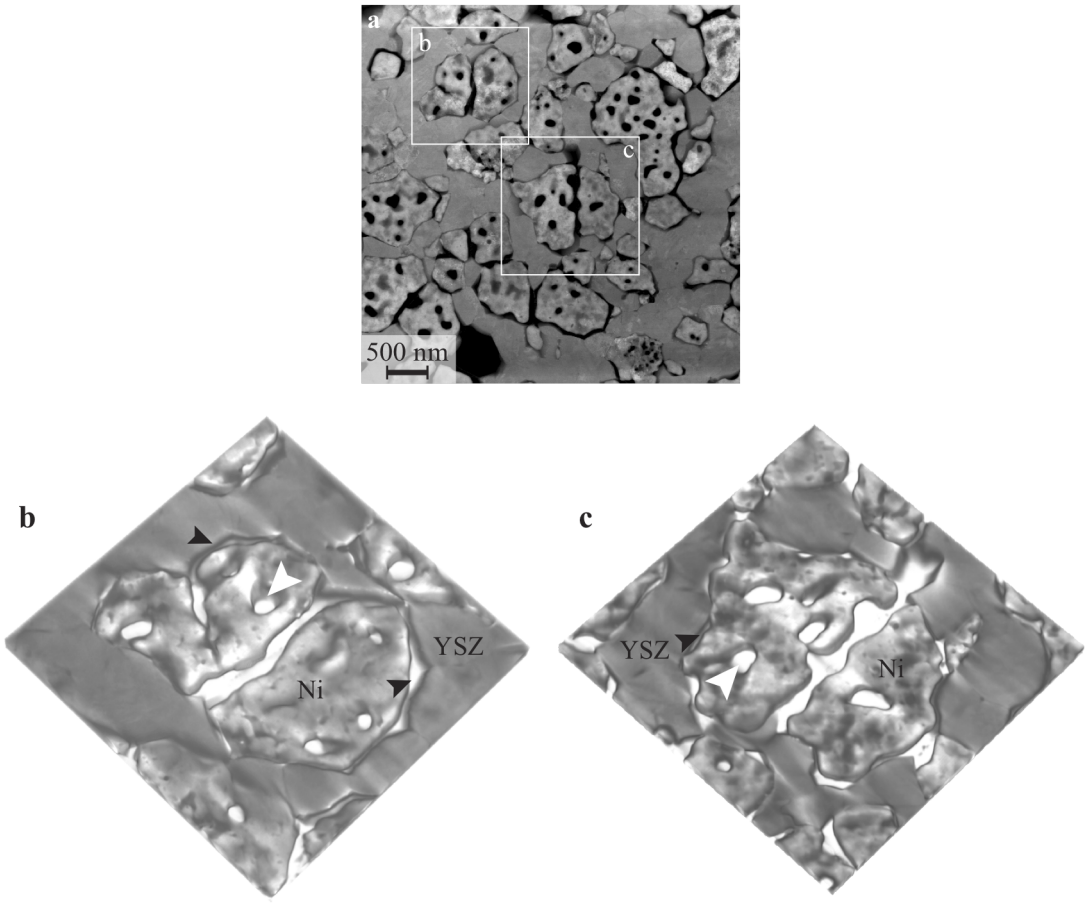

Figure 5.17 – STEM HAADF tomograms. From tilt series acquired from -65° to +65° with steps of 1°, two regions are reconstructed in (b) and (c) using the SIRT algorithm (40 iterations, shown as a solid representation), with (b) corresponding to the region of interest labelled 1 in Figs. 5.8-5.9. Black arrowheads highlight voids at Ni/YSZ interfaces, white arrowheads intragranular voids in Ni.

5.2.4 Additional *in situ* reduction experiments

BF TEM micrographs of the H-bar sample reduced at 2 °C min^{-1} up to 700 °C in the ETEM are shown in Fig. 5.18. The first changes in the microstructure are observed at 412-428 °C. The initiation of the reduction appears at higher temperature and is more complex here when compared to Figs. 5.4 and 5.6, which detailed the reduction of TEM lamellae welded onto stainless steel grids. Voids are observed here to form uniformly within some NiO regions (white arrows in Fig. 5.18b and c), while the reaction appears to activate at the interfaces with YSZ elsewhere (black arrow in Fig. 5.18b). At temperatures of ∼444 °C (Fig. 5.18c), the reaction is observed to proceed through the formation of new voids towards the center of some NiO grains, with these voids originating either from the interfaces with YSZ or from the boundaries with Ni grains that started reducing at a lower temperature (arrows). Black arrowheads mark the appearance of voids at the initial position of both NiO/NiO and NiO/YSZ grain boundaries at 460 °C (Fig. 5.18d), which eventually increase in size as the temperature increases regularly to 700 °C (Fig. 5.18g). Voids become larger in size but smaller in number as the temperature is maintained at 700 °C during 134 additional minutes (arrowhead in Fig. 5.18h). The Ni region circled in Fig. 5.18a and h exhibits a different void structure at the end of the experiment when compared to other areas (Fig. 5.18b). Fig. 5.18i shows the superposition of two diffraction patterns obtained from the same Ni grain, where the SADP in red acquired at 30 °C (NiO [110] zone axis) is coherent with the SADP in black obtained after the reduction experiment (Ni [110] with faint NiO reflections along the same [110] zone axis, which leads to satellite spots).

When the heating rate is increased to 4 °C min^{-1} (Fig. 5.19), reduction proceeds directly through the reaction of the free surface at 497 °C without first activating at the interfaces with YSZ (Fig. 5.19c). Some YSZ is redeposited at the edges of initial holes due to FIB sample preparation (arrowheads) and forms a thin layer that does not react during reduction (Fig. 5.19d-f). Most of the intragranular voids formed during reduction disappear when the temperature reaches 850 °C (Fig. 5.19f). Micrographs and diffraction patterns of the reference H-bar, which was not observed during reduction at high temperature, are shown in Fig. 5.19R. These highlight similar Ni structures to those observed *in situ* and also satellite spots in the SADP at room temperature, which reveals the presence of small NiO domains that are coherent with the Ni phase after reduction up to 850 °C.

Fig. 5.20a provides a STEM EDX assessment after reduction up to 700 °C in the ETEM (Fig. 5.18). The quantified maps highlight the segregation of trace elements at the Ni interfaces but also demonstrate the formation of large Al-rich clusters at some of these interfaces, which may explain to some extent the differences in void structure observed in Fig. 5.18.

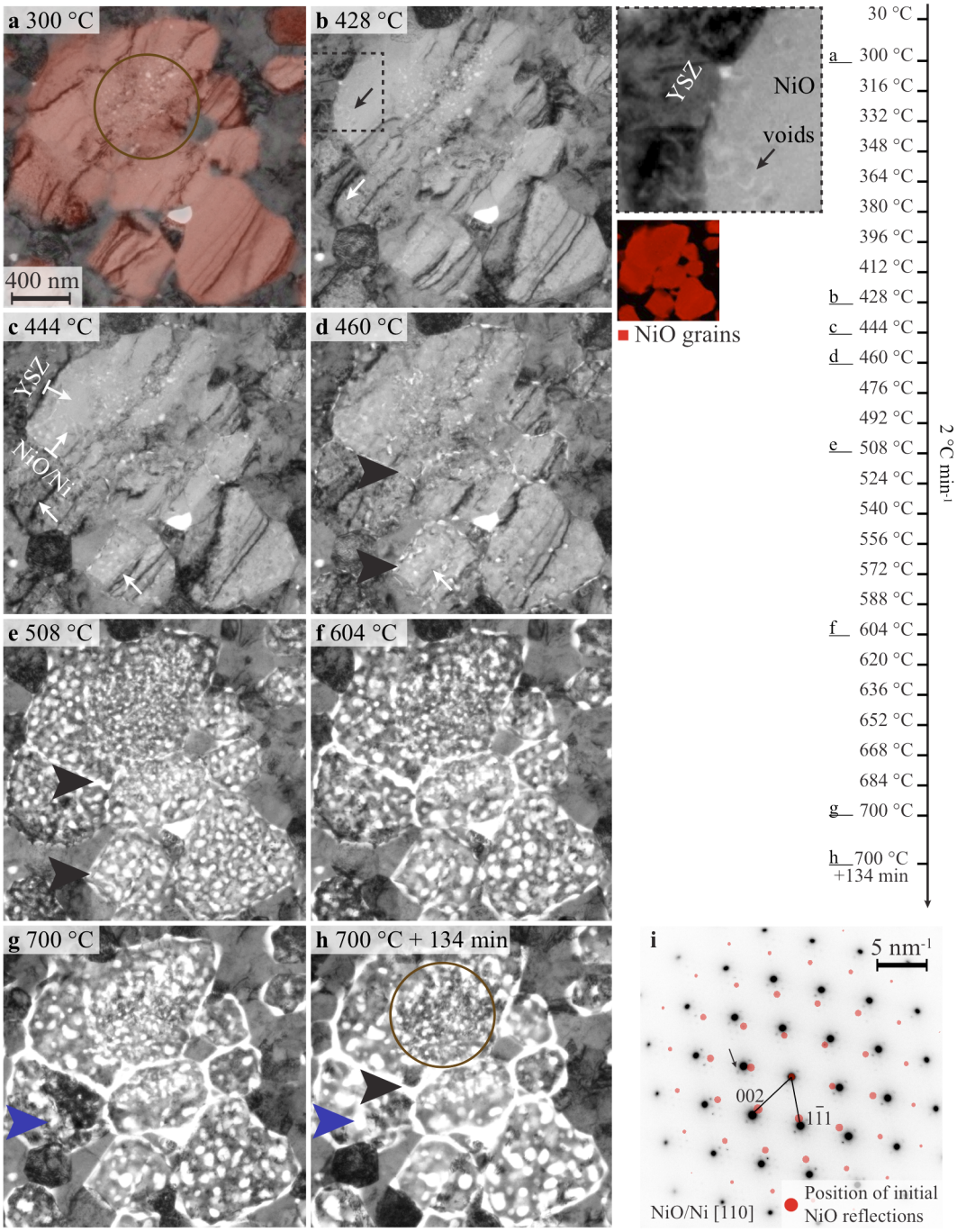

Figure 5.18 – (a-h) Selection of TEM BF micrographs illustrating the reduction of a H-bar up to 700 °C, whilst heating at 2 °C min^{-1} in 1.3 mbar of H_2. A Ni EDX map is coloured in red and superposed to (a). Voids are arrowed in black at interfaces with YSZ in (b) and in white at the centres of NiO domains (c-d). Black arrowheads show voids at the position of NiO/NiO and NiO/YSZ boundaries, while blue arrowheads show voids coarsening. The region circled in (a) and (h) exhibits a different structure before and after reduction. (i) Superposition of two NiO/Ni selected area diffraction patterns (inverted contrast) of the same region acquired before (red) and after reduction (black), with satellite spots arrowed.

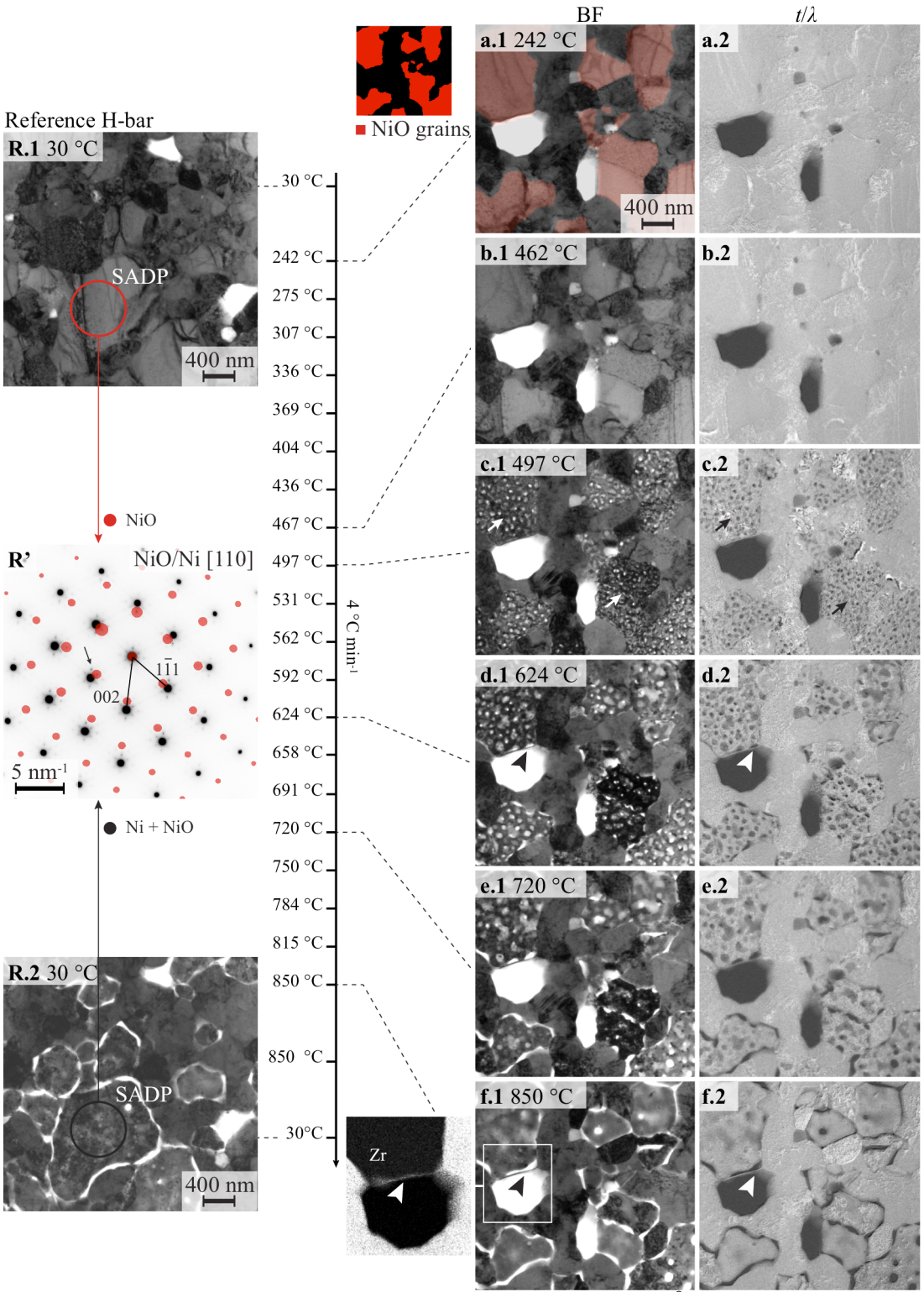

Figure 5.19 – (R) BF images of the reference window acquired at 30 °C (1) before and (2) after reduction, with (R') showing a comparison of SADPs (inverted contrast) before (red) and after reduction (black). (a-f) Selection of (1) TEM BF and (2) t/λ images of a 2nd window acquired, whilst heating at 4 °C min^{-1} in 1.3 mbar of H_2 up to 850 °C. A red Ni map is superposed to (a.1). Arrows show voids and arrowheads redeposited YSZ resulting from FIB (Zr EDX map in f).

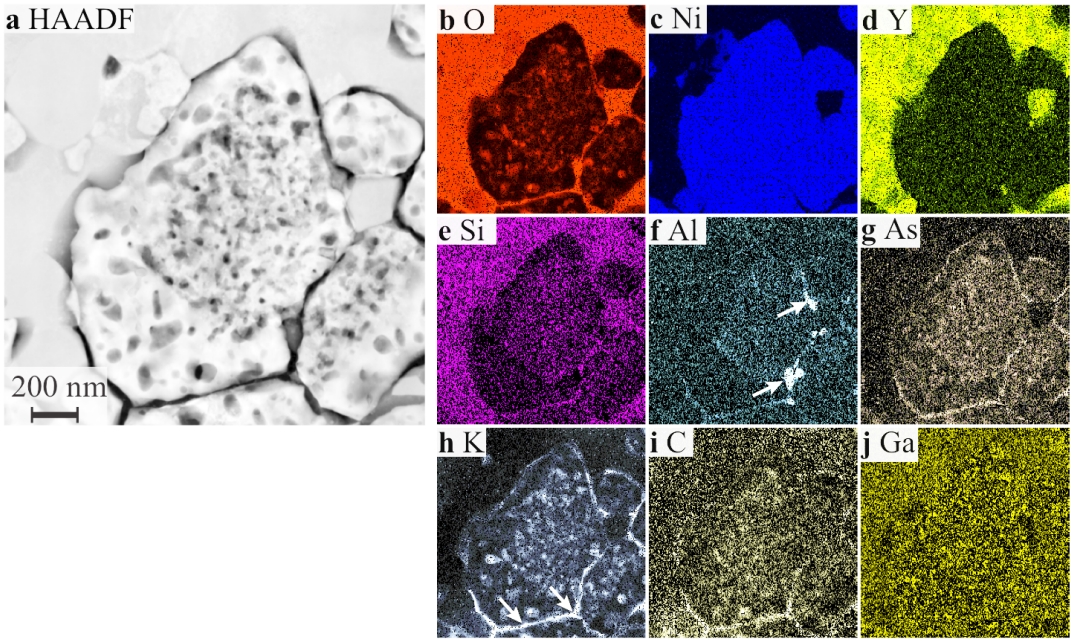

Figure 5.20 – (a) Ni/YSZ structure after reduction up 700 °C, whilst heating at 2 °C min^{-1} (specimen shown in Fig. 5.18), with (b-j) quantified STEM EDX elemental distribution mapping (deconvolved and background-subtracted, with contrast/brightness adapted for visibility) of O Kα, Ni Kα, Y Kα, Si Kα, Al Kα, As Kα, K Kα, C Kα, Ga Kα, respectively.

5.3 Discussion

5.3.1 Changes in structure and crystallography during reduction

Volume loss and intragranular voids

Reduction of the NiO/YSZ samples results in the formation of porous Ni grains and leaves the YSZ phase unaffected (Figs. 5.4, 5.6, 5.18 and 5.19). These voids form due to oxygen removal from the NiO phase, which should result in a total volume shrinkage of -41.6% of the NiO phase upon reduction [9]. Local measurements performed using estimates of λ_{NiO} and λ_{Ni} (Appendix D.1) and average intensity measured in reduced Ni areas of the t/λ images were found to be in good agreement with this theoretical value (-41%, Fig. 5.9). While λ_{NiO} and λ_{Ni} are only approximations, which may in turn induce errors in the thickness calculation, the volume shrinkage is a relative computation and is thus less sensitive to systematic errors. Overall, diffraction is observed to induce a variation in the results from -36% to -46%. These effects are reduced when the intensity in the t/λ images is averaged over larger areas. Post-H_2 exposure STEM HAADF tomography indicates that intragranular porosity is open to the atmosphere (Fig. 5.17), which is consistent with the fact that H_2O must be evacuated from the reaction sites to continue the NiO reduction reaction. The number and size of these intragranular voids depend on the final temperature. Indeed, these voids are observed to merge into larger ones as the temperature reaches 600 °C (Fig. 5.6) and then mostly disappear as the temperature tends to 850 °C as a result of surface energy minimisation (Figs. 5.18 and 5.19).

Similar Ni structures containing voids were observed *ex situ* by Andrzejczuk *et al.* [268], who investigated using FIB and TEM techniques Ni/scandia-stabilised ZrO_2 structures resulting from reduction in pure and diluted hydrogen atmospheres at 600 °C. Waldbillig *et al.* observed in a thin TEM sample a similar intragranular porosity after 5 min in 5% H_2 at 700 °C [17]. Moreover, Hidayat and co-workers [32,33] investigated using post-exposure SEM observations the resulting Ni porosity after reduction in various conditions and demonstrated the coalescence of the fine porosity upon heating to 800-1000 °C. Overall, these literature findings indicate that the structure observed here *in situ* during the reduction of thin lamellae relates to those observed *ex situ* in the bulk.

Reduction activation

While all the samples result in similar Ni porous structures that eventually coalesce with increasing temperature, the reaction activates at different positions of the NiO phase and at different temperatures depending on sample geometry/size and heating rate.

First of all, the thermocouple temperature readings obtained when reducing stainless steel supported TEM lamellae cannot be compared directly to measurements obtained during reduction of self-supporting H-bars due to differences in thermal conductivity of the support. Moreover, the thermal conductivity of H-bar specimens changes during reaction as the NiO phase of the support reduces to metallic Ni, which may in turn affect

the difference in temperature between the region of interest and the thermocouple.

When heating at 2 °C min^{-1}, stainless steel supported TEM lamellae reduce first through reaction of the NiO regions at the interfaces with YSZ and then through NiO free surface reduction (Figs. 5.4 and 5.6). Activation of the reaction at the grain boundaries with YSZ does not appear related to any high density of defects as incoherent NiO/NiO grain boundaries, which are also expected to contain defects, react only when NiO free surface reduction is triggered (Figs. 5.4 and 5.6). Alternatively, this two-step reduction mechanism is not as clear when H-bar samples are reduced, whilst heating at the same rate of 2 °C min^{-1} (Fig. 5.18). Indeed, the reaction at the interfaces with YSZ occurs only in some regions and appears to overlap with reduction of the free surface, which occurs in a similar temperature range (428-444 °C, Fig. 5.18b-c). The Ni/NiO reaction front seems to originate either from the YSZ interfaces, the NiO free surface or from a neighbouring Ni(O) grain that started reducing at a lower temperature (Fig. 5.18). This latter process was also observed during reduction of NiO particles (Chap. 3). When the heating rate is increased to 4 °C min^{-1}, reduction is triggered directly on the free surface and not at the interfaces with YSZ at ∼500 °C (Fig. 5.19).

This difference in activation mechanism depending on specimen size/geometry and heating rate is related to differences in conditions at the region of interest. As measured using EFTEM images in Figs. 5.7 and 5.8, reduction proceeds with different kinetics, i.e with a different rate-controlling mechanism, depending on the activation mechanism and, as a result, these processes may respond differently when the reaction conditions are modified. Indeed, H_2 starvation and H_2O stagnation effects are expected to be significant in H-bar samples due to the larger amount of reducible NiO (∼µg) when compared to the stainless steel supported TEM lamellae (∼ng). In addition, the edges of the NiO/YSZ support in the H-bar design are at higher temperature when compared to the central thin window and hence react earlier, consume the H_2 available and form H_2O, with both processes eventually hindering the reaction of the thin window. Indeed, the mechanism that drives the reduction of the NiO regions at the interfaces with YSZ may be delayed to a temperature higher than the temperature at which the free surface starts to reduce. Overall, Erri *et al.* [55] highlighted the importance of probing NiO samples with a small mass/volume at a low heating rate to prevent falsification of the NiO reduction kinetics by external parameters. Indeed, the authors demonstrated that their thermogravimetry measurements assessing the reduction of NiO particles were affected by mass-transfer limitations at heating rates as low as 5 °C min^{-1}. Waldbillig and co-workers [22], who used thermogravimetry to assess the reduction of NiO/YSZ bulk samples, demonstrated a modification of the reduction kinetics depending on heating rate. Some features of the $\alpha - T$ curves were suppressed at heating rates higher than 5 °C min^{-1} hence indicating a modification of the mechanism controlling the reaction. All these observations indicate that a combination of fast heating rate and non-ideal specimen size may have suppressed the activation of the NiO reduction reaction at the

interfaces with YSZ in H-bar specimens. Overall, H-bar specimens can withstand higher reduction temperatures but external parameters probably affect the reaction mechanism of these samples. Alternatively, stainless steel supported TEM lamellae appear more suited to the study of the mechanisms controlling the reaction due to the small amount of reducible material involved and the stability of the stainless steel support.

Ni/NiO epitaxy

In situ observations demonstrate that the metallic Ni domains are coherent with respect to the original NiO phase, independent of the activation mechanism (Figs. 5.4, 5.18 and 5.19). This Ni/NiO epitaxy gives rise to satellite spots in the diffraction pattern due to double diffraction effects. These satellite spots, synonymous with the presence of NiO within the selected area, are observed up to temperatures as high as 850 °C. As the reaction is autocatalytic, the crystallographic orientation of the first Ni domains that form during reduction is likely to determine the final Ni orientation. Here, the first Ni domains either form at the interfaces with YSZ or at the free surface but are in both cases coherent with the initial NiO phase.

While nucleation of Ni on NiO may be affected by FIB-induced amorphisation of the specimen surface [203], the surface is expected to recrystallise to some extent due to the elevated temperature. Moreover, similar NiO/Ni epitaxial relationships were found in the literature. Indeed, Ni/NiO coherency was reported by Waldbillig *et al.* [17], who observed satellite spots when they examined a TEM lamella of a sample that was partially reduced *ex situ* at 700 °C. In addition, Little *et al.* reduced thin NiO foils *ex situ* in hydrogen and observed Ni/NiO epitaxy during the initial stages of the reaction using TEM, with randomly oriented Ni domains forming at longer reaction times and larger thicknesses. In Chap. 3, heating NiO particles at a rate of 2-7 °C min^{-1} resulted in the nucleation of randomly oriented Ni domains, while NiO/Ni epitaxy was observed in nearly isothermal experiments. Predictions of NiO/Ni orientation relationship appear complex and highly dependent on surface properties, reaction conditions, etc.

Formation of Ni nanoparticles during reduction

Ni nanoparticles form during reduction on and around Ni grains (Fig. 5.5b-c) but also on the YSZ surface (Fig. 5.17b-c). Their origin does not appear to be from FIB milling during TEM sample preparation as similar Ni nanoparticles were observed during reduction of NiO particles (Chap. 3). These Ni nanoparticles may originate either from redeposition of Ni (through the evaporation and recondensation of volatile nickel hydroxide [76, 252, 253]) or due to the separation of Ni nuclei from the bulk [250]. Based on SEM images of a sample that underwent reduction-oxidation cycles in an environmental SEM (Appendix F), these separated Ni domains appear to increase in size and number with reaction time and number of redox cycles, indicating that evaporation and recondensation of volatile nickel hydroxide during exposure to H_2 is likely to occur.

On the other hand, such continuous formation of separated Ni domains would not be possible if those formed only during reduction as a result of Ni nuclei detachment from the bulk.

NiO/NiO grain boundaries during reduction

NiO/NiO grain boundaries exhibit various behaviours during reduction depending on their symmetry (Fig. 5.6). Indeed, while NiO grains separated by an incoherent boundary are observed to detach during reduction, leaving a void at the initial position of the boundary, coherent twin boundaries are maintained throughout the reaction (Fig. 5.15). Voids appear to follow initial incoherent grain boundaries once reduction of the free surface is triggered, which indicates a preferential reduction of the NiO phase located at the boundary when compared to the bulk. When the temperature is increased to 600 °C and above, the Ni phase tends to minimise its surface energy and the Ni grains located across an initial incoherent boundary plane fully detach. On the other hand, coherent Ni boundaries maintain their symmetry throughout the reaction and react similarly to one single Ni grain. This difference in behaviour during reduction is related to the free energy associated with each of these grain boundaries. Indeed, the free energy associated with incoherent boundaries is several orders of magnitude higher than the one measured for coherent twins [265]. Incoherent boundaries become energetically unfavourable during reduction at high temperature and grains detach. The connectivity of the Ni network will hence be determined by the nature of the grain boundaries prior to reduction.

Twinning in Ni grains

New coherent twin domains form within seemingly monocrystalline Ni grains at high temperature (Fig. 5.16). Dickey and co-workers [269] also noticed Ni twins about the (111) plane with respect to the initial NiO phase, whilst reducing directionally solidified NiO/YSZ eutectics. These domains are observed here to range from ∼10 to 100 nm. Mahajan and co-workers [270] developed a microscopic model to explain twinning in FCC materials in terms of nucleation of Shockley partial dislocation loops by growth accidents during grain growth. Dislocations in Ni are indeed observed after reduction (not shown here) but as Ni grain growth is not seen here, it appears more likely that these dislocations leading to twinning form as a result of two interdependent effects: reduction-induced strain at high temperature [267] and Ni growth accidents during reduction.

5.3.2 Segregation of trace elements at boundaries and interfaces

Elements such as Hf, Al, Si and As are detected in small amounts in the initial NiO/YSZ samples using STEM EDX (Fig. 5.3 and Tab. 5.1). While Si is also present initially in the NiO as demonstrated by the inductively coupled plasma (ICP) spectrometry

quantification results in Tab. 2.1, it appears mainly concentrated in the YSZ phase and on the specimen surface as shown in Fig. 5.3. The low concentration of the other elements, which is at the detection limit of the STEM EDX technique, does not allow to resolve any fluctuation in concentration. Hf is a known impurity in Zr [271] and should hence concentrate in the YSZ phase. After reaction in the ETEM up to 600-700 °C, Al, Si, As along with K and S, two elements that were detected initially by ICP in the NiO phase but not by EDX, segregate at the Ni interfaces, with some of them forming oxides (Figs. 5.13, 5.14 and 5.20). These segregated elements form a film rich in O that contains Ni nanoparticles in some samples (Fig. 5.14), while large Al-rich domains are observed elsewhere (Fig. 5.20). Overall, with the exception of As, whose origin is unknown, Si, Al, K, Hf, S, are impurities usually present in the raw YSZ or NiO materials [271,272]. Along with other elements such as Ca, Fe, Na, Ti that are not detected here, Si and Al are known to segregate as SiO_2 and Al_2O_3 at interfaces of the anode when annealed at temperatures from 800 and 1500 °C [273]. Y also segregates at the Ni interfaces as it supposedly incorporates into the SiO_2 phase [273], which is coherent with Fig. 5.13.

These elements and their segregation during reaction may influence the reduction reaction, which is sensitive to chemistry and surface properties, but also influence the operation of the anode as it may block certain active sites. In addition the amount of such trace elements may differ from one sample/batch to the other and hence induce subtle differences in the reaction process.

5.3.3 Reaction kinetics from EFTEM images

3-window elemental maps and jump-ratios

3-window O K elemental maps and O K jump-ratios both provide quantitative insights into the reduction kinetics with this information localised on the pixel scale (Figs. 5.7 and 5.8). The extraction of reliable information from the data is affected by different factors such as noise, diffraction effects in 3-window elemental maps, subjective removal of pixels with high intensity in jump-ratios, frame alignment, etc. As an acquisition time of 40 s is required per filtered image for this dose rate conditions, the chemical information obtained in 3-window elemental maps is an average over 120 s, while the acquisition time required to yield jump-ratios is reduced to 80 s. Nevertheless, 3-window maps and jump-ratios yield exploitable results that demonstrate the activation of the NiO reduction reaction at the interfaces with YSZ with NiO free surface reduction occurring at higher temperature (Figs. 5.7 and 5.8). The spatially-resolved reaction kinetics data can then be compared to measurements of Chap. 3 and literature to in turn support the development of a detailed description of the NiO/YSZ reduction.

Comparison of reduction kinetics with NiO particles

Fig. 5.21 shows a comparison of the reaction kinetics of NiO particles (from Chap. 3) and the NiO/YSZ composite, both obtained whilst ramping the temperature at 2 °C min^{-1} in 1.3 mbar of H_2. As the supports of the NiO particles and NiO/YSZ composite prepared by FIB have a different thermal conductivity (Cu-SiO_x versus stainless steel, respectively), the interpretation of small temperature shifts is not straightforward. However, the shape of the $\alpha - T$ curves of these two different systems can be related to each other (provided that the Ni and NiO references used to normalise the data are correct) as it should reflect the mechanism controlling the reaction.

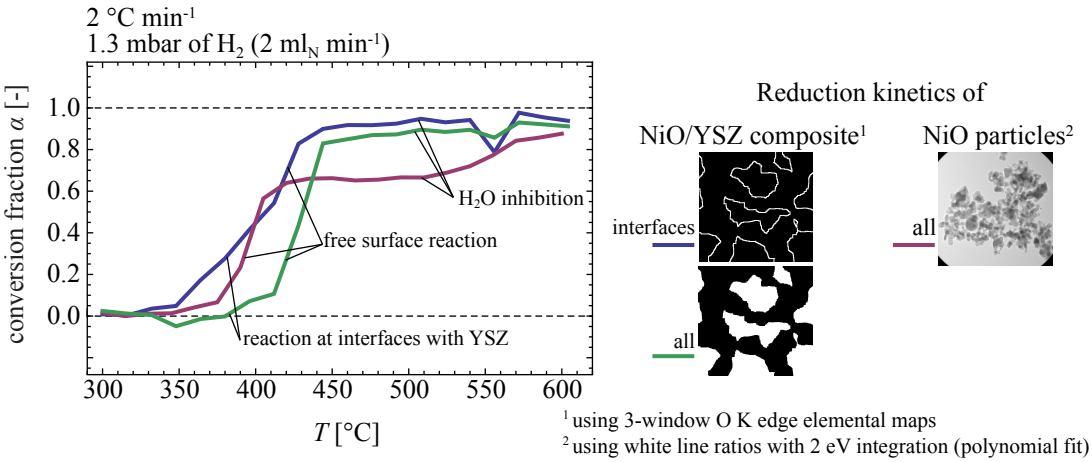

Figure 5.21 – Reduction kinetics of NiO particles obtained using EELS (white lines ratio method with 2 eV integration using polynomial fits) compared to reduction kinetics of a NiO/YSZ composite obtained using EFTEM (3-window O K elemental maps), both obtained whilst heating the samples at a rate of 2 °C min^{-1} in 1.3 mbar of H_2. For the NiO/YSZ composite, reduction kinetics of both the entire and interfacial NiO regions are shown.

From Fig. 5.21, it appears that the reaction rate of the NiO regions located at the interfaces with YSZ is controlled by a different mechanism than the NiO particles. On the other hand, free surface reduction of the NiO/YSZ composite appears to proceed similarly to NiO particles, which tends to indicate a similar rate-controlling mechanism. While differences in NiO/Ni orientation relationships are observed in NiO particles (random Ni seeds) compared to NiO/YSZ composites (epitaxial Ni layer), denoting different nucleation mechanisms, the subsequent growth of these Ni domains appears to be controlled by a similar mechanism. Based on experimental data and literature [38], this process was found in Chap. 3 to involve the adsorption, dissociation of H_2 directly on Ni and then the transfer of H to NiO. While reduction of the NiO/YSZ composite cannot be described by an Avrami model as Ni nucleation does not occur through the appearance of small seeds on the surface, the subsequent growth of the Ni domains may be controlled by the same mechanism as for reduction of NiO particles.

The reaction rate of both the NiO particles and the NiO/YSZ composite is observed to decrease when α reaches values of 0.6 or 0.8, respectively. This decrease in reaction rate was associated in Chap. 3 (based on the findings of Richardson *et al.* [38]) to the presence of H_2O on the surface of the Ni particles, which eventually inhibits the reaction. This plateau in the $\alpha - T$ curves occurs at a lower value of α for NiO particles ($\alpha > 0.6$) compared to the NiO/YSZ composite ($\alpha > 0.8 - 0.9$) as a result of differences in specimen geometries. Indeed, the FIB-prepared NiO/YSZ lamella exhibits a large specific area with its two faces exposed to the environment, while the presence of the SiO_x film and the organisation of the NiO particles may hinder the reaction at lower values of α. In general, the termination of the reaction of the Ni grains requires long exposure times and high temperatures. Indeed, small amounts of NiO are observed in the form of satellite spots in diffraction patterns as high as 850 °C (Figs. 5.19).

Comparison of reaction kinetics with literature

Fouquet and co-workers compared the reduction kinetics of NiO particles and NiO/YSZ composites as a function of temperature, whilst heating at a rate of 10 °C min^{-1} [63]. NiO/YSZ composite samples were observed to start reducing at higher temperatures when compared to the NiO powder, with the latter system also proceeding with a faster reaction rate. The delay of activation temperature of the reduction reaction of the NiO/YSZ composite was explained in terms of Ni nucleation inhibition by the YSZ ceramic, which appears contrary to the observations presented in this chapter.

Several experimental differences may explain those divergent observations. First of all, a fast heating rate of 10 °C min^{-1} was used in Ref. [63], which may suppress the activation of the reduction at NiO interfaces with YSZ as seen in Chap. 5.3.1. Indeed, Erri *et al.* [55] demonstrated that the reduction kinetics of NiO could be falsified by diffusional effects at heating rates as low as 5 °C min^{-1}, while Waldbillig *et al.* [22] also showed that some rate-controlling mechanisms may be inhibited when heating NiO/YSZ in H_2 at 5 °C min^{-1}. These results, in addition to the *in situ* XRD experiments presented in Chap 3.2.4, which highlighted the importance of non-limiting experimental parameters to assess the intrinsic kinetics, tend to indicate that the results presented in Ref. [63] may not be representative of the intrinsic NiO reduction reaction. As the reaction proceeds in Ref. [63], these diffusional effects then appear more severe in the dense NiO/YSZ samples as the YSZ inhibits H_2/H_2O transport. The size of the sample is another factor that may explain the differences between the findings of this chapter and those of Ref. [63]. Indeed, the volume investigated here of 3 x 3 x 0.1 μm^3 (with both surfaces in contact with the H_2 gas) correlates only with the surface of the bulk NiO/YSZ sample that is assessed using thermogravimetry. Details about the reaction of this first 50 nm of NiO/YSZ (half thickness of the TEM lamella as both faces are exposed to H_2) is lost in thermogravimetry as the measurement is averaged over a volume of $\sim 10^8$ μm^3. Activation of the NiO reaction at the interfaces with YSZ at low temperatures

is not observed using thermogravimetry in literature, presumably due to the low NiO mass actually converted to Ni by this process with respect to the entire bulk sample and the sensitivity of this interface reaction mechanism with respect to experimental parameters.

Avrami models were found to describe satisfyingly the reaction of bulk NiO/YSZ samples using thermogravimetry [66]. While this model takes into account induction time before the reaction is triggered, a phenomenon observed here, microstructural observations of the NiO/YSZ samples do not appear coherent with an Avrami description as the reaction does not proceed though the formation of small randomly-localised Ni nuclei, which are inherent to the Avrami model. Indeed, Ni nucleates here uniformly at the interfaces with YSZ or on the NiO free surface and forms a distinct layer (Fig. 5.4, 5.6, 5.18 and 5.19). Other results found in the literature indicate that the reaction is described by an interface-controlled model [65], which involves the rapid formation of a uniform layer of Ni on the surface of NiO, with the reactions at the NiO/Ni reaction front controlling the reaction. While more coherent with the microstructural observations of this chapter, this model does not include induction time and substantial autocatalysis [28], two important features of the NiO reduction reaction [30]. These two models are hence incomplete and a more detailed description of the reaction is required. Moreover, the role of the YSZ phase on the NiO nucleation mechanism needs to be clarified.

5.3.4 Mechanism controlling the reduction of NiO/YSZ

The procedure introduced in Chap. 2.5 to yield the activation energy and the reaction model cannot be applied here as only one heating rate experiment is presented. In addition, different mechanisms are observed to control the reaction over its entire duration, which complicates the application of Eq. 2.23. However, the EFTEM images acquired here provide quantitative information about thickness and degree of reduction on the pixel scale, which can be correlated to provide detailed insights into the reaction mechanism.

NiO reduction at the interfaces with YSZ

Density functional theory computations performed for this study (by Dr. U. Aschauer) along with literature findings provide some details into a possible reduction mechanism of NiO regions located at the interfaces with YSZ. However, it should be mentioned that, due to the complexity of the NiO properties, theoretical and computational challenges [274], the results of these simulations should be interpreted with care as these may not fully grasp the processes involved.

A nudged elastic band calculation was performed to assess the relative defect energy of an oxygen ion transferred across the interface from NiO to an oxygen vacancy inherent

to the YSZ ionic conductor (Fig. 5.22). The result shows that for this interface model the relative defect energy is much lower when oxygen is in the YSZ part, which translates to the vacancy being in the NiO part of the interface. As electrostatics cannot account for this decrease in energy, improved misfit strain relaxation with the vacancy in NiO is likely to be the origin of this energy difference. The relatively large energy difference indicates that the population of vacancies in the YSZ close to the interface with NiO should be negligible. Although this is clearly only a single model interface, the magnitude of the result provides some confidence that results should be similar for other possible interface structures.

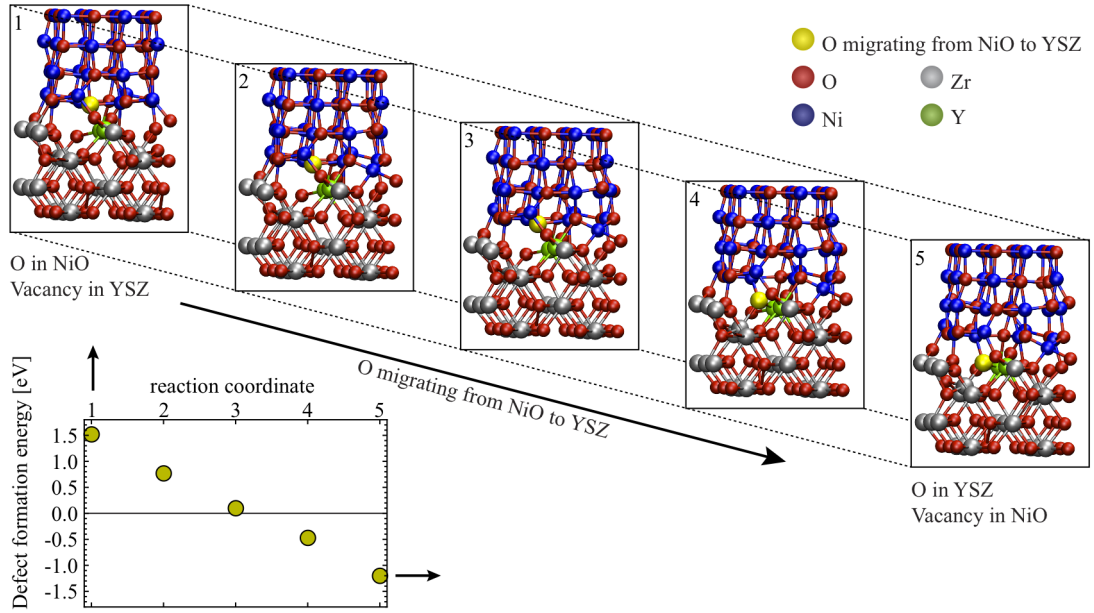

Figure 5.22 – Nudged elastic band calculations to determine the formation energy of an oxygen vacancy across the NiO/YSZ interface. The defect formation energy decreases as O is transferred from NiO to a vacancy in YSZ.

In the YSZ phase, Shishkin *et al.* [275] demonstrated using DFT that H_2 adsorption, dissociation and reaction with this externally provided oxygen (i.e. from NiO) to form H_2O is exothermic. The YSZ phase may hence remove O^{2-} from the NiO phase through this pathway. Following the experimental work of Bonvalot-Dubois *et al.* [64], who studied the reduction of NiO/ZrO_2(CaO doped) lamellar composites, two separate reactions are proposed to describe the transfer of oxygen ions from NiO to YSZ and subsequent H_2O desorption. Using the Kröger-Vink notation [276], the following reaction may occur at the inner YSZ/NiO interface:

$$O_O(\text{NiO}) + V_O^{\cdot\cdot}(\text{YSZ}) \rightarrow O_O(\text{YSZ}) + V_O^{\cdot\cdot}(\text{NiO}) \tag{5.4}$$

where O_O(NiO) is an oxygen ion in NiO, $V_O^{\cdot\cdot}$(YSZ) is an oxygen vacancy in YSZ, O_O(YSZ)

is an oxygen ion in YSZ and $V_O^{\cdot\cdot}$(NiO) is an oxygen vacancy in NiO. Subsequently at the NiO/YSZ/gas interface:

$$H_2 + O_O(YSZ) \rightarrow H_2O(g) + V_O^{\cdot\cdot}(YSZ) + 2e^-(NiO) \tag{5.5}$$

Ni ions located at the interface then combine with the e^- released by the oxidation of H_2 to form metallic Ni. The first Ni domains may hence nucleate as a result of this reaction pathway at the interface with YSZ. Once this small layer of Ni is formed at the interfaces with YSZ, the reaction then proceeds along the directions x,y (specimen plane) and z (along the specimen thickness) as the temperature increases.

The reaction may first proceed as illustrated in Chap. 3.16. Indeed, oxygen vacancies and metallic Ni domains form as a result of reactions Eq. 5.4 and Eq. 5.5 and these are known to be active sites for H_2 adsorption and dissociation, with adsorbed H then transferring to NiO and desorbing as H_2O [30,38,39]. The reaction rate of the NiO particles resulting from this mechanism was however measured to be faster than the reaction rate of the NiO regions located at the interfaces with YSZ in the composite (Fig. 5.21). This observation indicates that the description of the NiO reduction mechanism at the interfaces with YSZ is incomplete and other effects must be accounted for.

First of all, this difference in reaction rate between NiO/YSZ composite and NiO particles may arise to some extent from the autocatalytic behaviour of NiO reduction, i.e. from the fact that the reduction rate depends on the Ni/NiO interfacial area [30]. In Chap. 3, new Ni domains formed randomly on the entire NiO particle surface, which thus resulted in a large Ni/NiO contact area. In the NiO/YSZ composites observed here, new metallic Ni domains can only add up to the ones formed previously at the interfaces with YSZ, i.e. new Ni seeds cannot nucleate on NiO at these temperatures without the presence of the YSZ phase. And as the thickness of the FIB-prepared TEM sample is fixed, the Ni/NiO interfacial area cannot increase significantly as the reaction proceeds, which may eventually limit the reaction rate when compared to NiO particles.

Secondly, an other effect, which involves the YSZ phase, may be envisaged. Based on estimates of the Ni/NiO reaction front position in the NiO/YSZ composite, the reaction rate is anisotropic and is measured to proceed faster along the x,y plane (given by $w(T)$, specimen plane) when compared to the z direction ($d(T)$, along the specimen thickness, Fig. 5.12). Different mechanisms hence appear to control the reaction depending on direction, with this anisotropy probably originating from two processes. First of all, mass-transfer of H_2 and H_2O may limit the advancement of the reaction front below the specimen surface when compared to regions at the free surface, where Ni/NiO and H_2 are in direct contact. In addition, similarly to the model developed by Bonvalot-Dubois and co-workers [64], O^{2-} may transfer from the NiO to the oxygen vacancies that are inherent to the YSZ phase at the position of the Ni/NiO reaction front located at a certain depth. O^{2-} may in turn diffuse through the ion-conducting YSZ phase to the free

surface and react with H_2, with DFT calculations indicating that H_2 oxidation with O^{2-} probably occurs directly at the Ni/YSZ interface [277]. Overall, this mechanism would allow NiO regions that are not in direct contact with H_2 to reduce to Ni by combining with electrons released at the free surface by H_2 oxidation. This possible mechanism should proceed with a slower rate when compared to the reaction occurring at the free surface (as shown in Fig. 5.21), where Ni, NiO and H_2 are in direct contact. Some observations tend to support such a pathway. Indeed, while voids quickly separate Ni and YSZ grains when the reduction activates directly at the free surface (Fig. 5.19), Ni/YSZ contact is maintained longer when the reaction activates the YSZ interfaces, with Ni/YSZ separating only when coarsening of Ni becomes significant at 600 °C (Fig. 5.6). This prolonged Ni/YSZ contact may arise from the fact that O is removed from NiO through the YSZ with metallic Ni forming at the interface as detailed above, a phenomenon that may hence maintain Ni/YSZ interfaces.

NiO free surface reduction

NiO free surface reduction activates at higher temperatures. This process is observed either after reduction of the interfaces with YSZ (Figs. 5.4 and 5.6) or directly without this preliminary reaction in the case of high heating rates and due to mass-transfer limitations (Figs. 5.18 and 5.19). The free surface reaction of both NiO particles and NiO/YSZ composite proceed with the same rate and thus probably through the same mechanism. This mechanism illustrated in Chap. 3.16 involves the generation of active sites for H_2 adsorption and dissociation, i.e. oxygen surface vacancies, Ni nucleation and growth at Ni/NiO interfaces through H spillover from Ni to NiO [30, 38, 39]. A sufficient number of those active sites is present on the surface of the NiO grains at 430-500 °C to trigger the free surface reaction (Figs. 5.4, 5.6, 5.18 and 5.19).

5.3.5 Factors affecting ETEM results

Different factors affect the acquisition and interpretation of reliable *in situ* data during reaction at elevated temperature. For example, FIB-induced gallium implantation and surface amorphisation effects on NiO reduction are not yet fully understood. Surface amorphisation may be reduced to some extent by recrystallisation as a result of the elevated temperature involved in the experiments. While the Ga content in the specimen itself was measured to be initially small at a value of 0.2 wt% and mostly concentrated around as-sintered porosity (Tab. 5.1), the Ga contained in the protective C layer (Fig. 5.3) diffused at elevated temperatures either towards the top surface to form an oxide or towards the Ni grains in contact with the C layer (Fig. 5.23a). While these Ni grains have a similar structure compared to those located further away from the C layer, regions of interest were selected at some distance from the Ga-rich C layer to minimise any possible artefact. Moreover, this layer was removed in H-bar samples to reduce these effects. Recently developed low-voltage argon ion milling systems with

focused ion beams may remove Ga implantation and reduce surface amorphisation more efficiently. However, such a milling system may induce the redeposition of milled material in the porosity of the as-sintered specimen as shown in Fig. 5.19. Eroded and redeposited Ni may not react like pristine Ni. Moreover, materials from the support may be redeposited at the region of interest and influence the observations. A comparison of unprocessed raw NiO powders and FIB-prepared NiO/YSZ samples that have the same chemistry appears essential to investigate sample preparation effects, even if the YSZ phase modifies the reaction pathway. Indeed, it could be inferred from such a comparison that Ni nanoparticles that form during reduction do not originate from FIB milling and redeposition.

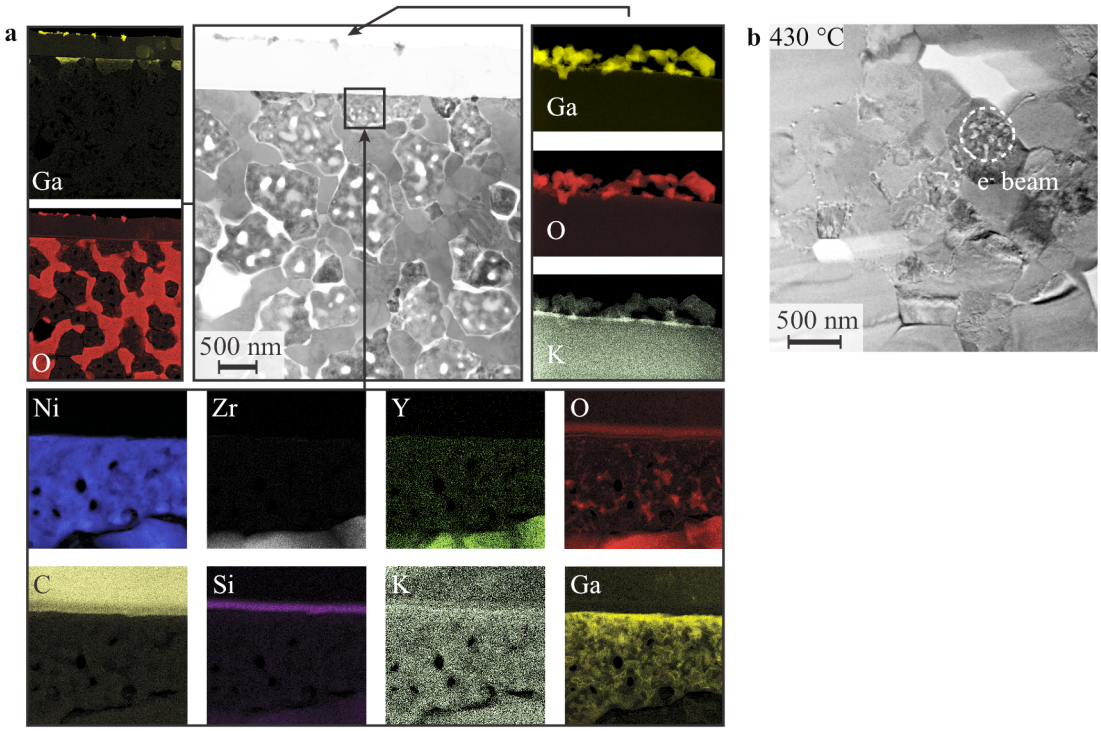

Figure 5.23 – (a) Post-exposure STEM BF image along with corresponding EDX maps, highlighting Ga diffusion and oxidation, (b) TEM image at 430°C in 1.3 mbar of H_2 exhibiting more voids at the position where the electron beam was focused.

Thermal drift decreases the quality of energy-filtered images acquired over long exposure times. Although the use of a stainless steel grid instead of a conventional Cu grid reduced the overall drift of the sample, a low heating rate was still required to acquire interpretable energy-filtered images. The recent introduction of heating holders based on microelectromechanical systems (MEMS) decreases thermally induced drift significantly and thus allows the acquisition of reliable data during ramping at higher heating rates [179]. However, preliminary experiments showed that the geometry of such a holder is not optimised for studies of FIB-prepared lamellae or low-voltage argon cleaning.

Electron beam-induced artefacts may also alter the observations [249,255,278]. Indeed, the reaction was observed to proceed faster in regions irradiated with a focused probe (Fig. 5.23b). Such an effect may be caused by local heating due to the electron beam, knock-on damage of O, which may in turn create active sites for H_2 adsorption and dissociation [39] and/or ionisation of the molecular hydrogen gas by the electron beam, which modifies the adsorption energy of hydrogen. While operating the microscope at a low electron dose can reduce these effects, a sufficient signal is still required to obtain statistically relevant data within the desired acquisition time, especially with EFTEM images. The acquisition of EFTEM images of core-losses while the sample reacts is hence not suited to the study of fast processes. Electrostatic charging may be induced by the electron beam. The presence of charges at the NiO/YSZ interfaces may in turn influence the activation of the reaction that is observed at this position. However, using the same dose rate in all experiments, this NiO/YSZ interface activation mechanism could be suppressed by changing the specimen size/geometry and the heating rate. This observation indicates this interface activation process is probably not resulting solely from charging, yet more work is required to fully understand those electrostatic charging effects.

Data processing may also induce errors. Misalignment of the filtered images may lead to artefacts as the same region may not be located at the same (x,y) position throughout the EFTEM series. As the intensity is averaged over regions of $\sim$100 pixels or more to yield statistically relevant data, this effect did not appear significant. As mentioned in Chap. 5.3.3, diffraction affects the intensity in EFTEM images and in turn modify local measurements of thickness and reduction kinetics. These effects are always present to some extent in EFTEM images as an objective aperture is required to guarantee a sufficient spatial resolution [204]. While jump-ratios are less sensitive to these effects, the removal of artefacts related to the division procedure may be subjective and hence may affect the measurements. Diffraction can be mitigated using a rocking beam illumination [204] but this technique may be time-consuming and hence not adapted to *in situ* studies.

Similar structures were observed *in situ* (Figs. 5.4, 5.6, 5.18, 5.19), in reference thin windows (Fig. 5.19) and *ex situ* [131,268], which indicate that the processes observed *in situ* are to some extent representative. Moreover, complex Ni(O)/YSZ interactions were also reported in literature [64,269,275,277,279], which tend to support those *in situ* observations underlining reduction activation at the NiO/YSZ interfaces (Fig. 5.4-5.8).

5.3.6 Qualitative description of the reduction mechanism of NiO/YSZ

Based on the NiO/YSZ atomistic model proposed by Dickey *et al.* [269], a qualitative description of the reduction mechanism of the NiO/YSZ composites that were observed in the ETEM is proposed. At low heating rates and in the absence of mass-transfer limitations, experiments and DFT calculations have demonstrated that O^{2-} may transfer

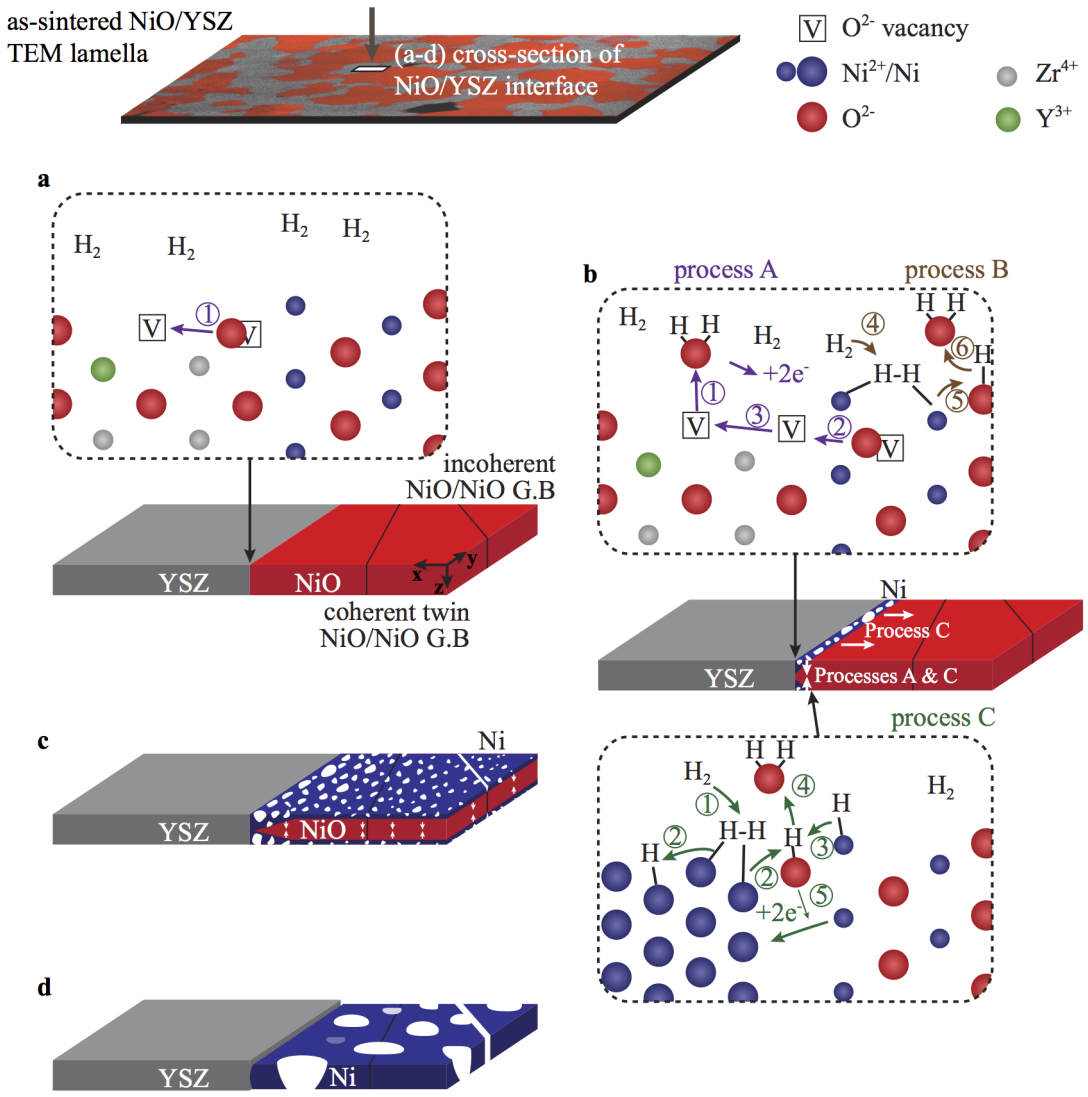

Figure 5.24 – Qualitative description of the reaction mechanism of the NiO/YSZ sample in the ETEM using an atomistic model based on [269], showing in (a) the YSZ/NiO interface at the start of the reduction process at > 300 °C, with O^{2-} transferring from NiO to YSZ, a process leaving a vacancy in the NiO phase, (b) H_2 adsorbs, dissociates and reacts with O^{2-} transferred from NiO to form H_2O (process A), with the oxygen vacancy left in the NiO phase acting as a preferential H_2 dissociation site, with adsorbed H then reacting with oxygen to form H_2O (process B). Once Ni domains have nucleated at the interface, H_2 dissociates on metallic Ni and is transferred to the oxygen sites at the Ni/NiO interface (process C). (c) Above 400 °C, a sufficient number of oxygen surface defects is present to trigger direct reduction of the free surface. (d) At 600 °C, the structure contains large intragranular voids, which will eventually disappear at higher temperature as the system minimises its surface energy. Coherent twin NiO/NiO boundaries are maintained during reaction, whilst incoherent interfaces separate.

from NiO across the NiO/YSZ interface to fill oxygen vacancies that are inherent to the YSZ phase, leaving oxygen vacancies in NiO (Fig. 5.24a). In Fig. 5.24b, H_2 adsorbs, dissociates and desorbs as H_2O on YSZ, on which vacant sites are filled by the externally provided O^{2-} [275]. This process creates a new oxygen vacancy in the YSZ that can be filled by another O^{2-} originating from NiO and hence process A is triggered [64]. As a result, an oxygen vacancy surrounded by Ni^{2+} is formed in NiO at the interface with YSZ, which has been shown to act as a preferential H_2 dissociation site, with adsorbed H then desorbing as H_2O (process B [39]). Once Ni domains of a sufficient size have been formed through processes A and B, the reaction is expected to proceed through the adsorption and dissociation of H_2 directly on Ni and the transfer of adsorbed H to the oxygen reactive sites at the Ni/NiO interfaces (process C [38]), with the reaction front moving towards the center of the NiO grains and forming a porous Ni structure. Along the z axis, process A may also contribute to the reaction similarly to the findings of Bonvalot-Dubois and co-workers [64]. Indeed O^{2-} may transfer from NiO across the interface to a vacancy inherent YSZ, diffuse to the top surface of the YSZ through the oxygen vacancies and react with H_2 to form H_2O, which in turn releases electrons that may combine with Ni ions located at the reaction front. Above 400 °C (Fig. 5.24c), a sufficient number of oxygen vacancies, i.e. active sites for H_2 adsorption and dissociation, is present on the surface of the NiO grain to trigger direct reduction of the free surface (processes B and then C). At temperatures >600 °C, irregular Ni structures that contain intragranular voids are observed, with pores disappearing at higher temperatures and longer reaction times as the system minimises its surface energy (Fig. 5.24d). The intermediate Ni structure depends mostly on the reduction mechanism, while the structure observed at high temperature (> 600 °C) is also observed to depend on coarsening/sintering. The percolation of the Ni network is also found to be influenced by the symmetry of the initial NiO/NiO grain boundaries, with coherent twins remaining as such during reduction and incoherent interfaces separating.

5.4 Concluding remarks

The reduction of the NiO/YSZ anode was characterised using different *in situ* and post-exposure TEM techniques along with density functional theory computations. The acquisition of energy-filtered images during the reduction of a NiO/YSZ composite at different temperatures allowed information to be obtained about both chemistry (using O K images) and structure (using total inelastic mean free path images) on the pixel scale. While relative changes in thickness provide information about the three-dimensional evolution of the system and correspond to theoretical predictions, temperature-resolved 3-window O K elemental maps and jump-ratios allow the extraction of reaction kinetics that are localised on the nm scale. Combining these measurements, local differences in the reaction rate as a result of structural features (NiO interfaces with YSZ or entire NiO grains) or direction of reaction propagation could be investigated.

Based on these results, a qualitative description of the reduction/activation mechanism of the NiO/YSZ samples could be proposed. The reaction, which induces the formation of intragranular voids due to oxygen removal, activates at the NiO interfaces with YSZ as a result of the transfer of O^{2-} from NiO to YSZ. In turn, this process creates active sites for H_2 adsorption and dissociation in the NiO (vacancies). At higher temperature, the direct reduction of the NiO free surface is triggered due to formation of a sufficient number of surface vacancies. The reaction may proceed directly through this mechanism without prior activation at the interfaces when mass-transfer of the reactive species controls the reaction rate. These results highlight a complex interplay between the NiO and YSZ phases along with experimental parameters, which results in a reduction process that differs from the one observed in Chap. 3. The final porous Ni structure is coherent with the initial NiO and depends on the reaction mechanism at temperatures <600 °C and then on sintering/coarsening of Ni at higher temperatures, with intragranular voids disappearing as the system minimises its surface energy. Segregation of trace elements at interfaces was also observed during reaction and crystallographic characteristics of grain boundaries, which influenced the resulting Ni structure, were also investigated.

While several questions remain, notably related to possible artefacts induced by TEM sample preparation and extrapolation of the reaction mechanism to bulk samples, the acquisition of EFTEM images, whilst the sample reacts (slowly), appears as a powerful technique to assess solid-gas interactions at high temperature with nm-scale resolution.

6 Oxidation of Ni/YSZ composites

Oxidation of the Ni/YSZ composites initially reduced in Chap. 5 is studied here, whilst increasing the temperature up to 500-850 °C in 3.2 mbar of O_2. The results demonstrate that the oxidation mechanism of Ni/YSZ is similar to that controlling the oxidation of Ni particles. While a built-in field determines the growth of the first few nm of oxide, Ni^{2+} diffusion along the NiO grain boundaries controls most of the oxidation process. As this process is not balanced by inward transport of O^{2-}/O_2 or interface recession, voids are observed to form at the Ni/NiO interfaces. In addition, Ni of the internal metallic core is observed to self-diffuse to maintain some contact with the NiO film and in turn the oxidation process may continue in some regions, while the reaction is hindered elsewhere.

6.1 Experimental details

6.1.1 Materials

The nickel/yttria-stabilised zirconia (Ni/YSZ) samples that were prepared by focused ion beam (FIB, Zeiss NVision 40 CrossBeam) and investigated during reduction in Chap. 5 were characterised in this chapter during a subsequent oxidation reaction. Two sets of reduced Ni/YSZ samples were hence monitored here: TEM lamellae welded onto stainless steel grids and weld-less H-bar thin windows.

6.1.2 Electron microscopy

A Gatan Inconel 652 double-tilt heating holder was used for all experiments. As during reduction, the ETEM was operated at 300 kV at a constant electron dose rate of $\sim 10^3$ e^- nm^{-2}.

Structural and crystallographic changes during Ni/YSZ oxidation

The reduction of the TEM lamella welded onto a stainless steel grid investigated in this section was presented in Chap. 5.1.2. The specimen underwent reduction in 1.3 mbar of H_2 up to 500 °C, whilst heating at a rate of 2 °C min^{-1}, and was then maintained at 500 °C for 120 minutes. After cooling down to room temperature, H_2 was pumped out of the environmental cell and O_2 was introduced at a flow of 2 ml_N min^{-1}, corresponding to a measured pressure of 3.2 mbar around the sample. The temperature was increased to 200 °C and kept constant for 30 min for stabilisation. The sample was then heated to 250 °C, whereupon a temperature ramp of 2 °C min^{-1} similar to that used during *in situ* reduction was started (Fig. 6.1). The temperature was increased manually by 10 °C every 5 min and at each step, bright-field (BF) images and selected area diffraction patterns (SADPs) were acquired to study the evolution of the Ni/YSZ microstructure during oxidation. The radially averaged intensity of the NiO reflections measured in the diffraction patterns served as an indicator of the reaction kinetics.

After oxidation, scanning electron microscopy (SEM) in a FEI XL30 SFEG and FIB in a Zeiss NVision 40 CrossBeam were used to characterise the topography and the internal structure of the reoxidised NiO grains, respectively. Based on secondary electron SEM images acquired at sample tilt angles of -15°, 0° and +15°, three-dimensional reconstructions of the topography of a Ni grain were obtained using the program MeX [280], in the form of a stereoscopic image.

Ni/YSZ volume expansion using energy-filtered TEM

The H-bar sample that was reduced up to 850 °C with an overall heating rate of 4 °C min^{-1} in Chap. 5.1.2 was characterised here during oxidation. After cooling down to room temperature and evacuation of H_2 from the environmental cell of the micro-

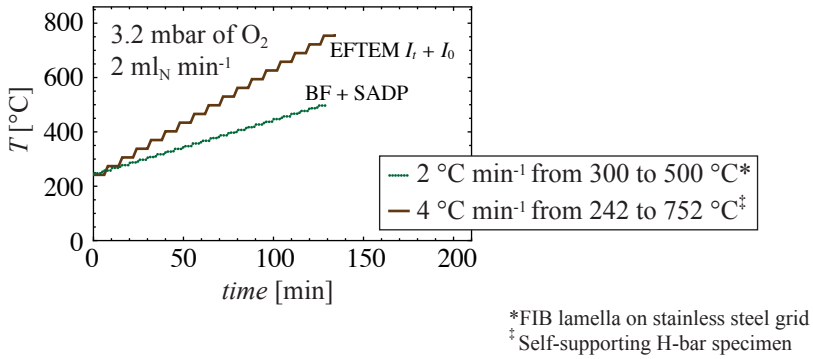

Figure 6.1 – Time and temperature parameters used to approximate constant heating rates during reduction of different samples. A set of measurements was performed at each step.

scope, O_2 was introduced at 2 ml_N min^{-1}, which resulted in 3.2 mbar of O_2 around the specimen. The temperature was then increased to 242 °C, where a heating ramp was started. Unfiltered BF images I_t and energy-filtered BF TEM (EFTEM) images of the zero-loss I_0 (with a slit width Δ of 10 eV centred on 0 eV of energy-loss, collection semi-angle of 6.8 mrad) were acquired every 6 minutes at a constant temperature, before increasing the temperature by a step of 32 °C over 2 min to maintain an overall rate of 4 °C min^{-1} up to 752 °C (Fig. 6.1). The temperature was then maintained above this temperature for 30 min.

All of the I_t and I_0 recorded images were aligned by cross-correlation after filtering using a Sobel operator [219]. Once aligned, I_t and I_0 were processed to yield as illustrated in Fig. 5.2a total inelastic mean free path images t/λ of the structure at each temperature step (where t is the effective thickness in nm and λ is the total inelastic mean free path, estimated here to be $\lambda_{Ni} = 127$ nm in Ni and $\lambda_{NiO} = 155$ nm in NiO, see Appendix D.1). The intensity measured within holes of the t/λ images was used to monitor the contributions of the O_2 gas to the plasmons. As in Chap. 5, the intensity in the ceramic phase was used as an invariant reference to remove possible intensity offsets. Each thickness map was divided by the average number of counts in its YSZ backbone and then multiplied by the average intensity in the YSZ phase measured within the entire t/λ sequence to yield images with comparable intensities.

6.2 Experimental results

6.2.1 Ni surface oxidation at room temperature

As the H_2 gas is pumped out of the environmental cell and the O_2 partial pressure increases to 10^{-7} mbar, the surface of the Ni grains oxidises as shown in Fig. 6.2. As already observed in Chap. 4, pseudo-DF images of the HRTEM image highlight the formation of a stable polycrystalline film of 3-4 nm of thickness (Fig. 6.2a-c). While NiO (200) and Ni (111) reflections overlap, it appears that only small randomly oriented domains are observed here. Those are inferred to be NiO as the Ni matrix is expected to be monocyrstalline based on the observations performed during reduction in Chap. 5. Ni nanoparticles that were formed during reduction in Chap. 5 also oxidise in these low pressure conditions (Fig. 6.2d-f).

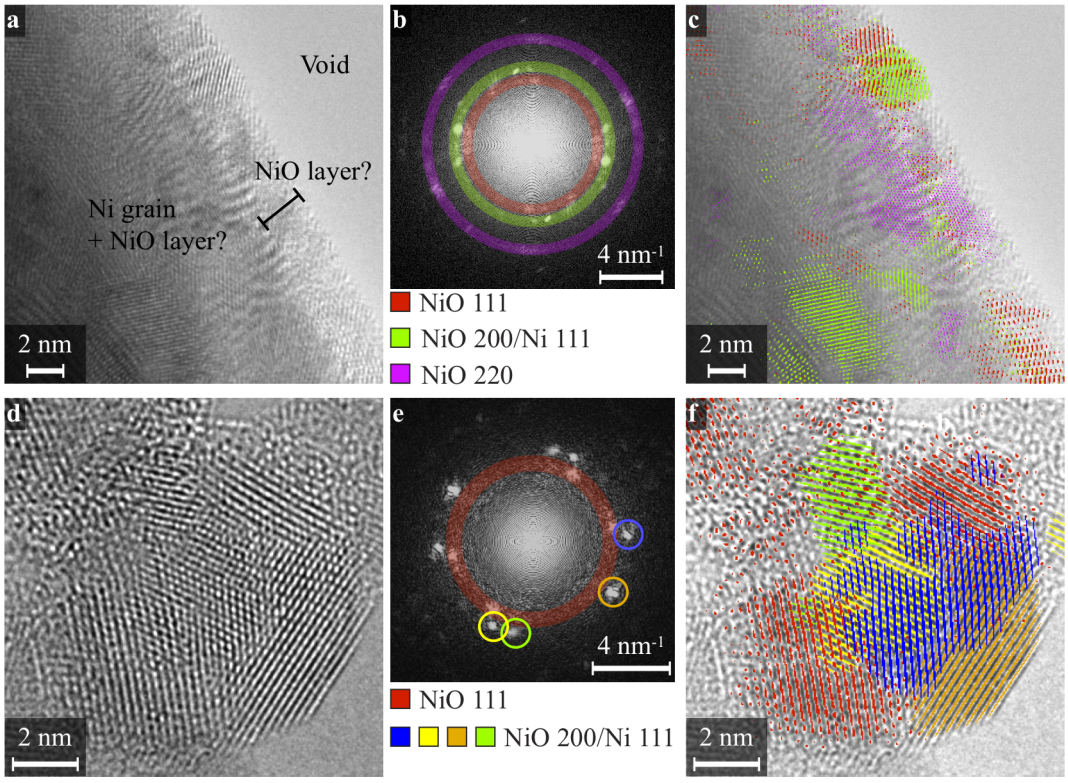

Figure 6.2 – NiO nucleation at room temperature in $\sim 10^{-7}$ mbar of O_2. (a) HRTEM image showing the border of one Ni grain, where a layer of polycrystalline domains is observed and (b) its FFT. (c) Superposition of inverse FFT (pseudo-DF) images generated from NiO (111) reflections (red), both NiO (200) and/or Ni (111) reflections (green) and NiO (220) reflections (magenta) with the HRTEM image added as a background. (d) HRTEM image of an oxidised Ni nanoparticle that initially formed during reduction with (e) its FFT and (f) superposition of inverse FFT images of NiO (111) reflections (red) and NiO (200) and/or Ni (111) reflections (blue, yellow, orange and green), with the HRTEM image added as a background.

6.2.2 Structure and crystallography during Ni/YSZ oxidation

Fig. 6.3 shows a sequence of BF images illustrating the *in situ* oxidation of the Ni/YSZ composite anode when 3.2 mbar of O_2 is introduced in the environmental cell and the temperature increased to 500 °C. The reduction of this sample was followed in Fig. 5.4 during reaction in 1.3 mbar of H_2, whilst heating at a rate of 2 °C min^{-1} up to 500 °C, and maintained 120 minutes at this temperature. As mentioned in Chap. 3, those experimental parameters did not allow to reach full reduction and the grains are composed of large Ni grains and some small NiO domains at the beginning of the oxidation experiment in Fig. 6.3a. Indeed, NiO reflections that are coherent with Ni are observed along a [012] zone axis at the beginning of the heating ramp, which results in double diffraction (triangles for initial NiO reflections and arrowheads for double diffraction in Fig. 6.3a).

As the temperature increases to 290 °C and above (Fig. 6.3b-e), NiO domains that are randomly oriented become apparent, which in turn create rings in the diffraction patterns. Changes in the structure involve the closing of the nanovoids that were created during reduction through the growth of small NiO domains (Fig. 6.3c-e). In contrast to the reduction process, which started at the NiO/YSZ interfaces (Fig. 5.4), oxidation occurs uniformly over the Ni surface in the form of small randomly oriented NiO domains, which induce an irregular contrast in the micrographs. At 500 °C (Fig. 6.3e), reflections resulting from both Ni and double diffraction are not observed in the SADP, demonstrating full oxidation of the region selected by the SA aperture.

The disappearance of nanovoids through the growth of randomly oriented NiO domains is observed more clearly in Fig. 6.4, which details the oxidation of one Ni grain at higher magnification. Contrast features that appear similar to the coherent twinned domains observed in Fig. 5.16a are arrowed in white at 260 and 280 °C in Fig. 6.4. As observed in Figs. 5.5 and 5.14, Ni nanoparticles are supported by a film at the beginning of the oxidation reaction. Those then incorporate in the growing NiO phase as the reaction proceeds (arrowed in black in Fig. 6.4). NiO seems to restructure at 500 °C and regions with dark contrast appear at the position of the holes created during reduction (see contrast changes in region circled in Fig. 6.4m-n).

Fig. 6.5 shows the sequence of radially averaged intensities measured in the SADP patterns acquired throughout the oxidation process, whilst heating at an overall rate of 2 °C min^{-1}. The intensity in the NiO reflections is measured to be > 0 initially as a result of an incomplete reduction reaction in Chap. 5 and then increases with temperature. Simultaneously, the intensity measured in the Ni reflections decreases to 0 as the temperature tends to 500 °C, denoting full oxidation of the grains at this temperature. All of the observed reflections can be indexed as either Ni and NiO using the software JEMS [36].

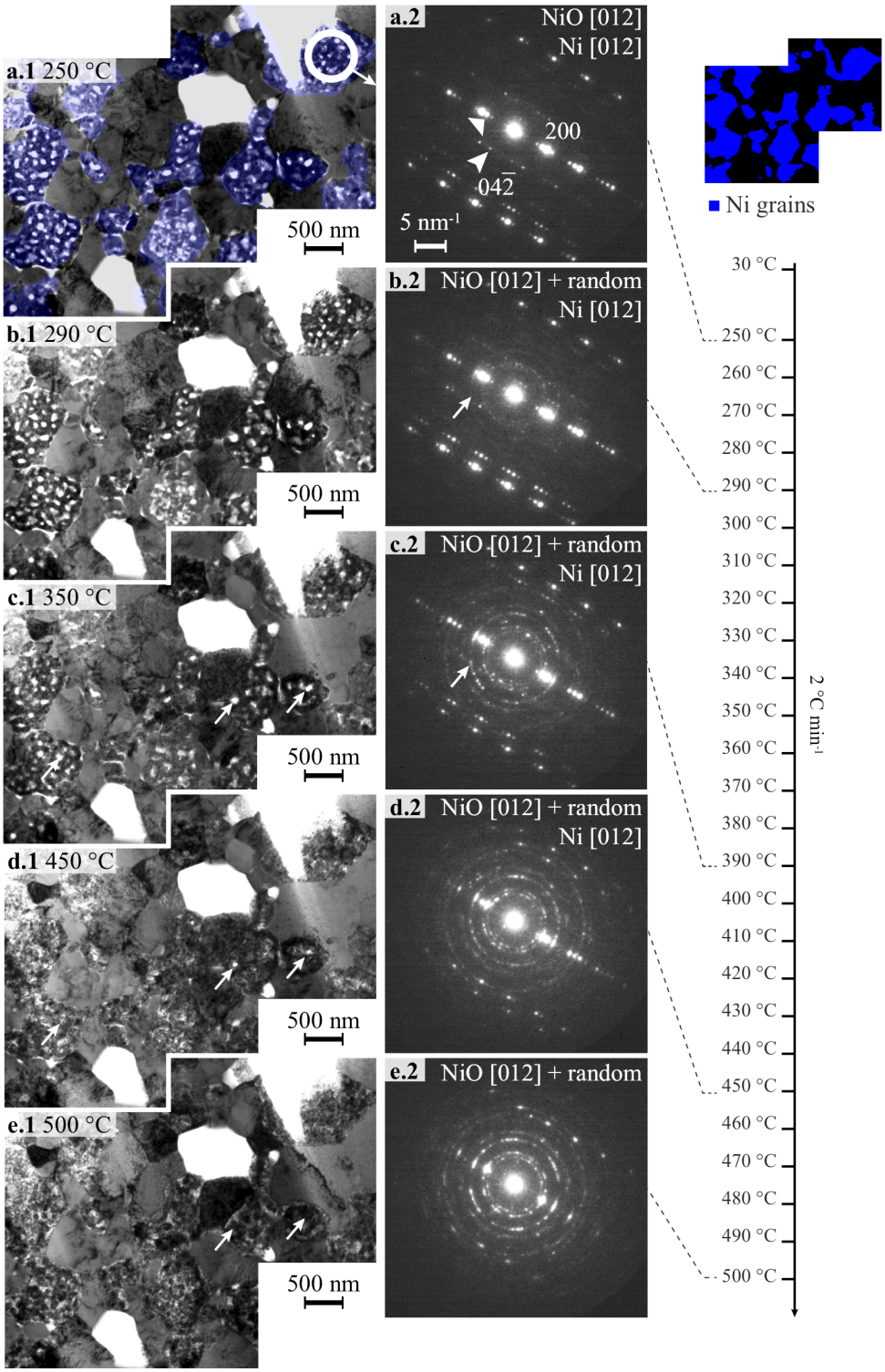

Figure 6.3 – (a-e) Stitching of 2 BF TEM images acquired during *in situ* oxidation of a Ni/YSZ anode in 3.2 mbar of O_2 up to 500 °C. Corresponding diffraction patterns from the region circled in (a.1) are shown, along with a processed Ni map obtained by EFTEM. Arrows show voids that are about to close in the images and randomly oriented Ni reflections in the SADPs. Triangles point to initial NiO reflections and arrowheads show double diffraction in SADPs.

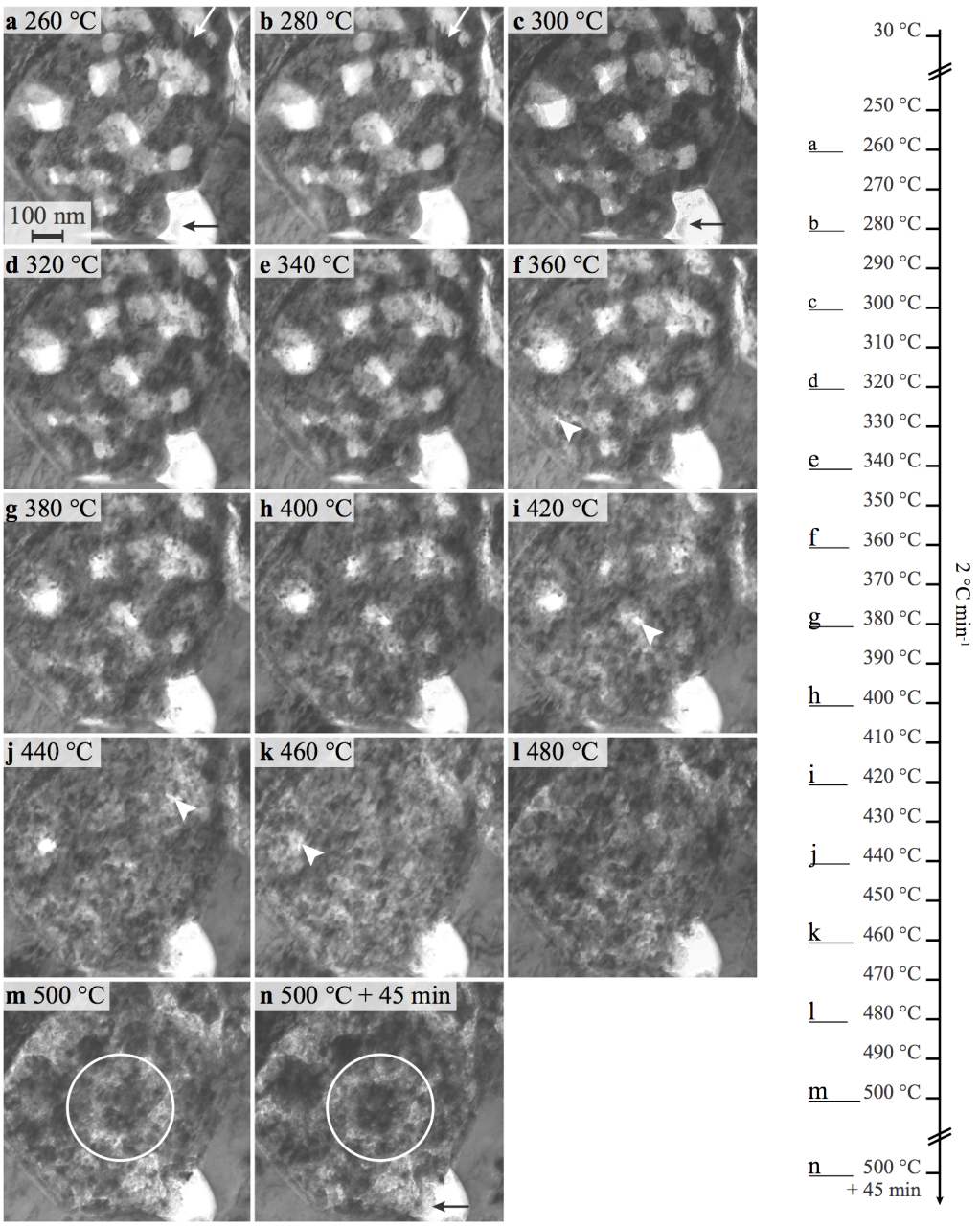

Figure 6.4 – (a-m) Sequence of BF images showing a higher magnification view of one Ni grain during oxidation, whilst heating at a rate of 2 °C min^{-1} in 3.2 mbar of O_2, with (n) showing the NiO structure 45 minutes after reaching 500 °C. White arrows in (a) and (b) show twinning in Ni, black arrows highlight Ni nanoparticles initially supported by a film and white arrowheads indicate intragranular voids on the brink of closing. The circled areas in (m-n) highlight contrast/structural changes at 500 °C.

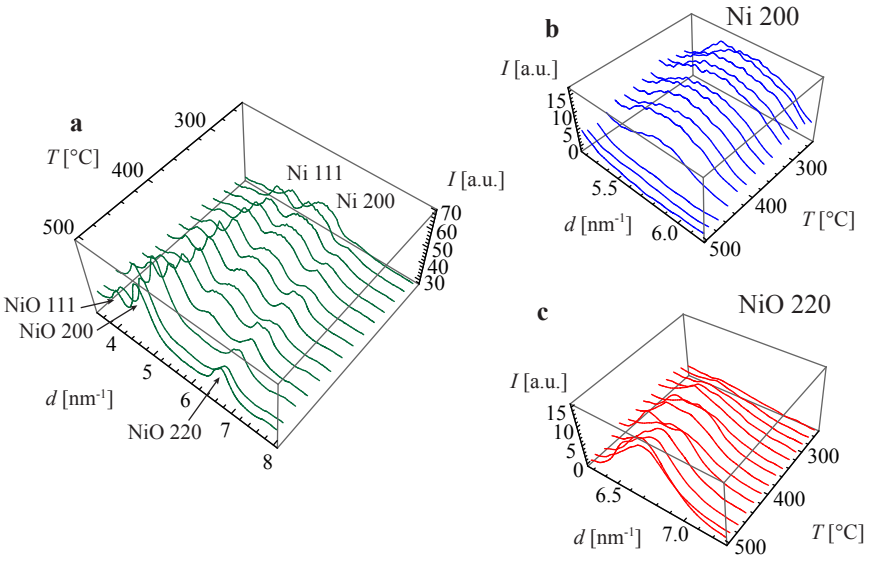

Figure 6.5 – (a) Radially averaged profiles of electron diffraction patterns acquired during *in situ* oxidation at 2 °C min^{-1}. (b) The Ni (200) reflections disappear, as shown after removing a power law background (Eq. 2.1), whilst (c) the NiO (220) reflections appear simultaneously as the temperature increases.

Reaction kinetics from NiO reflections

As mentioned above, the Ni and NiO phases that are initially present within the region selected by the SA aperture are both monocrystalline, coherent and oriented along the [012] zone axis. Those hence present a well defined symmetry in the SADPs (arrows in Fig. 6.6a). On the other hand, the NiO reflections that form during the oxidation process appear as diffraction rings (arrowheads in Fig. 6.6a). This difference in symmetry in the reciprocal space can be used to select only the NiO domains that formed as a result of reaction with O_2 and remove all of the other Ni/NiO/double diffraction reflections through the application of a suitable mask to each diffraction pattern (Fig. 6.6b). After application of the mask, the background-subtracted radially averaged intensity of each resulting NiO (111), (200) and (220) reflection is integrated over a 0.4 nm^{-1} window centred on each maximum at each temperature (Fig. 6.6c) to serve as an indicator of the oxidation kinetics (Fig. 6.6d). Indeed, by rescaling the integrated intensity of each radially averaged NiO (111), (200) and (220) reflection using a value of 0 as reference for a fully reduced sample and the maximum integrated intensity measured within the sequence, the conversion fraction of the oxidation reaction α can be estimated as a function of temperature T (Fig. 6.6d). These $\alpha - T$ curves, each obtained from a different NiO reflection, can be compared to the oxidation kinetics of Ni particles inferred from changes in shapes of the Ni $L_{2,3}$ white lines in the electron energy-loss spectra (EELS) acquired in Chap. 4 (Fig. 6.6d).

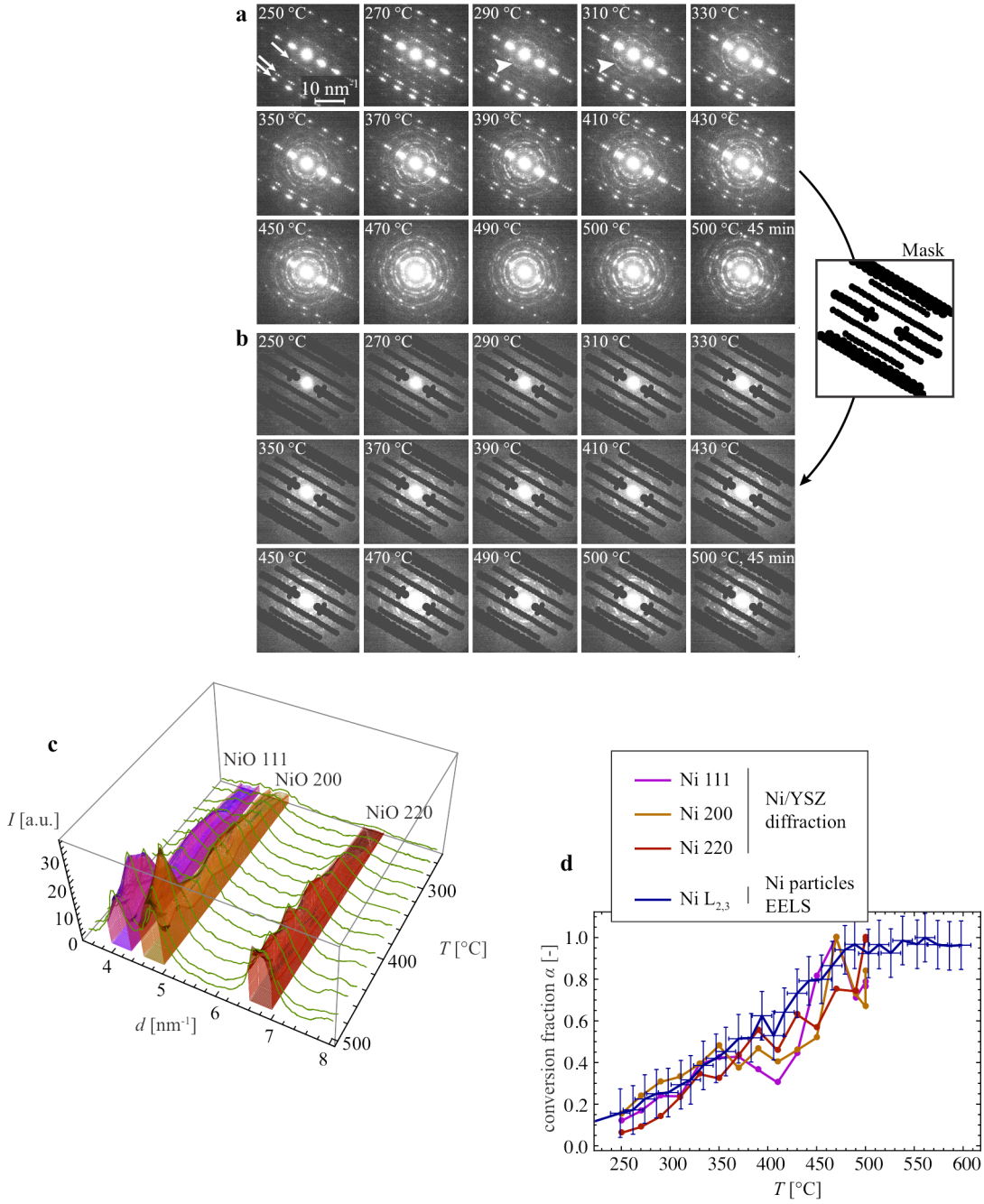

Figure 6.6 – (a) Diffraction patterns acquired whilst increasing the temperature at 2 °C min^{-1} in 3.2 mbar of O_2. (b) Processed diffraction patterns, where the initial NiO/Ni/double diffraction reflections oriented along the [012] zone axis are removed using a mask. (c) Radially averaged profiles of the processed NiO patterns shown in (b) after subtraction of a power law background (Eq. 2.1), where only reflections that result from the oxidation process are observed. (d) Reaction kinetics obtained by integrating over 0.4 nm^{-1} windows each NiO (111), (200) and (220) reflection and rescaling these values using 0 as reference for Ni and the maximum integrated intensity measured in each sequence as a reference for NiO. The reaction kinetics of Ni particles obtained from white lines ratios (4 eV integration windows) in similar reaction conditions (heating rate of 2 °C min^{-1} in 3.2 mbar of O_2) is also shown in (d).

Resulting NiO structure

Whereas the reduced Ni forms a network of bridges surrounding intragranular porosity (Fig. 6.7a), the pores disappear during *in situ* oxidation, with the NiO areas located at the former positions of the Ni bridges appearing less dense at 500 °C. Those regions appear to contain internal voids or a smaller thickness of NiO after oxidation (Fig. 6.7b).

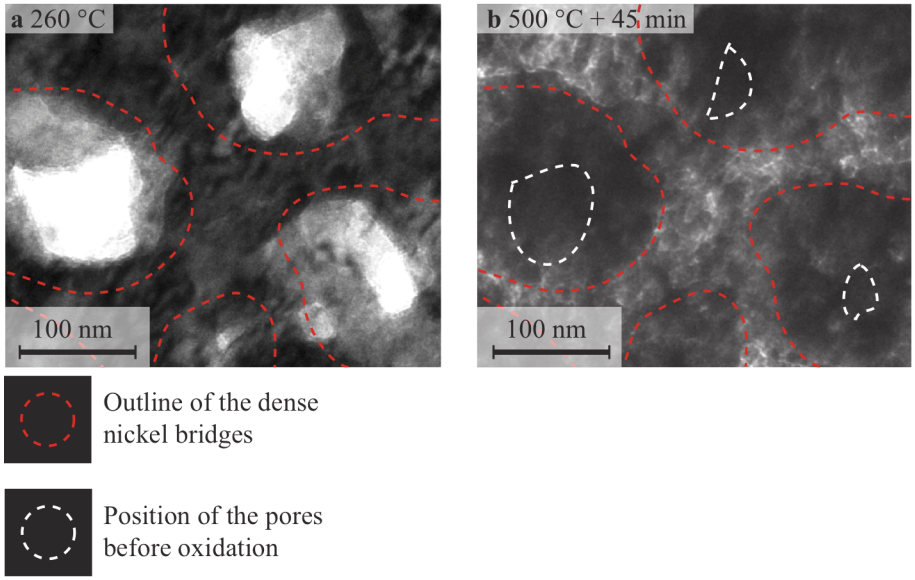

Figure 6.7 – BF TEM images illustrating the transfer of atoms from the initially dense Ni regions to the initial intragranular porosity during oxidation with (a) showing the mainly metallic Ni structure at the beginning of the temperature ramp at 260 °C and (b) the fully oxidised NiO structure at the end of the experiment at 500 °C.

The presence of internal porosity in the oxidised Ni is confirmed by secondary electron SEM images of FIB-milled cross-sections (Fig. 6.8a), in which partially interconnected pores that are ∼50 nm in size are observed in the NiO grains. As oxygen is incorporated in the structure, the Ni phase expands during reoxidation, not only into the original pores (arrowed in Fig. 6.4n) but also out of the sample plane, as shown using SEM followed by three-dimensional reconstruction of the sample surface topography obtained using the program MeX [280] (Fig. 6.8b-c).

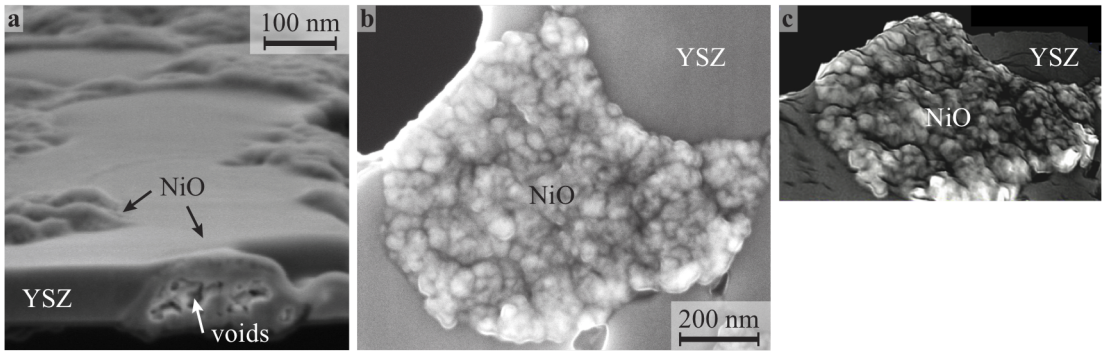

Figure 6.8 – (a) SEM image of a cross-section milled by FIB highlighting internal pores created during oxidation and expansion out of the specimen plane, (b) SEM secondary electron image and (c) corresponding three-dimensional reconstruction of the topography of a NiO grain (stereoscopic image).

6.2.3 Ni/YSZ volume expansion

Fig. 6.9 shows a selection of BF and t/λ images acquired during oxidation of one H-bar thin window in 3.2 mbar of O_2, whilst increasing the temperature at an overall rate of 4 °C min^{-1} up to 752 °C (sample detailed during reduction in Fig. 5.19). Intragranular voids that remain after reduction (Fig. 6.9a) disappear upon oxidation (arrowed in Fig. 6.9b-c). In addition, voids that formed at incoherent NiO/NiO grain boundaries during reduction also disappear due to NiO growth (arrowed in Fig. 6.9d-e). Above 591 °C, regions that contain less material are observed within t/λ (arrowheads in Fig. 6.9i-k). Voids seem to inject within some regions of the oxidising NiO grains, which supposedly separates locally the Ni core from the covering oxide film. In turn, some mobility (presumably) of the Ni core is observed in Fig. 6.9i-k, which indicate some self-diffusion of Ni and vacancies within the structure. A thicker NiO region eventually forms at the position where the Ni core previously agglomerated (arrowheads in Fig. 6.9l).

The intensity in the initial and final t/λ images can be analysed to provide quantitative details about the volume expansion upon oxidation (Fig. 6.10). Two assumptions must first be made: the initial Ni phase is presumed to be fully reduced (the intensity in the NiO reflections in the SADP reported in Fig. 5.19R' is close to 0) and the final structure at 752 °C is assumed to be fully oxidised (t/λ is not increasing upon further exposure to O_2 at this temperature in Fig. 6.10g). In turn, t/λ in the initial Ni phase is multiplied on the position of each pixel by λ_{Ni} (127 nm) and compared to the product of λ_{NiO} (155 nm) with t/λ measured in the NiO phase of the final NiO/YSZ image. The volume expansion of the Ni phase upon oxidation to NiO is measured to vary locally from +53% to +88% with the overall volume gain measured at +83%, which is higher than the theoretical prediction of +71.2% [9].

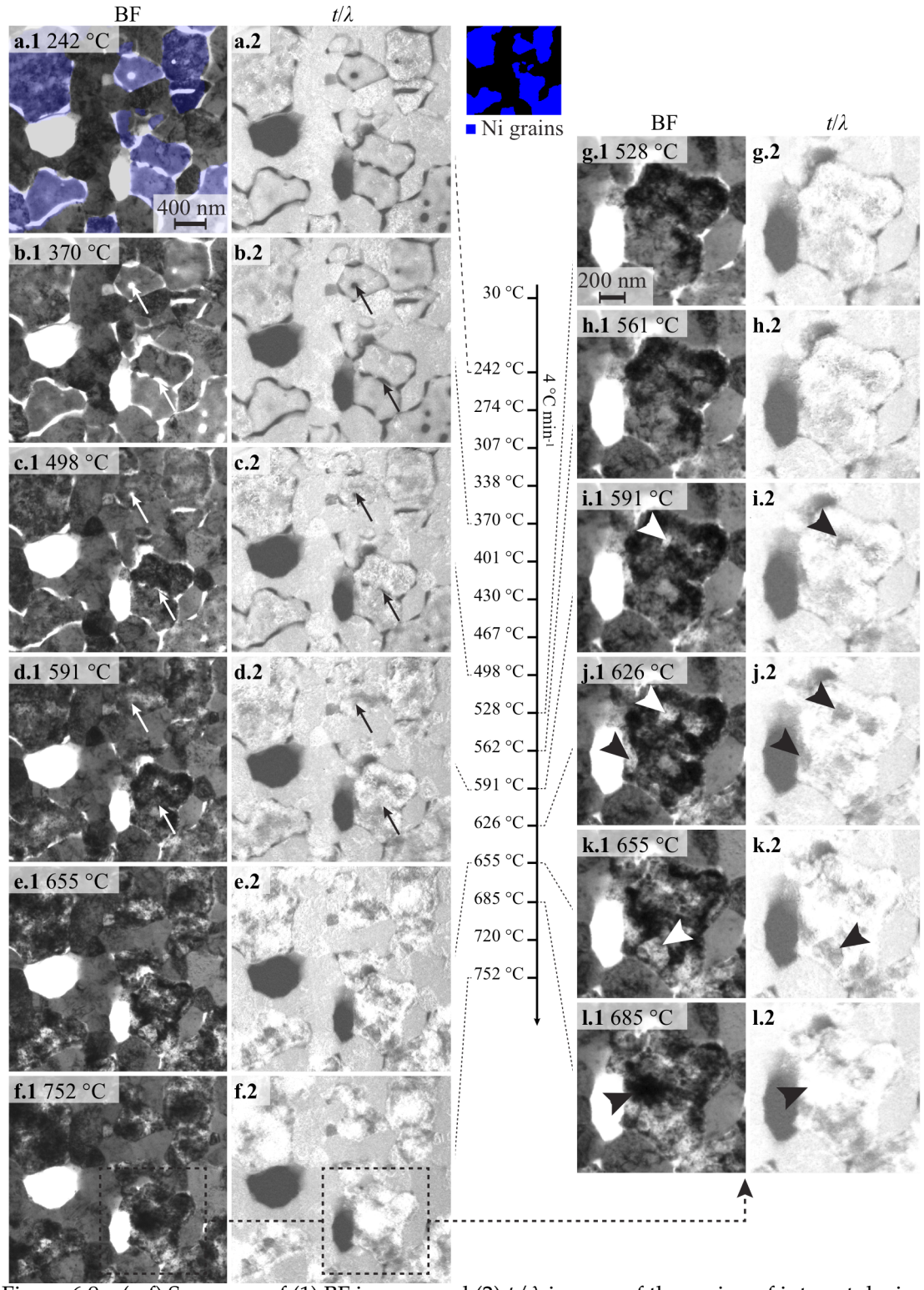

Figure 6.9 – (a-f) Sequence of (1) BF images and (2) t/λ images of the region of interest during oxidation up to 752 °C, whilst heating at a rate of 4 °C min^{-1} in 3.2 mbar of O_2. An EFTEM map of the Ni grains is coloured in blue and superimposed to (a). (g-l) Higher magnification sequence of (1) BF and (2) t/λ images of one selected region between 528 and 685 °C. Arrows show the closing of voids, while arrowheads show internal voids (j-k) and a thick NiO region (l).

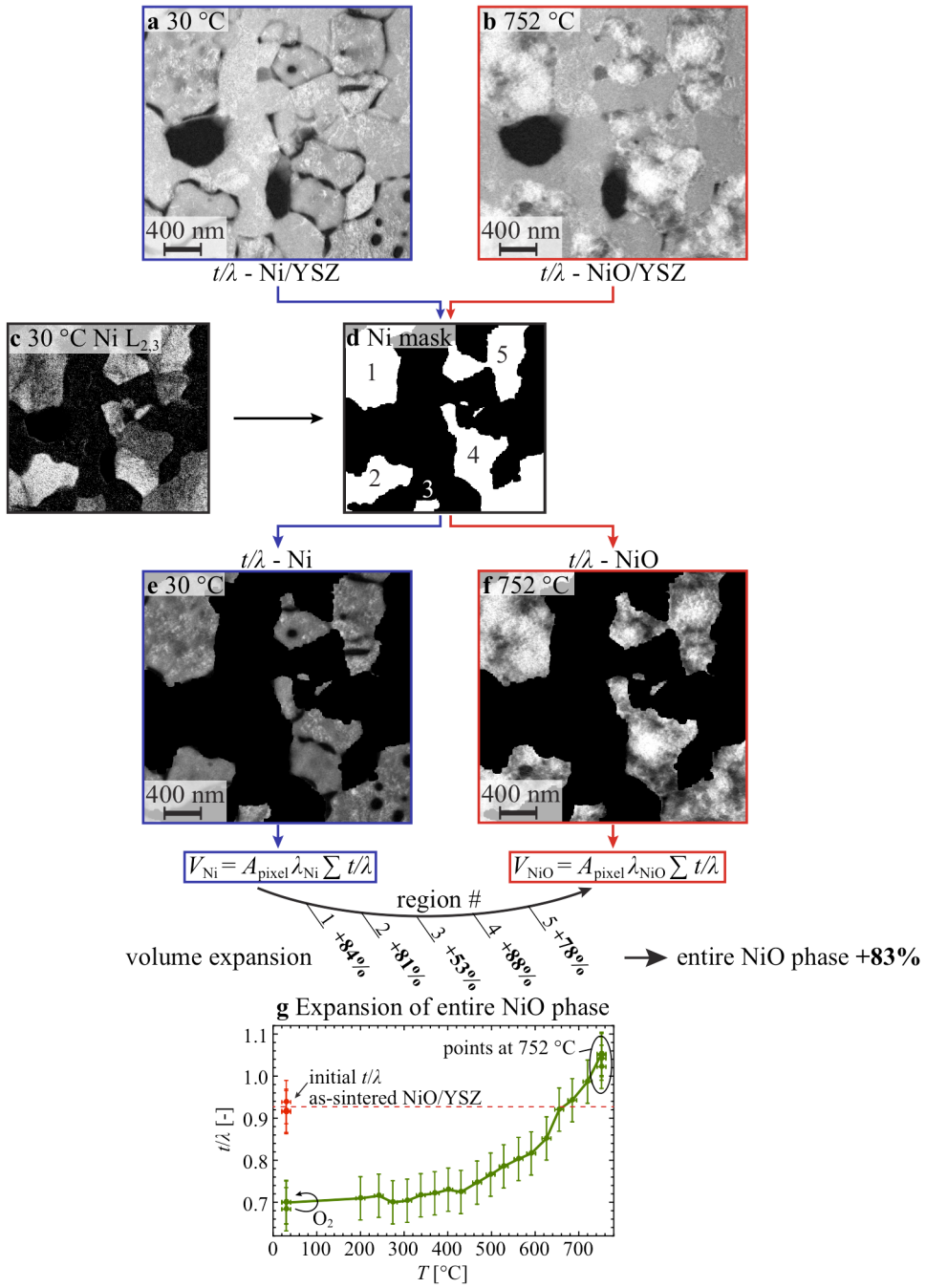

Figure 6.10 – Measurement of volume expansion during oxidation. (a) Initial t/λ image of the reduced Ni/YSZ. (b) Final t/λ image of NiO/YSZ, (c) Ni $L_{2,3}$ elemental map to infer (d), a mask with five Ni regions labelled. From (d), (e) and (f) are obtained and those contain the Ni and NiO phase before and after oxidation, respectively. From (e) and (f) and using λ_{Ni} and λ_{NiO} (127 and 155 nm, respectively), the volume expansion is measured to be +83%. The evolution of t/λ in the entire NiO phase shown in (e-f) is plotted as a function of temperature in (g), where data points acquired above 750 °C are circled. Values of t/λ measured at the same position in the initial as-sintered NiO/YSZ structure at 30 °C in high vacuum conditions (10^{-6} mbar) are also plotted in red. The introduction of O_2 does not increase significantly t/λ as arrowed in (g).

6.3 Discussion

6.3.1 Field-assisted surface oxidation

The initial stages of the oxidation of Ni in the shape of particles or in Ni/YSZ composites appear similar. In both cases, a stable NiO film of 3-4 nm forms in 10^{-7} mbar of O_2 as a result of a field-assisted mass transport process described by Mott and Cabrera [80]. As already mentioned in Chap. 4, after O_2 adsorption, dissociation and growth of NiO until impingement, electrons tunnel through the continuous NiO layer to ionise adsorbed oxygen, which in turns creates a large electric field that drives the transport of ions across the NiO film. This process stops once the NiO layer is too thick ($<$ 3-4 nm) for electrons to tunnel. This process does not appear to inject visible voids at the Ni/NiO interfaces, which tends to indicate either that the Ni/NiO interface may recess and annihilate vacancies that may have formed at this position or that inward transport O^{2-} may play a role during those initial stages of the oxidation process. Such NiO films were also observed using TEM after *ex situ* oxidation of Ni nanoparticles [99].

6.3.2 Structural and crystallographic changes during oxidation

The NiO grains are polycrystalline with irregular shapes after oxidation (Figs. 6.3 and 6.9) and appear similar to the NiO particles observed after oxidation in Chap. 4. In addition, these *in situ* oxidation observations corroborate investigations on a TEM lamella made by Waldbillig *et al.* [17], who observed similar polycrystalline diffraction rings after *ex situ* oxidation of a NiO/YSZ TEM sample. Those authors suggested that the intragranular pores that form during reduction provide sites at which NiO can nucleate in different orientations. Based on the present observations and those of Chap. 4, where randomly oriented NiO domains were also observed to nucleate on dense Ni structures, it appears more likely that the nucleation of this polycrystalline NiO film on monocrystalline Ni is inherent to the reaction and not related to the initial Ni structure. Indeed, the driving force for NiO nucleation appears large even in a low O_2 pressure of 10^{-7} mbar, where NiO domains with random orientations nucleate in a fraction of a second and cover the entire Ni surface (Fig. 4.2). Specific Ni/NiO orientation relationships that may reduce the interfacial energy are not required for NiO to nucleate on Ni and hence not observed here.

Fig. 6.8 demonstrates that Ni expands upon oxidation as multiple internal voids are injected within each NiO grain. As the reaction kinetics inferred from the evolution of the NiO reflections in Fig. 6.6 appears similar to that measured using EELS when oxidising Ni particles in Chap. 4, the mechanisms controlling the oxidation of Ni/YSZ and Ni particles are similar. The oxidation process hence involves in both cases the diffusion of Ni^{2+} along the NiO grain boundaries [92]. As inward diffusion of O^{2-} is several orders of magnitude slower [79], this process injects vacancies at the Ni/NiO interfaces and these do not appear to be annihilated by interface recession or movement

of dislocations. As vacancies coalesce into voids at Ni/NiO interfaces, Ni may separate in some regions from the NiO phase and in turn cannot provide new Ni^{2+} that can diffuse through the NiO film. As a result, the reaction is blocked locally as the supply of Ni^{2+} is interrupted. Ni is then observed to self-diffuse along with Ni vacancies to maintain NiO/Ni contact in specific regions as indicated by arrowheads in the sequence shown in Fig. 6.9i-l. This process creates some NiO regions that are thicker after oxidation when compared to the other parts of the NiO grain, where Ni/NiO contact was lost earlier (arrowhead in Fig. 6.9l). As a result of those imbalanced diffusion processes of Ni^{2+} and O^{2-}/O_2, initially dense Ni regions become porous after oxidation, while denser/thicker NiO regions appear at the position of initial voids (Fig. 6.7).

As shown in Fig. 6.10, measurements of t/λ before and after reaction overestimate the volume expansion induced by the oxidation process. Indeed, a value of +83% is estimated here, which differs from the theoretical prediction of +71.2% [9]. Moreover, the effective final NiO volume after oxidation (excluding internal voids) is measured to be 13% larger than the initial NiO volume measured after sintering. This apparent gain of new NiO material may be explained by different experimental aspects. Diffraction contrast may alter to some extent the intensity in the t/λ images. However, those effects were observed to be minimised when averaging over a sufficient number of pixels in Chap. 5 and reliable results were obtained when studying the reduction of NiO/YSZ composites. Some material from the sample, support or holder may also redeposit at the region of interest as a result of the high temperature involved in the experiment. However, such effect would be expected to contribute to a steady volume increase, while t/λ is observed to stabilise at 752 °C. It thus appears more likely that this apparent volume increase is an artefact that is induced by the irregular NiO structure that forms during oxidation. While the reduced Ni structure is composed of large monocrystalline grains with large intragranular voids that are observed to run through the specimen, the NiO structures observed after *in situ* oxidation are composed of small randomly oriented grains and a significant amount of internal voids as shown in Figs. 6.3 and 6.8. The oxidised structures hence contain a large number of internal defects/surfaces/interfaces, which may induce additional plasmonic excitations. In turn, the log-ratio method used to measure the thickness may be falsified if these features are heterogeneously distributed [262]. If those excitation sources are homogeneously distributed in the material, the log-ratio method could in principle still be valid, provided that the total inelastic mean free path is adjusted. While providing a trend about the thickness evolution, it appears that the log-ratio method cannot provide directly a quantitative assessment of the volume expansion induced by Ni oxidation to NiO without additional investigations about the strength of those interfacial excitations. It should be added that the presence of 3.2 mbar of O_2 around the specimen does not alter significantly the measurement of t/λ as it results in a negligible increase in intensity of $2 \cdot 10^{-3}$ (Fig. 6.10g).

6.3.3 Reaction kinetics

The reaction kinetics measurement inferred from NiO (111), (200) and (220) reflections is only an estimate as it may be affected by several factors not related to the chemistry of the specimen. Thermal drift of the holder induces small changes in orientation of the sample throughout the reaction, which modifies the intensity in the diffracted spots. In addition, the investigated region may be slightly different from one SADP to the other due to variations in the SA aperture position. However, these reaction kinetics results coincide with those obtained from white lines ratios in Chap. 4 and hence demonstrate that the rate-controlling oxidation mechanism of Ni particles and Ni/YSZ composites is the same. In addition, while delayed to a higher temperature due to a lower conductivity of the thin window support and the increased heating rate, the evolution of t/λ measured in the Ni phase of the H-bar specimen also appears to follow the same oxidation behaviour.

The reaction of Ni/YSZ composites observed in this chapter hence involves the solid-state diffusion of Ni^{2+} along the NiO grain boundaries, which results in a kinetics that deviates from the classical parabolic regime as the number of fast diffusion paths evolves throughout the reaction [79, 91, 92]. On the other hand, as reviewed in [26], different Ni/YSZ oxidation kinetics are reported in the literature based on thermogravimetry measurements, which range from parabolic, deviation from parabolic, logarithmic to cubic. The discrepancy in those literature results appears to be related to differences in microstructure, gas permeation properties and experimental parameters. As mentioned by Faes and co-workers [26], mass transfer of O_2 to metallic Ni regions may become rate-limiting, especially at high temperature and when the oxygen pressure is low. In turn, an inhomogeneous oxidation process is observed, where a NiO oxidised layer proceeds from the O_2 accessible surfaces to the other parts of the sample in the form of a reaction front. At low temperature and when the oxygen pressure is high, the oxidation reaction becomes homogeneous and is controlled by solid-state diffusion, in agreement with the results presented in this chapter. The transition between one regime to the other depends on experimental parameters and microstructural parameters such as tortuosity and porosity, which are specific to each study (and often not characterised in detail in thermogravimetric studies).

Contrary to the results presented here in Fig. 6.6, Fouquet *et al.* measured using thermogravimetry that the oxidation of Ni particles proceeds faster than the reaction of a Ni/YSZ sample, with both samples previously reduced up to 1100 °C, whilst heating at a rate of 10 °C min^{-1} [63]. Based on the results of Chap. 3, where Ni particles were observed to sinter at temperatures $\geq$ 600 °C in the ETEM, it appears that those authors investigated the oxidation of a dense Ni pellet, in which the mass transport of the reactive gas is limited. On the other hand, the YSZ backbone reduces sintering during reduction and maintains to some extent permeation paths for O_2 during oxidation of Ni/YSZ composites. Their results hence appear to reflect mass-transfer limitations of the gas in their microstructure rather than the intrinsic oxidation mechanism of Ni.

Overall, the results obtained here highlight that, in the absence of O_2 mass-transfer limitations, the oxidation of Ni/YSZ is controlled by the same mechanisms as Ni particles and hence that properties intrinsic to the Ni/NiO system are determining the reaction kinetics.

6.3.4 Factors affecting ETEM results

The same effects as those listed in Chap. 4.3.4 may alter the observations presented here. Based on regular comparisons with regions that were not irradiated by the electron beam during reaction, no significant influence was observed for the dose used in the present work. However, a post-exposure scanning TEM (STEM) energy-dispersive X-ray spectroscopy (EDX) characterisation of a H-bar sample reduced and then oxidised in a tubular oven (reduction at 700 °C during 3 hours in 9% H_2-91% N_2, oxidation at 700 °C during 3 hours in air) reveals Ga segregation at the NiO grain boundaries, with this element originating from FIB sample preparation (Fig. 6.11). As the dominant Ni^{2+} diffusion process that controls the overall reaction occurs at the NiO grain boundaries, it is expected that the presence of Ga traces at this position affect the reaction rate. However, both the reaction kinetics estimated using the NiO reflections and the structure of the NiO grains after oxidation appear similar to the observations of Chap. 4, where the oxidation of Ni was studied in the absence of Ga contamination. It hence appears that Ga does not alter significantly the overall reaction mechanism.

6.3.5 Qualitative description of the oxidation mechanism of Ni/YSZ

The results of this chapter are summarised qualitatively in Fig. 6.12. After nucleation and impingement of NiO domains on the Ni surface at room temperature in high vacuum conditions (10^{-7} mbar of O_2), a thin polycrystalline NiO film grows to stabilise at a thickness of 3-4 nm (Fig. 6.12a). This initial NiO growth is induced by the tunnelling of electrons through the thin oxide film to ionise oxygen that is adsorbed on the NiO surface. In turn, a large electric field is built within the oxide film, which drives the movement of ions across the NiO to continue the oxidation process [80]. This mechanism stops once the transport of electrons through tunnelling becomes negligible. Voids are not observed at Ni/NiO interfaces once the NiO layer has formed, presumably due to the recession of the Ni/NiO interfaces, movement of dislocations and/or inward diffusion of O^{2-}.

Above 250 °C, the growth of the NiO film continues through a diffusion-controlled process, where Ni^{2+} diffusion along the NiO grain boundaries appears to be the main rate-limiting process (Fig. 6.12b), with the number of fast diffusion paths evolving with reaction time and temperature. This process is probably assisted by an electric field as electrical neutrality in the oxide film is unlikely to be a fully valid assumption at this length scale [79] (especially in the presence of the electron beam). As inward diffusion of O_2 is several orders of magnitude slower, voids nucleate at the Ni/NiO

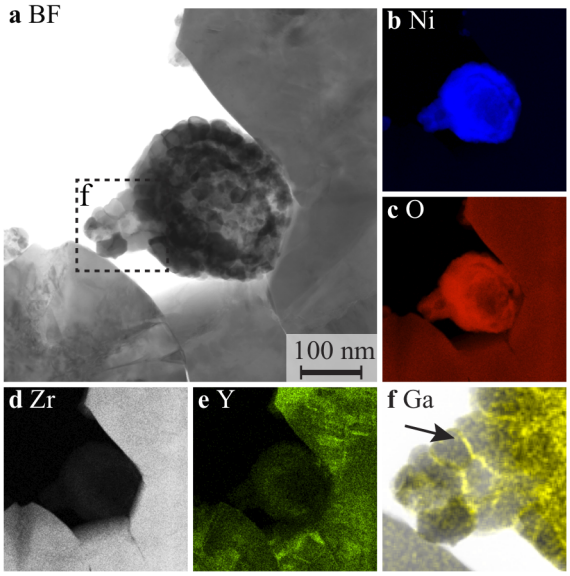

Figure 6.11 – (a) STEM BF image of a sample reduced in forming gas (9% H_2) during 3 hours at 700 °C and then oxidised in air during 3 hours at 700 °C along with corresponding STEM EDX maps of (b) Ni Kα, (c) O Kα, (d) Zr Kα, (e) Y Kα. A superposition of a STEM BF image of one region of interest with a STEM EDX Ga Kα map is shown in (f), which highlights Ga segregation at the NiO grain boundaries (arrowed).

interfaces, which in turn hinders the reaction locally. Ni and vacancies are observed to self-diffuse to maintain Ni/NiO contact in some regions (Fig. 6.12c). The final NiO thickness will eventually appear thicker at the positions where Ni/NiO contact was maintained throughout the reaction. At the end of the oxidation experiment, porous polycrystalline NiO structures are observed, with areas that were initially dense prior to reduction now appearing less dense/thick than the NiO regions that formed at the position of initial voids (Fig. 6.12d).

While the presence of oxide scale cracks could not be observed in the set of experiments presented here, this process is also expected to occur during the oxidation of Ni/YSZ samples similarly to the observations of Chap. 4.

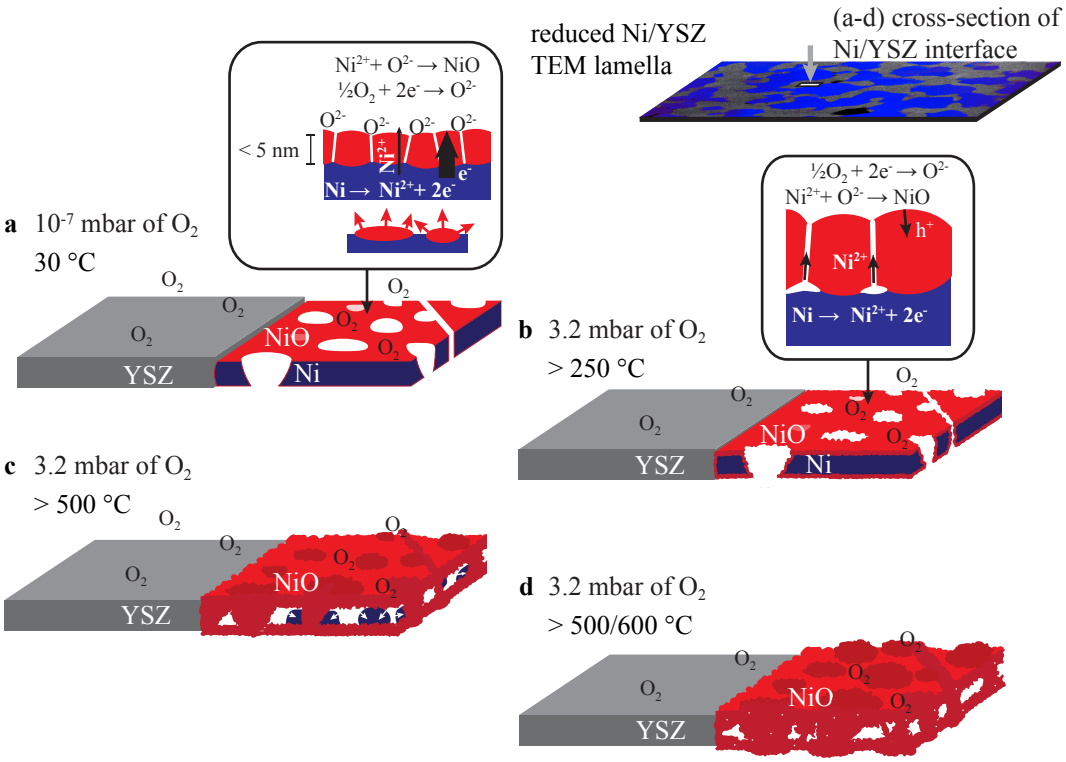

Figure 6.12 – Qualitative description of the oxidation mechanism of the Ni/YSZ composite samples in the ETEM showing in (a) a thin NiO layer forming at room temperature in 10^{-7} mbar of O_2 as a result of a process described by Cabrera and Mott [80], (b) the growth of the NiO layer above 250 °C, a process controlled mainly by the diffusion of Ni^{2+} along the NiO grain boundaries (probably assisted by an electric field), (c) Ni and vacancies self-diffusion to maintain some Ni/NiO contact as vacancies are injected at the Ni/NiO interfaces, (d) formation of a porous polycrystalline NiO structure, with initially dense Ni regions now appearing porous and denser/thicker NiO regions at the position of initial voids.

6.4 Concluding remarks

The combination of different electron microscopy techniques, either available in the environmental TEM or involving post-exposure characterisation using FIB and TEM, allowed the investigation of the oxidation of FIB-prepared Ni/YSZ samples. Using the sequence of diffraction patterns, the evolution of the radial intensity of the NiO reflections that formed due to oxidation was used to estimate the reaction kinetics, which was measured to be identical to that obtained by EELS in the same reaction conditions when oxidising Ni particles in Chap. 4. In addition, the structural changes observed here corresponded to those obtained in Chap. 4, demonstrating that the mechanism controlling the oxidation of Ni/YSZ composites and Ni particles is similar.

Oxidation of Ni/YSZ first involves the growth of a polycrystalline film of NiO of 3-4 nm at room temperature in high vacuum conditions, which was observed to form rapidly

as a result of a field-assisted diffusion process. At higher temperature in 3.2 mbar of O_2, the oxide film growth is mainly controlled by diffusion of Ni^{2+} along the NiO grain boundaries, a process likely to be assisted by an electric field (especially in the presence of the electron beam). As this outward diffusion process is not balanced by inward transport of O^{2-}/O_2 or interface recession, vacancies nucleate as voids at the Ni/NiO interfaces. In turn, Ni self-diffusion is observed to maintain some contact between the metallic Ni core and the NiO film. The final NiO structures are polycrystalline and contain internal porosity, especially in the regions that were initially dense prior to oxidation.

The porous and polycrystalline NiO structures did not allow the use of total inelastic mean free path images to measure the absolute thickness, presumably as a result of internal plasmonic excitations at the multiple interfaces. Those should be assessed in future experiments. Ga was observed to segregate at the NiO grain boundaries during oxidation but did not alter the reaction mechanism.

7 Implications for SOFCs

This chapter summarises the contributions of this research that are related to the solid oxide fuel cell technology. Specifically, the influence of the YSZ phase on the reduction and oxidation reactions of the Ni phase, the parameters controlling the connectivity of Ni after reduction and the mechanisms behind the reduction-oxidation irreversibility of Ni are highlighted here. The implications of those results regarding the durability and the performance of solid oxide fuel cells are investigated. In that regard, suggestions are proposed to improve those aspects of the technology.

7.1 SOFC results

7.1.1 Influence of the YSZ phase on the Ni reaction mechanisms

The influence of the YSZ phase on the NiO reduction and Ni oxidation reactions in Ni-based SOFC anodes is often investigated using thermogravimetry [26, 62, 63]. The reaction rate of NiO particles is usually observed to differ from that of NiO/YSZ composites and these modifications are inferred to result from the presence of the YSZ phase, yet often without any microstructural evidence. The eventual effect of the sample porosity/tortuosity, which controls how the gas permeates through the structure, on the reaction rate is rarely assessed in those thermogravimetry studies, despite its influence on the rate-controlling mechanism. Indeed, the reaction rate may reflect mass transport limitations and not the intrinsic mechanism if the experimental parameters are not adequately chosen as highlighted in [55, 230]. These limitations may then screen any eventual effect of the YSZ phase on the NiO/Ni reaction kinetics. Following those considerations and the results of Chaps. 3-6, environmental TEM enables a detailed understanding of the interactions between YSZ and NiO/Ni as the technique is able to capture *in situ* both the nanostructure and the composition of a small volume of specimen ($\leq \mu m^3$) with a large portion of its surface in direct contact with the gaseous atmosphere.

The results of Chaps. 3 and 5, which investigated the reduction of the same NiO powder as such and when co-sintered with YSZ, demonstrated a modification of the reaction mechanisms in the presence of the YSZ phase. Specifically, Chap. 5 highlighted a complex interplay between the YSZ and the NiO phases during reduction. Similarly to the findings of Bonvalot-Dubois *et al.* [64], oxygen ions appeared to transfer from the NiO phase to the vacancies inherent to the ion conducting YSZ at low temperature. This process enabled the nucleation of the first Ni domains at the interfaces with YSZ at lower temperatures when compared to the NiO free surface. When doubling the heating rate to 4 $^{\circ}C\ min^{-1}$ and increasing the overall specimen size, the reaction proceeded directly through the free surface, highlighting the sensitivity of the reaction to the experimental parameters. In general, those results highlight the importance of the formation of the first domains of Ni in the overall description of the reaction process. Slight changes in experimental parameters or surface properties may then modify the reaction pathway.

On the other hand, the oxidation process of Ni did not appear to be modified by the presence of the YSZ phase. Indeed, comparisons of kinetic data and images acquired *in situ* during oxidation of Ni (Chap. 4) and Ni/YSZ (Chap. 6) in the microscope demonstrated that the intrinsic oxidation mechanisms of Ni were not significantly altered. In the absence of transport limitations of the O_2 gas phase to the Ni reaction sites, Ni hence reacts similarly to Ni/YSZ. Those results are in agreement with the analysis of Faes *et al.*, who related the discrepancies reported in the literature to the presence of gas transport limitations depending on parameters such as temperature and sample tortuosity [26].

7.1.2 Ni connectivity depending on grain boundary symmetry

Automated crystal orientation maps performed in Chap. 5 revealed the influence of the symmetry of the initial NiO/NiO grain boundaries on the final Ni connectivity after activation/reduction. Indeed, the contact between Ni grains was observed to be maintained throughout the reduction reaction across coherent twin boundaries, while incoherent interfaces separated and resulted in two distinct Ni domains after reduction. While a more detailed study is required to assess in detail the number of those coherent twin boundaries in the as-sintered NiO/YSZ composites, those differences in interface symmetry prior to reduction may influence macro scale properties such as Ni conductivity by influencing the percolation of the Ni network during activation of the anode.

It could be envisaged to study the effect of those symmetry properties on the overall mechanical behaviour of the Ni/YSZ system using the methodology introduced in [281], which assessed the influence of the coherency of the Ni/YSZ interface on the overall mechanical behaviour of the Ni/YSZ system. Indeed, the initial structure of the Ni/YSZ composite after activation, which is influenced by the symmetry properties of the grain boundaries, will then affect the coarsening of the Ni phase during operation and in turn the reduction-oxidation stability of the Ni/YSZ anode as shown in the next chapter.

7.1.3 RedOx irreversibility

NiO particles and NiO/YSZ composites undergo irreversible structural changes when experiencing a reduction-oxidation cycle as investigated in Chaps. 3 to 6 and illustrated here in Fig. 7.1. While reduction results in porous Ni that eventually coarsens to form dense structures upon exposure to H_2 at high temperature (Fig. 7.1b), the subsequent oxidation mechanisms induce the formation of NiO grains containing randomly oriented grains and internal porosity (Fig. 7.1c). Indeed, the outward diffusion of Ni^{2+} along the NiO grain boundaries is not balanced by inward diffusion of O^{2-}, which is several orders of magnitude slower. As the Ni/NiO interface cannot recess inward in this spherical geometry to annihilate the vacancies resulting from the unbalanced outward mass flux of Ni^{2+}, voids nucleate inside the NiO structure during oxidation. Although the formation of cracks within the NiO film was observed to allow some permeation of O_2 towards unreacted Ni and hence some inward growth of NiO in Chap. 4, most of the NiO growth occurs outward. In turn, Ni swells upon a redox cycle (Fig. 7.1d).

Assuming a spherical geometry of the as-sintered, reduced and reoxidised Ni/NiO phases in the region circled in Fig. 7.1d, the volume expansion can be estimated based on measurements of the projected areas that are given in the legend of Fig. 7.1. NiO reduction to Ni results in a volume shrinkage of -20%, which is smaller than the expected value of -41% [9] as the reduced Ni structure is not fully dense due to the presence of volume/surface irregularities (see contrast changes arrowed in Fig. 7.1b). During the subsequent oxidation, the apparent NiO volume expands significantly more than

the theoretical prediction of +71% [9] due to the injection of voids inside the NiO structure: an increase of +115% is estimated between Fig. 7.1b and c. While only a rough approximation, the apparent NiO volume is estimated to expand by +65% between the initial as-sintered NiO (Fig. 7.1a) and the final reoxidised structure (Fig. 7.1c). Voids created upon reduction cannot fully accommodate this volume expansion of the NiO phase during reoxidation. In the thin samples investigated in this study, NiO expands freely into the third dimension without applying a significant stress on the YSZ backbone (Fig. 6.8). In a bulk SOFC anode, where the YSZ phase surrounds the Ni grains, the stresses on the YSZ that result from the expansion of the NiO phase are expected to be more significant. Those will accumulate over successive redox cycles [9] and hence result in the cracking of the YSZ phase of the anode and the electrolyte and in turn decrease the performance of the cell [17].

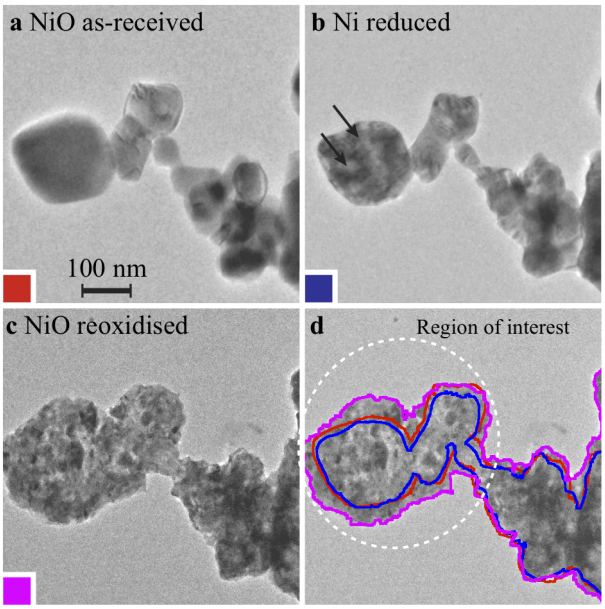

Figure 7.1 – (a) As-sintered NiO particles observed (b) after reduction (at 600 °C during 210 min in 1.3 mbar of H_2) and (c) after reoxidation (at 600 °C after heating from 250 °C at a rate of 4 °C min^{-1} in 3.2 mbar of O_2). In (d), the projected areas of (a–c) are superimposed to the image shown in (c). Reduction results in a shrinkage of the projected area of -15% between (a) and (b) in the region of interest circled in (d), while oxidation induces an expansion of the projected area of +65% between (b) and (c). The projected area of NiO expands by +40% between (a) and (c) after one redox cycle.

7.2 Suggestions regarding SOFC performance and durability

While the conditions inside the environmental TEM differ from those at which the anode of a SOFC is operated, some suggestions can be made based on the findings of this work to improve the efficiency and the durability of Ni-based anodes.

7.2.1 Ni connectivity

Based on the observations of Chap. 5, the use of a low heating rate of 2 °C min^{-1} in H_2 during the first activation of the SOFC anode may increase the initial number of triple phase boundaries Ni/YSZ/porosity due to initiation of the reduction of NiO at the interfaces with YSZ, an effect that is suppressed at higher heating rates. This initial higher number of active sites will however be difficult to maintain at standard operation temperatures of SOFCs (700-800 °C) due to coarsening of the Ni structure. While coarsening may initially improve in some cases the connectivity of the Ni network through the formation of necks between Ni grains (depending on the as-sintered Ni particle size and volume ratio compared to YSZ) [78], such process eventually results in a degradation of the conductivity of the Ni phase as described by Tanasini *et al.* [11]. Based on the observations of Chaps. 3 and 5, an operation temperature of 600 °C or below should minimise the reorganisation of the Ni phase in H_2 and hence reduce the loss of connectivity. However, the ionic conductivity of YSZ drops by one order of magnitude when the temperature is reduced from 800 °C to 600 °C [3].

Grahl-Madsen and co-workers [78] demonstrated an increase in electronic conductivity with increasing reduction temperature of Ni/YSZ cermets. Those authors also detailed that a subsequent heat treatment in H_2 at high temperature (up to 1000 °C) did not improve the conductivity of a Ni/YSZ sample reduced at lower temperature (600 °C). This phenomenon was explained by the reorganisation of the Ni phase only during reduction. At first sight, this statement may seem in contradiction with the findings of Chap. 3, which reported that Ni coarsening was more significant when the sample was fully reduced, while the presence of remaining NiO domains hindered the reorganisation of the Ni phase at the same temperature. The discrepancy between the results presented here and those in Ref. [78] may be explained by differences in H_2O partial pressure, which is known to accelerate Ni sintering due to the formation of Ni_2-OH and $Ni(OH)_2$ species [73, 76]. A combination of high temperature and presence of steam accelerates coarsening of Ni as demonstrated by Pihlatie *et al.* [75], with water vapour either originating from operation of the SOFC or from the reduction of NiO. The slow evacuation of H_2O from the environmental TEM chamber promotes coarsening of Ni once fully reduced (flow rate of 2 ml min^{-1}), while the large gas flow used by Grahl-Madsen and co-workers in Ref. [78] ($\sim 10^3$ ml min^{-1}) removes H_2O from the reaction chamber and hence hinders a subsequent reorganisation of the Ni phase. Overall, this would indicate that operating the SOFC at high gas flow on the anode side would reduce Ni coarsening. However, such operating conditions reduce the fuel utilisation and result in a larger anodic overpotential as the removal of H_2O appears to hinder the adsorption and desorption of hydrogen [282, 283]. Optimum operation conditions should hence compromise between those aspects.

In addition to coarsening, the connectivity of the Ni phase was also found in Chap. 5 to depend on the number of NiO/NiO coherent twin boundaries prior to activation of

the anode. While grain boundary engineering may be envisaged in some cases [284], it remains to be verified if such an approach could be used here to yield a connected Ni network.

7.2.2 Impurities

Impurities in the raw materials such as Si and Al were observed in Chap. 5 to segregate at some interfaces during reduction at temperatures of 600-700 °C and reaction times in the environmental TEM of a few hours. As those impurities may eventually accumulate at the triple phase boundaries and degrade the anode during operation [285], the purity of the raw materials should be assessed in detail along with the segregation of impurities at active sites. In that regard, the newest generation of scanning transmission electron microscopes equipped with four window-less silicon drift detectors coupled to a high brightness field effect electron gun opens new perspectives [221].

7.2.3 RedOx solutions

Redox solutions that involve alternative anode materials or system solutions to protect the stack by keeping the oxygen partial pressure low will not be assessed here and the reader is referred to the detailed reviews of Atkinson, Fu and Faes and co-workers [12, 26, 286]. Only solutions related to the present findings will be discussed here.

As shown in Chaps. 4 and 6, the final reoxidised NiO structure results from a complex interplay of different processes such as the rate-limiting Ni^{2+} diffusion along the NiO grain boundaries, NiO grain growth, nucleation of internal voids, self-diffusion of Ni and vacancies, permeation of O_2 through cracks that formed in the NiO film due to geometrically induced stresses, electric field induced transport of charged species, with each of these mechanisms depending on the reaction conditions. Although the NiO structures that result from reoxidation may differ in the ETEM and in SOFCs due to variations in the oxidation conditions, the fast outward diffusion of Ni^{2+} along the NiO grain boundaries is expected to remain unbalanced by inward transport of O^{2-}/O_2 up to temperatures as high as 1000 °C [91]. In turn, NiO swells upon a redox cycle as vacancies are injected at the Ni/NiO interfaces due to this imbalance and those cannot be annihilated by interface recession in this spherical geometry.

The reduction of the stresses generated by redox cycling can hence be achieved by hindering the fast outward transport of Ni^{2+} along the NiO grain boundaries, which in turn favours the inward growth of NiO, reduces internal porosity and hence reduces the volume expansion of the NiO shell. Reactive elements such as CeO_2 [287–290], La_2O_3 [291] and Y_2O_3 [292, 293] segregate at the NiO grain boundaries during oxidation and hence decrease the outward transport of Ni^{2+} along those fast diffusion paths and in turn reduce the oxidation rate typically by one or two orders of magnitude [91]. Such approach was deemed promising by Larsen *et al.*, who patented a redox stable

anode [294], in which the addition of an oxide such as Cr_2O_3, CaO, Al_2O_3, etc. hinders Ni coarsening, reduces the oxidation kinetics of Ni and also improves the mechanical properties of the anode. Pihlatie and co-workers demonstrated that the stability of standard anodes could be enhanced by coating NiO with Ti, Mg or Ce oxides prior to milling [295]. While the addition of such elements appears promising, a detailed assessment of their complete impact for SOFC applications is required as those may not only alter the redox stability of the anode but also its sintering behaviour, microstructure, catalytic properties, conductivity, etc.

Another option to reduce the detrimental effect of redox cycling is to act on the initial microstructure of the anode. Based on the *in situ* observations performed during oxidation in Chaps. 4 and 6, the presence of dispersed porosity after sintering appears essential to accommodate the volume expansion of the NiO phase due to redox cycling. If the Ni grains can expand into the porosity upon oxidation as shown in Fig. 7.2, then the stress on the YSZ will be reduced and the formation of cracks in the electrolyte delayed or avoided. Porous as-sintered NiO/YSZ can be obtained through different strategies, for example by using low sintering temperatures and short sintering times [63] or by the addition of specific pore formers [128, 129]. Pihlatie and co-workers measured a decrease in the redox strain by a factor of > 20 when increasing the as-sintered porosity from 9 to 34% [127]. In addition, Faes *et al.* defined an as-sintered porosity requirement on the order of 50% to reach redox-safety, with such structures expanding by less than the threshold value of 0.2 % upon redox cycling [16, 128, 129]. While resulting in redox tolerant anodes, such a high porosity reduces the number of triple phase boundaries and hence the electrochemical properties of the anode. Similarly to coarse redox-stable microstructures with large pores to accommodate the expansion of the Ni phase [22, 123], the addition of an anode functional layer, which is not redox resistant, may be required to obtain sufficient electro-chemical activity. While infiltration of Ni nanoparticles on YSZ scaffolds also appears as a promising route to create redox stable structures, such a process may be difficult to implement industrially [296].

Overall, it appears that a fine tuning of the porosity is required to obtain a redox tolerant Ni/YSZ anode, which still maintains sufficient electrochemical properties. In other words, porosity should be added only at the position where it is required to relieve the YSZ phase from stresses induced by Ni oxidation, while the rest of the structure should be kept intact. In that sense, an alternative route that exploits the oxidation mechanism of Ni particles appears promising as patented by Wood *et al.* [297]. It was proposed to apply a controlled redox cycle at low temperature (400-650 $^\circ$C), either to the anode as a component of the cell, to the anode prior to mounting the cell, or to the initial NiO/YSZ mixture of powder prior to formation of the green body and sintering, to enhance the redox stability of the anode. Based on the results presented in Chaps. 4 and 6, it appears that the oxidation of a fine Ni powder (diameter on the order of 100 nm), whilst increasing the temperature slowly in an oxygen atmosphere to prevent sintering of Ni,

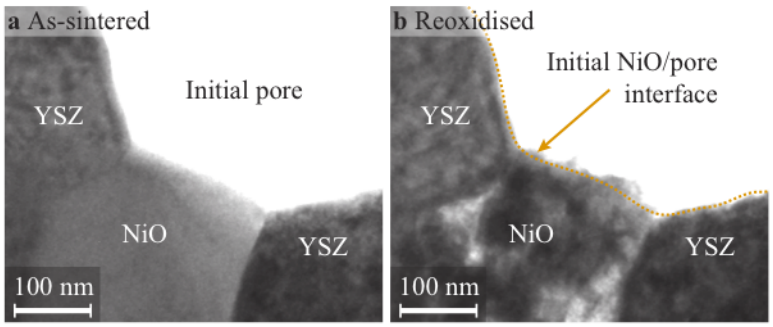

Figure 7.2 – (a-b) BF TEM images illustrating the expansion of Ni into as-sintered pores following a reduction-oxidation cycle of a FIB-prepared Ni/YSZ sample. Reduction and oxidation were performed, whilst heating at a rate of 2 °C min^{-1} up to 500 °C, in 1.3 mbar of H_2 and 3.2 mbar of O_2, respectively.

should induce the formation of irregular NiO structures containing internal voids and randomly oriented NiO domains. It can be proposed to use such fine NiO particles as the starting NiO powder in the sintering step with YSZ. While the NiO structure is expected to densify to some extent during sintering with YSZ particles, such an approach may result in a redox-resistant anode composite, which already includes internal voids at the exact position of the NiO grain to accommodate future redox cycles.

8 Conclusion & outlook

8.1 Environmental TEM methodology

The detailed assessment of the reduction and oxidation mechanisms of Ni(/YSZ) in the environmental transmission electron microscope required first the development of new methodologies. Indeed, it quickly appeared essential to gather nearly simultaneously as much structural, crystallographic and chemical information as possible to yield a detailed picture of the complex reduction and oxidation processes.

Specifically, experiments were designed in the environmental TEM in 1.3 mbar of H_2 and 3.2 mbar of O_2 to approximate constant heating rates up 500-850 °C through small heating steps, thermal drift stabilisation intervals and isothermal structural and chemical characterisation sequences. The sequences of measurements involved imaging, selected area diffraction, and electron energy-loss spectroscopy (EELS) (Chaps. 3 and 4) and, in separate experiments, energy-filtered TEM imaging (Chaps. 5 and 6) to provide a temperature-resolved information about the structure, crystallography and chemistry.

8.1.1 Reaction kinetics from EELS

In Chaps. 3 and 4, the sequences of EEL spectra of NiO or Ni particles were analysed using different methods that quantify the changes in shapes of the $L_{2,3}$ edges to retrieve the reduction and oxidation kinetics as a function of temperature. In turn, solid-state kinetic models were fitted to the EELS data to yield quantitative kinetic details such as the activation energy. The results of this kinetic analysis were then correlated to the images acquired at the same time in the microscope to critically assess the reliability of the chosen kinetic model. Indeed, the simultaneous knowledge of both structural changes and reaction kinetics enabled the analysis of the limitations of the solid-state kinetic models. Such a correlation of environmental TEM data with reaction models was not reported prior to this work.

The analysis relied on experimental reference $L_{2,3}$ spectra of Ni and NiO. In that regard, the diffraction patterns acquired along with the EEL spectra were essential to verify

the exact chemical nature of the NiO and Ni references. Indeed, some of the samples investigated here were supported by a thin amorphous film that contained oxygen (SiO_x), which hence prevented the use of the O K edge as such in the EEL spectra.

In addition, details that were not directly visible in the images such as the rate-controlling diffusion mechanism during Ni oxidation (Ni^{2+} through the NiO scale grain boundaries) could be inferred from the kinetic modelling procedure. In that regard, a structural assessment on the atomic scale was not always required as complementary information could be obtained through the analysis of the reaction kinetics. Instead, images could be acquired at a slightly lower magnification, which then reduced the overall electron beam damage to the specimen. Regarding potential artefacts during ETEM examination, the kinetic data obtained in the microscope could be compared to both additional in-house results investigating the reaction of larger NiO volumes using an *in situ* X-ray diffractometer and to thermogravimetric literature data. Those comparisons provided some insights into the artefacts altering the ETEM observations. Specifically, the effect of gas transport limitations on the reduction reaction and the systematic error in the measurement of the temperature in the ETEM could be assessed through those comparisons.

While EELS allowed the retrieval of quantitative data, several limitations, which included electron beam effects, the precision of the EELS measurement and the systematic error in the temperature measurement, meant that those results had to be analysed with care. With hindsight, the procedure should be labelled as "semi-quantitative" as it provides the order of magnitude rather than a precise number. In the outlook section, different suggestions are proposed to improve those aspects so as to obtain a more precise quantitative information in the ETEM.

8.1.2 Reaction kinetics and thickness evolution from EFTEM

The EELS data provided an averaged chemical information, here over an area of 10 μm^2, of the specimen during reaction. In Chaps. 5 and 6, it was demonstrated for the first time that energy-filtered environmental TEM can provide a temperature-resolved structural and chemical information during reaction, with this information localised this time on the pixel scale (here 6x6 nm^2). The evolution of different features of the EEL spectrum of FIB-prepared NiO/YSZ composites was investigated as a function of temperature using the energy-selecting slit: the plasmon peaks enabled the mapping of the thickness of the specimen using total inelastic mean free path images and, at higher energy-losses, the intensity in the oxygen K ionisation edge, obtained using both 3-window elemental maps and jump-ratios, gave the elemental distribution of oxygen atoms in different regions of interest.

Total inelastic mean free path images provided the changes in volume associated to the NiO reduction and Ni oxidation reactions, which could be correlated to theoretical predictions. The results were in good agreement with the prediction of a volume

shrinkage of -41 % due to reduction. On the other hand, plasmonic excitations occurring at the numerous interfaces of the irregular reoxidised NiO structures did not allow the extraction of quantitative volume expansion data during oxidation. The temperature-resolved sequences of 3-window maps and jump-ratios of the O K edge allowed the retrieval of the reaction rate at different locations in the structure. The rate-controlling mechanisms could then be assessed with respect to the region of interest.

The simultaneous knowledge on the same pixel of the degree of conversion of the reaction and the total inelastic mean free path (and hence thickness as the chemistry is known) allowed the retrieval of further details during reduction. Indeed, the equivalent Ni and NiO thicknesses could be estimated as a function of temperature during reduction, which enabled the estimation of the depth of the Ni/NiO reaction front (across the specimen thickness). This information as a function of temperature could then be correlated to the advancement of the reaction front along the specimen plane. This procedure allowed the estimation of the reaction rate depending on its propagation direction. Such results highlight the fact that, while TEM images capture a projection of the specimen, a combined knowledge of the thickness and the chemistry of the specimen on the same pixel position could be used to obtain meaningful data along the projection direction. Hence, insights into the 3^{rd} dimension could be obtained from 2D images.

While the chemical information is localised on the pixel scale in O K edge images, this data is affected by noise. Indeed, relatively short acquisition times (on the order 40 s per frame at the O K edge) were required to obtain a sufficient temporal resolution and minimise the effects of thermal drift. In addition, the electron dose rate was kept to a minimum value to reduce potential electron beam artefacts. As a consequence, the chemical information on the pixel scale had to be averaged over groups of pixels that exhibited a similar behaviour during reaction to reduce noise. The recent advances in MEMS-based heating holders that are compatible with FIB-prepared samples should improve the quality of EFTEM images acquired at high temperature as discussed in the outlook section.

8.2 NiO(/YSZ) reduction/oxidation

Different ETEM experiments, some using the methodology aforementioned, others involving high-resolution or scanning TEM imaging, investigated the reduction and oxidation pathways of NiO particles (Chaps. 3-4) and NiO/YSZ composites (Chaps. 5-6). Those results were then combined with a post-exposure scanning and transmission electron microscopy analysis, *in situ* X-ray diffraction experiments and computations that involved solid-state kinetic modelling and density functional theory.

In Chaps. 3 and 5, the nucleation of the first Ni domains during NiO reduction in 1.3 mbar of H_2 in the ETEM was observed to occur only after an induction time, or in other words only once a certain temperature was reached (on the order of 400 °C). Those first

domains were observed to form either uniformly on the surface of the NiO particles or at the interfaces with YSZ when studying NiO/YSZ composites. In both cases, the formation of the first Ni domains is an important rate-determining step in the overall description of the reduction reaction. The growth of the Ni domains then occurred in both cases through the movement of interfaces and resulted in porous Ni structures, pores that formed to accommodate the volume loss induced by the removal of oxygen. In the case of NiO particles (Chap. 3), both the structural changes observed in the TEM images and the chemical changes captured by EELS could be described by an Avrami process, where the nucleation, growth and impingement of Ni clusters on the NiO surface control the reaction. On the other hand, the description of the reduction of NiO/YSZ composites could not be related directly to an existing solid-state reaction model (Chap. 5). A well defined Ni/NiO reaction front was observed to propagate from the interfaces with the YSZ towards the centre of the NiO grains, while the free surface of the NiO grains reduced directly only at higher temperatures. A nudged elastic band computation combined with density functional theory indicated that, at the NiO/YSZ interfaces, O^{2-} may transfer from the NiO phase across the interface to fill the oxygen vacancies inherent to the YSZ phase once a certain temperature is reached ($\sim$340 $^{\circ}$C). This process triggers the reduction reaction at the interfaces with YSZ prior to the reduction of the free surface. Differences in the speed at which the Ni/NiO reaction front propagated depending on the direction were monitored and discussed with respect to the accessibility of the H_2 gas to the reactive sites and the role of the YSZ in the removal of oxygen from NiO. The open pore structure and the irregular surface morphology of the reduced Ni/YSZ anode were demonstrated using post-exposure scanning TEM tomography. In general, while the YSZ phase modifies the reduction pathway of NiO with respect to NiO particles only, the final Ni structure at high temperature is governed by the minimisation of the surface energy of Ni with or without YSZ, with intragranular voids disappearing to form dense structures. This process is detrimental to the connectivity of the Ni phase and decreases the number of electrochemically active sites in a solid oxide fuel cell anode (triple phase boundaries Ni/YSZ/voids).

The EELS data obtained in the ETEM and X-ray diffraction patterns, both acquired *in situ* during reaction in H_2, highlighted the retardation effect of H_2O on the latter stages of the reduction reaction in low gas flow and pressure conditions (Chap. 3). In that regard, the flexibility in terms of experimental parameters allowed in the *in situ* X-ray diffractometer enabled to bridge (at least partially) the gap between the low H_2 pressure/flow ETEM data and atmospheric pressure reduction studies.

The effect of the initial NiO/NiO grain boundary symmetry on the reduction process and the final Ni connectivity after reaction was also investigated (Chap. 5). Coherent twin boundaries remain throughout reduction, while incoherent boundaries detach during the process, with voids forming at their initial position. The symmetry of the

initial NiO/NiO grain boundaries thus influences the connectivity of the Ni phase after reduction/activation. In addition, the segregation of the impurities present in the as-sintered NiO/YSZ composites during reduction was also monitored using post-exposure energy-dispersive X-ray spectroscopy maps. The results show that these impurities segregate at the interfaces of the anode and may hence block the Ni/YSZ/voids active sites.

The oxidation of Ni is governed by the properties of the growing NiO film and hence does not appear influenced by the presence of YSZ as highlighted in Chaps. 4 and 6. Unlike reduction, the nucleation of the first NiO domains did not require high temperatures and those were observed to form and grow quickly up to a thickness of 3-4 nm at room temperature in high vacuum conditions as a result of the field-driven process described by Mott and Cabrera [80]. At higher temperature in an O_2 atmosphere, the diffusion of Ni^{2+} along the NiO grain boundaries appears to dominate the growth of the film, a process probably assisted by an electric field due to the small dimensions of the NiO scale and the presence of the electron beam. Vacancies were injected at the Ni/NiO interfaces as inward oxygen diffusion is several orders of magnitude slower than the outward Ni mass flux and interface recession was not observed. Consequently, voids formed inside the NiO scale. Ni was observed to self-diffuse to maintain some contact between the Ni core and the NiO scale so that the oxidation process could proceed. The formation of transverse cracks in the NiO film during oxidation could also be captured in the ETEM, a process that was predicted to occur during Ni oxidation on the basis of post-exposure observations and acoustic emission studies but to our best knowledge had not been visualised *in situ* at such spatial resolution. As a result of such cracks, permeation paths for O_2 towards unreacted Ni were created, which allowed some inward NiO growth that in turn resulted in double-scale NiO structures. Yet internal porosity remains within the irregular polycrystalline NiO structures at the end of the oxidation process. A volume expansion of $\sim$65% was estimated here between the initially dense as-received NiO and the reduced and then reoxidised NiO phase (redox cycle at 600 $^{\circ}$C) due to the presence of internal voids. This expansion of the NiO phase upon a redox cycle cannot be accommodated by the pores created during reduction and thus stress is applied on the ceramic, which may rupture if stress exceeds a certain value.

Overall, the NiO structure changes irreversibly during a reduction-oxidation cycle due to both the reorganisation of Ni during exposure to H_2 at high temperature and the increase in the apparent NiO volume due to injection of internal voids during oxidation, with both effects observed here *in situ* in the environmental TEM. As highlighted in Chap. 7, the reduction-oxidation tolerance of the Ni/YSZ solid oxide fuel call anode may be improved by modifying the initial NiO powder. Indeed, co-sintering YSZ particles with a porous NiO powder formed by the oxidation of small Ni particles at low temperature (up to 600 $^{\circ}$C) rather than the usual dense NiO particles should improve the tolerance of the anode towards reduction-oxidation cycles. Indeed, if maintained

during sintering, this additional internal porosity located exactly within the NiO grains themselves should reduce the stress applied on the YSZ phase during redox cycling by accommodating the volume increase associated to Ni oxidation.

Overall, environmental TEM data obtained *in situ*, coupled to post-exposure TEM experiments, to *in situ* X-ray diffraction studies, to solid-state kinetic models and to density functional theory computations allowed a detailed assessment of the NiO(/YSZ) systems during reduction and oxidation. Processes that are interpreted, sometimes incorrectly, on the basis of *in situ* measurements of a large volume combined with modelling and post-exposure microscopy examinations could be observed here directly in real time with a sub-nm spatial resolution. In other words, ETEM sheds light on processes that are usually investigated in a black box, where fine details are lost. And in turn, the data obtained in the microscope could be used to support the development of detailed reaction models.

8.3 Outlook

While the methodology employed here in the ETEM enabled the retrieval of new insights into the reduction and oxidation reactions of Ni/YSZ composites, numerous experiments can be envisaged to complement the data presented in this thesis.

The methodology introduced here that correlates structure, chemistry and solid-state models may benefit from some of the latest technical developments in the field of environmental TEM. In this respect, the gas mixing manifold system recently reported by Akatay and co-workers appears especially promising [298]. Indeed, it allows to switch from a gas environment to another, whilst maintaining the sample temperature constant and hence preventing drift. Isothermal experiments at high temperatures could thus be envisaged using an inert gas atmosphere to heat the specimen to the desired temperature. The experiments presented here would then be greatly simplified. Indeed, the time required to increase the temperature and for drift to stabilise cannot be attributed to the acquisition of data. Isothermal experiments would hence allow a higher temporal resolution, which was here on the order of 5-8 minutes. In addition, isothermal experiments reduce drastically the number of manual operations on the microscope. The manual increase of the temperature of the holder and the frequent realignments of the microscope to correct for thermal drift required a lot of time and effort. Moreover, the reduction-oxidation stability of Ni could be investigated at a constant temperature like in an operating solid oxide fuel cell device. Slow heating ramp experiments were required here to minimise thermal drift and hence to ensure that reliable data could be captured but, on the downside, the time required for one reduction/oxidation experiment was significant and multiple reduction-oxidation cycles could not be performed. The system reported by Akatay *et al.* would allow multiple reduction-oxidation cycles at a constant temperature on the order of 800 °C, which would then accelerate the reaction kinetics and hence reduce the time required for the operator to perform the experiment.

In complement to such a gas mixing system, the recent advances in the field of heating holders also appear promising. Double-tilt MEMS-based holders with a local temperature reading that does not rely on a high vacuum calibration are now available (DENS solutions [299]). While it remains to be verified if those are compatible with FIB-prepared TEM lamellae, such holders allow higher heating rates (1000 °C per 0.01 s), automated control of the temperature profile and a temperature measurement error less than 5 %. It could hence be envisaged to program directly heating ramp experiments with much greater control and reduced thermal drift when compared to the Gatan 652 holders. In addition, the recent development of single tilt tomographic heating holders also opens interesting perspectives with respect to this work [299, 300]. Indeed, it could be envisaged to obtain three-dimensional reconstructions from tilt series acquired at room temperature of regions that were previously followed *in situ* during reduction/oxidation at high temperature. The internal pore size and structure that form within NiO domains during oxidation could be investigated as a function of temperature, which would provide a detailed assessment of the volume changes associated to reduction-oxidation cycles. In turn, such data could support the development of predictive redox instability models.

In situ holography experiments in the environmental TEM may provide further details into the oxidation mechanisms of Ni. Indeed, it may bring some insights into the strength of the electric field that drives the initial growth of NiO, a parameter that is not fully characterised.

Following the preliminary results of Tavabi and co-workers [158], the operation of a single-chamber SOFC in a gas mixture of CH_4/O_2 inside the environmental TEM would be of great interest. Using the latest developments in MEMS-based holders with heating and biassing capabilities, such an experiment would allow the *in operando* investigation of the activation and degradation mechanisms of a solid oxide fuel cell, whilst it operates. The effects of current or voltage on the reduction, coarsening and reoxidation processes could hence be studied using such a setup.

Other studies may employ the same ETEM methodology to assess the reduction and reoxidation of Ni-ceria composites, which are often used as SOFC anodes. Also, the investigation of the reduction mechanism of NiO grains co-sintered with an insulator such as Al_2O_3 that does not present any ionic conductivity may improve the understanding of the complex interactions that were observed here between NiO and YSZ. In terms of fundamental research, the investigation of the reduction and oxidation pathways of spherical NiO particles may support the development of advanced solid-state kinetic models.

Future work should also investigate the performance and reduction-oxidation stability at the SOFC stack level of anodes composed of YSZ co-sintered with NiO grains formed by the oxidation at low temperatures in O_2 of Ni particles with an initial diameter on the order of 100 nm.

While this work laid some foundations both in terms of ETEM methodology and materials science aspects, numerous perspectives can be envisaged, which hopefully will continue to improve the understanding of the reduction and reoxidation mechanisms of Ni(/ceramic) systems and so enhance the durability of solid oxide fuel cells, as one among many potential applications.

A Crystal structures

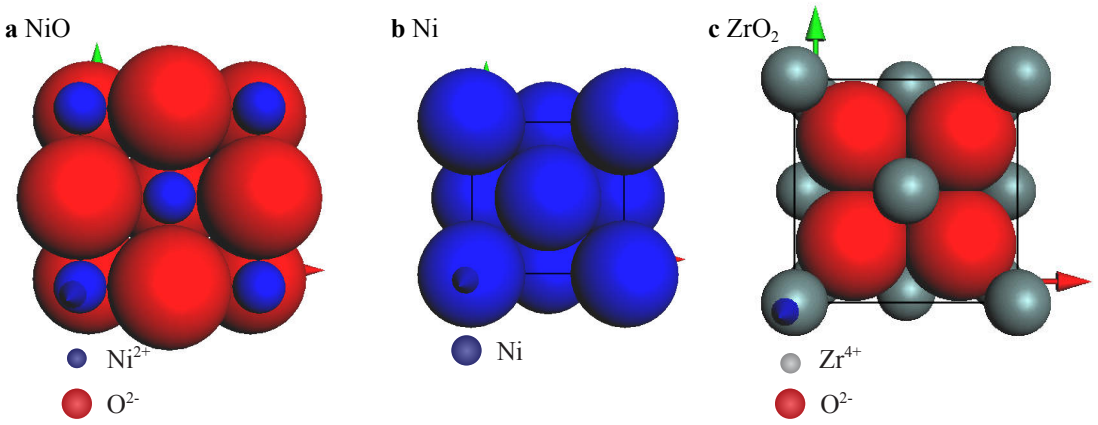

Figure A.1 – (a) cubic Fm-3m NiO atomic structure (lattice parameter a of 0.418 nm [36]), (b) cubic Fm-3m Ni atomic structure (lattice parameter a of 0.352 nm [37]) and (c) cubic Fm-3m ZrO_2 atomic structure (lattice parameter a of 0.513 nm [302]).

(hkl)	$d^*_{NiO}[nm^{-1}]$	$d^*_{Ni}[nm^{-1}]$	$d^*_{ZrO_2}[nm^{-1}]$
(111)	4.147	4.922	3.377
(200)	4.788	5.683	3.899
(220)	6.771	8.038	5.414
(311)	7.940	9.425	6.466
(222)	8.293	9.844	6.754

Table A.1 – Reciprocal (hkl) plane spacings of the NiO, Ni and ZrO_2 atomic structures shown in Fig. A.1.

B Thermodynamics

B.1 Ellingham diagram

The Ellingham diagram shown in Fig. 2.14 relies on the following thermodynamic data:

compound	$\Delta H^0_{298\,\mathrm{K}}$ [kJ mol^{-1}]	$S^0_{298\,\mathrm{K}}$ [J K^{-1}mol^{-1}]	$\Delta_{\mathrm{vap}} H^0_{373\,\mathrm{K}}$ [kJ mol^{-1}]
Ni(s)	0	29.9	
NiO(s)	−239.7	38.4	
O_2 (g)	0	204.8	
H_2 (g)	0	130.6	
H_2O (l)	−285.2	69.9	44.7

Table B.1 – Thermodynamic data from Refs. [235, 236].

Ni oxidises to NiO in the presence of O_2 according to:

$$2\mathrm{Ni} + \mathrm{O_2} \rightarrow 2\mathrm{NiO} \tag{B.1}$$

The reaction is at equilibrium if $\Delta_{\mathrm{B.1}} G = 0$ for a given $P_{\mathrm{O_2}}$ and T:

$$\Delta_{\mathrm{B.1}} G = \Delta_{\mathrm{B.1}} G^0 + RT\ln\left(\frac{1}{P_{\mathrm{O_2}}/P^{\mathrm{o}}_{\mathrm{O_2}}}\right) = 0 \tag{B.2}$$

$$\Delta_{\mathrm{B.1}} G^0 = RT\ln\left(P_{\mathrm{O_2}}/P^{\mathrm{o}}_{\mathrm{O_2}}\right) \tag{B.3}$$

The Ellingham diagram plots the standard free enthalpy $\Delta_{\mathrm{B.1}} G^0$ as a function of T in addition to a nomographic scale that provides the equilibrium $P_{\mathrm{O_2}}$ for each T. Other partial pressure scales can be added to account for reduction/oxidation in other atmospheres such as H_2/H_2O. In turn, equivalences to $P_{\mathrm{O_2}}$ must be obtained. For example in

the case of the following reaction to produce H_2O in vapour phase (at $T > 373$ K):

$$2H_2(g) + O_2(g) \rightarrow 2H_2O(g) \tag{B.4}$$

$$\ln(P_{O_2}/P^o_{O_2}) = \frac{\Delta_{B.4}G^0}{RT} - 2\ln\Big(\frac{P_{H_2}/P^o_{H_2}}{P_{H_2O}/P^o_{H_2O}}\Big) \tag{B.5}$$

$\Delta_{B.4}G^0$ can be calculated from the data at room temperature in Tab. B.1 using the Ellingham approximation (ΔH and S do not depend on T) through the following procedure:

$$\Delta_{B.4}H^0_{373\,K} = \Delta_{B.4}H^0_{298\,K} + 2\Delta_{vap\ (H_2O)}H^0_{373\,K} = -481 \text{ kJ mol}^{-1} \tag{B.6}$$

Similarly, the change in entropy is:

$$\Delta_{B.4}S^0_{373\,K} = \Delta_{B.4}S^0_{298\,K} + 2\Delta_{vap\ (H_2O)}S^0_{373\,K} = \Delta_{B.4}S^0_{298\,K} + 2\frac{\Delta_{vap\ (H_2O)}H^0_{373\,K}}{373} = -86.2 \text{ J mol}^{-1}\text{ K}^{-1} \tag{B.7}$$

And finally, the free enthalpy change associated to B.4 is:

$$\Delta_{B.4}G^0 = \Delta_{B.4}H^0_{373\,K} - T\Delta_{B.4}S^0_{373\,K} \tag{B.8}$$

C Reaction kinetics

C.1 Kissinger method

From Eq. 2.23, Kissinger proposed a method to extract the activation energy E_a from non-isothermal experiments performed at constant heating rates β without any knowledge of the reaction model $f(\alpha)$ [237]. The second temperature derivative of α is set to 0 at the temperature at which the reaction rate is maximum $T_{\max}$, which results in:

$$\frac{\mathrm{d}}{\mathrm{d}T}\left(\frac{\mathrm{d}\alpha}{\mathrm{d}T}\right)_{T=T_{\max}} = \frac{\mathrm{d}}{\mathrm{d}T}\left(\frac{A}{\beta}e^{-E_a/RT}\, f(\alpha)\right)_{T=T_{\max}} = 0 \tag{C.1}$$

$$\left(\frac{A}{\beta}\frac{E_a}{RT^2}\, e^{-E_a/RT}\, f(\alpha) + \frac{A}{\beta}\, e^{-E_a/RT}\, \frac{\mathrm{d}f(\alpha)}{\mathrm{d}\alpha}\frac{\mathrm{d}\alpha}{\mathrm{d}T}\right)_{T=T_{\max}} = 0 \tag{C.2}$$

Using Eq. 2.23, $\frac{A}{\beta}e^{-E_a/RT}f(\alpha)$ can be replaced by $\mathrm{d}\alpha/\mathrm{d}T$ and thus:

$$\cancel{\frac{\mathrm{d}\alpha}{\mathrm{d}T}}\left(\frac{E_a}{RT^2} + \frac{A}{\beta}e^{-E_a/RT}\, \frac{\mathrm{d}f(\alpha)}{\mathrm{d}\alpha}\right)_{T=T_{\max}} = 0 \tag{C.3}$$

$$\frac{E_a}{RT_{\max}^2} = \frac{A}{\beta}e^{-E_a/RT_{\max}}\, \left(-\frac{\mathrm{d}f(\alpha)}{\mathrm{d}\alpha}\right)_{T=T_{\max}} = 0 \tag{C.4}$$

Which finally results in the following expression:

$$\ln\Big(\frac{\beta}{T_{\max}^2}\Big) = \Big(-\frac{E_a}{R}\Big)\frac{1}{T_{\max}} - \ln\Big(\frac{E_a}{RA}\Big) + \ln\Big(-\frac{\mathrm{d}f(\alpha)}{\mathrm{d}\alpha}\Big)_{T=T_{\max}} \tag{C.5}$$

where $-\ln(E_a/RA) + \ln(-\mathrm{d}f(\alpha)/\mathrm{d}\alpha)_{T=T_{\max}}$ is constant for models where $f(\alpha)$ is linear in α and holds approximately for many models at the maximum rate [238]. Using data acquired at different β, the activation energy E_a is given by the slope of $\ln(\beta/T_{\max}^2)$ versus $1/T_{\max}$.

C.2 Avrami nucleation models

Avrami developed models to assess the kinetics of a phase change that is controlled by the nucleation of the new phase at reactive sites [43–45]. These models also apply to surface science and successfully describe the nucleation of domains on a solid reactant surface [303]. These nucleation models are also termed JMAEK, in recognition of the work of Johnson, Mehl, Avrami, Erofeyev and Kholmogorov, who all contributed to their development [41]. The full mathematical development of these models can be found in numerous references [40, 41, 43–45] and only key steps leading to final derivations will be given here (as in Chap. 5, p. 289 of Ref. [265]).

As illustrated in Fig. C.1, Avrami models assume that the product nucleates and grows (as growth nuclei) from germ nuclei that are inherent to the reactant.

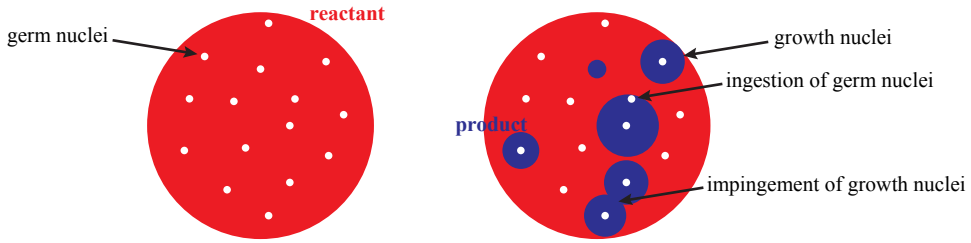

Figure C.1 – Avrami description of a phase transformation, which involves the growth of nuclei from germs randomly distributed within or on the reactant phase.

The Avrami models also suppose that nucleation from germ nuclei occurs randomly and uniformly within or on the reactant surface and that the growth of nuclei occurs at a constant and isotropic rate v. The volume of a nucleus V' that does not nucleate until a time τ with respect to a reference $t = 0$ can be expressed as:

$$V' = \frac{4}{3}\pi r^3 = \frac{4}{3}\pi v^3 (t-\tau)^3 \tag{C.6}$$

In turn, the number of new growth nuclei that appear in a time $\mathrm{d}\tau$ is given by $N\mathrm{d}\tau$, with N defining the constant rate at which germ nuclei transform to growth nuclei. At the beginning of the transformation, when growth nuclei are not impinging or covering germ nuclei, the conversion fraction α can be defined for a unit total volume as:

$$\alpha = \sum V' = \frac{4}{3}\pi N v^3 \int_0^t (t-\tau)^3 \,\mathrm{d}\tau. \tag{C.7}$$

And thus, for $\alpha \ll 1$:

$$\alpha = \frac{\pi}{3} N v^3 t^4 \tag{C.8}$$

As shown in Fig. C.1, the growth of nuclei will then be restricted by both ingestion

(suppression of nucleation sites through the growth of neighbouring nuclei) and coalescence (impingement of growing nuclei). Avrami and co-workers thus developed a valid expression for randomly distributed nuclei for both short and long reaction times:

$$\alpha = 1 - e^{-\frac{\pi}{3} N v^3 t^4} \tag{C.9}$$

Depending on the hypotheses made on the nucleation process and the subsequent growth of nuclei, Eq. C.9 can be generalised to:

$$\alpha = 1 - e^{-Kt^n} \tag{C.10}$$

where n depends on the nucleation mechanism and is insensitive to temperature (if the mechanism does not change), with $n = 2$, 3 or 4 for growth in 1, 2 or 3 directions, respectively. K depends on both nucleation and growth rates and hence on temperature. The integral reaction model $g(\alpha)$ required in Eq. 2.26 can be expressed as:

$$g(\alpha) = [-\ln(1-\alpha)]^{1/n} = kt \tag{C.11}$$

where $k = K^{1/n}$ and $n = 2,3,4$.

C.3 Spherical geometry diffusion model

The diffusion model developed in Ref. [81] provides a phenomenological description of the oxidation of small spherical particles. It assumes that oxidation is first controlled up to a critical thickness by non-linear effects, i.e. an electric field-induced diffusion process as described by Mott and Cabrera [80], and then by a linear mechanism, i.e. diffusion of ions in a gradient of oxygen chemical potential as described by Wagner [84].

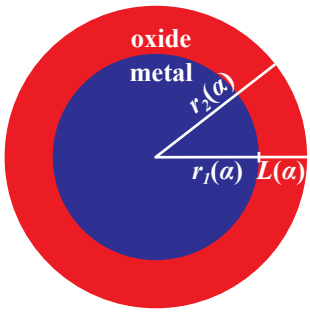

Figure C.2 – Spherical diffusion model including built-in field effects developed in Ref. [81], where $r_1(\alpha)$ is the metal core radius, $r_2(\alpha)$ the total radius of the particle and $L(\alpha)$ the oxide thickness, which all depend on the conversion fraction α.

Assuming the spherical geometry shown in Fig. C.2, where $r_1(\alpha)$ is the metal radius, $r_2(\alpha)$ the total radius of the particle and $L(\alpha) = r_2(\alpha) - r_1(\alpha)$ the oxide thickness, the

reaction rate $\mathrm{d}\alpha/\mathrm{d}t$ is defined in Ref. [81] as:

$$\frac{\mathrm{d}\alpha}{\mathrm{d}t} = \frac{RI}{qV} = \frac{4\pi k_p}{qV}\,\frac{r_1(\alpha)r_2(\alpha)}{L_{cr}}\,\sinh\left[\frac{L_{cr}}{L(\alpha)}\right] \tag{C.12}$$

where I is the total current at the reaction interface, which remains constant when evaluated at any radius in the oxide, V the initial metal particle volume, which is equal to $4/3\pi(d_0/2)^3$ (d_0 is the initial particle size), q the Pilling–Bedworth ratio, i.e the relative volume expansion upon formation of oxide (1.65 for Ni oxidation to NiO [257]), k_p the parabolic rate constant and L_{cr} the critical oxide thickness that marks the transition between between non-linear and linear regimes. $r_1(\alpha)$ and $r_2(\alpha)$ need to be expressed in terms of known parameters such as α, d_0 and q to obtain the reaction model $f(\alpha)$. First of all, $r_1(\alpha)$ can be defined as [242]:

$$r_1(\alpha) = (1-\alpha)^{1/3}(d_0/2) \tag{C.13}$$

In addition, $r_2(\alpha)$ can be expressed using the Pilling-Bedworth ratio:

$$q = \frac{r_2(\alpha)^3 - r_1(\alpha)^3}{(d_0/2)^3 - r_1(\alpha)^3} \tag{C.14}$$

$$r_2(\alpha)^3 = q(d_0/2)^3 - qr_1(\alpha)^3 + r_1(\alpha)^3 \tag{C.15}$$

And replacing $r_1(\alpha)$ using Eq. C.13, the following expression of $r_2(\alpha)$ is obtained:

$$r_2(\alpha) = \left[q + (1-\alpha)(1-q)\right]^{1/3}(d_0/2) \tag{C.16}$$

In turn, Eqs. C.13 and C.16 are injected into C.12 to yield:

$$\frac{\mathrm{d}\alpha}{\mathrm{d}t} = \frac{\cancel{4}\pi k_p}{q\cancel{\frac{4}{3}}\pi(d_0/2)^{\cancel{3}}}\,\frac{1}{L_{cr}}(1-\alpha)^{1/3}\cancel{(d_0/2)}\left[q + (1-\alpha)(1-q)\right]^{1/3}\cancel{(d_0/2)}$$
$$\sinh\left[\frac{L_{cr}}{\left[q + (1-\alpha)(1-q)\right]^{1/3}(d_0/2) - (1-\alpha)^{1/3}(d_0/2)}\right] \tag{C.17}$$

As mentioned in Chap. 2.5, $\mathrm{d}\alpha/\mathrm{d}t$ is expressed as the product of $f(\alpha)$ (the reaction model) and $Ae^{-E_a/RT}$ (Arrhenius function) [41]:

$$\frac{\mathrm{d}\alpha}{\mathrm{d}t} = Ae^{-E_a/RT}f(\alpha) \tag{C.18}$$

Based on Eqs. C.17 and C.18, the reaction model $f(\alpha)$ of the diffusion-controlled reaction

developed by Niklasson and Karmhag [81] is expressed as:

$$f(\alpha) = (1-\alpha)^{1/3}\left[q+(1-\alpha)(1-q)\right]^{1/3} \sinh\left[\frac{2L_{cr}}{d_0}\frac{1}{\left[q+(1-\alpha)(1-q)\right]^{1/3}-(1-\alpha)^{1/3}}\right] \quad \text{(C.19)}$$

which requires the knowledge of d_0, a parameter that can be obtained from TEM micrographs, and L_{cr}. The integral from of this reaction model $g(\alpha)$ is then:

$$g(\alpha) = \int_0^\alpha \frac{\mathrm{d}\alpha}{f(\alpha)} = \int_0^\alpha \frac{1}{(1-\alpha)^{1/3}[q+(1-q)(1-\alpha)]^{1/3}\sinh\left[\frac{2L_{cr}}{d_0}\frac{1}{[q+(1-q)(1-\alpha)]^{1/3}-(1-\alpha)^{1/3}}\right]}\mathrm{d}\alpha \quad \text{(C.20)}$$

The parabolic rate constant k_p is defined as:

$$k_p(T) = \frac{qd_0L_{cr}}{6}Ae^{-Ea/RT} \quad \text{(C.21)}$$

where k_p is usually expressed in $\mathrm{cm}^2\ \mathrm{s}^{-1}$, meaning that d_0 and L_{cr} must be defined in cm and A in s^{-1}. In non-isothermal experiments, the heating rate $\mathrm{d}\alpha/\mathrm{d}T$ must be expressed in $\mathrm{K\ s}^{-1}$. E_a and T are expressed in $\mathrm{J\ mol}^{-1}$ and in K, respectively.

D Energy-filtered TEM

D.1 Total inelastic mean free paths

Total inelastic mean free path images t/λ, where t is the thickness (in nm) and λ the total inelastic mean free path (in nm), can be estimated from an unfiltered image I_t (or the total area in a low-loss spectrum) and an image I_0 of the zero-loss (or the area under the zero-loss peak) as shown in Eq. D.1 (see also Chap. 5 in [172]):

$$t/\lambda = \ln(I_t/I_0) \tag{D.1}$$

In turn, the thickness of the specimen t can be obtained though the estimation of λ. This value λ depends on the collection semi-angle $\beta_{\text{collection}}$ (in mrad), the initial energy of the electrons E_0 (in keV) and the effective atomic number Z and can be estimated using the following equations [172]:

$$\lambda \approx \frac{106F(E_0/E_m)}{\ln(2\beta_{\text{collection}}E_0/E_m)} \tag{D.2}$$

where F is a relativistic factor defined as:

$$F = \frac{1 + E_0/1022\ \text{keV}}{(1 + E_0/511\ \text{keV})^2} \tag{D.3}$$

E_m is a mean energy-loss defined in eV, which can either be obtained from Tables (Tab. 5.2, p. 296 of Ref. [172]) or be estimated from the atomic number Z [172]:

$$E_m \approx 7.6Z^{0.36} \tag{D.4}$$

In Chap. 5, λ in NiO and Ni is estimated using Eqs. D.2 to D.4 using a value of E_0 of 300 kV and a collection semi-angle $\beta_{\text{collection}}$ of 6.8 mrad (defined by the objective aperture of 20 µm). While a measured value of E_m is used for NiO (19.8 eV, taken from Tab. 5.2, p. 296 of Ref. [172]) to yield a value of λ_{NiO} (155 nm), the atomic number of Ni (28) was used to estimate E_m (25.2 eV) and then λ_{Ni} (127 nm).

D.2 3-window elemental mapping

The 3-window method to yield an elemental map of an ionisation edge involves the acquisition of two filtered images before the edge onset ($I_{\text{pre-edge 1}}$, $I_{\text{pre-edge 2}}$) and one image that contains the ionisation edge ($I_{\text{post-edge}}$). The image $I_{\text{pre-edge 1}}$ is acquired by selecting the energy-losses centred around the value E_1 (in eV), $I_{\text{pre-edge 2}}$ is centred around E_2 and $I_{\text{post-edge}}$ around E_3 ($E_1 < E_2 < E_3$). All of the filtered images are acquired with a slit width Δ (in eV). The subtraction of the power law background $I_{\text{background}} = AE^{-r}$ (energy-loss E, fit parameters A and r) from the $I_{\text{post-edge}}$ image to yield the corresponding 3-window elemental map $I_{\text{elemental map}}$ involves the following procedure:

$$r = \frac{\ln(I_{\text{pre-edge 1}}/\Delta) - \ln(I_{\text{pre-edge 2}}/\Delta)}{\ln(E_2) - \ln(E_1)} \tag{D.5}$$

$$\ln(A) = \ln(I_{\text{pre-edge 1}}/\Delta) + r\ln(E_1) \tag{D.6}$$

$$B = \ln(A) - r\ln(E_3) \tag{D.7}$$

$$I_{\text{background}} = \Delta e^{B} \tag{D.8}$$

$$I_{\text{elemental map}} = I_{\text{post-edge}} - I_{\text{background}} \tag{D.9}$$

E Density functional theory

To assess the possible transfer of oxygen from NiO to YSZ and confirm the reduction model proposed in Chap. 5, density functional theory (DFT) calculations were performed by Dr. U. Aschauer (now at ETH Zürich) using the Quantum ESPRESSO code [304], applying the generalised gradient approximation (GGA), Perdew–Burke–Ernzerhof (PBE) exchange and correlation functional [305]. Vanderbilt Ultrasoft pseudopotentials [306] were used to describe the interaction of the Ni(3d, 4s), Y(4s, 4p, 4d, 5s), Zr(4s, 4p, 4d, 5s), O(2s, 2p) electrons with the cores. The wave functions were expanded in plane-waves up to a kinetic energy cut-off of 50 Ry, while using 500 Ry for the augmented density. The large simulation cell size allowed reciprocal space sampling to be restricted to the gamma point.

The simulation cell for the YSZ/NiO interface was constructed by putting a 6 Å thick (100) slab of NiO (lateral dimensions 8.3 x 8.3 Å) on top of a 5.5 Å thick (110) slab of cubic ZrO_2 (lateral dimensions: 10.1 x 14.3 Å), which contained two Y atoms at the interface (effective concentration 6.67%), while keeping the top-most NiO and bottom-most ZrO_2 layer fixed. The accumulation of Y at the interface is justified due to segregation resulting from ionic radii mismatch between Y (0.90 Å) and Zr (0.72 Å). As a detailed study of the Y distribution around the interface was beyond the scope of the present work, the two Y atoms were placed in the same row in the interface plane. This is reasonable as previous work demonstrated the existence of yttrium in this pair configuration [307]. It should also be noted that while in this setup the periodicity of NiO is not preserved parallel to the interface plane, the inner part of the resulting interface retains the desired structure as indicated by limited relaxations in this zone. After complete relaxation (forces $<10^{-3}$ a.u. = 0.05 eV $Å^{-1}$), vacancies were created close to the interface in both parts and a nudged elastic band (NEB) calculation [264] run between these two states, keeping the same atoms fixed as during relaxation.

F Environmental SEM

NiO/YSZ specimens were taken through multiple reduction-oxidation cycles in a Philips FEI XL30 FEG environmental scanning electron microscope (ESEM) to complement the results presented in this thesis. The as-received NiO/YSZ anodes were polished prior to observation in the environmental SEM. A total forming gas (3% H_2) pressure of 1.3 mbar was used to reduce the samples, while they were reoxidised in 1.3 mbar of O_2. Two different experiments were performed in the ESEM as illustrated in Fig. F.1. The first sample was heated at an overall rate of 4 °C min^{-1} from 200 °C to 808 °C. The specimen was left at this temperature for 20 minutes before purging the forming gas with Ar. Then O_2 was introduced in the microscope chamber to investigate the reoxidation of the specimen during 60 minutes. In another experiment, four isothermal redox cycles were performed at 850 °C. The first three reduction reactions lasted 60 minutes, while the subsequent reoxidations were 30 minutes long. The last cycle was shorter: 40 minutes in forming gas and 15 minutes in O_2. In both cases, the microscope was operated at 20 kV and images were acquired using the gaseous secondary electron detector at various steps of the reactions. Frames were then aligned using cross-correlation [219].

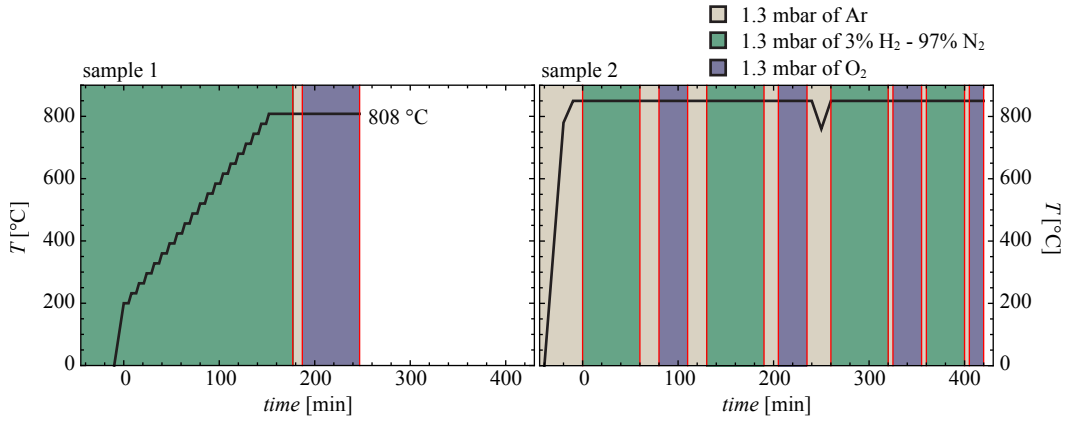

Figure F.1 – Time, temperature and gas parameters used in the ESEM.

The initial NiO/YSZ surface is flat, with the exception of some polishing marks as shown in Fig. F.2a.1. Upon reduction at an overall rate of 4 °C min^{-1}, small voids start to appear

in the NiO phase at the interfaces with YSZ (Fig. F.2a.2). Unlike the environmental TEM observations of Chap. 5, Ni grains appear dense and regular throughout the reduction process as shown in the sequence Fig. F.2a.3-9. This difference is likely to stem from the higher reduction temperature in the ESEM (P_{H_2} is lower than in the ETEM) and differences in sample geometry and resolution between these two techniques. Indeed, TEM images capture a projection of a thin specimen at high resolution, in which small surface irregularities and voids that may run through this thickness of 100 nm are easily identified. On the other hand, ESEM images only assess the surface at much lower resolution and thus cannot resolve irregularities of a few nm or tens of nm. Overall, Ni grains shrink and separate upon reduction as shown in Fig. F.2a.9, yet it cannot be verified using ESEM if they have fully reacted.

The NiO grains become irregular during reoxidation in agreement with the ETEM observations of Chaps. 4 and 6 and those NiO structures evolve slowly (changes are barely visible over the duration of 40 min in O_2 as shown in Fig. F.2b.1-3). Those NiO structures, which are most likely polycrystalline, do not appear to fully occupy the voids that were created during reduction. This observation indicates that the oxidation process may not be complete after 60 minutes at 808 °C and (more likely) that the NiO phase is expanding out of the specimen plane (as observed in the ETEM experiments of Chap. 6). In addition, some bright features appear on the surface of the specimen during the oxidation reaction as circled in Fig. F.2b.1-3. These features become clearly visible during exposure to O_2, yet it appears that they formed during reduction in H_2 (circled regions in Fig. F.2a.1 and 9). Such observations are in agreement with those of Nakagawa *et al.*, who also observed the agglomeration of NiO on the specimen surface in both ESEM and from *ex situ* experiments [120].

As shown in Fig. F.3a-i, the formation of NiO domains on the surface of the specimen is more severe in the second experiment, which involved four isothermal redox cycles at 850 °C. A focused ion beam cross section (Zeiss NVision 40) reveals that NiO structures of a few hundred nm formed on the surface of the specimen during those four redox cycles (Fig. F.3j). Those Ni domains appear, grow and coalesce on the surface during exposure to H_2 and then form characteristic irregular NiO structures during exposure to O_2, with their size and number increasing upon redox cycling (Fig. F.3a-i).

Such results are concordant with the recent report of Hanasaki and co-workers, who also observed through post-exposure microscopy observations the coarsening of Ni grains on the surface of Ni/scandia-stabilised zirconia composites after thermal cycling [308]. The large mobility of the Ni phase was related to the evaporation and redeposition of $Ni(OH)_2$ species that formed in the presence of H_2O, which originates here from NiO reduction by H_2.

Overall, the results clearly highlight that the Ni phase is mobile during reduction in H_2 (i.e. in the presence of H_2O to form $Ni(OH)_2$ species). This effect is also clearly visible in the ESEM images presented by Klemensø and co-workers acquired during redox cycling

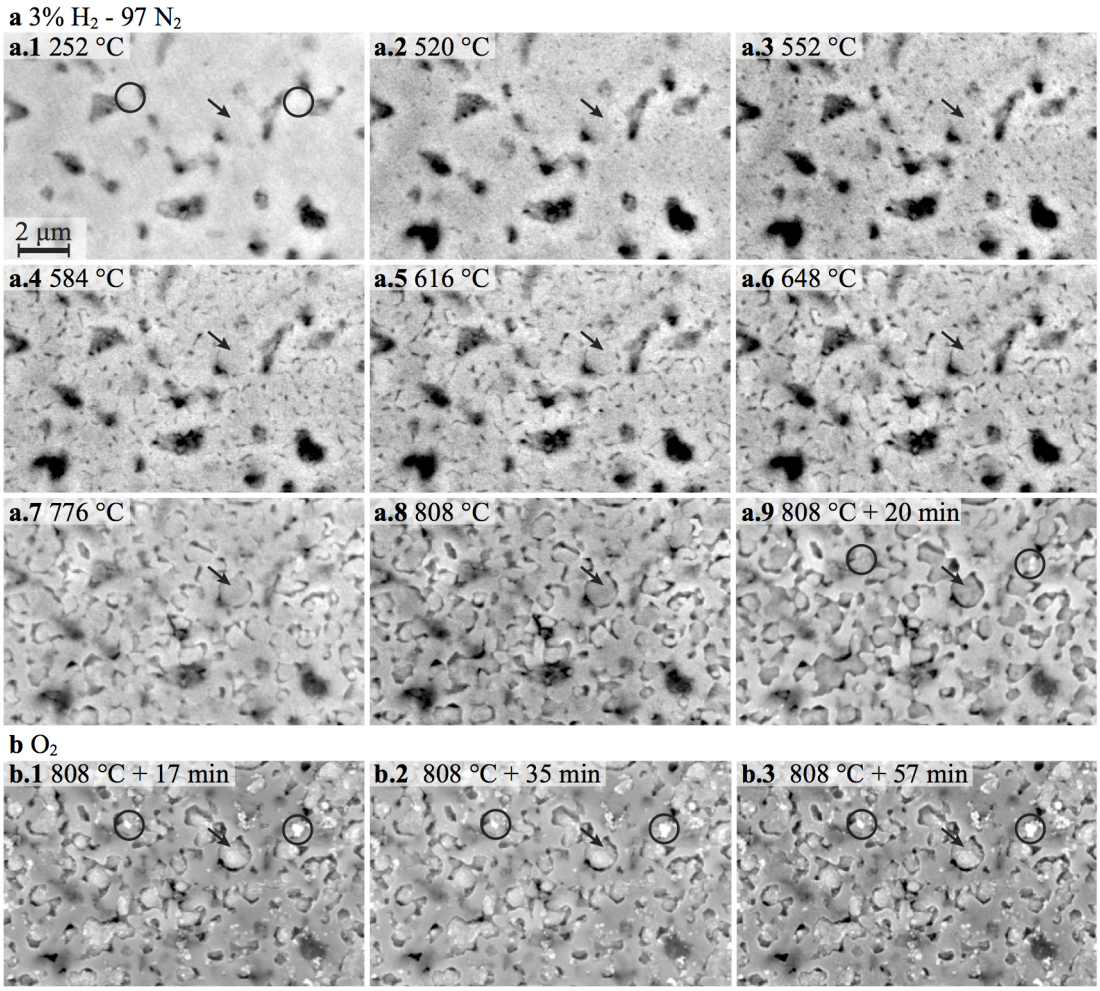

Figure F.2 – (a) Secondary electron images during reduction in a forming gas (3% H_2) pressure of 1.3 mbar, whilst heating at an overall rate of 4 °C min^{-1} up to 808 °C. (b) Isothermal reoxidation in 1.3 mbar of O_2 during 60 minutes. Arrows in (a-b) highlight the same NiO/Ni grains during a redox cycle, while circles show the growth of Ni/NiO domains on the specimen surface.

in similar conditions, yet those features were not discussed in their paper [20]. ESEM experiments should hence be analysed with care as the processes observed, which are by nature surface observations, may not fully represent the changes occurring within the bulk. With respect to the ETEM observations, those ESEM images demonstrate that the volatilisation and redeposition of $Ni(OH)_2$ species is likely to be the main mechanism behind the formation of new Ni domains separated from the initial Ni bulk. Finally, it should be mentioned that a chemical analysis to assess the degree of reduction/oxidation of the specimen is not possible in the ESEM and the specimen may not be fully reduced/oxidised at the end of each step (e.g. Fig. F.3j is not fully oxidised).

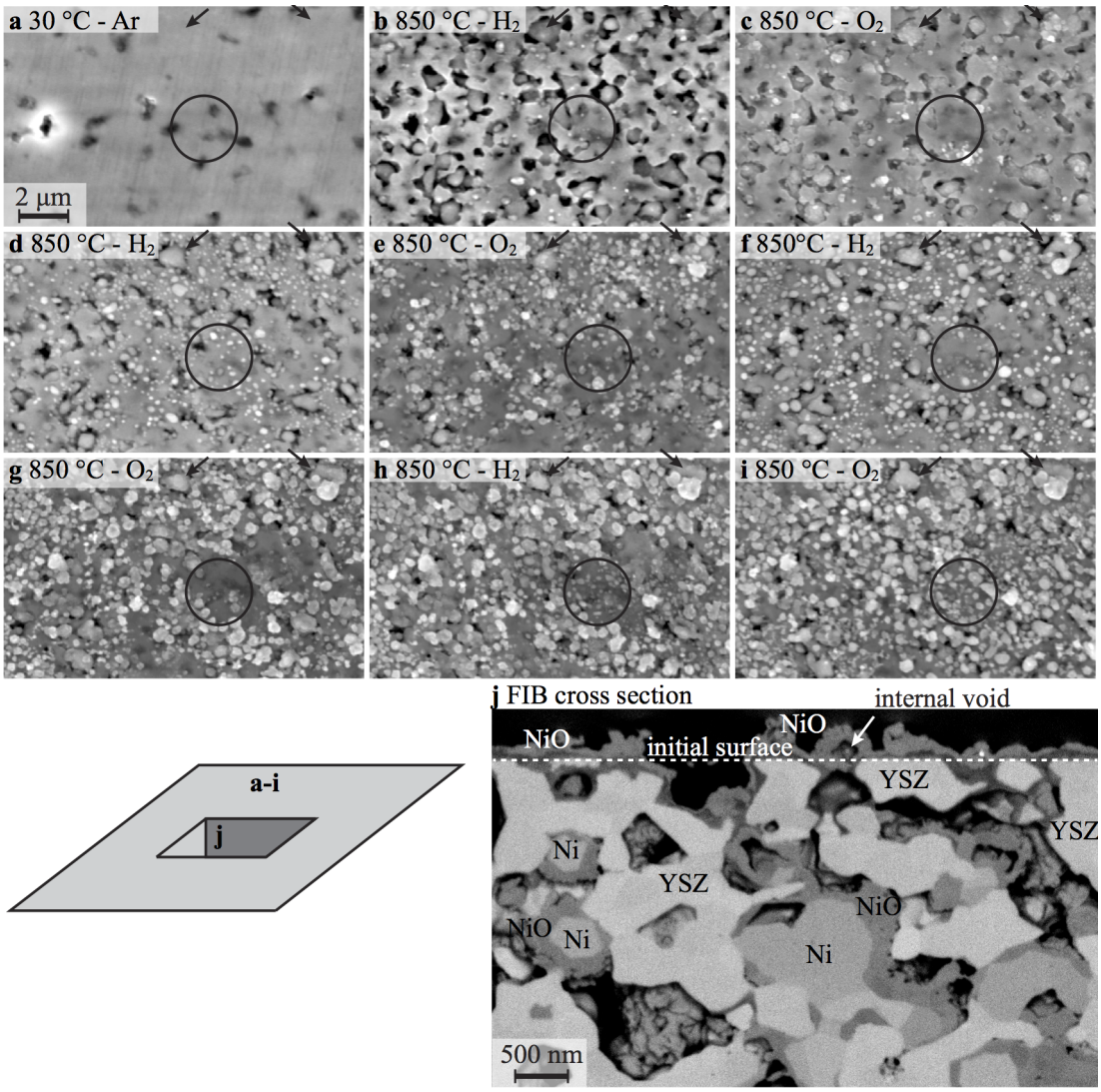

Figure F.3 – (a-j) Secondary electron images of the four redox cycles performed at 850 °C (total pressure of 1.3 mbar of forming gas (3% H_2) or O_2). Arrows mark the same NiO/Ni grain, while circles show the agglomeration of NiO on the specimen surface. Circles highlight the formation, growth and coalesce of Ni domains on the surface and their oxidation to NiO. (j) In-lens backscattered electron image (2 kV) of a focused ion beam cross-section of the specimen after redox cycling showing the NiO surface layer.

Bibliography

[1] S.C. Singhal and K. Kendall. *High Temperature Solid Oxide Fuel Cell - Fundamentals, Design and Applications*. Elsevier, Oxford, 2003.

[2] N.Q. Minh. Ceramic fuel cells. *Journal of the American Ceramic Society*, 76(3):563–588, 1993.

[3] S.C. Singhal. Solid Oxide Fuel Cells: Past, Present and Future. In J.T.S. Irvine and P. Connor, editors, *Solid Oxide Fuels Cells: Facts and Figures*, Green Energy and Technology, pages 1–23. Springer London, 2013.

[4] K. Föger and T. Rowe. Ultra-high-efficiency residential power system. In *3rd European Fuel Cell Technology Applications Conference*, pages 1–28, 2009.

[5] K.D. Kreuer. *Fuel Cells: Selected Entries from the Encyclopedia of Sustainability Science and Technology*. Springer, 2013.

[6] S.J. McPhail, L. Leto, and C. Boigues-Munoz. The yellow pages of SOFC technology. Technical report, National Agency for New Technologies, Energy and Sustainable Economic Development, 2013.

[7] J.B. Goodenough. Oxide-ion electrolytes. *Annual Review of Materials Research*, 33:91–128, 2003.

[8] H.S. Spacil. Electrical device including nickel-containing stabilized zirconia electrode, March 1970. US Patent 3,503,809.

[9] A. Faes, A. Nakajo, A. Hessler-Wyser, D. Dubois, A. Brisse, S. Modena, and J. Van herle. Redox study of anode-supported solid oxide fuel cell. *Journal of Power Sources*, 193:55–64, 2009.

[10] G.J. Nelson, K.N. Grew, J.R. Izzo Jr., J.J. Lombardo, W.M. Harris, A. Faes, A. Hessler-Wyser, J. Van herle, S. Wang, Y.S. Chu, A.V. Virkar, and W.K.S. Chiu. Three-dimensional microstructural changes in the Ni-YSZ solid oxide fuel cell anode during operation. *Acta Materialia*, 60(8):3491–3500, 2012.

[11] P. Tanasini, M. Cannarozzo, P. Costamagna, A. Faes, J. Van herle, A. Hessler-Wyser, and C. Comninellis. Experimental and theoretical investigation of degradation mechanisms by particle coarsening in SOFC electrodes. *Fuel Cells*, 9(5):740–752, 2009.

[12] A. Atkinson, S. Barnett, R.J. Gorte, J.T.S. Irvine, A.J. McEvoy, M. Mogensen, S.C. Singhal, and J. Vohs. Advanced anodes for high-temperature fuel cells. *Nature Materials*, 3(1):17–27, 2004.

[13] W.R. Grove. On a new voltaic combination. *Philosophical Magazine Series 3*, 13(84):430–431, 1838.

[14] U. Bossel. *The Birth of the Fuel Cell, 1835-1845: Including the First Publication of the Complete Correspondence from 1839 to 1868 Between Christian Friedrich Schoenbein (discoverer of the Fuel Cell Effect) and William Robert Grove (inventor of the Fuel Cell)*. European Fuel Cell Forum, 2000.

[15] H. Yokokawa, H. Tu, B. Iwanschitz, and A. Mai. Fundamental mechanisms limiting solid oxide fuel cell durability. *Journal of Power Sources*, 182(2):400–412, 2008.

[16] D. Sarantaridis and A. Atkinson. Redox cycling of Ni-based solid oxide fuel cell anodes: A review. *Fuel Cells*, 7(3):246–258, 2007.

[17] D. Waldbillig, A. Wood, and D.G. Ivey. Electrochemical and microstructural characterization of the redox tolerance of solid oxide fuel cell anodes. *Journal of Power Sources*, 145(2):206–215, 2005.

[18] T. Klemensø, C. Chung, P.H. Larsen, and M. Mogensen. The mechanism behind redox instability of anodes in high-temperature SOFCs. *Journal of the Electrochemical Society*, 152(11):A2186–A2192, 2005.

[19] M. Cassidy, G. Lindsay, and K. Kendall. The reduction of nickel-zirconia cermet anodes and the effects on supported thin electrolytes. *Journal of Power Sources*, 61(1-2):189–192, 1996.

[20] T. Klemensø, C.C. Appel, and M. Mogensen. *In situ* observations of microstructural changes in SOFC anodes during redox cycling. *Electrochemical and Solid-State Letters*, 9(9):A403–A407, 2006.

[21] J. Malzbender, E. Wessel, and R.W. Steinbrech. Reduction and re-oxidation of anodes for solid oxide fuel cells. *Solid State Ionics*, 176(29-30):2201–2203, 2005.

[22] D. Waldbillig, A. Wood, and D.G. Ivey. Thermal analysis of the cyclic reduction and oxidation behaviour of SOFC anodes. *Solid State Ionics*, 176(9-10):847–859, 2005.

[23] D. Sarantaridis, R. J. Chater, and A. Atkinson. Changes in physical and mechanical properties of SOFC Ni-YSZ composites caused by redox cycling. *Journal of the Electrochemical Society*, 155(5):B467–B472, 2008.

[24] H. Galinski, A. Bieberle-Hütter, J.L.M. Rupp, and L.J. Gauckler. Nonlinear oxidation kinetics of nickel cermets. *Acta Materialia*, 59(16):6239–6245, 2011.

[25] M. Ettler, H. Timmermann, J. Malzbender, A. Weber, and N.H. Menzler. Durability of Ni anodes during reoxidation cycles. *Journal of Power Sources*, 195:5452–5467, 2010.

[26] A. Faes, A. Hessler-Wyser, A. Zryd, and J. Van herle. A review of redox cycling of solid oxide fuel cells anode. *Membranes*, 2(3):585–664, 2012.

[27] A.F. Benton and P.H. Emmett. The reduction of nickelous and ferric oxides by hydrogen. *Journal of the American Chemical Society*, 46(12):2728–2737, 1924.

[28] H.H. Kung. *Transition metal oxides: surface chemistry and catalysis*. Elsevier, New York, 1989.

[29] J.M. Thomas and W.J. Thomas. *Principles and practice of heterogeneous catalysis*. Wiley VCH, New York, 1996.

[30] R.P. Furstenau, G. McDougall, and M.A. Langell. Initial stages of hydrogen reduction of NiO(100). *Surface Science*, 150(1):55–79, 1985.

[31] B. Lescop, J.P. Jay, and G. Fanjoux. Reduction of oxygen pre-treated Ni(111) by H_2 exposure: UPS and MIES studies compared with Monte Carlo simulations. *Surface Science*, 548(1-3):83–94, 2004.

[32] T. Hidayat, M.A. Rhamdhani, E. Jak, and P.C. Hayes. The characterization of nickel metal pore structures and the measurement of intrinsic reaction rate during the reduction of nickel oxide in H_2-N_2 and H_2-H_2O atmospheres. *Minerals Engineering*, 21(2):157–166, 2008.

[33] T. Hidayat, M.A. Rhamdhani, E. Jak, and P.C. Hayes. Investigation of nickel product structures developed during the gaseous reduction of solid nickel oxide. *Metallurgical and Materials Transactions B: Process Metallurgy and Materials Processing Science*, 40(4):462–473, 2009.

[34] T. Hidayat, M.A. Rhamdhani, E. Jak, and P.C. Hayes. On the relationships between the kinetics and mechanisms of gaseous hydrogen reduction of solid nickel oxide. *Metallurgical and Materials Transactions B: Process Metallurgy and Materials Processing Science*, 40(4):474–489, 2009.

[35] T. Hidayat, M.A. Rhamdhani, E. Jak, and P.C. Hayes. The kinetics of reduction of dense synthetic nickel oxide in H_2-N_2 and H_2-H_2O atmospheres. *Metallurgical and Materials Transactions B: Process Metallurgy and Materials Processing Science*, 40(1):1–16, 2009.

[36] P.A. Stadelmann. EMS - a software package for electron diffraction analysis and HREM image simulation in materials science. *Ultramicroscopy*, 21(2):131–145, 1987.

[37] R.W.G. Wyckoff. *Cubic closest packed, CCP, structure - Crystal Structures 1*. Interscience Publishers, New York, 1963.

[38] J.T. Richardson, R. Scates, and M.V. Twigg. X-ray diffraction study of nickel oxide reduction by hydrogen. *Applied Catalysis A: General*, 246(1):137–150, 2003.

[39] J.A. Rodriguez, J.C. Hanson, A.I. Frenkel, J.Y. Kim, and M. Perez. Experimental and theoretical studies on the reaction of H_2 with NiO: Role of O vacancies and mechanism for oxide reduction. *Journal of the American Chemical Society*, 124(2):346–354, 2002.

[40] A. Tarfaoui. *Modelling the Kinetics of Reduction by Temperature Programming*. PhD thesis, Delft University of Technology, 1996.

[41] A. Khawam and D.R. Flanagan. Solid-state kinetic models: basics and mathematical fundamentals. *The Journal of Physical Chemistry B*, 110(35):17315–17328, 2006.

[42] Z. Zhou, L. Han, and G.M. Bollas. Kinetics of NiO reduction by H_2 and Ni oxidation at conditions relevant to chemical-looping combustion and reforming. *International Journal of Hydrogen Energy*, 39(16):8535–8556, 2014.

[43] M. Avrami. Kinetics of phase change I: General theory. *The Journal of Chemical Physics*, 7(12):1103–1112, 1939.

[44] M. Avrami. Kinetics of phase change II: Transformation-time relations for random distribution of nuclei. *The Journal of Chemical Physics*, 8(2):212–224, 1940.

[45] M. Avrami. Granulation, phase change, and microstructure kinetics of phase change III. *The Journal of Chemical Physics*, 9(2):177–184, 1941.

[46] S. Yagi and D. Kunii. Studies on combustion of carbon particles in flames and fluidized beds. *Symposium (International) on Combustion*, 5(1):231–244, 1955.

[47] T.A. Utigard, M. Wu, G. Plascencia, and T. Marin. Reduction kinetics of goro nickel oxide using hydrogen. *Chemical Engineering Science*, 60(7):2061–2062, 2005.

[48] J. Szekely and J.W. Evans. A structural model for gas-solid reactions with a moving boundary. *Chemical Engineering Science*, 25(6):1091–1107, 1970.

[49] J. Szekely and J.W. Evans. A structural model for gas-solid reactions with a moving boundary-II. The effect of grain size, porosity and temperature on the reaction of porous pellets. *Chemical Engineering Science*, 26(11):1901–1913, 1971.

[50] J. Szekely and J.W. Evans. Studies in gas-solid reactions: Part I. A structural model for the reaction of porous oxides with a reducing gas. *Metallurgical Transactions*, 2(6):1691–1698, 1971.

[51] J. Szekely and J.W. Evans. Studies in gas-solid reactions: Part II. An experimental study of nickel oxide reduction with hydrogen. *Metallurgical Transactions*, 2(6):1699–1710, 1971.

[52] B.V. L'vov. Thermochemical approach to the mechanism and kinetics of NiO reduction with hydrogen. *Russian Journal of Applied Chemistry*, 83(5):778–786, 2010.

[53] M.M. Hossain and H.I. De Lasa. Reactivity and stability of Co-Ni/Al_2O_3 oxygen carrier in multicycle CLC. *AIChE Journal*, 53(7):1817–1829, 2007.

[54] B. Janković, B. Adnađević, and S. Mentus. The kinetic study of temperature-programmed reduction of nickel oxide in hydrogen atmosphere. *Chemical Engineering Science*, 63(3):567–575, 2008.

[55] P. Erri and A. Varma. Diffusional effects in nickel oxide reduction kinetics. *Industrial and Engineering Chemistry Research*, 48(1):4–6, 2009.

[56] S.S.A. Syed-Hassan and C.Z. Li. Effects of crystallite size on the kinetics and mechanism of NiO reduction with H_2. *International Journal of Chemical Kinetics*, 43(12):667–676, 2011.

[57] V.V. Boldyrev, M. Bulens, and B. Delmon. *The Control of the Reactivity of Solids*. Elsevier, 1979.

[58] H. Charcosset, R. Frety, A. Soldat, and Y. Trambouze. Increase of reducibility of NiO by H_2 due to pretreatment with salt solutions. *Journal of Catalysis*, 22(2):204–212, 1971.

[59] H. Charcosset, R. Frety, G. Labbe, and Y. Trambouze. Increase of the rate of reduction of NiO by H_2, due to pretreatment with CO or NH_3. *Journal of Catalysis*, 35(1):92–99, 1974.

[60] J.T. Richardson, B. Turk, M. Lei, K. Forster, and M.V. Twigg. Effects of promoter oxides on the reduction of nickel oxide. *Applied Catalysis A, General*, 83(1):87–101, 1992.

[61] Y. Iida and K. Shimada. Hydrogen reduction of a single crystal of nickel oxide. *Bulletin of the Chemical Society of Japan*, 33(6):790–793, 1960.

[62] S. Modena, S. Ceschini, A. Tomasi, D. Montinaro, and V.M. Sglavo. Reduction and reoxidation processes of NiO/YSZ composite for solid oxide fuel cell anodes. *Journal of Fuel Cell Science and Technology*, 3(4):487–491, 2006.

[63] D Fouquet, A.C. Müller, A. Weber, and E. Ivers-Tiffée. Kinetics of oxidation and reduction of Ni/YSZ cermets. *Ionics*, 1862-0760:103–108, 2003.

[64] B. Bonvalot-Dubois, G. Dhalenne, J. Berthon, A. Revcolevschi, and R.A. Rapp. Reduction of NiO platelets in a NiO/ZrO_2(CaO) directional composite. *Journal of the American Ceramic Society*, 71(4):296–301, 1988.

[65] N.M. Tikekar, T.J. Armstrong, and A.V. Virkar. Reduction and reoxidation kinetics of nickel-based SOFC anodes. *Journal of the Electrochemical Society*, 153(4):A654–A663, 2006.

[66] M. Pihlatie, A. Kaiser, and M. Mogensen. Redox stability of SOFC: Thermal analysis of Ni-YSZ composites. *Solid State Ionics*, 180(17-19):1100–1112, 2009.

[67] K.V. Hansen, T. Jacobsen, K. Thyden, Y. Wu, and M.B. Mogensen. *In situ* surface reduction of a NiO-YSZ-alumina composite using scanning probe microscopy. *Journal of Solid State Electrochemistry*, 18(7):1869–1878, 2014.

[68] Z.Z. Fang. *Sintering of Advanced Materials - Fundamentals and Processes*. Woodhead Publishing, 2010.

[69] T.W. Hansen. *Sintering and particle dynamics in supported metal catalysts*. PhD thesis, Technical University of Denmark, 2006.

[70] B. Iwanschitz. *Degradation von Ni-Cermet-Anoden in keramischen Hochtemperaturbrennstoffzellen*. PhD thesis, Technischen Hochschule Aachen, 2012.

[71] D. Simwonis, F. Tietz, and D. Stöver. Nickel coarsening in annealed Ni/8YSZ anode substrates for solid oxide fuel cells. *Solid State Ionics*, 132(3):241–251, 2000.

[72] R. Vassen, D. Simwonis, and D. Stöver. Modelling of the agglomeration of Ni-particles in anodes of solid oxide fuel cells. *Journal of Materials Science*, 36(1):147–151, 2001.

[73] J. Sehested, J.A.P. Gelten, I.N. Remediakis, H. Bengaard, and J.K. Nørskov. Sintering of nickel steam-reforming catalysts: effects of temperature and steam and hydrogen pressures. *Journal of Catalysis*, 223(2):432–443, 2004.

[74] A. Hagen, R. Barfod, P.V. Hendriksen, Y.-L. Liu, and S. Ramousse. Degradation of anode supported SOFCs as a function of temperature and current load. *Journal of the Electrochemical Society*, 153(6):A1165–A1171, 2006.

[75] M.H. Pihlatie, A. Kaiser, M. Mogensen, and M. Chen. Electrical conductivity of Ni-YSZ composites: Degradation due to Ni particle growth. *Solid State Ionics*, 189(1):82–90, 2011.

[76] A. Gubner, H. Landes, J. Metzger, H. Seeg, and R. Stübner. Investigations into the degradation of the cermet anode of a solid oxide fuel cells. In U. Stimming, S.C. Singhal, H. Tagawa, and W. Lehnert, editors, *Solid Oxide Fuel Cells V*, The Electrochemical Society, pages 844–850, 1997.

[77] L. Holzer, B. Iwanschitz, T. Hocker, B. Münch, M. Prestat, D. Wiedenmann, U. Vogt, P. Holtappels, J. Sfeir, A. Mai, and T. Graule. Microstructure degradation of cermet anodes for solid oxide fuel cells: Quantification of nickel grain growth in dry and in humid atmospheres. *Journal of Power Sources*, 196(3):1279–1294, 2011.

[78] L. Grahl-Madsen, P.H. Larsen, N. Bonanos, J. Engell, and S. Linderoth. Mechanical strength and electrical conductivity of Ni-YSZ cermets fabricated by viscous processing. *Journal of Materials Science*, 41(4):1097–1107, 2006.

[79] A. Atkinson. Transport processes during the growth of oxide films at elevated temperature. *Reviews of Modern Physics*, 57(2):437–470, 1985.

[80] N. Cabrera and N.F. Mott. Theory of the oxidation of metals. *Reports on Progress in Physics*, 12(1):163–184, 1949.

[81] G.A. Niklasson and R. Karmhag. Oxidation kinetics of metallic nanoparticles. *Surface Science*, 532-535:324–327, 2003.

[82] H.T. Liu, A.F. Armitage, and D.P. Woodruff. Anisotropy of initial oxidation kinetics of nickel single crystal surfaces. *Surface Science*, 114(2-3):431–444, 1982.

[83] M.J. Graham and M. Cohen. On the mechanism of low-temperature oxidation (23 °C - 450 °C) of polycrystalline nickel. *Journal of Electrochemical Society*, 119(7):879–882, 1972.

[84] C. Wagner. Beitrag zur Theorie des Anlaufvorgangs. *Zeitschrift für Physikalische Chemie*, B41:41, 1933.

[85] A. Atkinson and R.I. Taylor. The self-diffusion of Ni in NiO and its relevance to the oxidation of Ni. *Journal of Materials Science*, 13(2):427–432, 1978.

[86] A. Atkinson, R.I. Taylor, and P.D. Goode. Transport processes in the oxidation of Ni studied using tracers in growing NiO scales. *Oxidation of Metals*, 13(6):519–543, 1979.

[87] A. Atkinson, D.P. Moon, D.W. Smart, and R.I. Taylor. Tracer diffusion studies in NiO bicrystals and polycrystals. *Journal of Materials Science*, 21(5):1747–1757, 1986.

[88] A. Atkinson and D.W. Smart. Transport of nickel and oxygen during the oxidation of nickel and dilute nickel/chromium alloy. *Journal of the Electrochemical Society*, 135(11):2886–2893, 1988.

[89] C. Dubois, C. Monty, and J. Philibert. Influence of oxygen pressure on oxygen self-diffusion in NiO. *Solid State Ionics*, 12(C):75–78, 1984.

[90] S. Perusin, D. Monceau, and E. Andrieu. Investigations on the diffusion of oxygen in nickel at 1000 °C by SIMS analysis. *Journal of the Electrochemical Society*, 152(12):E390–E397, 2005.

[91] R. Haugsrud. On the high-temperature oxidation of nickel. *Corrosion Science*, 45(1):211–235, 2003.

[92] A. Atkinson, R.I. Taylor, and A.E. Hughes. Quantitative demonstration of the grain boundary diffusion mechanism for the oxidation of metals. *Philosophical Magazine A: Physics of Condensed Matter, Structure, Defects and Mechanical Properties*, 45(5):823–833, 1982.

[93] M.J. Graham, R.J. Hussey, and M. Cohen. Influence of oxide structure on the oxidation rate of nickel single crystals. *Journal of the Electrochemical Society*, 120(11):1523–1529, 1973.

[94] A.M. Huntz, M. Andrieux, and R. Molins. Relation between the oxidation mechanism of nickel, the microstructure and mechanical resistance of NiO films and the nickel purity. I. Oxidation mechanism and microstructure of NiO films. *Materials Science and Engineering A*, 415(1-2):21–32, 2006.

[95] A.M. Huntz, M. Andrieux, and R. Molins. Relation between the oxidation mechanism of nickel, the microstructure and mechanical resistance of NiO films and the nickel purity. II. Mechanical resistance of NiO films. *Materials Science and Engineering A*, 417(1-2):8–15, 2006.

[96] R. Hales and A.C. Hill. The role of metal lattice vacancies in the high temperature oxidation of nickel. *Corrosion Science*, 12(11):843–853, 1972.

[97] N. Chopra, L. Claypoole, and L. Bachas. Morphological control of Ni/NiO core/shell nanoparticles and production of hollow NiO nanostructures. *Journal of Nanoparticle Research*, 12:2883–2893, 2010.

[98] M. Feygenson, A. Kou, L.E. Kreno, A.L. Tiano, J.M. Patete, F. Zhang, M.S. Kim, V. Solovyov, S.S. Wong, and M.C. Aronson. Properties of highly crystalline NiO and Ni nanoparticles prepared by high-temperature oxidation and reduction. *Physical Review B - Condensed Matter and Materials Physics*, 81(1):1–9, 2010.

[99] J.G. Railsback, A.C. Johnston-Peck, J. Wang, and J.B. Tracy. Size-dependent nanoscale kirkendall effect during the oxidation of nickel nanoparticles. *ACS Nano*, 4(4):1913–1920, 2010.

[100] B. Rellinghaus, S. Stappert, E.F. Wassermann, H. Sauer, and B. Spliethoff. The effect of oxidation on the structure of nickel nanoparticles. *European Physical Journal D*, 8(3):249–252, 2000.

[101] R. Peraldi, D. Monceau, and B. Pieraggi. Correlations between growth kinetics and microstructure for scales formed by high-temperature oxidation of pure nickel. I. Morphologies and microstructures. *Oxidation of Metals*, 58(3-4):249–273, 2002.

[102] R. Peraldi, D. Monceau, and B. Pieraggi. Correlations between growth kinetics and microstructure for scales formed by high-temperature oxidation of pure nickel. II. Growth kinetics. *Oxidation of Metals*, 58(3-4):275–295, 2002.

[103] R. Peraldi, D. Monceau, and B. Pieraggi. Le nickel, matériau modèle pour les études d'oxydation à haute température: Premiers pas vers une modélisation prédictive du phénomène. *La revue de Métallurgie*, 102(2):135–146, 2005.

[104] C.K. Kim and L.W. Hobbs. Microstructural evidence for short-circuit oxygen diffusion paths in the oxidation of a dilute Ni-Cr alloy. *Oxidation of Metals*, 45(3-4):247–265, 1996.

[105] A.W. Harris and A. Atkinson. Oxygen transport in growing nickel oxide scales at 600-800 °C. *Oxidation of Metals*, 34(3-4):229–258, 1990.

[106] P. Kofstad. Fundamental aspects of corrosion by hot gases. *Materials Science and Engineering A*, A120-1(1 -2 pt 1):25–29, 1989.

[107] W. Przybilla and M. Schütze. Role of growth stresses on the structure of oxide scales on nickel at 800 and 900 °C. *Oxidation of Metals*, 58(1-2):103–145, 2002.

[108] L.C. Dufour and F. Morin. The growth of oxide platelets on nickel in pure oxygen. II. Surface analyses and growth mechanism. *Oxidation of Metals*, 39(1-2):137–154, 1993.

[109] F. Morin, L.C. Dufour, and G. Trudel. The growth of oxide platelets on nickel in pure oxygen. I. Morphology and oxidation kinetics. *Oxidation of Metals*, 37(1-2):39–63, 1992.

[110] H.M. Flower and B.A. Wilcox. *In situ* oxidation of Ni30 wt% Cr and TDNiCr in the high voltage electron microscope. *Corrosion Science*, 17(3):253–264, 1977.

[111] T.N. Le, J.L. Hutchison, and B. Derby. *In situ* HREM observation of the oxidation of nickel thin foils. In *Materials Research Society Symposium - Proceedings*, volume 357, pages 225–229, 1995.

[112] P. Marikar, M.B. Brodsky, C.H. Sowers, and N.J. Zaluzec. *In-situ* HVEM studies of the early stages of oxidation of nickel and nickel-chromium alloys. *Ultramicroscopy*, 29(1-4):247–256, 1989.

[113] P. Rez, E.S. Moore, and R. Sharma. *In situ* measurements of Ni oxidation using electron energy-loss spectroscopy. *Microscopy and Microanalysis*, 14(SUPPL. 2):1382–1383, 2008.

[114] S. Chenna, R. Banerjee, and P.A. Crozier. Atomic-scale observation of the Ni activation process for partial oxidation of methane using *in situ* environmental TEM. *ChemCatChem*, 3(6):1051–1059, 2011.

[115] S. Hildebrandt, C. Hagendorf, T. Doege, C. Jeckstiess, R. Kulla, H. Neddermeyer, and T. Uttich. Real time scanning tunneling microscopy study of the initial stages of oxidation of Ni(111) between 400 and 470 K. *Journal of Vacuum Science and Technology A: Vacuum, Surfaces and Films*, 18(3):1010–1015, 2000.

[116] G.M. Raynaud and R.A. Rapp. *In situ* observation of whiskers, pyramids and pits during the high-temperature oxidation of metals. *Oxidation of Metals*, 21(1-2):89–102, 1984.

[117] B. Schmid, N. Aas, Ø. Grong, and R. Ødegård. High-temperature oxidation of nickel and chromium studied with an *in-situ* environmental scanning electron microscope. *Scanning*, 23(4):255–266, 2001.

[118] A.M. Kiss, W.M. Harris, S. Wang, J. Vila-Comamala, A. Deriy, and W.K.S. Chiu. *In-situ* observation of nickel oxidation using synchrotron based full-field transmission X-ray microscopy. *Applied Physics Letters*, 102(5):1–4, 2013.

[119] Y. Zhang, B. Liu, B. Tu, Y. Dong, and M. Cheng. Redox cycling of Ni-YSZ anode investigated by TPR technique. *Solid State Ionics*, 176(29-30):2193–2199, 2005.

[120] Y. Nakagawa, K. Yashiro, K. Sato, T. Kawada, and J. Mizusaki. Microstructural changes of Ni/YSZ cermet under repeated redox reaction in environmental scanning electron microscope (ESEM). *ECS Transactions*, 7(1):1373–1380, 2007.

[121] G. Stathis, D. Simwonis, F. Tietz, A. Moropoulou, and A. Naoumides. Oxidation and resulting mechanical properties of Ni/$8Y_2O_3$-stabilized zirconia anode substrate for solid-oxide fuel cells. *Journal of Materials Research*, 17(5):951–958, 2002.

[122] M. Pihlatie, A. Kaiser, P.H. Larsen, and M. Mogensen. Dimensional behavior of Ni-YSZ composites during redox cycling. *Journal of the Electrochemical Society*, 156(3):B322–B329, 2009.

[123] D. Waldbillig, A. Wood, and D.G. Ivey. Enhancing the redox tolerance of anode-supported SOFC by microstructural modification. *Journal of the Electrochemical Society*, 154(2):B133–B138, 2007.

[124] T. Klemensø. *Relationships between structure and performance of SOFC anodes*. PhD thesis, Technical University of Denmark, 2005.

[125] M. Ettler, G. Blafl, and N.H. Menzler. Characterisation of Ni-YSZ-cermets with respect to redox stability. *Fuel Cells*, 7(5):349–355, 2007.

[126] G. Robert, A. Kaiser, and E. Batawi. Anode substrate design for redox-stable ASE cells. *European SOFC Forum Proceedings*, 1:193–200, 2004.

[127] M. Pihlatie, T. Ramos, and A. Kaiser. Testing and improving the redox stability of Ni-based solid oxide fuel cells. *Journal of Power Sources*, 193(1):322–330, 2009.

[128] A. Faes, J.-M. Fuerbringer, D. Mohamedi, A. Hessler-Wyser, G. Caboche, and J. Van herle. Design of experiment approach applied to reducing and oxidizing tolerance of anode supported solid oxide fuel cell. Part I: Microstructure optimization. *Journal of Power Sources*, 196(17):7058–7069, 2011.

[129] A. Faes, Z. Wuillemin, P. Tanasini, N. Accardo, S. Modena, H.J. Schindler, M. Cantoni, H. Lübbe, S. Diethelm, A. Hessler-Wyser, and J. Van herle. Design of experiment approach applied to reducing and oxidizing tolerance of anode supported solid oxide fuel cell. Part II: Electrical, electrochemical and microstructural characterization of tape-cast cells. *Journal of Power Sources*, 196(21):8909–8917, 2011.

[130] T. Klemensø and M. Mogensen. Ni-YSZ solid oxide fuel cell anode behavior upon redox cycling based on electrical characterization. *Journal of the American Ceramic Society*, 90(11):3582–3588, 2007.

[131] A. Faes. *RedOx stability of anode supported solid oxide fuel cells*. PhD thesis, Ecole Polytechnique Fédérale de Lausanne, 2011.

[132] J. Yi, A. Kaloyannis, and C.G. Vayenas. High temperature cyclic voltammetry of Pt catalyst-electrodes in solid electrolyte cells. *Electrochimica Acta*, 38(17):2533–2539, 1993.

[133] S. Souentie, C. Falgairette, and C. Comninellis. Electrochemical investigation of the O_2(g), Ni/YSZ system using cyclic voltammetry. *Journal of the Electrochemical Society*, 157(5):P49–P52, 2010.

[134] M. Juhl, S. Primdahl, C. Manon, and M. Mogensen. Performance/structure correlation for composite SOFC cathodes. *Journal of Power Sources*, 61(1-2):173–181, 1996.

[135] E.P. Murray, T. Tsai, and S.A. Barnett. Oxygen transfer processes in (La,Sr)MnO_3/Y_2O_3-stabilized ZrO_2 cathodes: An impedance spectroscopy study. *Solid State Ionics*, 110(3-4):235–243, 1998.

[136] A. Bieberle, L.P. Meier, and L.J. Gauckler. The electrochemistry of Ni pattern anodes used as solid oxide fuel cell model electrodes. *Journal of the Electrochemical Society*, 148(6):A646–A656, 2001.

[137] A. Weber, B. Sauer, A.C. Müller, D. Herbstritt, and E. Ivers-Tiffée. Oxidation of H_2, CO and methane in SOFCs with Ni/YSZ-cermet anodes. *Solid State Ionics*, 152-153:543–550, 2002.

[138] S. Diethelm, A. Closset, J. Van herle, and K. Nisancioglu. Determination of chemical diffusion and surface exchange coefficients of oxygen by electrochemical impedance spectroscopy. *Journal of the Electrochemical Society*, 149(11):E424–E432, 2002.

[139] M. Backhaus-Ricoult, K. Adib, T. St.Clair, B. Luerssen, L. Gregoratti, and A. Barinov. *In-situ* study of operating SOFC LSM/YSZ cathodes under polarization by photoelectron microscopy. *Solid State Ionics*, 179(21-26):891–895, 2008.

[140] S.C. Decaluwe, M.E. Grass, C. Zhang, F.E. Gabaly, H. Bluhm, Z. Liu, G.S. Jackson, A.H. McDaniel, K.F. McCarty, R.L. Farrow, M.A. Linne, Z. Hussain, and B.W. Eichhorn. *In situ* characterization of ceria oxidation states in high-temperature electrochemical cells with ambient pressure XPS. *Journal of Physical Chemistry C*, 114(46):19853–19861, 2010.

[141] A.R. Rojas, H.E. Esparza-Ponce, L. Fuentes, A. Lopez-Ortiz, A. Keer, and J. Reyes-Gasga. *In situ* X-ray Rietveld analysis of Ni-YSZ solid oxide fuel cell anodes during NiO reduction in H_2. *Journal of Physics D: Applied Physics*, 38(13):2276–2282, 2005.

[142] A. Hagen, H.F. Poulsen, T. Klemensø, R.V. Martins, V. Honkimäki, T. Buslaps, and R. Feidenshans. A depth-resolved *in-situ* study of the reduction and oxidation of Ni-based anodes in solid oxide fuel cells. *Fuel Cells*, 6(5):361–366, 2006.

[143] H. Sumi, K. Ukai, M. Yokoyama, Y. Mizutani, Y. Doi, S. Machiya, Y. Akiniwa, and K. Tanaka. Changes of internal stress in solid-oxide fuel cell during red-ox cycle evaluated by *in situ* measurement with synchrotron radiation. *Journal of Fuel Cell Science and Technology*, 3(1):68–74, 2006.

[144] K. Tanaka, Y. Akiniwa, H. Kimura, K. Ukai, M. Yokayama, and Y. Mizutani. *In situ* synchrotron measurement of internal stresses in solid-oxide fuel cell during red-ox cycle. *Materials Science Forum*, 571 - 572:339–344, 2008.

[145] G. Nurk, T. Huthwelker, A. Braun, C. Ludwig, E. Lust, and R.P.W.J. Struis. Redox dynamics of sulphur with Ni/GDC anode during SOFC operation at mid- and low-range temperatures: An operando S K-edge XANES study. *Journal of Power Sources*, 240:448–457, 2013.

[146] R.J. Woolley, M.P. Ryan, and S.J. Skinner. *In situ* measurements on solid oxide fuel cell cathodes - simultaneous X-ray absorption and AC impedance spectroscopy on symmetrical cells. *Fuel Cells*, 13(6):1080–1087, 2013.

[147] P.R. Shearing, R.S. Bradley, J. Gelb, S.N. Lee, A. Atkinson, P.J. Withers, and N.P. Brandon. Using synchrotron X-ray nano-CT to characterize SOFC electrode microstructures in three-dimensions at operating temperature. *Electrochemical and Solid-State Letters*, 14(10):B117–B120, 2011.

[148] P. Fuoss, K.C. Chang, and H. You. *In situ* X-ray studies of film cathodes for solid oxide fuel cells. *Journal of Electron Spectroscopy and Related Phenomena*, 190, Part A(0):75–83, 2013.

[149] Z. Cheng and M. Liu. Characterization of sulfur poisoning of Ni-YSZ anodes for solid oxide fuel cells using *in situ* Raman microspectroscopy. *Solid State Ionics*, 178(13-14):925–935, 2007.

[150] M. Liu, M.E. Lynch, K. Blinn, F.M. Alamgir, and Y. Choi. Rational SOFC material design: new advances and tools. *Materials Today*, 14(11):534–546, 2011.

[151] C. Zhang, M.E. Grass, A.H. McDaniel, S.C. DeCaluwe, F. Gabaly, Z. Liu, K.F. McCarty, R.L. Farrow, M.A. Linne, Z. Hussain, G.S. Jackson, H. Bluhm, and B.W. Eichhorn. Measuring fundamental properties in operating solid oxide electrochemical cells by using *in situ* X-ray photoelectron spectroscopy. *Nature Materials*, 9(11):944–949, 11 2010.

[152] M.B. Pomfret, J.C. Owrutsky, and R.A. Walker. *In situ* optical studies of solid-oxide fuel cells. *Annual Review of Analytical Chemistry*, 3:151–174, 2010.

[153] J.D. Kirtley, B.C. Eigenbrodt, and R.A. Walker. *In situ* optical studies of oxidation kinetics of Ni/YSZ cermet anodes. *ECS Transactions*, 33(40):25–37, 2011.

[154] J.D. Kirtley, D.M. Halat, M.D. McIntyre, B.C. Eigenbrodt, and R.A. Walker. High-temperature "Spectrochronopotentiometry": Correlating electrochemical performance with *in situ* raman spectroscopy in solid oxide fuel cells. *Analytical Chemistry*, 84(22):9745–9753, 2012.

[155] J.D. Kirtley, A. Singh, D. Halat, T. Oswell, J.M. Hill, and R.A. Walker. *In situ* Raman studies of carbon removal from high temperature Ni-YSZ cermet anodes by gas phase reforming agents. *Journal of Physical Chemistry C*, 117(49):25908–25916, 2013.

[156] V. Sharma. *Synthesis and in situ environmental transmission electron microscopy investigations of ceria-based oxides for solid oxide fuel cell anodes*. PhD thesis, Arizona State University, 2011.

[157] A.H. Tavabi, Z. Yasenjiang, and T. Tanji. *In situ* off-axis electron holography of metal-oxide hetero-interfaces in oxygen atmosphere. *Journal of Electron Microscopy*, 60(5):307–314, 2011.

[158] A.H. Tavabi. *In situ analytical electron microscopy for fundamental studies of fuel cells*. PhD thesis, Nagoya University, 2012.

[159] A.H. Tavabi, S. Arai, T. Tanji, and S. Muto. Single chamber SOFC operation in ETEM. *Microscopy and Microanalysis*, 18:1288–1289, 2012.

[160] A.H. Tavabi, S. Arai, and T. Tanji. *In situ* analytical electron microscopy studies of redox reactions at a YSZ/Pt interface. *Microscopy and Microanalysis*, 18(3):538–544, 2012.

[161] F. Meirer, J. Cabana, Y. Liu, A. Mehta, J.C. Andrews, and P. Pianetta. Three-dimensional imaging of chemical phase transformations at the nanoscale with full-field transmission X-ray microscopy. *Journal of Synchrotron Radiation*, 18(5):773–781, 2011.

[162] Y.C.K. Chen-Wiegart, W.M. Harris, J.J. Lombardo, W.K.S. Chiu, and J. Wang. Oxidation states study of nickel in solid oxide fuel cell anode using X-ray full-field spectroscopic nano-tomography. *Applied Physics Letters*, 101(25):1–4, 2012.

[163] J.C. Andrews and B.M. Weckhuysen. Hard X-ray spectroscopic nano-imaging of hierarchical functional materials at work. *ChemPhysChem*, 14(16):3655–3666, 2013.

[164] E. Ruska. Beitrag zur übermikroskopischen abbildung bei höheren drucken. *Kolloid-Zeitschrift*, 100(2):212–219, 1942.

[165] H. Hashimoto, T. Naiki, T. Eto, and K. Fujiwara. High temperature gas reaction specimen chamber for an electron microscope. *Japanese Journal of Applied Physics 7*, 7:946–952, 1968.

[166] P.B. Hirsch. *Electron microscopy of thin crystals*. Kireger Publishing Company, 1977.

[167] E.D. Boyes and P.L. Gai. Environmental high resolution electron microscopy and applications to chemical science. *Ultramicroscopy*, 67(1-4):219–232, 1997.

[168] P.L. Hansen, J.B. Wagner, S. Helveg, J.R. Rostrup-Nielsen, B.S. Clausen, and H. Topsøe. Atom-resolved imaging of dynamic shape changes in supported copper nanocrystals. *Science*, 295(5562):2053–2055, 2002.

[169] M. Haider, H. Rose, S. Uhlemann, E. Schwan, B. Kabius, and K. Urban. A spherical-aberration-corrected 200 kV transmission electron microscope. *Ultramicroscopy*, 75(1):53–60, 1998.

[170] C.C. Ahn. *Transmission Electron Energy Loss Spectrometry in Materials Science and The EELS Atlas*. Wiley-VCH Verlag GmbH, 2005.

[171] D.B. Williams and C.B. Carter. *Transmission electron microscopy, Part 3: Spectrometry*. Springer, Second edition, New-York, 2008.

[172] R.F. Egerton. *Electron Energy-Loss Spectroscopy in the Electron Microscope*. Springer, 2011.

[173] J.R. Jinschek. Advances in the environmental transmission electron microscope (ETEM) for nanoscale *in situ* studies of gas-solid interactions. *Chemical Communications*, 50(21):2696–2706, 2014.

[174] T.W. Hansen, J.B. Wagner, and R.E. Dunin-Borkowski. Aberration corrected and monochromated environmental transmission electron microscopy - challenges and prospects. *Materials Science and Technology*, 26(11):1338–1344, 2010.

[175] G.M. Parkinson. High resolution, *in-situ* controlled atmosphere transmission electron microscopy (CATEM) of heterogeneous catalysts. *Catalysis Letters*, 2(5):303–307, 1989.

[176] S. Giorgio, S. Sao Joao, S. Nitsche, D. Chaudanson, G. Sitja, and C.R. Henry. Environmental electron microscopy (ETEM) for catalysts with a closed E-cell with carbon windows. *Ultramicroscopy*, 106(6):503–507, 2006.

[177] J.F. Creemer, S. Helveg, G.H. Hoveling, S. Ullmann, A.M. Molenbroek, P.M. Sarro, and H.W. Zandbergen. Atomic-scale electron microscopy at ambient pressure. *Ultramicroscopy*, 108(9):993–998, 2008.

[178] J.B. Wagner, F. Cavalca, C.D. Damsgaard, L.D.L. Duchstein, and T.W. Hansen. Exploring the environmental transmission electron microscope. *Micron*, 43(11):1169–1175, 2012.

[179] L.F. Allard, W.C. Bigelow, M. Jose-Yacaman, D.P. Nackashi, J. Damiano, and S.E. Mick. A new MEMS-based system for ultra-high-resolution imaging at elevated temperatures. *Microscopy Research and Technique*, 72(3):208–215, 2009.

[180] J.R. Jinschek. Atomic scale structure-function relationship of heterogeneous catalysts: investigation of gas-solid interactions by ETEM. *Microscopy and Microanalysis*, 26:5–10, 2012.

[181] J.R. Jinschek. Use of an environmental transmission electron microscope for dynamic *in situ* studies of nano-structured materials at the atomic scale. *American Laboratory*, 45(3):12–16, 2013.

[182] T.W. Hansen and J.B. Wagner. Catalysts under controlled atmospheres in the transmission electron microscope. *ACS Catalysis*, 4(6):1673–1685, 2014.

[183] J. Sehested, J.A.P. Gelten, and S. Helveg. Sintering of nickel catalysts: Effects of time, atmosphere, temperature, nickel-carrier interactions, and dopants. *Applied Catalysis A: General*, 309(2):237–246, 2006.

[184] S.B. Simonsen, I. Chorkendorff, S. Dahl, M. Skoglundh, J. Sehested, and S. Helveg. Direct observations of oxygen-induced platinum nanoparticle ripening studied by *in situ* TEM. *Journal of the American Chemical Society*, 132(23):7968–7975, 2010.

[185] S.R. Challa, A.T. Delariva, T.W. Hansen, S. Helveg, J. Sehested, P.L. Hansen, F. Garzon, and A.K. Datye. Relating rates of catalyst sintering to the disappearance of individual nanoparticles during Ostwald ripening. *Journal of the American Chemical Society*, 133(51):20672–20675, 2011.

[186] S. Hofmann, R. Sharma, C.T. Wirth, F. Cervantes-Sodi, C. Ducati, T. Kasama, R.E. Dunin-Borkowski, J. Drucker, P. Bennett, and J. Robertson. Ledge-flow-controlled catalyst interface dynamics during Si nanowire growth. *Nature Materials*, 7(5):372–375, 2008.

[187] H. Yoshida, Y. Kuwauchi, J.R. Jinschek, K. Sun, S. Tanaka, M. Kohyama, S. Shimada, M. Haruta, and S. Takeda. Visualizing gas molecules interacting with supported nanoparticulate catalysts at reaction conditions. *Science*, 335(6066):317–319, 2012.

[188] P.A. Crozier, R. Wang, and R. Sharma. *In situ* environmental TEM studies of dynamic changes in cerium-based oxides nanoparticles during redox processes. *Ultramicroscopy*, 108(11):1432–1440, 2008.

[189] R. Sharma, P.A. Crozier, Z.C. Kang, and L. Eyring. Observation of dynamic nanostructural and nanochemical changes in ceria-based catalysts during *in-situ* reduction. *Philosophical Magazine*, 84(25-26):2731–2747, 2004.

[190] V. Sharma, P.A. Crozier, R. Sharma, and J.B. Adams. Direct observation of hydrogen spillover in Ni-loaded Pr-doped ceria. *Catalysis Today*, 180(1):2–8, 2012.

[191] R. Wang, P.A. Crozier, R. Sharma, and J.B. Adams. Measuring the redox activity of individual catalytic nanoparticles in cerium-based oxides. *Nano Letters*, 8(3):962–967, 2008.

[192] R. Wang, P.A. Crozier, and R. Sharma. Structural transformation in ceria nanoparticles during redox processes. *Journal of Physical Chemistry C*, 113(14):5700–5704, 2009.

[193] R. Wang, P.A. Crozier, and R. Sharma. Nanoscale compositional and structural evolution in ceria zirconia during cyclic redox treatments. *Journal of Materials Chemistry*, 20(35):7497–7505, 2010.

[194] J. Ciston, R. Si, J.A. Rodriguez, J.C. Hanson, A. Martínez-Arias, M. Fernandez-García, and Y. Zhu. Morphological and structural changes during the reduction and reoxidation of CuO/CeO_2 and $Ce_{1-x}Cu_xO_2$ nanocatalysts: *In situ* studies with environmental TEM, XRD, and XAS. *The Journal of Physical Chemistry C*, 115(28):13851–13859, 2011.

[195] S. Chenna and P.A. Crozier. Operando transmission electron microscopy: A technique for detection of catalysis using electron energy-loss spectroscopy in the transmission electron microscope. *ACS Catalysis*, 2(11):2395–2402, 2012.

[196] B.K. Miller and P.A. Crozier. Analysis of catalytic gas products using electron energy-loss spectroscopy and residual gas analysis for operando transmission electron microscopy. *Microscopy and Microanalysis*, 20(3):815–824, 2014.

[197] R. Sharma. Kinetic measurements from *in situ* TEM observations. *Microscopy Research and Technique*, 72(3):144–152, 2009.

[198] T. Riedl, T. Gemming, and K. Wetzig. Extraction of EELS white-line intensities of manganese compounds: Methods, accuracy, and valence sensitivity. *Ultramicroscopy*, 106(4-5):284–291, 2006.

[199] D.B. Williams and C.B. Carter. *Transmission Electron Microscopy, A Text Book for Materials Science*. Springer, Second Edition, New-York, 2009.

[200] L. Reimer and H. Kohl. *Physics of Image Formation*. Springer, 2008.

[201] E.J. Kirkland. *Advanced computing in electron microscopy*. Springer, 2010.

[202] S.J. Pennycook and P.D. Nellist. *Scanning transmission electron microscopy*. Springer, 2011.

[203] J. Mayer, L.A. Giannuzzi, T. Kamino, and J. Michael. TEM sample preparation and FIB-induced damage. *MRS Bulletin*, 32:400–4007, 2007.

[204] F. Hofer and P. Warbichler. *Transmission Electron Energy Loss Spectrometry in Materials Science and The EELS Atlas*, chapter Elemental Mapping Using Energy Filtered Imaging, pages 159–222. Wiley, 2005.

[205] D.B. Williams and C.B. Carter. *Transmission electron microscopy, Part 3: Imaging*. Springer, Second edition, New-York, 2008.

[206] D.B. Williams and C.B. Carter. *Transmission electron microscopy, Part 2: Diffraction*. Springer, Second edition, New-York, 2008.

[207] C. Gammer, C. Mangler, C. Rentenberger, and H.P. Karnthaler. Quantitative local profile analysis of nanomaterials by electron diffraction. *Scripta Materialia*, 63(3):312–315, 2010.

[208] *Mathematica Edition: Version 8.0*. Wolfram Research, Inc., Champaign, Illinois, 2010.

[209] R.F. Egerton, F. Wang, M. Malac, M.S. Moreno, and F. Hofer. Fourier-ratio deconvolution and its Bayesian equivalent. *Micron*, 39(6):642–647, 2008.

[210] F. Wang, R.F. Egerton, and M. Malac. Fourier-ratio deconvolution techniques for electron energy-loss spectroscopy (EELS). *Ultramicroscopy*, 109(10):1245–1249, 2009.

[211] R.D. Leapman, L.A. Grunes, and P.L. Fejes. Study of the $L_{2,3}$ edges in the 3d transition metals and their oxides by electron-energy-loss spectroscopy with comparisons to theory. *Physical Review B*, 26(2):614–635, 1982.

[212] N Bonnet, , E. Simova, , and X. Thomas. Application of multivariate statistical analysis to time dependent spectroscopy. *Microsc. Microanal. Microstruct.*, 2(1):129–142, 1991.

[213] N. Bonnet, N. Brun, and C. Colliex. Extracting information from sequences of spatially resolved EELS spectra using multivariate statistical analysis. *Ultramicroscopy*, 77(3-4):97–112, 1999.

[214] G. Lucas, P. Burdet, M. Cantoni, and C. Hébert. Multivariate statistical analysis as a tool for the segmentation of 3D spectral data. *Micron*, 52-53:49–56, 2013.

[215] D.H. Pearson, C.C. Ahn, and B. Fultz. White lines and d-electron occupancies for the 3d and 4d transition metals. *Physical Review B*, 47(14):8471–8478, 1993.

[216] P.A. Van Aken, B. Liebscher, and V.J. Styrsa. Quantitative determination of iron oxidation states in minerals using Fe $L_{2,3}$-edge electron energy-loss near-edge structure spectroscopy. *Physics and Chemistry of Minerals*, 25(5):323–327, 1998.

[217] P.A. Van Aken and B. Liebscher. Quantification of ferrous/ferric ratios in minerals: New evaluation schemes of Fe L_{23} electron energy-loss near-edge spectra. *Physics and Chemistry of Minerals*, 29(3):188–200, 2002.

[218] I. Sobel and G. Feldman. A 3x3 isotropic gradient operator for image processing. In *Stanford Artificial Intelligence Project (SAIL)*, pages 1–5, 1968.

[219] B. Schaffer, W. Grogger, and G. Kothleitner. Automated spatial drift correction for EFTEM image series. *Ultramicroscopy*, 102(1):27–36, 2004.

[220] Z.L. Wang, J. Bentley, and N.D. Evans. Mapping the valence states of transition-metal elements using energy-filtered transmission electron microscopy. *The Journal of Physical Chemistry B*, 103(5):751–753, 1999.

[221] P. Schlossmacher, D.O. Klenov, B. Freitag, and H.S. von Harrach. Enhanced detection sensitivity with a new windowless XEDS system for AEM based on silicon drift detector technology. *Microscopy Today*, 18:14–20, 7 2010.

[222] G. Cliff and G.W. Lorimer. The quantitative analysis of thin specimens. *Journal of Microscopy*, 103(2):203–207, 1975.

[223] M. Weyland and P.A. Midgley. *Nanocharacterisation*, chapter Electron Tomography, pages 184–267. The Royal Society of Chemistry, 2008.

[224] C. Messaoudi, T. Boudier, C. Sorzano, and S. Marco. TomoJ: tomography software for three-dimensional reconstruction in transmission electron microscopy. *BMC Bioinformatics*, 8(1):1–9, 2007.

[225] P. Gilbert. Iterative methods for the three-dimensional reconstruction of an object from projections. *Journal of theoretical biology*, 36(1):105–117, 1972.

[226] E.F. Pettersen, T.D. Goddard, C.C. Huang, G.S. Couch, D.M. Greenblatt, E.C. Meng, and T.E. Ferrin. UCSF Chimera - A visualization system for exploratory research and analysis. *Journal of Computational Chemistry*, 25(13):1605–1612, 2004.

[227] E.F. Rauch, J. Portillo, S. Nicolopoulos, D. Bultreys, S. Rouvimov, and P. Moeck. Automated nanocrystal orientation and phase mapping in the transmission electron microscope on the basis of precession electron diffraction. *Zeitschrift fur Kristallographie*, 225(2-3):103–109, 2010.

[228] E.F. Rauch and L. Dupuy. Rapid spot diffraction patterns identification through template matching. *Archives of Metallurgy and Materials*, 50(1):87–99, 2005.

[229] J.I. Langford and D. Louer. Powder diffraction. *Reports on Progress in Physics*, 59:131–234, 1996.

[230] P. Malet and A. Caballero. The selection of experimental conditions in temperature-programmed reduction experiments. *J. Chem. Soc., Faraday Trans. 1*, 84:2369–2375, 1988.

[231] P. Scherrer. Bestimmung der Grösse und der inneren Struktur von Kolloidteilchen mittels Röntgenstrahlen. *Nachr. Ges. Wiss. Göttingen*, 26:98–100, 1918.

[232] J.I. Langford and A.J.C. Wilson. Scherrer after sixty years: A survey and some new results in the determination of crystallite size. *Journal of Applied Crystallography*, 11(2):102–113, 1978.

[233] H.J.T. Ellingham. Reducibility of oxides and sulfides in metallurgical processes. *Journal of the Society of Chemical Industry*, 63(125):125–133, 1944.

[234] F.D. Richardson and J.H.E. Jeffes. The thermodynamics of substances of interest in iron and steel making from 0 °C to 2400 °C: I-Oxides. *Iron and Steel Inst.*, 160:261, 1948.

[235] H. Gamsjäger, J. Bugajski, T. Gajda, R.J. Lemire, and W. Preis. Nuclear energy agency data bank, organisation for economic co-operation and development. In *Chemical Thermodynamics*, volume 6, pages 1–645. Elsevier, 2005.

[236] ©DoITPoMS. Ellingham diagrams, University of Cambridge.

[237] H.E. Kissinger. Reaction kinetics in differential thermal analysis. *Analytical Chemistry*, 29(11):1702–1706, 1957.

[238] J. Kranervo. *Kinetic analysis of temperature-programmed reactions*. PhD thesis, Helsinki University of Technology, 2003.

[239] F.J. Gotor, José, M. Criado, J. Malek, and N. Koga. Kinetic analysis of solid-state reactions: The universality of master plots for analyzing isothermal and nonisothermal experiments. *Journal of Physical Chemistry A*, 104(46):10777–10782, 2000.

[240] G.I. Senum and R.T. Yang. Rational approximations of the integral of the arrhenius function. *Journal of Thermal Analysis*, 11(3):445–447, 1977.

[241] J.A. Nelder and R. Mead. A simplex method for function minimization. *The Computer Journal*, 7(4):308–313, 1965.

[242] R.E. Carter. Kinetic model for solid-state reactions. *The Journal of Chemical Physics*, 34(6):2010–2015, 1961.

[243] A.T. Fromhold. Growth rate of low-space-charge oxides on spherical metal particles. *Journal of Physics and Chemistry of Solids*, 49(10):1159–1166, 1988.

[244] D.J. Young. *High Temperature Oxidation and Corrosion of Metals*, volume Volume 1, chapter Oxidation of Pure Metals, pages 81–137. Elsevier Science, 2008.

[245] S. Mrowec and Z. Grzesik. Oxidation of nickel and transport properties of nickel oxide. *Journal of Physics and Chemistry of Solids*, 65(10):1651–1657, 2004.

[246] C. Mitterbauer, G. Kothleitner, W. Grogger, H. Zandbergen, B. Freitag, P. Tiemeijer, and F. Hofer. Electron energy-loss near-edge structures of 3d transition metal oxides recorded at high-energy resolution. *Ultramicroscopy*, 96(3-4):469–480, 2003.

[247] J.T. Richardson, M. Lei, B. Turk, K. Forster, and Martyn V. Twigg. Reduction of model steam reforming catalysts: NiO/α-Al_2O_3. *Applied Catalysis A: General*, 110(2):217–237, 1994.

[248] B. Adnađević and B. Janković. Dispersive kinetic model for the non-isothermal reduction of nickel oxide by hydrogen. *Physica B: Condensed Matter*, 403(21-22):4132–4138, 2008.

[249] M.I. Buckett and L.D. Marks. Electron irradiation damage in NiO. *Surface Science*, 232(3):353–366, 1990.

[250] J.A. Little, J.W. Evans, and K.H. Westmacott. Early stages of reduction of nickel oxide single crystals: An investigation by transmission electron microscope. *Metallurgical Transactions B*, 11(3):519–524, 1980.

[251] K.M. Ostyn and C.B. Carter. On the reduction of nickel oxide. *Surface Science*, 121(3):360–374, 1982.

[252] G.R. Belton and A.S. Jordan. Gaseous hydroxides of cobalt and nickel. *The Journal of Physical Chemistry*, 71(12):4114–4120, 1967.

[253] K. Du, F. Ernst, M. Garrels, and J. Payer. Formation of nickel nanoparticles in nickel-ceramic anodes during operation of solid-oxide fuel cells. *International Journal of Materials Research*, 99(5):548–552, 2008.

[254] E.J. Mittemeijer and U. Welzel. The "state of the art" of the diffraction analysis of crystallite size and lattice strain. *Zeitschrift fur Kristallographie*, 223(9):552–560, 2008.

[255] R.F. Egerton, P. Li, and M. Malac. Radiation damage in the TEM and SEM. *Micron*, 35(6):399–409, 2004.

[256] Z. Zhang and D. Su. Behaviour of TEM metal grids during *in-situ* heating experiments. *Ultramicroscopy*, 109(6):766–774, 2009.

[257] H.E. Evans. Stress effects in high temperature oxidation of metals. *International Materials Reviews*, 40(1):1–40, 1995.

[258] R. Karmhag, G.A. Niklasson, and M. Nygren. Oxidation kinetics of nickel nanoparticles. *Journal of Applied Physics*, 89(5):3012–3017, 2001.

[259] S. Mrowec. On the mechanism of high temperature oxidation of metals and alloys. *Corrosion Science*, 7(9):563–578, 1967.

[260] P. Hancock and R.C. Hurst. The mechanical properties and breakdown of surface oxide films at elevated temperatures. In M.G. Fontana and R.W. Staehle, editors, *Advances in Corrosion Science and Technology*, pages 1–84. Springer US, 1974.

[261] D.L. Douglass. The role of oxide plasticity on the oxidation behavior of metals: A review. *Oxidation of Metals*, 1(1):127–142, 1969.

[262] N. Jiang, D. Su, and J.C.H. Spence. On the measurement of thickness in nanoporous materials by EELS. *Ultramicroscopy*, 111(1):62–65, 2010.

[263] H. Jónsson, G. Mills, and K.W. Jacobsen. *Classical and Quantum Dynamics in Condensed Phase Simulations*, chapter Nudged Elastic Band Method for Finding Minimum Energy Paths of Transitions, pages 285–404. World Scientific, 1998.

[264] G. Henkelman, B. P. Uberuaga, and H. Jónsson. Climbing image nudged elastic band method for finding saddle points and minimum energy paths. *Journal of Chemical Physics*, 113(22):9901–9904, 2000.

[265] D.A. Porter and K.E. Easterling. *Phase Transformation in Metals and Alloys*. Taylor & Francis, 1992.

[266] S.I. Wright and R.J. Larsen. Extracting twins from orientation imaging microscopy scan data. *Journal of Microscopy*, 205(3):245–252, 2002.

[267] C.B. Thomson and V. Randle. A study of twinning in nickel. *Scripta Materialia*, 35(3):385–390, 1996.

[268] M. Andrzejczuk, O. Vasylyev, I. Brodnikovskyi, V. Podhurska, B. Vasyliv, O. Ostash, M. Lewandowska, and K.J. Kurzydłowski. Microstructural changes in NiO-ScSZ composite following reduction processes in pure and diluted hydrogen. *Materials Characterization*, 87:159–165, 2014.

[269] E.C. Dickey, V.P. Dravid, P.D. Nellist, D.J. Wallis, S.J. Pennycook, and A. Revcolevschi. Structure and bonding at Ni-ZrO_2 (cubic) interfaces formed by the reduction of a NiO-ZrO_2 (cubic) composite. *Microscopy and Microanalysis*, 3(5):443–450, 1997.

[270] S. Mahajan, C.S. Pande, M.A. Imam, and B.B. Rath. Formation of annealing twins in f.c.c. crystals. *Acta Materialia*, 45(6):2633–2638, 1997.

[271] H. Hidalgo, E. Reguzina, E. Millon, A.-L. Thomann, J. Mathias, C. Boulmer-Leborgne, T. Sauvage, and P. Brault. Yttria-stabilized zirconia thin films deposited by pulsed-laser deposition and magnetron sputtering. *Surface and Coatings Technology*, 205(19):4495–4499, 2011.

[272] A. Hauch, S.H. Jensen, J.B. Bilde-Sørensen, and M. Mogensen. Silica segregation in the Ni/YSZ electrode. *Journal of the Electrochemical Society*, 154(7):619–626, 2007.

[273] A.E. Hughes and S.P.S. Badwal. Impurity and yttrium segregation in yttria-tetragonal zirconia. *Solid State Ionics*, 46(3-4):265–274, 1991.

[274] M. Shishkin and T. Ziegler. Direct modeling of the electrochemistry in the three-phase boundary of solid oxide fuel cell anodes by density functional theory: a critical overview. *Phys. Chem. Chem. Phys.*, 16:1798–1808, 2014.

[275] M. Shishkin and T. Ziegler. The oxidation of H_2 and CH_4 on an oxygen-enriched yttria-stabilized zirconia surface: A theoretical study based on density functional theory. *Journal of Physical Chemistry C*, 112(49):19662–19669, 2008.

[276] F.A. Kröger and H.J. Vink. Relations between the concentrations of imperfections in crystalline solids. In *Solid State Physics*, volume 3, pages 307–435. Elsevier, 1956.

[277] M. Shishkin and T. Ziegler. Hydrogen oxidation at the Ni/yttria-stabilized zirconia interface: A study based on density functional theory. *The Journal of Physical Chemistry C*, 114(25):11209–11214, 2010.

[278] M.I. Buckett, J. Strane, D.E. Luzzi, J.P. Zhang, B.W. Wessels, and L.D. Marks. Electron irradiation damage in oxides. *Ultramicroscopy*, 29(1-4):217–227, 1989.

[279] M. Shishkin and T. Ziegler. Oxidation of H_2, CH_4, and CO molecules at the interface between nickel and yttria-stabilized zirconia: A theoretical study based on DFT. *The Journal of Physical Chemistry C*, 113(52):21667–21678, 2009.

[280] Alicona®. Mex™, 2009.

[281] F. Abdeljawad and M. Haataja. Microstructural coarsening effects on redox instability and mechanical damage in solid oxide fuel cell anodes. *Journal of Applied Physics*, 114(183519):1–9, 2013.

[282] C. Wen, R. Kato, H. Fukunaga, H. Ishitani, and K. Yamada. Overpotential of nickel/yttria-stabilized zirconia cermet anodes used in solid oxide fuel cells. *Journal of the Electrochemical Society*, 147(6):2076–2080, 2000.

[283] W.Z. Zhu and S.C. Deevi. A review on the status of anode materials for solid oxide fuel cells. *Materials Science and Engineering A*, 362(1-2):228–239, 2003.

[284] V. Randle. Twinning-related grain boundary engineering. *Acta Materialia*, 52(14):4067–4081, 2004.

[285] Y.L. Liu, S. Primdahl, and M. Mogensen. Effects of impurities on microstructure in Ni/YSZ-YSZ half-cells for SOFC. *Solid State Ionics*, 161(1-2):1–10, 2003.

[286] Q.X. Fu and F. Tietz. Ceramic-based anode materials for improved redox cycling of solid oxide fuel cells. *Fuel Cells*, 8(5):283–293, 2008.

[287] A.T. Chadwick and R.I. Taylor. Trace element effects in oxidation: The influence of cerium on grain boundary transport in nickel oxide. *Solid State Ionics*, 12(C):343–351, 1984.

[288] D.P. Moon. The reactive element effect on the growth rate of nickel oxide scales at high temperature. *Oxidation of Metals*, 32(1-2):47–66, 1989.

[289] D.P. Moon. Role of reactive elements in alloy protection. *Materials Science and Technology*, 5(8):754–764, 1989.

[290] F. Czerwinski and J.A. Szpunar. The correlation between the surface roughness and growth mechanism in thin NiO films modified by CeO_2. *Corrosion Science*, 39(1):147–158, 1997.

[291] R. Haugsrud. On the effects of surface coatings on the high-temperature oxidation of nickel. *Corrosion Science*, 45(6):1289–1311, 2003.

[292] A.A. Moosa, S.J. Rothman, and L.J. Nowicki. Effect of yttrium additions to nickel on the volume and grain boundary diffusion of Ni in the scale formed on the alloy. *Oxidation of Metals*, 24(3-4):115–132, 1985.

[293] A.A. Moosa and S.J. Rothman. Effect of yttrium additions on the oxidation of nickel. *Oxidation of Metals*, 24(3-4):133–148, 1985.

[294] P.H. Larsen, C. Chung, and M. Mogensen. Redox-stable anode, August 2012. US Patent 8,252,478B2.

[295] M.H. Pihlatie, A. Kaiser, and M.B. Mogensen. Electrical conductivity of Ni-YSZ composites: Variants and redox cycling. *Solid State Ionics*, 222-223:38–46, 2012.

[296] G. Xiao and F. Chen. Redox stable anodes for solid oxide fuel cells. *Frontiers in Energy Research*, 2(18), 2014.

[297] A. Wood and D. Waldbillig. Preconditioning treatment to enhance redox tolerance of solid oxide fuel cells, June 2006. US Patent 0141300A1.

[298] M.C. Akatay, Y. Zvinevich, P. Baumann, F.H. Ribeiro, and E.A. Stach. Gas mixing system for imaging of nanomaterials under dynamic environments by environmental transmission electron microscopy. *Review of Scientific Instruments*, 85(3):1–5, 2014.

[299] www.denssolutions.com/. DENS solutions.

[300] L.C. Gontard, R.E. Dunin-Borkowski, A. Fernández, D. Ozkaya, and T. Kasama. Tomographic heating holder for *in situ* TEM: Study of Pt/C and $PtPd/Al_2O_3$ catalysts as a function of temperature. *Microscopy and Microanalysis*, 20(3):982–990, 2014.

[301] P. Thévoz. Place the word hot air balloon in your thesis. *Everything is awesome*, pages 1–1, 2014.

[302] U. Martin, H. Boysen, and F. Frey. Neutron powder investigation of tetragonal and cubic stabilized zirconia, TZP and CSZ, at temperatures up to 1400 K. *Acta Crystallographica Section B*, 49(3):403–413, 1993.

[303] M. Fanfoni and M. Tomellini. The Johnson-Mehl-Avrami-Kolmogorov model: A brief review. *Nuovo Cimento della Societa Italiana di Fisica D - Condensed Matter, Atomic, Molecular and Chemical Physics, Biophysics*, 20(7-9):1171–1182, 1998.

[304] P. Giannozzi, S. Baroni, N. Bonini, M. Calandra, and *et al.* Quantum espresso: a modular and open-source software project for quantum simulations of materials. *Journal of Physics-Condensed Matter*, 21(39):395502, 2009.

[305] J.P. Perdew, K. Burke, and M. Ernzerhof. Generalized gradient approximation made simple. *Physical Review Letters*, 77(18):3865, 1996.

[306] D. Vanderbilt. Soft self-consistent pseudopotentials in a generalized eigenvalue formalism. *Physical Review B*, 41(11):7892, 1990.

[307] X. Xia, R. Oldman, and R. Catlow. Computational modeling study of bulk and surface of yttria-stabilized cubic zirconia. *Chemistry of Materials*, 21(15):3576–3585, 2009.

[308] M. Hanasaki, C. Uryu, T. Daio, T. Kawabata, Y. Tachikawa, S.M. Lyth, Y. Shiratori, S. Taniguchi, and K. Sasaki. SOFC durability against standby and shutdown cycling. *Journal of the Electrochemical Society*, 161(9):F850–F860, 2014.

Contributions & CV

Peer-reviewed publications

1. ***In situ* redox cycle of a nickel-YSZ fuel cell anode in an environmental transmission electron microscope**
   Q. Jeangros, A. Faes, J.B. Wagner, T.W. Hansen, U. Aschauer, J. Van herle, A. Hessler-Wyser, and R.E. Dunin-Borkowski, *Acta Materialia*, 58:4578-4589, 2010

2. **Combined Cr and S poisoning in solid oxide fuel cell cathodes**
   J. A. Schuler, H. Yokokawa, C.F. Calderone, Q. Jeangros, Z. Wuillemin, A. Hessler-Wyser, and J. Van herle, *Journal of Power Sources*, 201:112-120, 2012

3. **Reduction of nickel oxide particles by hydrogen studied in an environmental TEM**
   Q. Jeangros, T.W. Hansen, J.B. Wagner, C.D. Damsgaard, R.E. Dunin-Borkowski, C. Hébert, J. Van herle, and A. Hessler-Wyser, *Journal of Materials Science*, 48, 2893-2907, 2014

4. **Measurements of local chemistry and structure in Ni(O)-YSZ composites during reduction using energy-filtered environmental TEM**
   Q. Jeangros, T.W. Hansen, J.B. Wagner, R.E. Dunin-Borkowski, C. Hébert, J. Van herle, and A. Hessler-Wyser, *Chemical Communications*, 50:1808-1810, 2014

5. **Oxidation mechanism of nickel particles studied in an environmental transmission electron microscope**
   Q. Jeangros, T.W. Hansen, J.B. Wagner, R.E. Dunin-Borkowski, C. Hébert, J. Van herle, and A. Hessler-Wyser, *Acta Materialia*, 67:363-372, 2014

6. **Silicon heterojunction solar cells with copper-plated grid electrodes: status and comparison with silver thick-film techniques**
   J. Geissbuhler, J., S. Wolf, A. Faes, N. Badel, Q. Jeangros, A. Tomasi, L. Barraud, A. Descoeudres, M. Despeisse and C. Ballif. *IEEE Journal of Photovoltaics*, 4:1055-1062, 2014

7. **Low-temperature plasma-deposited silicon epitaxial films: growth and properties**
   B. Demaurex, R. Bartlome, J.P. Seif, J. Geissbuhler, D.T.L. Alexander, Q. Jeangros, C. Ballif and S. De Wolf *Journal of Applied Physics*, 116:053519-1-9, 2014

8. **Hydrogen plasma treatment for improved conductivity in amorphous aluminum doped zinc tin oxide thin films**
   M. Morales-Masis, L. Ding, F. Dauzou, Q. Jeangros, A. Hessler-Wyser, S. Nicolay, C. Ballif, *APL Materials*, In press, 2014

Oral presentations

1. *In situ* reduction and reoxidation of a solid oxide fuel cell anode in an environmental TEM
   Materials Science and Engineering, 2010, Darmstadt, Germany
   Abstract and oral presentation
2. Kinetic analysis of NiO reduction in an environmental TEM
   Groupe des Utilisateurs en Microscopie Electronique Philips, spring 2011, Guadeloupe, France
   Abstract and oral presentation
3. NiO reduction studied by environmental TEM and *in situ* XRD
   EPFL-TITECH workshop, 2012, Hakone, Japan
   Abstract, poster and oral presentation
4. NiO reduction studied by environmental TEM
   European Materials Research Society Spring Meeting, 2012, Strasbourg, France
   Abstract and oral presentation
5. Nickel oxide reduction studied by environmental TEM
   European Fuel Cell Forum, 2012, Lucerne, Switzerland
   Abstract, proceeding and oral presentation
6. Reduction of nickel oxide particles in an environmental TEM
   European Microscopy Congress, 2012, Manchester, United Kingdom
   Abstract and oral presentation
7. Oxidation kinetics of nickel particles by EELS in an environmental TEM
   Enhanced Data Generated by Electrons, 2013, Sainte Maxime, France
   Abstract and oral presentation
8. Insights into the oxidation mechanisms of nickel particles by environmental TEM
   Societé Française des Microscopies, 2013, Nantes, France
   Abstract and oral presentation
9. Insights into the oxidation mechanisms of nickel particles by environmental TEM
   Modelling and Simulation Meet Innovation in Ceramics Technology, 2013, Trento, Italy
   Abstract and oral presentation
10. Oxidation mechanism of nickel particles studied in an environmental transmission electron microscope
    Symposium for Fuel Cell and Battery Modeling and Experimental Validation, 2014, Winterthur, Switzerland
    Abstract and oral presentation
11. Measurements of local chemistry and structure in NiO-YSZ composites during reduction using energy-filtered environmental TEM
    Challenges and Opportunities in In Situ Studies of Solid Oxide Electrodes, 2014, Technical University of Denmark, Risø, Denmark
    Invited oral presentation
12. Measurements of local chemistry and structure in NiO-YSZ composites during reduction using energy-filtered environmental TEM
    European Fuel Cell Forum, 2014, Lucerne, Switzerland
    Abstract, proceeding and oral presentation

13. Measurements of local chemistry and structure in NiO-YSZ composites during reduction using energy-filtered environmental TEM
International Microscopy Congress, 2014, Prague, Czech Republic
Abstract and oral presentation

Poster presentations

1. *In situ* redox cycle of a nickel–YSZ fuel cell anode in an environmental transmission electron microscope
Transport in Porous Materials, 2010, Paul Scherrer Institute, Villigen, Switzerland
Abstract and poster
2. NiO reduction at the nanoscale: An environmental TEM study
Microscopy & Microanalysis, 2012, Phoenix, USA
Abstract and poster
3. Reduction of NiO by hydrogen studied by environmental TEM
Materials Science and Engineering, 2012, Darmstadt, Germany
Abstract and poster
4. Insights into the oxidation mechanisms of Ni particles using environmental TEM,
Microscopy & Microanalysis, 2013, Indianapolis, USA
Abstract and poster
Student poster award

Student projects

1. Behaviour of Ni particles on SOFC anode surfaces, F. Loisy
Semester master project, spring 2012
2. Electron microscopy analysis of NiO during *ex situ* reduction for solid oxide fuel cell applications, M. Hadad, F. Parsapour & L. Batooli
Advanced TEM techniques course, spring 2011
3. RedOx cycling of NiO particles, A.K. Mohamed, C. Olk & F. Nabiei
Advanced TEM techniques course, spring 2012
4. EFTEM study of reduction of NiO/YSZ composite anode microstructures, K. Rolle, E. Ponomarev & A. Shah
Advanced TEM techniques course, spring 2013

Born in 1986
Swiss & French citizenship

Chemin des Morettes 16
CH-1197 Prangins, Switzerland
+41 (0)76 495 84 81
quentin.jeangros@gmail.com

Quentin Jeangros

- PhD at EPFL on *in situ* characterisation of solid oxide fuel cells
- Expertise in advanced scanning and transmission electron microscopy techniques
- International experience in Europe & Asia, fluent in English

Education

2010–2014 **PhD** at the *Interdisciplinary Centre for Electron Microscopy*
Ecole Polytechnique Fédérale de Lausanne, Switzerland

2004–2009 **Bachelor & Master in Materials Science & Engineering**, *Ecole Polytechnique Fédérale de Lausanne*
Specialization in **materials for energy & materials characterization**
Exchange program at the *Nanyang Technological University, Singapore* (2007/8)

2001–2004 High school degree at the Gymnase de Nyon, Vaud, Switzerland (physics & mathematics)

Academic projects, publications & awards

PhD ***In situ* transmission electron microscopy study of reduction and reoxidation of Ni(O)-ceramic composites**
Development of new strategies to relate at the nanoscale structure & chemistry of solid oxide fuel cell anode materials during reduction/oxidation to understand their reaction and degradation pathways
Collaboration with the *Technical University of Denmark* and the *Fuelmat Group* at EPFL
Poster prize at the Micoscopy & Microanalysis conference, Indianapolis, USA (2013)
Selected for the **Lindau Nobel Laureate Meeting** (2010)

Master thesis **Solid oxide fuel cell anode redox instability characterised by *in situ* transmission electron microscopy**
First live observations at high magnification of a degradation mechanism in fuel cells
Swiss Association for Materials Science and Technology prize

Main peer-reviewed publications
Jeangros Q, Hansen TW *et al.*, Acta Materialia 67 (2014) p.363
Jeangros Q, Hansen TW *et al.*, Chemical Communications 50 (2014) p.1808
Jeangros Q, Hansen TW *et al.*, Journal of Materials Science 48 (2013) p.289
Jeangros Q, Faes A *et al.*, Acta Materialia 58 (2010) p.4578

Skills

Languages **French (native), English (C1, proficient), German (B1, intermediate)**

Computer Adobe Photoshop & Illustrator, Keynote, Office, LaTeX, ImageJ, JEMS
programming: C, Mathematica & Digital Micrograph

Laboratory **Advanced electron microscopy techniques** (diffraction, Cs-corrected high-resolution, electron energy-loss spectroscopy, energy-filtered imaging, tomography, energy-dispersive X-ray spectroscopy, focused ion beam, environmental & heating techniques), *in situ* X-ray diffraction, thermogravimetry, solid-state kinetic modeling

Communication **Oral presentations at 12 national & international scientific conferences**, including the European Microscopy Congress (Manchester, UK, 2012), European Fuel Cell Forum (Lucerne, Switzerland, 2012/14), European Materials Research Society Spring Meeting (Strasbourg, France, 2012), International Microscopy Congress (Prague, 2014)

Experience

Teaching Training of new users to transmission electron microscope techniques, tutorial assistant in physics (undergraduate), practical work assistant in advanced electron microscopy techniques (graduate), supervision of student projects

Civil service completed - social worker, collaborator in agricultural research, electron microscopist in photovoltaics research

Others Football coach, member of the organizing comity of a student music festival at EPFL (2006/7, 15'000 festival-goers)

Interests

Sport Marathon & mountain trails, ski touring in the Alps

Travels Avid traveller, still looking for the best noodle soup in Asia